ARKTALAS HOAVVA PROJECT

DELIVERABLE 170: FINAL REPORT

Customer	ESA
Author	Consortium
Distribution	Consortium and ESA
ESA Contract Number	4000127401/19/NL/LF
Document Reference	Final Report (FR)
SoW Deliverable Reference	Deliverable D-170
Version/Revision	1.0
Date of issue	13. October 2023

Approved by (NERSC)	Johnny A. Johannessen NERSC Project Manager	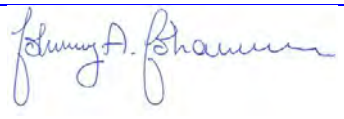
Approved by (ESA)	Craig Donlon ESA Technical Officer	esa Digitally signed by Craig James Donlon Date: 2023.10.22 09:18:23 +02'00'

Revision Change log

Issue	Date	Type	Change description
0.1	8. August 2023	Draft FR	ToC and structure
0.5	19. September	1st draft final	Contents from D-10 to D-150
1.0	13. October	Delivered to ESA	Contains contents from all deliverables

The Arktalas Hoavva Final Report (D-170) shall include a complete description of all the work done during the study and shall be self-standing, not requiring to be read in conjunction with reports previously issued. It shall cover the whole scope of the study, i.e. a comprehensive introduction of the context, a description of the programme of work and report on the activities performed and the main results achieved.

The Final Report is a mandatory deliverable, due upon completion of the work performed under the Contract. For the avoidance of doubt, "completion of the work performed under the Contract" shall mean the finalisation of a series of tasks as defined in a self-contained Statement of Work.

Table of Content

EXECUTIVE SUMMARY

The overall aim of the *Arktalas Hoavva* project is to demonstrate the current capabilities and future needs in use of satellite measurements, in synergy together with in situ and modelling tools, to characterize and quantify the processes driving change in the Arctic sea ice and the Arctic Ocean. To achieve this the project has addressed four major interlinked Arctic Scientific Challenges (ASC):

- Characterize the Arctic Amplification and its impact (ASC-1)
- Characterize the impact of more persistent and larger area of open water on sea ice dynamics (ASC-2)
- Characterize and predict the impact of extreme event storms on sea-ice formation pattern and structures (ASC-3)
- Characterize and predict the Arctic Ocean spin-up (ASC-4)

These ASC have been explored and examined through the following 8 scientific publications:

1. Esau, I.; Pettersson, L.H.; Cancet, M.; Chapron, B.; Chernokulsky, A.; Donlon, C.; Sizov, O.; Soromotin, A.; Johannessen, J.A. **The Arctic Amplification and Its Impact: A Synthesis through Satellite Observations**. *Remote Sens.* **2023**, *15*, 1354. https://doi.org/10.3390/rs15051354
2. Collard, F., Marié, L., Nouguier, F., Kleinherenbrink, M., Ehlers, F., & Ardhuin, F. (2022). **Wind-wave attenuation in Arctic sea ice: A discussion of remote sensing capabilities.** *Journal of Geophysical Research: Oceans*, 127, e2022JC018654. https://doi.org/10.1029/2022JC018654
3. Boutin G, Williams T, HorvatC, Brodeau L. (2022). **Modelling the Arctic wave-affected marginal ice zone: acomparison with ICESat-2 observations.** *Phil.Trans. R. Soc. A380: 20210262.* https://doi.org/10.1098/rsta.2021.0262
4. Rheinlænder, J. W., Davy, R., Ólason, E., Rampal, P., Spensberger, C., Williams, T. D., Korosov, A. and Spengler, T. (2022). **Driving mechanisms of an extreme winter sea ice breakup event in the Beaufort Sea.** *Geophysical Research Letters*, 49, e2022GL099024. https://doi.org/10.1029/2022GL099024
5. H. Regan, C. Lique, C. Talandier and G. Meneghello (2020). **Response of Total and Eddy Kinetic Energy to the recent spin up of the Beaufort Gyre.** Published in *J. Physic. Oceangr.*, p. 575-594, 1. March 2020, https://doi.org/10.1175/JPO-D-19-0234.1
6. Cassianides, A., Lique, C., & Korosov, A. (2021). **Ocean eddy signature on SAR-derived sea ice drift and vorticity.** *Geophysical Research Letters*, 48, e2020GL092066. https://doi.org/10.1029/2020GL092066
7. Mathilde Cancet, Florent H. Lyard, and Ergane Fouchet (submitted 2023). **Impact of sea-ice friction on tidal modelling in the Arctic Ocean, modelling insights at various time and space scales**. Submitted to Ocean Modelling.
8. Lucas, S.; Johannessen, J.A.; Cancet, M.; Pettersson, L.H.; Esau, I.; Rheinlænder, J.W.; Ardhuin, F.; Chapron, B.; Korosov, A.; Collard, F.; Herlédan, S.; Olason, E.; Ferrari, R.; Fouchet, E.; Donlon, C. (2023). **Knowledge Gaps and Impact of Future Satellite Missions to Facilitate Monitoring of Changes in the Arctic Ocean.** *Remote Sens.* 2023, *15*, 2852. https://doi.org/10.3390/rs15112852

Based on the findings and scientific results highlighted in these papers as well as the generation of the Arktalas Data Archive System (ADAS) and Arktalas analyses and Visualization System (AVS) tools the *Arktalas Hoavva* project bring forward the following lessons learned with respect to characterize and quantify the processes driving change in the Arctic sea ice and the Arctic Ocean.

In order to fully benefit from the satellite-based observation capabilities there is a crucial need for Fiducial Reference Measurement (FRM) data for calibration and validation, in particular as finer spatial resolution are emerging. Moreover, towards 2030 advances in development of Digital Arctic Twin components jointly with regular reprocessing, use of sensor synergy and multi-modal physical constrained co-variability analytics are likely to deliver more reliable estimates of sea ice drift, damage, break-up, lead fraction, new ice formation, sea ice freeboard height, sea ice volume, mean sea level and sea surface height. In turn, the quantitative understanding of the dominant multidisciplinary physical interactive processes that drive the sea ice thermodynamic state and variability in the Arctic Ocean and its marginal ice zones is anticipated to strengthen, notably regarding:

- atmospheric boundary layer stratification and thermodynamics;
- upper ocean stratification and thermodynamics;
- momentum, gas and heat fluxes;
- freshwater spreading;
- local and non-local connexions.

The identified key technical and organizational needs are rather generic and can be summarized to the following needs:

- to provide efficient and interoperable frameworks and architectures to access data and model resources across institutions and organizations;
- to constitute large, homogeneous, curated multi-variable datasets for model training and validation (AI-ready datasets);
- to refine mathematical approaches tailored to cope with sparse data and analysis of rare and/or extreme events;
- to consider software infrastructure and common tools for supporting developments of hybrid model components.

Prioritizing the collection, synthesis and curation of reference data (including in situ, satellite, and numerical simulations) is key to create AI-ready datasets for model training and validation. Reanalysis models, assimilating satellite and in-situ observations already offer open-access data-cube facilities to help apply AI techniques (i.e. reanalysis performs a consistent dynamical space-time gridded interpolation of the different variables). Still, these models do not manage to precisely identify all the multiple and complex interactions between variables (e.g. atmospheric boundary layer, upper ocean physical and biological coupling across differing space-time scales including rare and extreme events). As such it is

highly important to systematically combine the present-day available model-data cubes with direct satellite-based and in-situ based observations to strengthen the generation of AI-ready datasets.

In particular the Arktalas Scientific Roadmap identifies the following priority activities to be addressed in the short-term future:

Advanced sensor synergy retrievals of sea ice drift trajectories from Sentinel-1 SAR, as a model-driven precursor to demonstrate the advanced Digital Twin Component capabilities. To be used to simulate complex processes that are not properly characterized in state sea ice models, with targeted focus on CIMR, Rose-L, and Cristal missions in combination with operational meteorological satellites.

Validation of the sea ice rheology in satellite data, through a novel metric building on multi-sensor satellite observation synergy needs to evaluate Lagrangian model simulations (e.g. neXtSIM) including detection and tracking of linear kinematic features associated with sea ice damage and lead formation.

Improving air and ocean drag coefficient parametrization in the neXtSIM sea ice model, by using ICESat-2 in synergy with CryoSat-2 and Sentinel-1 to derive sea ice roughness at much higher spatial resolution. Time- and space-varying fields of sea ice roughness can then be used for computing the air and ocean drag coefficients and expectedly improve the quality of the operational sea ice forecasts.

Detection and characterization of marginal ice zone on Sentinel-1 SAR. Train ML-algorithms on Sentinel-1 SAR data and ice charts for robust detection of marginal ice zone dynamics and characterization of the sea ice in terms of floe size distribution. To be applied to series of SAR images for their assimilation into a future integrated neXtSIM-wave model to be tested in an operational setup.

Longer time series of sea ice age fraction maps. Develop a new sea ice age algorithm that provides a distribution of ice age fractions for each pixel in homogenous fields to be explored for the AMSR2 era (2002 to present) and using OSI-SAF ice drift in winter and TOPAZ (or neXtSIM) reanalysis data in summer extending the consistent ice fraction maps back to 1994.

Simulation of CIMR brightness temperatures in sea ice model. High resolution CIMR radiometer data of the ice and snow emissivity can be plugged into neXtSIm to simulate CIMR data at high resolution. The simulated data can be used for testing / developing CIMR algorithms, for instance, starting activities of assimilating CIMR data at brightness temperature level.

Ground truthing of present and future missions: Capitalizing on the regular UNIS (Svalbard) field studies as the opportunity to use Svalbard as a "*Sustainable Climate Reference Laboratory for Earth Observation*". Such refence observations is highly needed for

establishing consistent time series (like the Manoa Loa CO_2 measurements) for both pre- and post-launch Copernicus expansion missions (CRISTAL, CIMR, Rose-L and the Next generation Sentinel-3 altimeter) field campaigns. Primary products might include SST, local sea ice concentration, thickness, extent, type, snow cover and depth, presence of meltwater ponds, salinity, water vapor and cloud liquid water content. In particular, it is recommended to conduct a pilot study over a sea ice reference site in vicinity of the Svalbard including access to coincident scanning laser data take.

All in all these recommended near future activities will, in turn, strengthen the research and understanding of the important role of the Arctic Ocean in transition at the regional to global scales, notably regarding:

- transport of freshwater and Atlantic Water in the Arctic Ocean in the presence of declining sea ice extent;
- changes in biogeochemistry, biology and ecosystem under the transition towards a blueArctic;
- vertical mixing processes from the top of the atmospheric boundary layer to the depth of the halocline layer in the upper ocean;
- the regional water cycle, energy cycle and carbon cycle;
- teleconnection and influence on weather and climate at lower latitudes (globally in fact).

The Arktalas Hoavva project activities and deliverables are available here and the the NERSC Arctic Portal (user front end) for visualisation and synergetic analysis of environmental data and model simulations for the Arctic sea ice and oceans.

1 INTRODUCTION

The overall aim of the *Arktalas Hoavva* study is to demonstrate the current capabilities and future needs in use of satellite measurements, in synergy together with in situ and modelling tools, to characterize and quantify the processes driving change in the Arctic sea ice and the Arctic Ocean.

In the high latitude seas and the Arctic Ocean, global warming and Arctic Amplification are considered to occur across a range of environmental state variables with complex interactions and feedback mechanisms at regional to global scales. Central among these are changes in the radiation balance, changes in ocean-sea ice-atmosphere momentum, heat and gas exchanges, reduction in the sea ice extent and thickness, and changes in the bio-optical properties in the upper ocean. In turn, the Arctic Polar Regions experience increased air temperature, delayed onset of sea ice freezing, early onset of sea ice melting, increasing area of melt ponds, polynyas and surface meltwater, increased lead fraction and sea ice drift, reduction of near shore fast ice area, changes of snow cover, snow water equivalent (SWE), changes in albedo, a much larger wind fetch and enhanced wave-sea ice interaction leading to sea ice break-up and delays in freeze-up , as well as shifts in and expansions of the Marginal Ice Zone (MIZ). Moreover, the atmospheric boundary layer adjustment to these changes is anticipated to alter the weather patterns and influence the Arctic vortex, with corresponding atmospheric teleconnection to lower latitudes.

Accordingly, in the *Arktalas Hoavva* project, the four below major interlinked Arctic Scientific Challenges (ASC) are justified and have been investigated with the goals to:

- **Characterize the Arctic Amplification and its impact (ASC-1)**
  In the high latitude seas and Arctic Ocean global warming and Arctic amplification are considered to occur across a range of quantities and their interactions and feedback mechanisms. Central among these (not exclusive) are: - changes in the radiation balance; - increased air temperature; - delayed onset of sea ice freezing; - early onset of sea ice melting; - increasing area of melt ponds and polynias; - increased lead fraction; - reduction in sea ice extent; - changes in albedo; - changes in snow cover and SWE; - changes in ocean-atmosphere momentum, heat exchange and gas exchanges; - reduction in fast ice area; - thinning of sea ice thickness; - larger fetch; - enhanced wave-sea ice interaction; - changes in optical conditions in the upper ocean with influence on the biology and marine ecosystem; - more favourable conditions for sea ice drift; - more meltwater; - more wave induced sea ice break-up; - modifications to atmospheric boundary layer and changes in weather pattern; - influence on Arctic vortex and hence teleconnection to mid-latitudes.
- **Characterize the impact of more persistent and larger area of open water on sea ice dynamics (ASC-2)**

This research challenge is associated with: - increasing momentum transfer to the upper ocean leading to more turbulent mixing and possibly entrainment of warm Atlantic Water below the halocline; - increasing Ekman effects; - changes in sea ice growth, salt rejection and halocline formation; - larger fetch and lower frequency waves penetrating further into the ice covered regions leading to more floe-break-up; - increasing lead fraction and more sea ice melting; - reduction in sea ice flow size, age, thicknesses and extent and subsequent change in sea ice mechanical behaviour; - possibly more abundance of internal waves and mesoscale and sub-mesoscale eddies generated in the open ocean with subsequent abilities to propagate into the ice covered regions leading to changes in sea ice deformation and dynamics (e.g. Cole et al., 2018).

- **Characterize and predict the impact of extreme event storms on sea-ice formation pattern and structures (ASC-3)**
  Growing areas of open water within the Arctic Ocean will be more effectively exposed to extreme events. A central question is eventually whether this favour increasing frequency and strength of extremes. Polar lows and cold air outbreak, for instance, are known to have strong impact in the Marginal Ice Zone (MIZ), including; - enhanced momentum transfer and vertical mixing; - enhanced sea ice formation; - enhanced formation of unstable stratification in the atmospheric boundary layer; - more low cloud formations changing the radiation balance; - set up of abnormal wave field to strengthen wave induced sea ice break-up; - abnormal impact on the pycnocline and subsequent entrainment of heat into the upper mixed.
- **Characterize and predict the Arctic Ocean spin-up (ASC-4)**
  A central question is how the ongoing Arctic amplification and subsequent changes, mutual interactions and feedback mechanisms influence the basin scale atmospheric and ocean circulation within the Arctic Ocean. This will in particular address the: - freshwater distribution and transport; - importance of Ekman pumping; - changes in water mass properties; - changes in upper ocean stratification and mixing; - changes in sub-surface heat exchange; - possibly more abundance of internal waves and mesoscale and sub-mesoscale eddies generated in the open ocean with subsequent abilities to propagate into the ice covered regions.

The investigations have been executed across seven interlinked specific scientific objectives, including:

- **OBJ-1:** Define and implement scientific analysis, with a focus on synergy application building on a multi-modal data-driven analyses framework.
- **OBJ-2:** Develop and generate a multi-mission database of satellite, model outputs and in-situ measurements for the Arctic Ocean over a period of at least 10+ year including the implementation of a data access system and data visualisation and scientific analysis tool.

- **OBJ-3:** Undertake at least 6 science driven case studies addressing the Arktalas Scientific Challenges.
- **OBJ-4:** Analyse the impact of planned future missions on Arktalas Scientific Challenges with a focus on their likely impacts and contribution to synergic application of EO data sets.
- **OBJ-5:** Prepare and submit 7 scientific journal articles reporting the scientific outcomes of the Arktalas study.
- **OBJ-6:** Prepare a Scientific Roadmap of potential future activities and collaborations.
- **OBJ-7:** Promote the Arktalas study and application of ESA satellite missions in the Arctic Ocean.

2 IMPLEMENTATION OF THE ARKTALAS HOAVVA PROJECT

Connected to the seven scientific objectives, the *Arktalas Hoavva* project approach has been executed through the following nine major tasks , which are strongly interconnected as illustrated in the project work-breakdown (**Figure 1**):

- **Task 1:** Preparation and planning of the data collection and corresponding scientific analyses ***(OBJ-1)****;*
- **Task 2a:** *Arktalas Hoavva* data collection and quality control ***(OBJ-2)****;*
- **Task 2b:** Implementation of analyses and visualization system ***(OBJ-2)****;*
- **Task 3:** Scientific analyses of the *Arktalas Hoavva* data set ***(OBJ-3 and OBJ-5)****;*
- **Task 4:** Analyses of future satellite mission impacts in understanding the changes to the Arctic Ocean ***(OBJ-4 and OBJ-5)****;*
- **Task 5:** Promotion of the *Arktalas Hoavva* study and scientific community outreach ***(OBJ-7)****;*
- **Task 6a:** Creating a scientific roadmap ***(OBJ-6)****;*
- **Task 6b:** Final report ***(OBJ-6);***
- **Task 7:** *Arktalas Hoavva* Project Management.

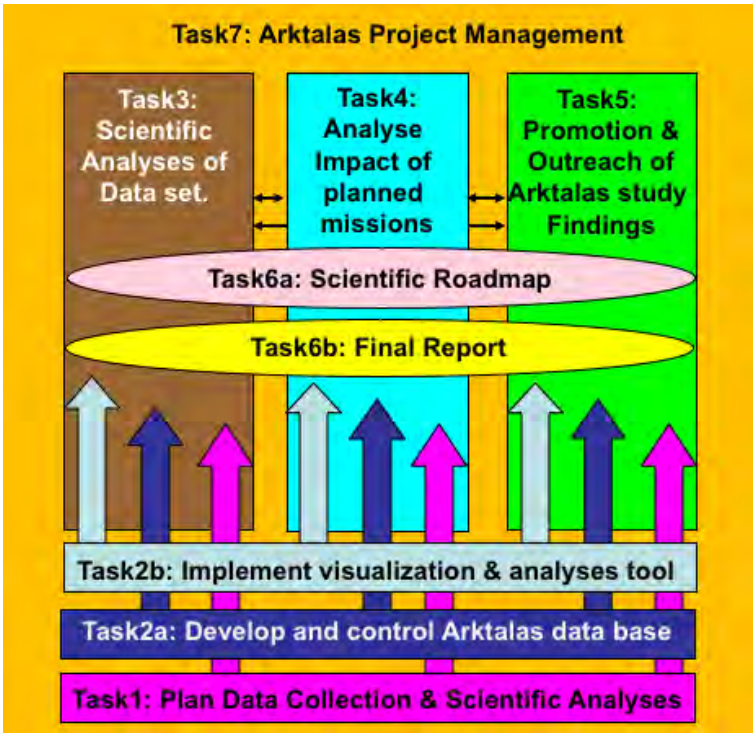

Figure 1: *Schematic outline of the Arktalas Hoavva work breakdown and approach.*

The projects tasks have been implemented and documented through the major project deliverables, which are summarized in **Table 1**.

Table 1: *The Arktalas Hoavva project deliverables with identifications in the SoW, their brief content and their status and availability.*

ID	Short Name	Deliverable Title	Brief description of content	Status and due at Mtg.# Link to Arktalas web-site
D-10	TN-1	Arktalas Science Analysis and Data Requirements Plan.	Following the template provided in the SoW this plan describes the data collection approach and the corresponding scientific analyses targeting, in particular the four major Arktalas Scientific Challenges.	Issued November 2019 Signed 6 February 2020 https://arktalas.nersc.no/node/33
D-20	TN-2	Design of the Arktalas Data and Archive System (ADAS).	The Arktalas Data Archive System (ADAS) is distributed and store priority satellite data and other complementary data sets including in-situ data and model fields covering areas north of 50 N. It capitalizes on existing data repositories residing among the partners.	Issued July 2020 Signed September 2020 https://arktalas.nersc.no/node/60
D-30	ADAS-UG	ADAS user guide and QC results.	This guide describes the equality control procedures and the corresponding documentation of the equality outcome.	Issued October 2020 Signed October 2020 https://arktalas.nersc.no/node/61
D-40	TN-3	Design of the Arktalas Visualization and Analysis system (AVS).	The Analyses and Visualization System (AVS) is based on the SynTool software, a Web portal developed by ODL for the interactive visualisation of satellite data, in-situ data and numerical simulation results. The SynTool software suite contains processing tools to extract time and space coverage from the raw data files and generate graphical representations for them while preserving their native geometry and resolution.	Issued July 2020 Signed September 2020 https://arktalas.nersc.no/node/62 The Arctic Visualization Portal https://arctic-portal.ad.nersc.no/ will be opened for project partner use via VPN on 15 May 2023. After security check the aim is to go open in June 2023.
D-50	TN-4	Verification Report for ADAS and AVS implementation.	This report documents and confirms the functionality and interoperability of ADAS and AVS.	Issued April 2021 https://arktalas.nersc.no/node/99

ID	Short Name	Deliverable Title	Brief description of content	Status and due at Mtg.# Link to Arktalas web-site
D-60	AVS-UG	AVS user guide and QC results.	This guide will describe the functionality of the AVS.	Issued October 2020 Signed October 2020 https://arktalas.nersc.no/node/63
D-70	Paper 1	Science paper 1	Arctic Amplification: A synthesis of the contributions from sea ice and cloudiness *(Relevant to ASC-1).* https://arktalas.nersc.no/node/90	Esau, I.; Pettersson, L.H.; Cancet, M.; Chapron, B.; Chernokulsky, A.; Donlon, C.; Sizov, O.; Soromotin, A.; Johannesen, J.A. **The Arctic Amplification and Its Impact: A Synthesis through Satellite Observations**. *Remote Sens.* **2023**, *15*, 1354. https://doi.org/10.3390/rs15051354
D-80A	Paper 2	Science paper 2a.	Wind-waves and currents across the ice edge: Exploring mechanical effects and feedbacks with models and remote sensing (*Relevant to ASC-2)* https://arktalas.nersc.no/node/98	Collard, F., Marié, L., Nouguier, F., Kleinherenbrink, M., Ehlers, F., & Ardhuin, F. (2022). **Wind-wave attenuation in Arctic sea ice: A discussion of remote sensing capabilities.** *Journal of Geophysical Research: Oceans*, 127, e2022JC018654. https://doi.org/10.1029/2022JC018654
D-80B		Science paper 2b	https://arktalas.nersc.no/node/87	Boutin G, Williams T, HorvatC, Brodeau L. (2022). **Modelling the Arcticwave-affected marginal ice zone: acomparison with ICESat-2 observations.** *Phil.Trans. R. Soc. A380: 20210262.* https://doi.org/10.1098/rsta.2021.0262
D-90	Paper 3	Science paper 3.	On the assessment of Arctic storm effects on sea ice dynamics, new sea ice formation and ice-ocean stress *(Relevance to ASC-3).* https://arktalas.nersc.no/node/86	Rheinlænder, J. W., Davy, R., Ólason, E., Rampal, P., Spensberger, C., Williams, T. D., Korosov, A. and Spengler, T. (2022). **Driving mechanisms of an extreme winter sea ice breakup event in the Beaufort Sea.** *Geophysical Research Letters*, 49, e2022GL099024. https://doi.org/10.1029/2022GL099024
D-100	Paper 4	Science paper 4	Variability of the mesoscale activity in response to the spin up of the Beaufort Gyre (*Relevant ASC-4).* https://arktalas.nersc.no/node/97	H. Regan, C. Lique, C. Talandier and G. Meneghello (2020). **Response of Total and Eddy Kinetic Energy to the recent spin up of the Beaufort Gyre.** Published in *J. Physic. Oceangr.*, p. 575-594, 1. March 2020, https://doi.org/10.1175/JPO-D-19-0234.1
D-110	Paper 5	Science paper 5	Observational evidences of eddy-sea ice interactions in the pack-ice and in the MIZ *(Relevance to ASC-2).* https://arktalas.nersc.no/node/88	Cassianides, A., Lique, C., & Korosov, A. (2021). **Ocean eddy signature on SAR-derived sea ice drift and vorticity.** *Geophysical Research Letters*, 48, e2020GL092066. https://doi.org/10.1029/2020GL092066
D-120	Paper 6	Science paper 6	Impact of sea-ice friction on tidal modelling in the Arctic Ocean *(Relevance to ASC-1).* https://arktalas.nersc.no/node/91	Mathilde Cancet, Florent H. Lyard, and Ergane Fouchet. **Impact of sea-ice friction on tidal modelling in the Arctic Ocean, modelling insights at various time and space scales**. Submitted to Ocean Modelling.

ID	Short Name	Deliverable Title	Brief description of content	Status and due at Mtg.# Link to Arktalas web-site
D-130	Paper 7	Science paper 7	Impact of future satellite missions on the understanding of changes in the Arctic Ocean. https://arktalas.nersc.no/node/92	Lucas, S.; Johannessen, J.A.; Cancet, M.; Pettersson, L.H.; Esau, I.; Rheinlænder, J.W.; Ardhuin, F.; Chapron, B.; Korosov, A.; Collard, F.; Herlédan, S.; Olason, E.; Ferrari, R.; Fouchet, E.; Donlon, C. (2023). **Knowledge Gaps and Impact of Future Satellite Missions to Facilitate Monitoring of Changes in the Arctic Ocean.** *Remote Sens.* **2023**, *15*, 2852. https://doi.org/10.3390/rs15112852
D-70-130	8 papers	Scientific publications	A collection of all eight papers in one report deliverable.	https://arktalas.nersc.no/node/102
D-140	Web-Stories	Arktalas Web Stories (one every 3 months)	Web-based news stories reflecting the achievements of the project during its implementation. https://arktalas.nersc.no	Ten web stories related to the scientific publications and the Arktalas Hoavva workshop are presented on the project-web site. https://arktalas.nersc.no/node/103
D-150	PROC	Scientific Review Proceedings.	Based on the main presentations and outcome of the open scientific meeting.	ARKTALAS Hoavva Science Workshop Report issued 7 June 2022. https://arktalas.nersc.no/node/96
D-160	SR	Arktalas Scientific Roadmap	The Arktalas Scientific Roadmap (SR) will summarize the outputs, lessons learned, knowledge, international collaboration, and tools developed by the project. These findings will then be mapped into potentially future activities.	Delivered 4 weeks prior to FM. https://arktalas.nersc.no/node/104
D-170	FR	Final Report	A complete self-standing description of the work done in the different Tasks of Arktalas Hoavva covering the whole scope of the project. The FR includes a comprehensive introduction of the context, a description of the programme of work and report on the activities performed and the main results achieved.	Delivered 4 weeks prior to FM. https://arktalas.nersc.no/node/105
D-180	TDP	Technical Data Package	The TDP contains of the final version of all approved technical documents.	FM at USB-stick
D-190	QSR	Quarterly Status Reports	QSR on running activities including: • Action items completed during the reporting period; • Description of progress: actual vs. schedule, milestones and events accomplished; • Reasons for slippages and/or problem areas, if any, and corrective actions planned and/or taken, with revised completion date per activity; • Events anticipated during the next reporting period (e.g. milestones reached); • Milestone payment status, • Any other aspect considered important to report to the Agency.	QSR1- QSR4 2020 QSR1- QSR4 2021 QSR1- QSR4 2022 QSR1- 2023 QSR2- 2023
D-200	CCD	Contract Closure Documentation	CCD document conforming with the layout as provided in Annex A to the SoW.	End of contract, included in D-180

Based on the findings reported in the above *Arktalas Hoavva* Deliverables the project Tasks are described chronologically in the following sections.

2.1 Task 1: Preparation and planning of the data collection and corresponding scientific analyses

Based on an analysis of the identified requirements and data needs for implementing the scientific studies (see Sections 3.6), the Arktalas Science Analysis and Data Requirement Plan (D-10), includes the specifications and contents of the Arktalas Data Archive System (ADAS) to be developed and implemented. ADAS has been designed as a distributed data repository and a centralized data search interface. For efficient exploitation of the data in ADAS a Arktalas Analysis and Vitalization System (AVS) has been implemented based on the OceanDataLab Syntool web interface for data analysis and visualization. The interactions between Arktalas ADAS and AVS are illustrated in Figure 2, being the main components of the NERSC Arctic Portal (user front end) for visualisation and synergetic analysis of environmental data for the Arctic Oceans.

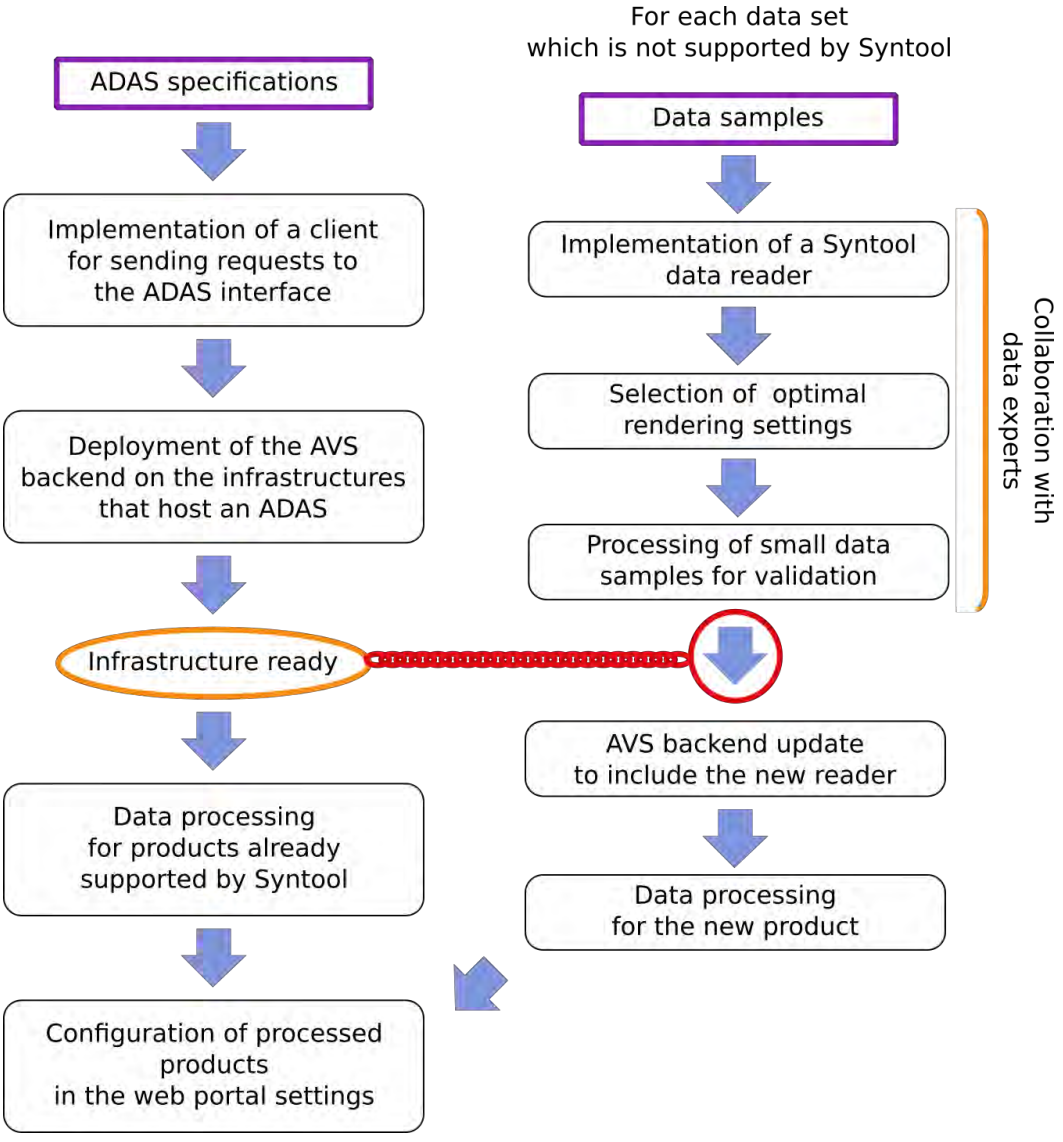

Figure 2: *Schematic illustration of the functions of the Arktalas Analyses and Visualisation System (AVS) including the connection to Arktalas Data Archive System (ADAS), being the core elements of the NERSC Arctic Portal.*

The distributed data repository comprises of the data archives provided by the project partners and data available from other data and service providers including ESA Scientific Hub, ESA CCI Portal, Collaborative Ground Segments, NSIDC, etc. The data will cover the pan-Arctic domain including the oceanic regions north of 55° N. Different data access and ingestion solutions will be used to facilitate easy and open access to the Arktalas data set for scientific analysis (e.g. web based, cloud solutions, on-line data processing, sftp, etc.). The satellite sensor data acquired are summarized in **Table 2**. Among the future approved and planned missions focus has been towards the SWOT mission and the joint ESA-EU planned Copernicus High Priority Candidate Missions (HPCM) (Copernicus High Priority Missions), notably: CIMR, ROSE-L and CRISTAL as well as the Earth Explorer 10 proposed mission HARMONY. The overall (satellite, in situ and modelled) data available to and used in the Arktalas scientific studies (see Task 3) and available to the project partners are summarized in Table 3.

Table 2: *Candidate satellites and sensors for the sea ice and ocean observations grouped into: ESA and Eumetsat missions (yellow), 3rd Party Missions (green) and new approved and planned missions (blue).*

Candidate satellite and sensors for sea ice and ocean observations						
Passive-μwaves	**Scatterometer**	**SAR**	**Altimeter & LIDAR**	**Spectrometer**	**Infrared**	**Gravimetry**
SMOS	Metop ASCAT	Sentinel-1 A/B	CRYOSAT-2	Sentinel-3	Sentinel-3	GOCE
			Sentinel-3	Sentinel-2	Metop AVHRR	
AMSR-2	CFOSAT	Radarsat2	Altika	Aqua MODIS	Aqua MODIS	GRACE
SSMI	Oceansat2	Radarsat constellation	ICESat ICESat 2			GRACE FO
SMAP			CFOSAT			
Aquarius						
CIMR		ROSE-L	SWOT			
		BIOMASS	CRISTAL			
		HARMONY				

Table 3: Overview of datasets that are fully or partly available at repositories within the Arktalas project team.

Partner	Satellite data		In-situ data	Model fields and Tools
	Level 1	Level 2, 3, 4		
NERSC	Subset of SAR data from Sentinel-1 A/B Subset of SAR data from Radarsat	SIC from AMSR-2, SSMI and OSISAF; SID from OSISAF; SIT from merged SMOS and Cryosat 2; Sea ice types from OSISAF and Arctic-ROOS. Gridded Level 4 Altimetry data from ESA CCI data set	NISE, NorDataNet, Argo, ITP, IABP, NorArgo2 Research Infrastructure	neXtSIM, HYCOM, TOPAZ, NorESM, NorCPM, LES, GeoSPaaS
ODL				Syntool visualization platform
Ifremer	Microwave radiometer from SMOS, SMAP, Aquarius, SSMI, AMSR; Scatterometer from Metop; Brightness temperatures from Sentinel-3; Altimetry from Sentinel-3	SIC from CCI Sea ice, CMEMS, OSI SAF; SID from CMEMS; SST from GHRSST, OSI SAF; sea ice types from CMEMS; SSS from pi-mep; sea ice edge contour from CMEMS; winds from scatterometer, SMOS, SSMI, AMSR	Euro-Argo Research Infrastructure	NEMO-LIM3 coupled ocean- sea model
Noveltis	Topex/Jason Sentinel-3 RA ENVISAT/SARAL CryoSat-2	RTopo-2.0.4 global dataset NSIDC daily and monthly sea ice products ESA CyoSat-2 Level-2 GOP Baseline C	UHSLC database GESLAv3 database GEBCO-2020 Global tidal atlases (GOT, TPXO, FES)	TUGO-m hydrodynamic model Arctide2017 regional model

The ADAS and the AVS is hosted on the same infrastructure to avoid unnecessary data transfers and to simplify the orchestration of data processing operations. It does not mean that data discovery, storage and processing are limited to a single infrastructure: multiple systems, each comprised of one ADAS and one AVS, can be deployed on different infrastructures (institutions). Search interfaces were provided to access the distributed data available in ADAS via OpeNDAP, FTP or on local file servers at NERSC, IFREMER and ODL. The search interface will be realized as an online web form and as Python API e.g., in Jupyter Notebooks and as specifies in the Data Access Requirements Document (DARD). All data used in the Arktalas project will be available in ADAS and AVS infrastructures and integrated in the Arktalas Arctic visualisation portal, as shown in **Figure 3**. This distributed architecture makes the overall solution easy to extend, the addition of a new ADAS-AVS couple requiring only a few changes in the portal configuration file.

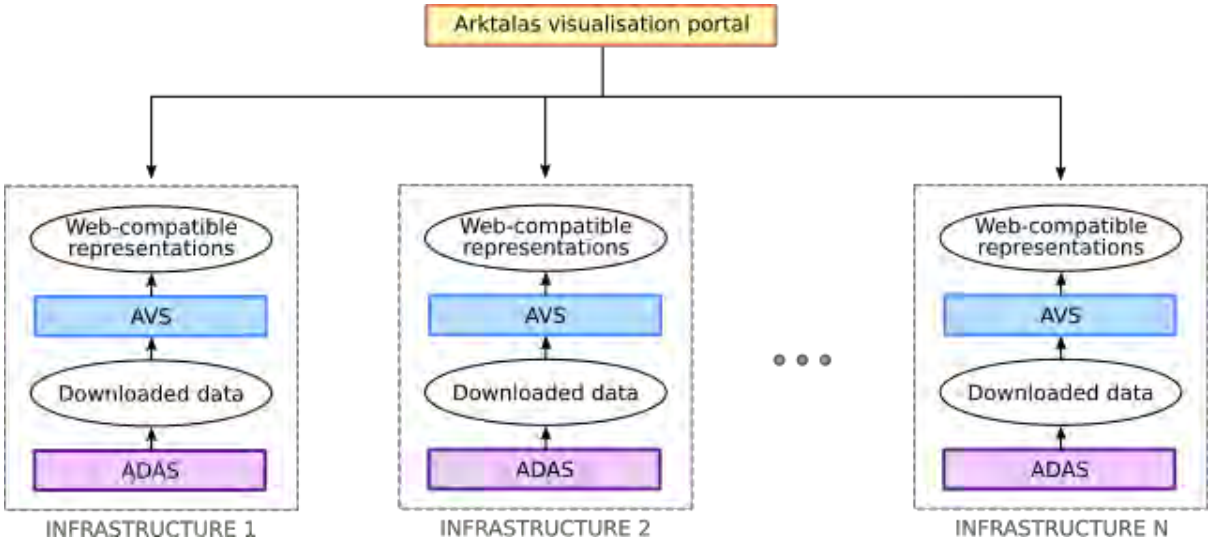

Figure 3: *Distributed architecture for the backend of the Arktalas NERSC Arctic Portal for data visualisation, integration and analysis. The modular infra structure facilitate portal expansion across different projects and institutions providing data to the Portal.*

2.2 Task 2a: *Arktalas Hoavva* data collection and quality control

The main component of Arktalas Data Archive System (ADAS – see Figure 4) is the Django-Geo-SPaaS (Geo-Scientific Platform as a Service) system, developed at the Nansen Center. Geo-SPaaS is an open source Python application written using Django-framework for storage and search of discovery metadata and providing web-based Graphical User Interface (GUI) and Python Application Programming Interface (API). The discovery metadata is stored in a relational database following GCMD-DIFF standard. Django Object-Relational Mapping (ORM) provides an efficient API for accessing the database. GUI uses Django ORM, displays a webpage for defining searching criteria and shows the results of search.

In ADAS the Django-Geo-SPaaS is complemented with a Harvester, which is also a Python application for collecting discovery metadata from (external) data repositories (e.g., ESA Scientific Hub, ESA CCI, OSI SAF, etc.). The Administrator launches harvesters to start collecting metadata from external data repositories. The Harvesters instantiate crawlers for automatic retrieval of all dataset URLs available in a data repository. The ingesters read metadata from the URLs of the data repositories and write it to the discovery metadata database in ADAS. The harvesting Docker container can initiate several data harvesting processes in parallel.

A user access GUI for searching in a database and can then download the files from data repositories. Integration with AVS is realized as an application which uses Django-Geo- SPaaS for finding relevant datasets, downloading of these datasets from remote data repositories and launching AVS backend for visualization (see Task 2B).

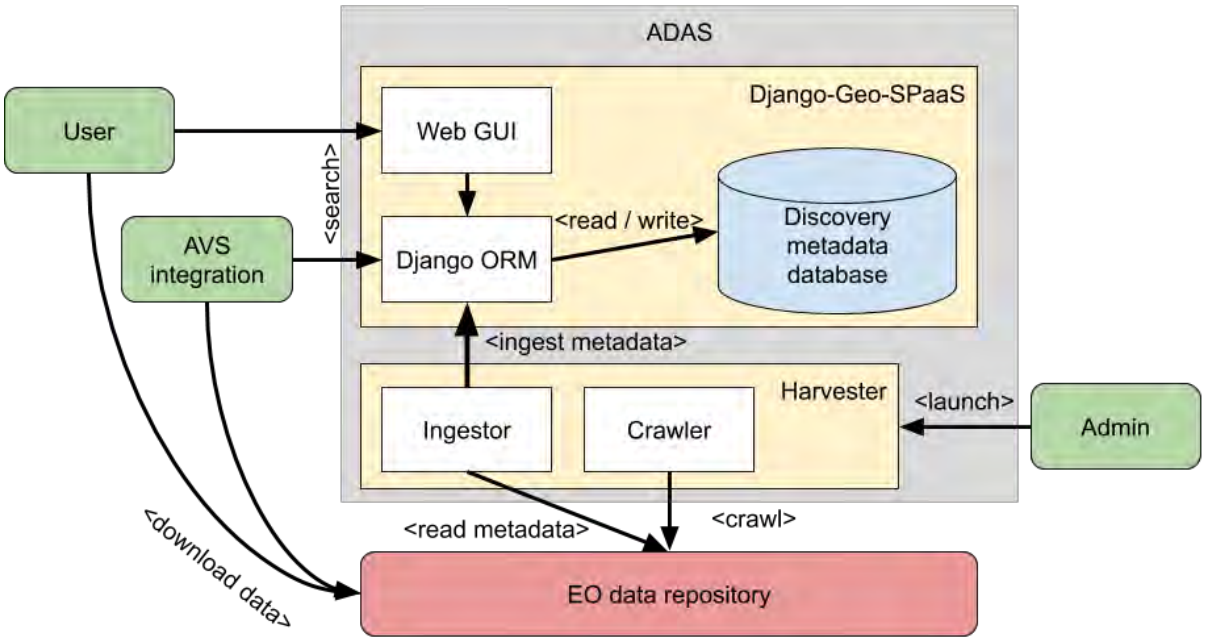

Figure 4: *Overall architecture of ADAS (shown by gray block). Green blocks denote external clients, red block - distributed data repositories, yellow block - Django-Geo-SPaaS and Harvesters, blue block - centralized metadata database, white blocks - main software components. Arrow direction shows invocation sequence - arrows points from an active actor to a resource.*

The ADAS-harvester consists of a list of crawlers and an ingester, which can be used to harvest data from a given provider, such as e.g. a Copernicus Sentinel harvester, searching the Copernicus API open access hub, or a harvester for OSISAF server. Three workflows have been developed to harvest the needed environmental data (either satellite, in situ and/or modelled output) from external data repositories for use in ADAS for the scientific analysis and scientific studies to be performed:

- Harvesting initiated by an Administrator searching for data with a priori known/ identified metadata,
- Searching with a Graphical User Interface and
- Searching using Python routines (e.g. periodic CRON jobs for regular updating with new available data).

The Arktalas Visualisation and Analysis System (AVS) is the main user interface for the *Arktalas Hoavva* project, and user interactions with the ADAS are limited. Still, an ADAS web interface is provided so that users can directly check the contents of the ADAS without going through the AVS (**Figure 5**). The ADAS web interface can filter the metadata sets using graphical or search commands for:

- Time coverage
- Source
- The name of the parameter/variable contained in the dataset.

The ADAS web application is freely available as a Docker image in a Github repository at the Nansen Center. Deployment to a new server, inventory files for a new environment can be written by taking the existing ones as an example and following the technical requirements and command scripts. The routines for quality check of data harvesting have been implemented, to assure that the needed/requested data sets are identified and made available in ADAS.

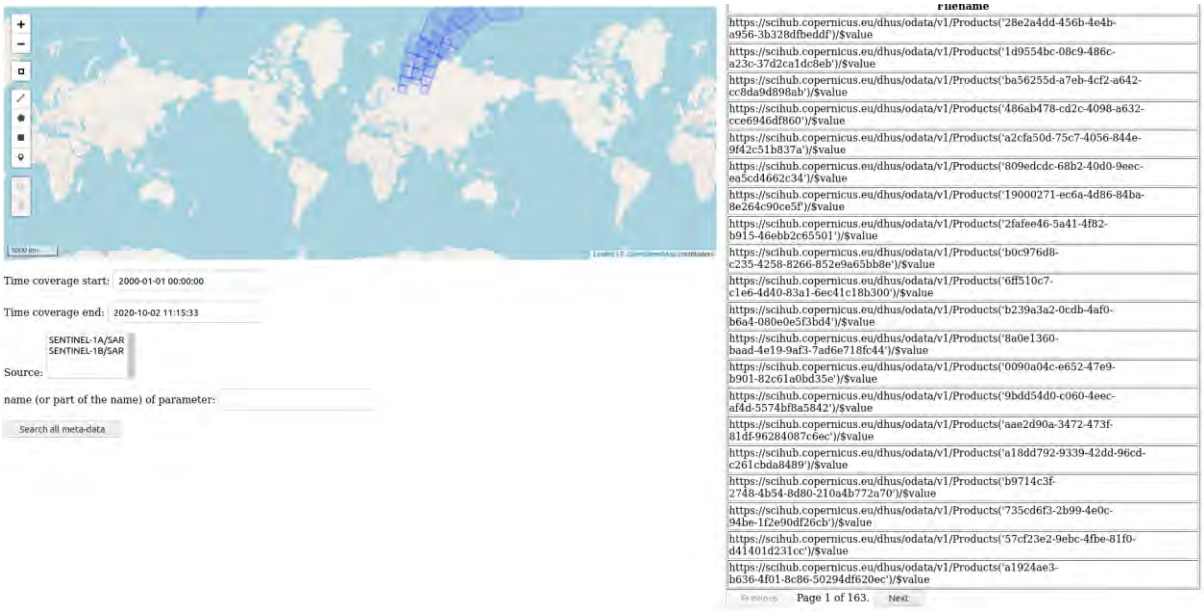

Figure 5: *Web interface composed of the graphical search form (left) and the tabular search results as the URLs of the datasets (right).*

2.3 Task 2b: Implementation of analyses and visualization system

The goal of the Arktalas Analysis and Visualisation System (AVS) is to display data representations at full resolution on an interactive map for the data sets acquired and stored in the Arktalas Data Archive System (ADAS), for each infrastructure (institution) providing data to the overall NERSC Arctic Portal, integrating the *Arkatlas Hoavva* infrastructures.

To achieve this objective, the AVS have been developed to provide an intuitive web interface to browse and display the EO data sets collected for the *Arktalas Hoavva* scientific case studies, offering a graphical support for project members and external users to display and discuss their results, explore the synergy between available products and potentially discover interesting new relations between the different data sets.

The implementation of the AVS is based on the Syntool software suite, developed by OceanDataLab, as it provides all the features required for rendering EO data on an interactive map integrated in a website, which includes (**Figure 6**):

- a web application which embeds an interactive map and controls to select products, dates, times, and areas in an intuitive manner.

- a web service for searching data that match a set of criteria, using a database which contains the spatial and temporal coverage of all data available in the system.
- processing tools that transform EO data into web-compatible representations and extract the metadata required to populate the Arktalas scientific studies database.

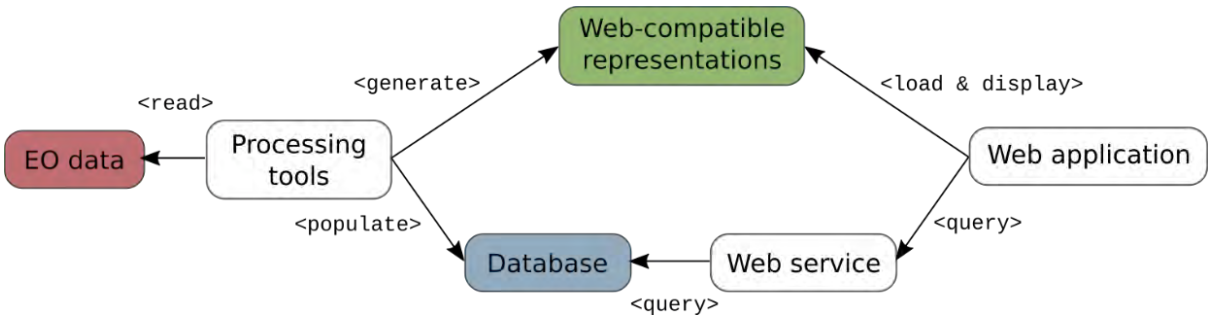

Figure 6: *High level overview of a Syntool architecture, being the core of the Arktalas AVS.*

The AVS and ADAS are hosted in the same data infrastructure at NERSC (and other external infrastructures, e.g. at Ifremer or ODL) and their integration is realized on file level through an automated Downloader (see **Figure 7**). ADAS is responsible for searching relevant datasets and AVS for their visualization. Key components of ADAS in this perspective are Harvesters that collect metadata from remote data repositories and Django-Geo-SPaaS that stores metadata in a database and provides searching interface. Moreover, as shown in the workflow (Figure 8) the Downloader is launched by an administrator for a given range of dates, regions of interest and dataset sources. It finds the relevant datasets using ADAS, downloads them and provides the files to AVS. The AVS backend automatically scans the temporary directory and generates PNGs files for the web frontend. A user can access the frontend to interactively browse the visualise satellite products through the AVS.

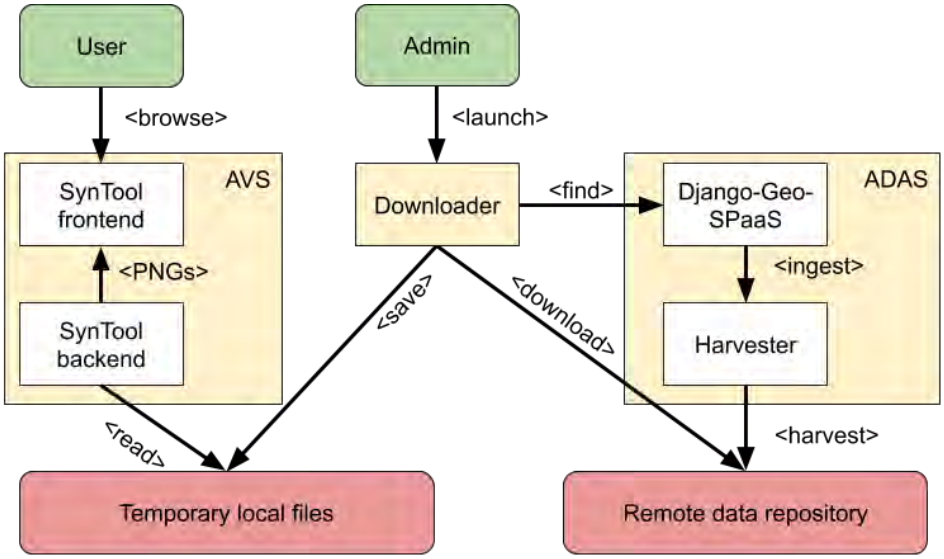

Figure 7: *Overview of ADAS and AVS integration. Green blocks show external clients, yellow blocks - ADAS, AVS and Downloader, white blocks - main software components, red blocks - local and remote data repositories. Arrow direction shows invocation sequence - arrows points from an active actor to resource.*

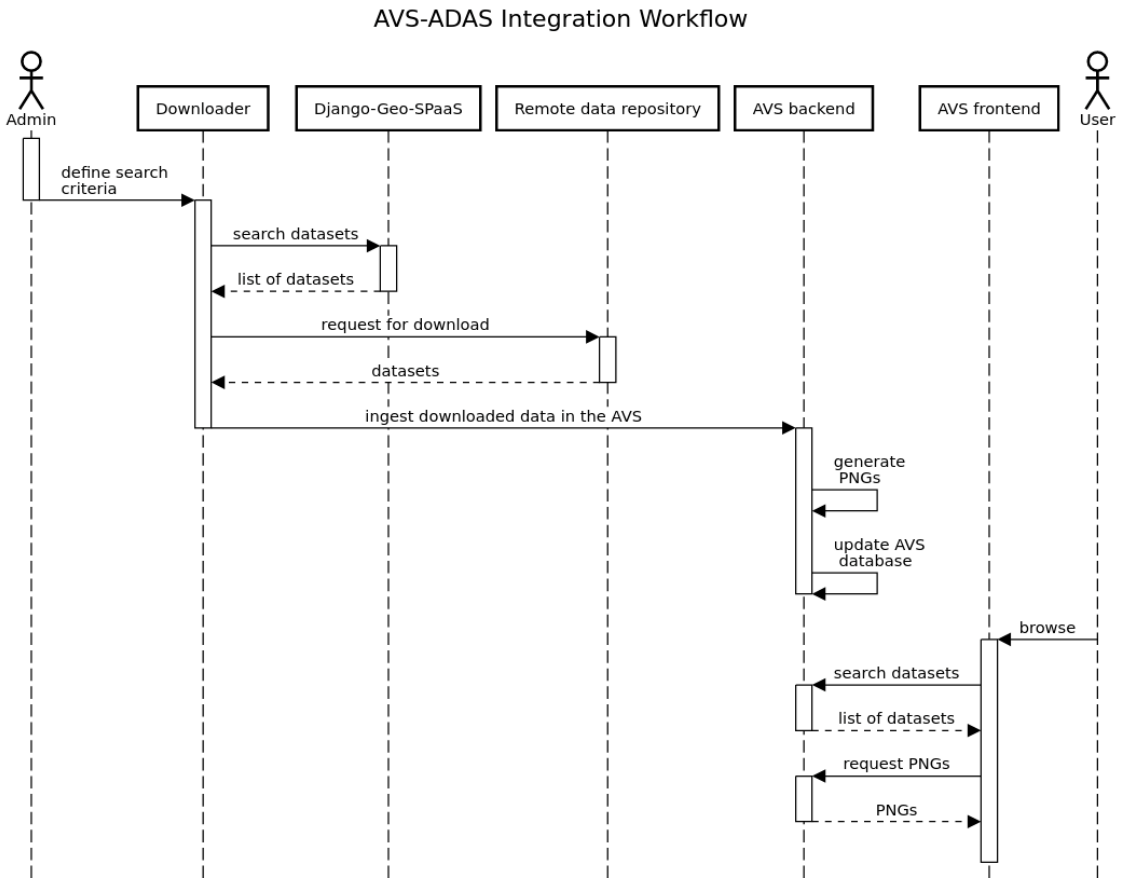

Figure 8: *Sequence diagram for the AVS - ADAS integration workflow from the system Administrator to the scientific User, exploiting the data.*

ADAS-AVS system developed in *Arktalas Hoavva* is not developed to be used for operational 24-7 services, so there is no real time error reporting. Failures can be detected quite easily though, either by looking for processing jobs that have been dispatched but not completed in the AVS jobs database, or by searching for files older than a threshold in the AVS spool directory. The data flow starting from the files downloaded by the ADAS and ending with their publication in the Arktalas visualisation portal (AVS) is outlined in **Figure 9**.

The AVS web application features a mechanism to save its selected date, time, viewport, and products in the form of a simple web link that can be embedded in an email, an article or a message in social media. Sharing these links allows other users to open the web application in the exact same state and can therefore be used as an interactive illustration for an article or as a graphical support during discussions with other members of the scientific community.

It also provides a way to create local (but shareable) bookmarks so that the web links appear with a descriptive title directly in the application. Bookmarks (or "hotspots" as they are called in Syntool) can be pre-configured, which could be used to give a quick access to cases of interest for the Arktalas studies.

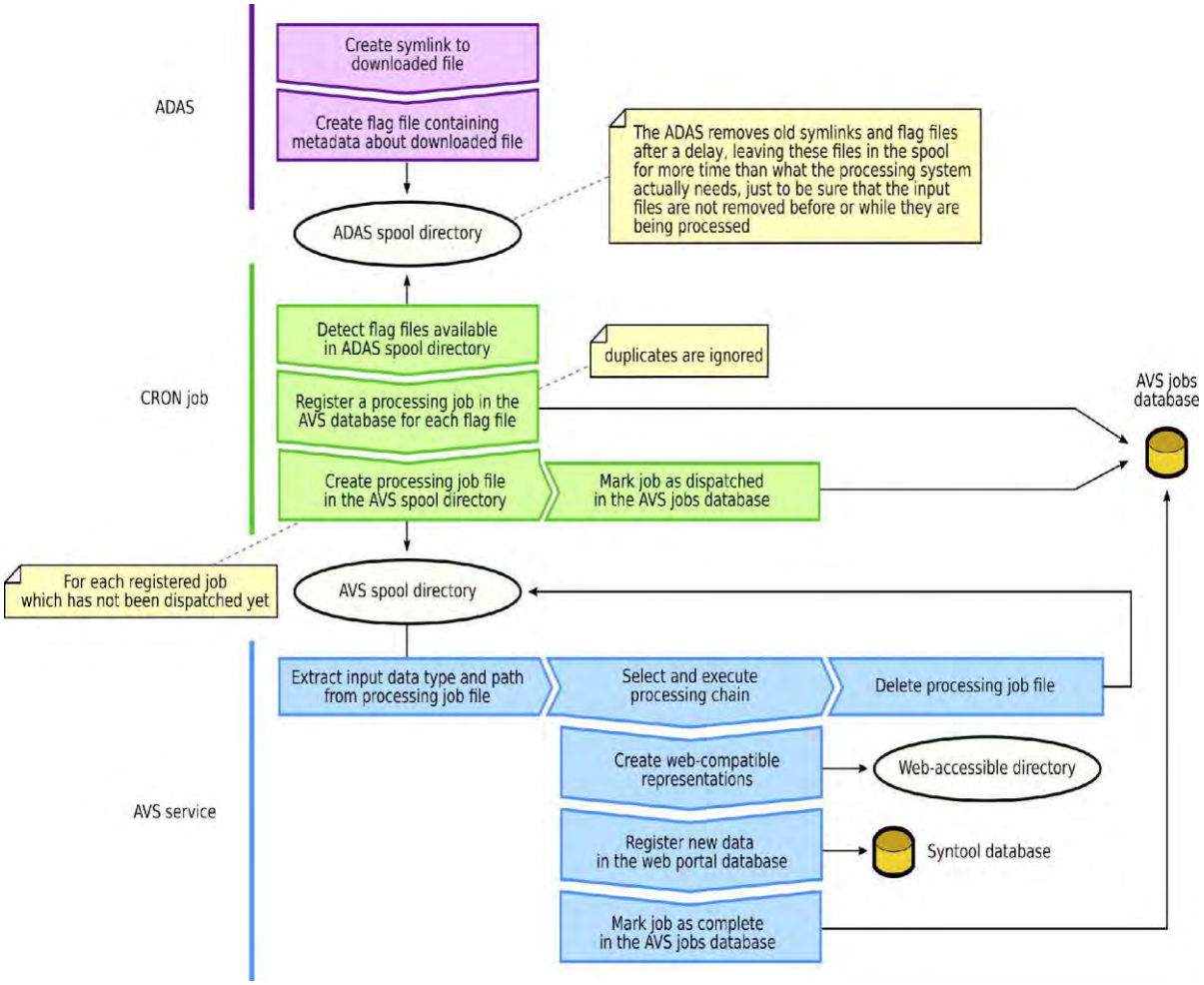

Figure 9: *The data flow and interactions between the Arktalas ADAS and AVS systems for acquisition and visualisation for environmental data in the Arktalas portal (i.e. the NERSC Arctic portal - see* ***Figure 11****).*

Processing tools are the only components of the Syntool software suite that interact directly with EO data. Although these tools are already able to handle a variety of products, some development will be needed to implement support for the Arktalas data sets: ad hoc data readers must be written to handle the specificities of these data sets so that they can be converted into a common format which can then be used as inputs by generic tools that intervene downstream in the processing chain.

The Syntool web application is also able to connect to several web services, which grants the possibility to distribute data among several hosting platforms if they allow public access to the web-compatible representations and to the Syntool web service. In the context of the Arktalas project, this mechanism has demonstrated several advantages:

- It eliminates the need to have all the data hosted in a single infrastructure, therefore reducing the amount of data transfers between partners and a central authority, also allowing several partners to participate actively in the data gathering process.
- It makes the AVS more resilient to failures, as the data portal will still be able to run in a degraded mode in case one of the hosting platforms is offline as data from the other platforms will still be available.

- It allows the AVS to grow in the future as connecting to new instances of the Syntool web service only requires minor changes in the configuration, making this solution both extensible (web services providing new data) and scalable (distributing data among a larger number of Syntool web service instances), as illustrated in **Figure 10**.

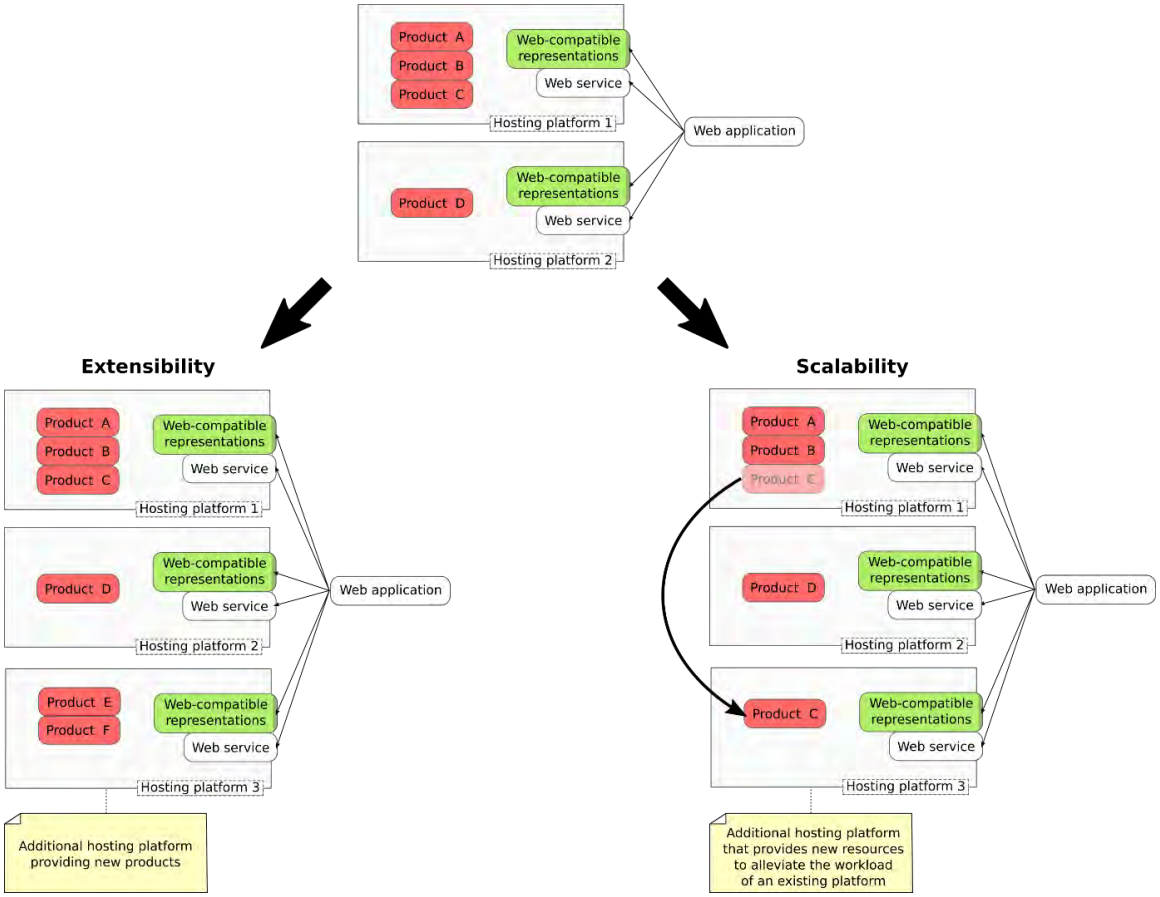

Figure 10: *Extensibility and scalability of the system is achieved by integrating new backends in the AVS.*

The efficient the backend of the AVS is composed of three main parts:

1. A crawler that will find the EO data (in raw format) to include in the AVS
2. Processing chains to produce web-compatible representations and extract metadata from EO data in order to populate the ADAS database
3. A Web service that can be accessed from the Internet.

Only the third-party databases (source data) have to be permanently online: the AVS processes delayed-time data archives downloaded by the ADAS for temporal windows identified as being of interest for the case studies, not a permanent incoming feed of data. Processing resources are only required temporarily when the ADAS completes a download batch and resources that must be allocated permanently are thus limited. The Arktalas AVS frontend, i.e. the NERSC Arctic Portal, has been implemented at the data infrastructure at NERSC as the public web front-end interface (**Figure 11**). It comprises three main elements:

- an interactive map that users can zoom and pan: its viewport is used as geographical filter to find the relevant EO granules.
- a list of all the products available in ADAS, with checkboxes to select the ones that must be displayed on the map.
- a timeline which allows users to select a time range to filter to EO granules that must be displayed on the map and provides an intuitive way to modify this time range in order browse the content of the AVS.

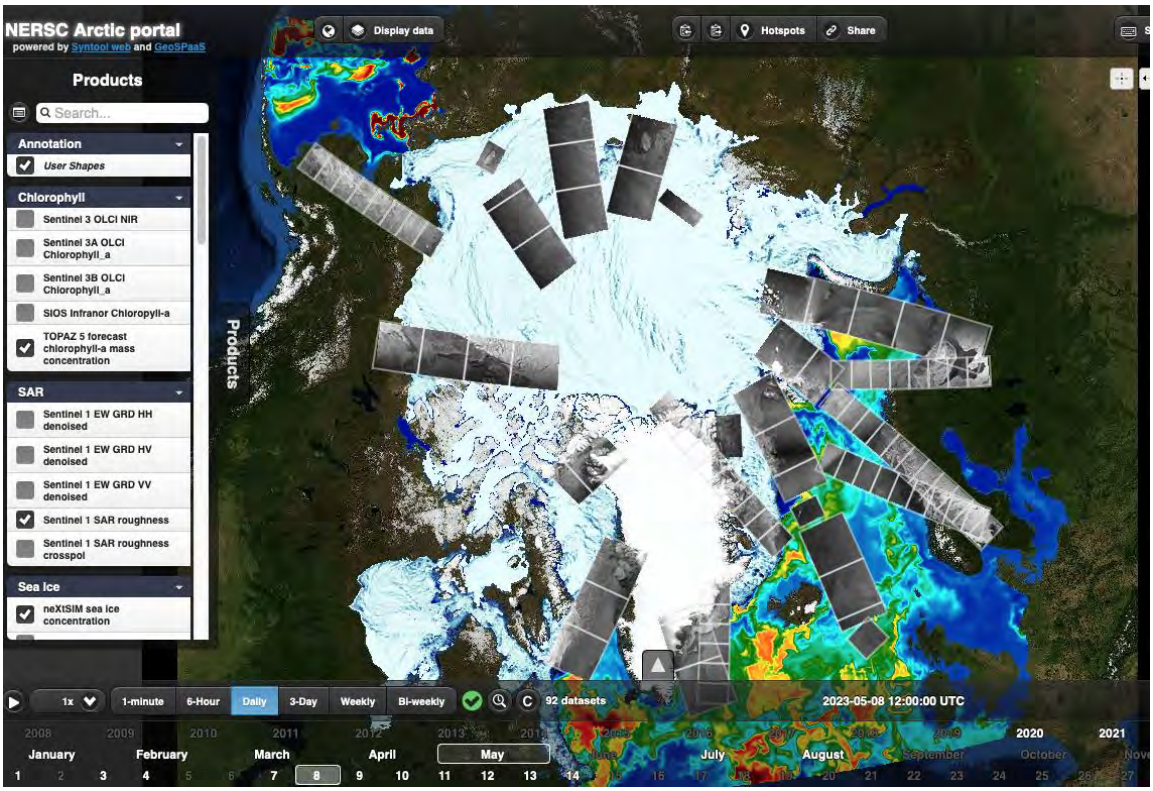

Figure 11: *The [NERSC Arctic Portal] is the public accessible version of the Arktalas AVS. Here displaying modelled products of sea ice cover and chlorophyll-a concertation for 8. May 2023 superimposed the Sentinel-1 SAR roughness.*

The NERSC Arctic Portal Syntool web application relies on the OpenLayers JavaScript library for the map component, with some customization to improve its performance and add support for the variety of data representations that Syntool-ingestor can produce.

The AVS map can render several overlapping EO granules at the same time, with settings to change their transparency as well as the order in which they are rendered so that users can see the details provided by each of these granules to build a more complete representation of a geophysical phenomenon (synergy between products).

The timeline not only serves as a date/time selection control but also as an indicator for data availability: after each change in the products list or in the map viewport, the application calls the /coverage endpoint to update the content of the timeline component and to clearly show the days/months/years when data are available for the selected products over the visible area.

Details about geophysical variables, product version, algorithms applied during processing, flags used to mask invalid data, provider, etc... can be associated with each product and displayed either as a tooltip or a popup window that appears upon hovering or clicking on an item of the products list.

After each change of the map viewport, the selection in the products list or in the timeline, the application calls the /datasets endpoint to list all the EO granules that match the new set of constraints, build their footprint on the map, and load the associated representation.

Selecting a granule by clicking on its footprint on the map triggers a call to the /getGranuleInfo endpoint: if additional information is available for the selected granule, it will be displayed in a contextual menu. This information can take several forms: it may be a simple text, an image, or a link to an external resource.

2.4 Task 3: Scientific analyses of the *Arktalas Hoavva* data set

The *Arktalas Hoavva* project adopted a stepwise multi-modal analyses framework approach to address the four a priori formulated Arctic Scientific Challenges (ASC´s). This approach benefits from multiscale resolution satellite observations together with complementary in-situ data, computer model simulations, data assimilation, analyses, and the integrated visualization tools – the NERSC Arctic Portal. The major findings and results that emerged from the following eight scientific research publications, which are summarized hereafter and included in their full published versions in Annex 2 to the Arktalas Hoavva Final report:

1. Esau, I.; Pettersson, L.H.; Cancet, M.; Chapron, B.; Chernokulsky, A.; Donlon, C.; Sizov, O.; Soromotin, A.; Johannessen, J.A. **The Arctic Amplification and Its Impact: A Synthesis through Satellite Observations**. *Remote Sens.* **2023**, *15*, 1354. https://doi.org/10.3390/rs15051354
2. Collard, F., Marié, L., Nouguier, F., Kleinherenbrink, M., Ehlers, F., & Ardhuin, F. (2022). **Wind-wave attenuation in Arctic sea ice: A discussion of remote sensing capabilities.** *Journal of Geophysical Research: Oceans*, 127, e2022JC018654. https://doi.org/10.1029/2022JC018654
3. Boutin G, Williams T, HorvatC, Brodeau L. (2022). **Modelling the Arcticwave-affected marginal ice zone: acomparison with ICESat-2 observations.** *Phil.Trans. R. Soc. A380: 20210262.* https://doi.org/10.1098/rsta.2021.0262
4. Rheinlænder, J. W., Davy, R., Ólason, E., Rampal, P., Spensberger, C., Williams, T. D., Korosov, A. and Spengler, T. (2022). **Driving mechanisms of an extreme winter sea ice breakup event in the Beaufort Sea.** *Geophysical Research Letters*, 49, e2022GL099024. https://doi.org/10.1029/2022GL099024
5. H. Regan, C. Lique, C. Talandier and G. Meneghello (2020). **Response of Total and Eddy Kinetic Energy to the recent spin up of the Beaufort Gyre.** Published in *J. Physic. Oceangr.*, p. 575-594, 1. March 2020, https://doi.org/10.1175/JPO-D-19-0234.1

6. Cassianides, A., Lique, C., & Korosov, A. (2021). **Ocean eddy signature on SAR-derived sea ice drift and vorticity.** *Geophysical Research Letters*, 48, e2020GL092066. https://doi.org/10.1029/2020GL092066
7. Mathilde Cancet, Florent H. Lyard, and Ergane Fouchet (submitted 2023). **Impact of sea-ice friction on tidal modelling in the Arctic Ocean, modelling insights at various time and space scales**. Submitted to Ocean Modelling.
8. Lucas, S.; Johannessen, J.A.; Cancet, M.; Pettersson, L.H.; Esau, I.; Rheinlænder, J.W.; Ardhuin, F.; Chapron, B.; Korosov, A.; Collard, F.; Herlédan, S.; Olason, E.; Ferrari, R.; Fouchet, E.; Donlon, C. (2023). **Knowledge Gaps and Impact of Future Satellite Missions to Facilitate Monitoring of Changes in the Arctic Ocean.** *Remote Sens.* 2023, *15*, 2852. https://doi.org/10.3390/rs15112852

Esau et al., (2023) have reviewed and assessed how the remote sensing data, and particularly climate products, have captured signals of the Arctic Amplification such as the rapid and massive transition from multiyear to seasonal sea ice, and from tundra to tall shrubs and forest.

The Arctic Amplification of surface temperature has been observed to come in pulses. Long periods of high internal climate variability and slow climate trends are followed by intense decades of rapid and considerable changes. The most recent such periods have been captured by a multitude of satellite observations.

The traditional paradigm put the weight on local climate processes and feedbacks, such as, e.g., the ice-albedo feedback. However, a new paradigm attributes the Amplification drivers to the global energy sink and source redistribution, and therefore to dynamic effects in the atmospheric and oceanic meridional circulation. The local feedbacks are following in this paradigm making the Amplification apparent in the surface changes such as in the recent rapid temperature raise at the Barents Sea northern margins. Decades ago the multiyear sea ice kept both the surface air temperature and the sea surface temperature at melting point during summer, thus, inhibiting heat accumulation and related surface-layer feedbacks. In 2000s, on the other hand, multiyear ice has largely retreated and the solar heating has got access to the upper ocean storage reservoir triggering further warming and setting back winter ice formation. In addition, as land cover is more responsive to heat inflow in the atmosphere, Arctic vegetation productivity began to increase earlier with dominant effect of tundra shrubification and afforestation.

Collard et al. (2022) have applied an innovative sensor synergy combination of data from ICESat-2, Sentinel-2, Sentinel-1, Sentinel-3 Fully-Focused SAR altimetry and CFOSAT-SWIM to detect wave patterns in the sea ice field. These multi-sensor observations are highly important to advance the understanding of interactions of waves and sea ice with possible consequences for sea ice cover breakup.

A consistent quantitative interpretation of ICESat-2 and Sentinel-2 data is made on waves generated by storms in the Barents Sea that are observed to travel hundreds of kilometers

across the marginal ice zone and into the pack ice. The use of multi senor data strongly expand the quantity of available wave information for scientific investigations and operational applications in the polar oceans. This clearly advocates for a synergetic approach, building co-located datasets to achieve better quantitative understanding of the propagation and interactions of waves and sea ice. The quantification of wave heights, on the other hand, are still subject to validation.

Boutin et al. (2021) have evaluated the ability of wave-in-ice models at the scale of the Arctic Ocean and over periods longer than a few days with the goal to explore how far waves can propagate into the sea ice field.

The study makes use of the wave-affected fraction dataset from ICESat-2 to assess the ability of a coupled wave—sea ice model to capture the extent to which the waves propagate into the sea ice field. The comparison is not straightforward as model and observations data are very different. Moreover, the observations are also sparse and only detect waves above a certain wave height. All in all, the simulated wave propagation agrees well with observations, especially in winter. In autumn, on the other hand, the model underestimates the area affected by waves in the western part of the Arctic Basin. The study clearly highlights the need for wave-in-ice models to maintain strong wave attenuation in thick, compact ice, whereas weaker attenuation are preferable in summer or during sea ice formation periods. Improved quality of wave-in-sea ice modelling will, in turn, lead to better understanding of wave-sea ice interactions and estimation of wave-induced sea ice breakup. It will also enable better assessment of the impact of a more persistent and larger area of open water on sea ice dynamics in a future Artic Ocean.

***Rheinlaender et al. (2022*)** have investigated whether the thinning of sea ice and enhanced areas of open water in the Arctic Ocean may be more effectively exposed to extreme events. A distinct large sea-ice breakup event in the Beaufort Sea in response to a series of storms encountered in February–March 2013 formed the baseline for the study. The novel sea ice model - neXtSIM invoked with sea ice thickness derived from Cryosat-SMOS was used to simulate this storm-induced breakup. In comparison to lead detections obtained from MODIS the model has shown promising capabilities to reproduce the timing, location, and propagation of sea-ice leads associated with the breakup event.

Sea ice breakup events may furthermore have a large effect on local heat and moisture transfer and cause enhanced sea ice production, but also increased sea ice drift. Moreover, a complementary question is whether the changes in the sea ice extent and thickness will favour increasing frequency and strength of extreme events. These extreme sea ice breakup events are generally not captured by climate models and may thus potentially limit the accuracy in projections of future Arctic sea ice conditions.

Regan et al. (2020) have explored the impact of increased temperatures in the Arctic (manifested through the Arctic Amplification) on the basin scale atmospheric and ocean

circulation using altimetry-based datasets together with a high-resolution eddy-resolving model with focus on the Beaufort gyre over the period 1990-2014.

The Beaufort Gyre is an anticyclonic upper-ocean circulation feature that is the largest reservoir of fresh- water in the Arctic Ocean. The gyre has spun up over the past two decades in response to changes of the wind forcing and sea ice conditions, accumulating a significant amount of freshwater. This has an impact on the circulation in the Arctic Ocean as well as the variability of freshwater export from the Arctic, which again has the potential to influence the North Atlantic circulation and climate affecting the deep-water formation and global conveyor belt circulation. The simulation performed with a high-resolution, eddy-resolving model reveals the spatial-temporal evolutions of the mean and eddy kinetic energy in the Canada Basin with a higher level of mean kinetic energy that is generally not accompanied by higher levels of eddy kinetic energy. On average the levels of mean and eddy kinetic energy are of the same order of magnitude, with the eddy kinetic energy only intensified along the boundary and in the subsurface. In response to the strong anomalous atmospheric conditions in 2007, the gyre spins up and the mean kinetic energy almost doubles, while the eddy kinetic energy does not increase significantly for a long time period. This is because the isopycnals are able to flatten and the gyre expands outwards, reducing the potential for baroclinic instability. All in all, the results have implications for understanding the mechanisms at play for equilibrating the Beaufort Gyre and the variability and future changes of the Arctic Ocean freshwater system and its export to the global oceans through the Fram Strait, Canadian Archipelago and Bering Strait.

Cassianides et al. (2020) have developed a promising new method to detect ocean eddies in SAR images of the sea ice field. While evidence of mesoscale eddies expressed in the sea ice field has been impeded by the presence of compact sea ice concentration in the past, the recent decline in sea ice concentration and extent allow for clearer expressions of mesoscale features in the sea ice field.

By combining directly observed upper ocean currents under the sea ice in the Beaufort Gyre Exploration Project, the expression of ocean surface eddies revealed in the sea ice vorticity field have been derived from analysis of high-resolution images SAR data. Through processing of pairs of SAR images the sea ice drift is estimated by combining feature tracking and pattern matching techniques. Combining two or more images the sea ice vorticity are then calculated over several time periods, to evaluate the persistence of the signal.

Cancet et al. (2023) have investigated the impact of sea ice change on ocean tides in the Arctic Ocean, considering model simulations and observations from satellite altimetry and tide gauges. Although ocean tides are one of the major contributors to the energy dissipation in the Arctic Ocean, their characteristics are far from fully known. In particular, the interactions between tides, the sea-ice, grounded-ice and fast-ice cover are often simply ignored in tidal modelling simulations or considered through relatively simple combinations with the bottom friction.

Moreover, they also highlight the fact that most of the past and present altimetry missions that reach high latitudes are sun-synchronous. This strongly limits their capability to observe part of the ocean tidal cycles. However, thanks to the higher density of ground tracks in high latitude regions, it is possible to bin the altimetry measurements to reconstruct time series with finer time sampling and consequently reduce the tidal aliasing effects. A mission like CryoSat-2, for instance, has brought remarkable measurements to improve the tidal estimates in the Arctic Ocean, thanks both to its SAR along track and SAR-interferometric modes that enable more accurate SSH estimations in sea-ice covered coastal regions. In addition, the non-sun-synchronous orbit offer more reliable recovery of the major tidal components in contrast to the aliased signals retrieved in sun-synchronous orbits. As such, a long observational gap between the CryoSat-2 and CRISTAL missions may have serious impact on the quality of the tidal retrievals. In turn, this will hamper the uncertainty estimates from tidal models of the Arctic Ocean, which are used to remove the ocean tide signals from the altimeter SSH measurements to build the climate products.

2.5 Task 4: Analyses of future satellite mission impacts in understanding the changes to the Arctic Ocean

The *Arktalas Hoavva* synergy publication, ***Lucas et al. (2023)*** addressed how the satellite-based continuity and new approved missions (Figure 12) are expected to advance the understanding of the air - sea ice - ocean interactive processes in the Arctic Ocean and its marginal ice zones. The Sankey diagram evidences a broad and sustainable satellite-based observation capabilities of the key sea ice related variables with a promising outlook in the coming decade thanks to the addition of Explorer missions and Copernicus expansion missions. This will be increasingly important when human presence is expected to grow through increased shipping, fisheries and other activities in the Arctic Ocean and surrounding high latitude seas. By bringing new observations, often at higher spatial resolution, the approved future satellite missions will also contribute to improve the ability for model validation and assimilation in higher-resolution numerical models. In turn, this will contribute to better understanding of the complex processes in the Arctic Ocean and allow the revision and upgrade of the sea ice thermodynamics and rheology modelling approaches to better reproduce the complexity of the atmosphere - sea ice - ocean interactions and multiple feedback processes. In turn, more accurate simulations, re-analyses and reliable reconstruction of long time series can be expected, that are of prime importance to characterize an Arctic Ocean in transformation.

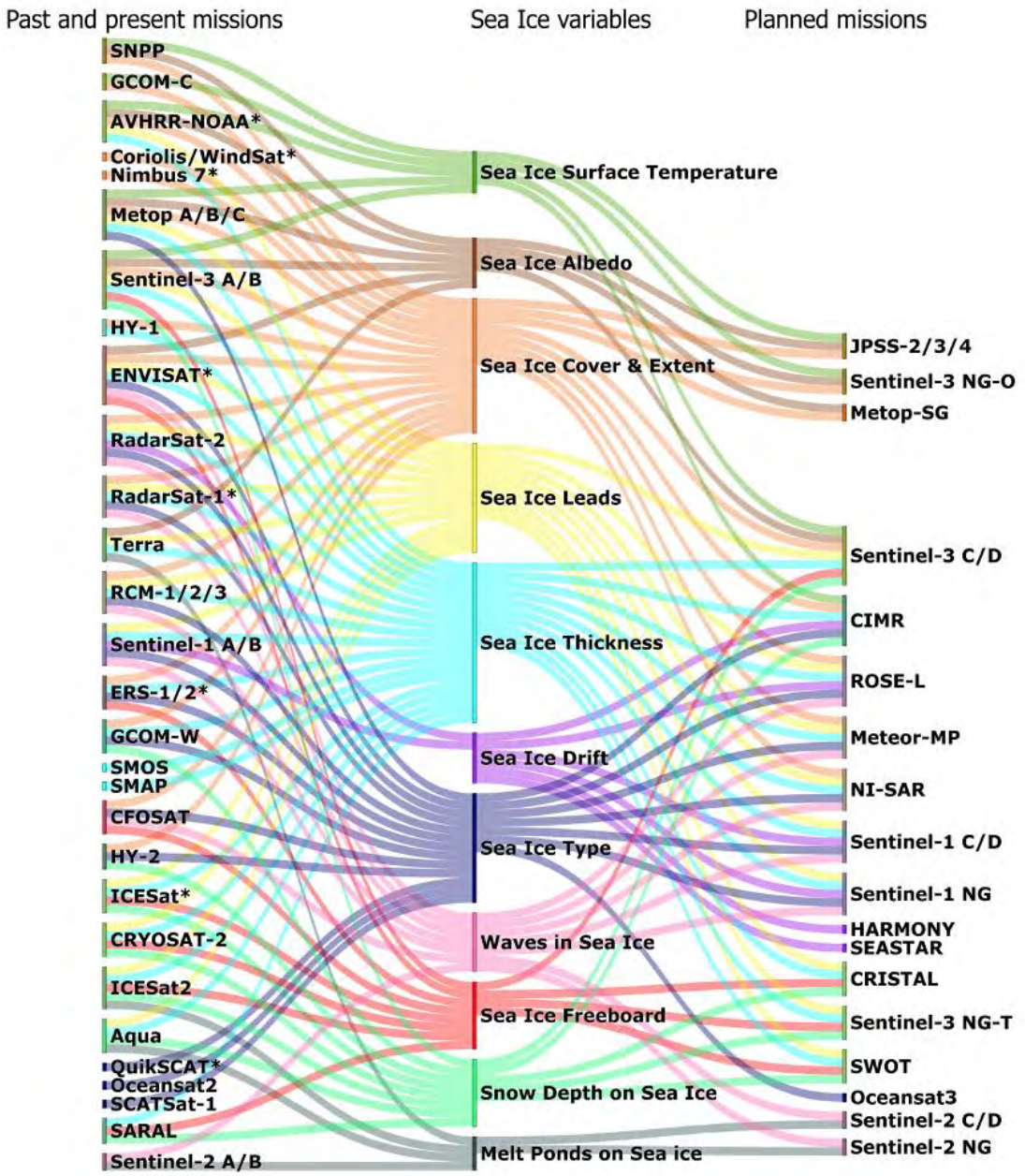

Figure 12: *Sankey diagram linking a subset of past, present and future approved satellite missions and their sea ice measurement capabilities. (left) Past (identified with *) and present satellite missions; (center) retrieved sea ice variables; (right) future approved missions (Lucas et al., 2023).*

2.6 Task 5: Promotion of the *Arktalas Hoavva* study and scientific community outreach

The *Arktalas Hoavva* promotional activities comprises of:

Task 5.1: Production and provision of high-quality plots and educational material. This will be used at the regular ESA ocean training courses.

Task 5.2: Develop and operate an open and public *Arktalas Hoavva* project website to provide a communication and study management portal for the project.

Task 5.3: Maintain, review, update and operate the web portal for a duration of the project plus 2-years including short news stories at a monthly basis during the project.

Task 5.4: Organise an open scientific meeting located in the Arctic region to review the outcomes and results of the Arktalas study and to set priorities for potential future activities. This shall be held at Svalbard at will be timed around month 21 of the study, potentially in February-March 2021.

2.6.1 Education and Training

The Syntool visualization platform, also used in Arktalas Hoavva, was an essential part of the Nansen Center-ESA Advanced Ocean Synergy Training Course 2023 in education and training in operational oceanography. The developments made in *Arktalas Hoavva* were integrated and used in the weekly three hours on-line training for 65 students from 29 countries, during 5th September to 5th December 2022. The lectures were also recorded and available for later use. The student participation in the on-line training course was free of charge.

Among the students successfully completing the on-line course, 20 students from the Member States of the European Space Agency and 40 students and Post Docs were selected and sponsored under the Norwegian PECO2 project to participate in the practical training course onboard the tall-ship *Statsraad Lehmkuhl.* During the around 1200 nautical miles and 10 days voyage from Maputo to Cape Town, of the One Ocean Expedition, an advanced practical at sea training course in satellite oceanography was conducted. The training was supporting awareness and recruitments to marine services tailored to regional environmental and climate change studies of the oceans around southern Africa. Abroad range of scientific disciplines were covered in satellite oceanography, upper ocean dynamics, air-sea interaction, coupling of ocean physics to biogeochemistry, marine biology, ocean modelling and data assimilation, and environmental and climate change. The students were grouped and tasked with delivery of group reports of their analyses and findings during the voyage. The student reports are the foundation of their later joint scientific publications. Travel grants at economy class tickets to reach Maputo in Mozambique and return home from Cape Town in South Africa as well as free accommodation onboard were offered to the selected students.

2.6.2 The Arktalas Hoavva project web site

The *Arktalas Hoavva* project website was established soon after the project Kick-off meeting in July 2019 and has been maintained since then (**Figure 13**).

The project web-site have the following content and structure:

- Project News stories; presenting the project results and progress.
- Results - in terms of publications and public data
    - The NERSC Arctic Data Portal

- Project partners
- Calendar of project events and related activities
- Related links (to external activities and missions)
- Documents
    - Publications
    - Project deliverables
    - PPT material
    - Minutes of Meetings

Figure 13: *A screen dump of the Arktalas Hoavva web front page.*

Throughout the project duration, on major events and achievements, popular language news stories have been. Published on the *Arktalas Hoavva* website, including:

- The *ARKTALAS HOAVVA* project
- *Arktalas Hoavva* Final Scientific Workshop
- Mechanisms for extreme sea ice break-ups events in the Arctic
- Waves plays an increasing role in shaping the sea ice dynamics in a warmer Arctic Ocean
- Consecutive satellite images detects mesoscale ocean eddies in ice-covered waters
- An emerging apparent Arctic Amplification: A synthesis of paradigms and satellite observations
- Exploration of the linkages between sea ice and ocean tides in the Arctic Ocean
- Response of Total and Eddy Kinetic Energy to the Recent Spinup of the Beaufort Gyre
- Wind-wave attenuation under sea ice in the Arctic Ocean: a review of remote sensing capabilities.

- Observing the changes in the Arctic Ocean: current gaps and impact of the future satellite missions

2.6.3 The Arktalas Hoavva Scientific Workshop in Longyearbyen

An open *Arktalas Hoavva* scientific workshop was organized at UNIS in Longyearbyen 26th to 20th April 2022, with 15 on-site or on-line participants from the project team, ESA, local and international scientific institutions and beyond.

The key achievements and findings of the project (focusing on the eight scientific publications) were reviewed contributing valuable input to the (at that time) remaining publications, as well as setting the priorities for development of usage of satellite Earth observation (EO) data in the Arctic Ocean.

For the Scientific Roadmap a SWOT (Strengths, Weaknesses, Opportunities and Threats) analysis were conducted on the four initial Arctic Scientific Challenges (ASC´s) addressed in *Arktalas Hoavva* to further advance Arctic science (see Task 6A Scientific Road Map).

2.7 Task 6a: Creating a scientific roadmap

2.7.1 Lessons learned in Arktalas Hoavva

In order to fully benefit from the satellite-based observation capabilities there is a crucial need for Fiducial Reference Measurement (FRM) data for calibration and validation, in particular as finer spatial resolution are emerging. Moreover, towards 2030 advances in development of Digital Arctic Twin components jointly with regular reprocessing, use of sensor synergy and multi-modal physical constrained co-variability analytics are likely to deliver more reliable estimates of sea ice drift, damage, break-up, lead fraction, new ice formation, sea ice freeboard height, sea ice volume, mean sea level and sea surface height. In turn, the quantitative understanding of the dominant multidisciplinary physical interactive processes that drive the sea ice thermodynamic state and variability in the Arctic Ocean and its marginal ice zones is anticipated to strengthen, notably regarding:

- atmospheric boundary layer stratification and thermodynamics;
- upper ocean stratification and thermodynamics;
- momentum, gas and heat fluxes;
- freshwater spreading;
- local and non-local connexions.

Indeed, the approach must advance better understandings of the role of the changing sea ice cover for the marine ecosystem, coastal erosion and the long-distance atmospheric teleconnection that, in turn, influences the weather and climate at mid-latitudes. As the sea ice cover breaks up, it exposes the underlying warmer ocean to the atmosphere within polynyas and narrow elongated openings in the sea ice cover known as leads. This has important consequences for air-sea momentum, heat and gas exchanges, mesoscale eddy

generation and dynamics and sea ice production, in particular, during winter months when the heat fluxes over sea ice are generally low, the oceanic heat loss within polynyas and leads may cause local air surface air temperature rise of more than 20°C. In turn, this enhances turbulent convection in the atmospheric boundary layer, possibly driving further breakup and sea ice production. The sea ice breakup in winter due to storm events combined with long-distance wave propagation also weaken the sea ice cover, potentially preconditioning the minimum sea ice extent in the subsequent summer (Babb et al., 2019), and thus create positive feedback to the Arctic amplification (Esau et al, 2023). Extreme sea ice breakup events, expected to increase due to global warming, are therefore of crucial importance for understanding the seasonal to long-term evolution and change of sea ice extent and volume, which, in turn, affects weather, ecosystems, and local communities in polar regions and beyond (Forbes et al., 2016; Rheinlaender et al., 2020). Moreover, sea ice thinning and gradually disappearance can increase upper ocean currents and intensify upper ocean turbulence, particularly over the continental shelf edge. In turn, this can enhance upward heat flux to the surface to further reduce sea ice thickness and cover, even during winter.

Satellite measurements in the Arctic are unique but may be influenced by several technical, observational, and environmental challenges related to orbit, instrument type, cross-calibration and retrieved Earth system variables. Although the converging ground tracks of polar orbiting satellites favours improved coverage, limited coverage across the true North Pole of the central Arctic Ocean leads to the Polar gaps. The use of optical satellite instruments is also limited due to the polar night and commonly harsh meteorological conditions including clouds and haze. Long-term optical satellite data products are therefore fragmented, likely leading to biases towards observations in clear sky conditions, with both potential seasonal and geographical variations. Interpolation and gap closure methods are thus always questionable as they rely on assumption that the statistics under clear sky and overcast are the same. Systematic comparisons and analysis of optical and high-resolution radar observations are still limited but shall be considered to identify these statistical changes. Climate datasets like the ESA Climate Change Initiative (CCI) that today are facing limitations should benefit from these studies. Further note that radiative transfer models are incomplete, radar backscatter from mixed pixels often difficult to quantify and partition into individual geophysical signal sources, spatial resolution largely insufficient, sensor frequency selections limited, and empirical-based relationships predominantly driving the retrieval algorithms. These deficiencies largely impact proper satellite-based identification of the dominant spatial and temporal scales of key variables.

Moreover, the compilation of satellite observations to build homogenous, cross-calibrated and cross-validated, long and continuous data records of climate quality, across multiple satellite missions, is also challenging. Sensors and platforms degrade with time, sometimes stop to function, and need to be replaced or substituted, often with different technical specifications and performances. Hence, even a single year with lower quality data can

cause significant deviations and uncertainty for long-term climate records. The lack of in-situ FRM for accurate calibration and validation of satellite observations in the Arctic Ocean clearly hampers the generation and provision of homogeneous datasets. Foremost, incorporating new sensor observations to help revisiting previous processing strategies and retrieval algorithms, is still an essential step to better understand air - sea ice - ocean interactions and identify the slow-fast dynamic processes. Several initiatives have been launched by ESA to define FRM strategies for satellite observations, but these are currently limited to a few types of observations (e.g. FRM4SOC for ocean colour, FRM4STS for surface temperature, FRM4Alt and St3TART for radar altimetry-based sea surface height). These are designed to develop and apply rigorous approaches to ensure that satellite data are traceable to given S.I. units with a full uncertainty budget.

In particular in the Arctic region, high-resolution satellite data may be more directly interpreted. Radar textural properties at high resolution have indeed demonstrated unique and quite straight forward abilities to detect sea ice breakup and lead formation, sea ice drift, deformation, and damage, but also to detect wave pattern in ice to evaluate sea ice thinning. From an Earth-Observation perspective, an important component of the Digital Twin Ocean-Arctic (DTO-Arctic) development will largely build on these high-resolution data-centric approaches to become one of the essential layers to derive these interactive digital replicas of the Arctic system. This layer will inform and help to train numerical and statistical simulations about processes and feedback in response to external forces. As already mentioned, a more fractured ice cover will impact the momentum, heat, moisture, and gas exchanges between the atmospheric boundary layer and the upper ocean in the Arctic, and also strongly impact the upper ocean biology as the primary production is highly dependent on availability of light and nutrients.

Among high-resolution satellite data, fully-focused altimeter measurements have emerged and already demonstrated promising abilities to detect wave propagation in the highly dynamic marginal ice zone. The same has been shown using satellite sun glitter imagery such as the Sentinel-2 Multi-Spectral Instrument (MSI) for ocean wave detection in the presence of sea ice (Collard et al., 2022). All these measurements could be used to complement the Sentinel-1 measurements. While strong temperature and humidity gradients in the atmospheric boundary layer make the Arctic a very cloudy and hazy place that severely limits the availability of exploitable Sentinel-2 optical images, systematic comparisons with radar measurements will likely help to train efficient Machine Learning algorithms. While wave pattern detection from imaging spectrometers like Sentinel-2 certainly requires favourable sun illumination angle, and alignment between the instrument and the surface wave field, they provide reference measurements to help refine the retrieval algorithms from SAR nadir and off-nadir measurements.

A targeted generic demonstration is to continue to develop a more advanced physical-based model constrained with data. Already, some what-if scenarios can be simulated using

existing models such as the ArcMFC within CMEMS and the neXtSIM (Rheinlaender et al., 2022). But continuous progresses on advances in machine learning and observations will certainly help new developments to estimate evolving sea ice mechanical properties to deliver improved kinematic forecasting capability. This new capability is a very good candidate for a DTC, as it combines advanced high-resolution EO (e.g. SAR-altimeter, SWOT, Sentinel-1 and Radarsat SAR measurements, Sentinel-2, … and associated deformation-field products), contemporary machine learning algorithms and a novel physics-based model. For instance, it can be used to better test and understand sea ice break-ups (as influenced by sea ice extent and sea ice thickness) due to strong winds and their consequences. Such developments will also further provide means to guide more direct interpretation of high-resolution EO snapshots, to envisage and manage what/if scenario questions relevant to a wide range of stakeholders need for making informed decisions. Note, operational services are crucial to the Arctic region's shipping, tourism, fishing industries and search and rescue, to meet the scientific ambitions to advance in understanding of how the sea ice reacts to climate change, and to consider climate mitigation and adaptation. In the current geopolitical climate, operations in the Arctic region may also have significant implications for national and regional security. Additionally, DTCs will be able to generate what-if scenarios using existing missions together with new approved Sentinel and Earth Explorer satellite missions to support the planning, design and operation of future satellite missions.

All in all, the approach to advance the design and implementation of a DTC of the Arctic Ocean will build on data-driven physical constrained analytics, where satellite-based multi-sensor high-resolution EO data will be combined with available in-situ data and regularly sampled numerical model fields, such as from the advanced neXtSIM sea-ice model. An Arctic Ocean DTC will help: (a) visualize, intercompare, analyze, and validate the sea ice conditions; and (b) augment the irregularly sampled satellite-based EO-data using the neXtSIM model to assess the impact of the high-resolution sea ice conditions at the larger scales and longer-terms covering the entire Arctic region. In this respect the NERSC Arctic Portal, implemented in the *Arktalas Hoavva* project, will be an efficient tool for acquiring, synergetic analysis and presentation of existing and future satellite and *in situ* data, as well as model results for scientific studies of the Arctic Ocean.

2.7.2 Priority areas to potentially be addressed in future activities

Observations are crucial to building our understanding of the physical Earth system. For up-to-date information on the state of the Arctic climate system, continuous monitoring and reprocessing are required to support both short-term forecasting and seasonal and decadal prediction efforts.

In the coming decade the satellite-based observation capabilities will clearly strengthen in combination with advances in machine learning and numerical modelling. Towards 2030 a new generation of high-resolution satellite sensors including the Copernicus Expansion missions (e.g., ROSE-L, CMIR, CRISTAL), the Explorer missions (e.g Harmony) and the next

generation of meteorological satellites (e.g., MetOp-SG, AWS) will be launched. Complemented with the series of Sentinels (e.g., Sentinel 1, 2, 3, 6), the MAGIC mission and 3rd party missions this offers a unique and unprecedented capability to strengthen the satellite-based observation capabilities in the Polar regions. New approaches to use multiple native resolution satellite measurements (i.e. single image snapshots, altimeter transects, visible/thermal infrared, microwave imaging radiometry, scatterometry and synthetic aperture radar imagery) rather than gridded fields (that often smear important features) in a broader data-centric analysis framework will emerge. In combination with access to in-situ data, high fidelity Large Eddy Simulation (LES) experiments and advances in development of AI/ML will help better understand governing sub-grid unresolved and coupled processes.

In that context, the Arctic Digital Twin Components continuous research will therefore secure more reliable analyses and estimates of sea ice damage, break-up, lead and polynya formation, sea ice roughness, sea ice drift, new ice formation, sea ice freeboard height, snow depth, meltwater ponds, sea ice volume and mean sea level. Better determination of fluxes driving changes in the atmospheric boundary layer, sea ice and upper Arctic Ocean is also anticipated, while better validation of higher-resolution models will strengthen assimilation, reanalyses and reconstruction of more reliable long time series.

The key remaining challenges that have emerged along the Arktalas Hoavva project are rather generic and can be summarized to the following needs:

- to provide efficient and interoperable frameworks and architectures to access data and model resources across institutions and organizations;
- to constitute large, homogeneous, curated multi-variable datasets for model training and validation;
- to refine mathematical approaches tailored to cope with sparse data and analysis of rare and/or extreme events;
- to consider software infrastructure and common tools for supporting developments of hybrid model components.

Prioritizing the collection, synthesis and curation of reference data (including in situ, satellite, and numerical simulations) is key to create AI-ready datasets for model training and validation. Reanalysis models, assimilating satellite and in-situ observations already offer open-access data-cube facilities to help apply AI techniques (i.e. reanalysis performs a consistent dynamical space-time gridded interpolation of the different variables). Still, these models do not manage to precisely identify all the multiple and complex interactions between variables (e.g. atmospheric boundary layer, upper ocean physical and biological coupling across differing space-time scales including rare and extreme events). As such it is highly important to systematically combine the present-day available model-data cubes with direct satellite-based and in-situ based observations to strengthen the generation of AI-ready datasets.

In particular, efforts should rapidly target:

Advanced sensor synergy (extension of the RGPS approach) retrievals of sea ice drift trajectories from Sentinel-1 SAR. Building on systematic use of satellite C-band SAR data the Radarsat Geophysical Processor System (RGPS) sea ice drift and deformation product has been widely used for studying sea ice kinematics as well as for calibration/validation of sea ice models. In this respect, it was essential for stimulating the development of the next generation sea ice model (neXtSIM). There is a need to re-enforce the unique capability of this method by extending observations (from visible to microwave L-band), operating at different resolution but offering a potential very high-temporal sampling. In particular, it is proposed to generate multi-satellite product to advance understandings of the sea ice dynamics and drift and to open for calibration of data-driven methodologies to downscale estimates from medium and low-resolution observations (e.g. L-band SMOS). This effort enters precursor demonstrations of model-driven strategies to demonstrate the advanced Digital Twin Component capabilities and usage to simulate complex processes that are not properly characterized in sea ice models, with targeted focus on CIMR, Rose-L, Cristal in combination with operational meteorological satellites.

Validation of the sea ice rheology on satellite data. Simulation of accurate sea-ice thickness distribution, which is especially important for predicting regional winter climate and Arctic amplification remains a challenge. Sea-ice motion plays an important role in the ice thickness distribution and a more realistic sea ice rheology is required that is consistent with the observed mechanical behavior of sea-ice. A novel metric building on multi-sensor satellite observation synergy needs to be developed to evaluate Lagrangian model simulations (e.g. neXtSIM) including detection and tracking of linear kinematic features associated with sea ice damage and lead formation. By invoking neXtSIM results as input in a Conventional Neural Network (CNN) approach the output can include sea ice rheological parameters. Once trained satellite observations can then be used as input for the output retrieval of optimal parameter values.

Improving air and ocean drag coefficient parametrization in the neXtSIM sea ice model. Despite the strong dependence of the air and ocean drag on sea ice roughness, it is currently represented in neXtSIM by only two coefficients, which are not varying neither in space, nor in time. Recent studies show successful retrieval of ice roughness from ICESat-2 data on pan-Arctic scale but with low spatial resolution. Capitalizing on these studies it is recommended to use ICESat-2 in synergy with CryoSat-2 and Sentinel-1 to derive sea ice roughness at much higher spatial resolution. Time- and space-varying fields of sea ice roughness can then be used for computing the air and ocean drag coefficients in netXtSIM. The transfer function can be tuned using satellite-derived sea ice drift. All in all this approach will expectedly improve sea ice forecast.

Detection and characterization of marginal ice zone on Sentinel-1 SAR. ML-algorithm based on convolutional neural networks will be trained on Sentinel-1 SAR data and ice charts for

robust detection of marginal ice zone dynamics and characterization of the sea ice in terms of floe size distribution. The algorithm will be applied to series of SAR images and the derived MIZ maps will be used for evaluation of the neXtSIM coupled with WW3 wave model followed by assimilation into neXtSIM-Wave model tested in operational setup.

Longer time series of sea ice age fraction maps. The sea ice age dataset from NSIDC is a long time series but is considered to overestimate the age in individual pixels and to deliver too high heterogeneity of the product due to the deficiencies in the advection method. A new sea ice age algorithm that provides a distribution of ice age fractions for each pixel in homogenous fields will be explored for the period 2002 to present (AMSR2 era) with an extension back to 1994 using OSI-SAF ice drift in winter and TOPAZ (or neXtSIM) reanalysis data in summer.

Simulation of CIMR brightness temperatures. High resolution CIMR radiometer data makes it more sensitive to anomalies in brightness temperature originating from narrow cracks in sea ice. neXtSIM is known to properly reproduce sea ice deformation at the model resolution and realistically simulate ice break-up. The thermodynamic part of the model can be extended to include salinity, porosity and other relevant properties of sea ice and snow. Moreover, the ice and snow emissivity model can be plugged into neXtSIm to simulate CIMR data at high resolution. The simulated data can be used for testing / developing CIMR algorithms, for instance, starting activities of assimilating CIMR data at brightness temperature level.

Ground truthing: Capitalizing on the regular UNIS (Svalbard) field studies the opportunity to use Svalbard as a "Sustainable Climate Reference Laboratory for Earth Observation" is highly interesting for establishing time series (like the Manoa Loa CO_2 measurements). Primary products might include SST, local sea ice concentration, thickness, extent, type, snow depth, presence of meltwater ponds, salinity, water vapor and cloud liquid water. Ideally this could contribute to both pre- and post-launch Copernicus expansion missions (CRISTAL, CIMR, Rose-L and the Next generation Sentinel-3 altimeter) field campaigns. In particular, it is recommended to conduct a pilot study over a sea ice reference site in vicinity of the Svalbard including access to coincident scanning laser data take.

All in all these recommended activities will, in turn, strengthen the research and understanding of the important role of the Arctic Ocean in transition at the regional to global scales, notably regarding:

- transport of freshwater and Atlantic Water in the Arctic Ocean in the presence of declining sea ice extent;
- changes in biogeochemistry, biology and ecosystem under the transition towards a blueArctic;
- vertical mixing processes from the top of the atmospheric boundary layer to the depth of the halocline layer in the upper ocean;

- the regional water cycle, energy cycle and carbon cycle;
- teleconnection and influence on weather and climate at lower latitudes (globally in fact).

3 CITED REFERENCES

Babb, D. G., Landy, J. C., Barber, D. G., & Galley, R. J. (2019). Winter sea ice export from the Beaufort Sea as a preconditioning mechanism for enhanced summer melt: A case study of 2016. *Journal of Geophysical Research: Oceans*, 124, 6575–6600. https://doi.org/10.1029/2019JC015053

Barthélémy, S., Brajard, J., Bertino, L., & Counillon, F. (2022). Super - resolution data assimilation. Ocean Dynamics, 72(July), 661–678. https://doi.org/10.1007/s10236-022-01523-x

Bertino et al. (2021) Report on ways to improve the description of the changing Polar Regions in all existing and planned marine Copernicus Services capability. KEPLER Deliverable 5.1 https://kepler380449468.files.wordpress.com/2021/06/kepler-deliverable-report-5.1.pdf

Bojinski, S., Verstraete, M., Peterson, T. C., Richter, C., Simmons, A., and Zemp, M. (2014). The Concept of Essential Climate Variables in Support of Climate Research, Applications, and Policy. Bull. Am. Meteorol. Soc. 95, 1431–1443. doi: 10.1175/BAMS-D-13-00047.1.

Boutin, G., T. Williams, C. Horvat and L. Brodeau (2021) Modelling the Arctic wave-affected marginal ice zone, comparison with ICESat-2 observations. *Philosophical Transactions A.* ***380****.* https://doi.org/10.1098/rsta.2021.0262

Brajard, J., Carrassi, A., Bocquet, M., & Bertino, L. (2020). Combining data assimilation and machine learning to emulate a dynamical model from sparse and noisy observations: A case study with the Lorenz 96 model. Journal of Computational Science, 44, 101171. https://doi.org/10.1016/j.jocs.2020.101171

Cancet, Mathilde , Florent H. Lyard, Ergane Fouchet (2023), Impact of sea ice friction on ocean tides in the Arctic Ocean, modelling insights at various time and space scales, *submitted to Ocean Modelling.*

Cassianides, A., C. Lique, A. Korosov (2021), Ocean eddy signature on SAR-derived sea ice drift and vorticity, *Geophys. Res. Letter*, 16 February 2021, https://doi.org/10.1029/2020GL092066

Cole, S.T., J.M. Toole, L. Rainville, C.M. Lee (2018), Internal Waves in the Arctic: Influence of Ice Concentration, Ice Roughness, and Surface Layer Stratification, JGR Oceans, 18 July 2018 https://doi.org/10.1029/2018JC014096

Collard, Fabrice, Louis Marie, Frederic Nouguier, Marcel Kleinherenbrink, Frithjof Ehlers, and Fabrice Ardhuin (2022), Wind-wave attenuation under sea ice in the Arctic: A review of remote sensing capabilities, *Journal of Geophys. Res. – Ocean, 2022, DOI: 10.1002/essoar.1051096.1*

Esau, Pettersson, Cancet, Chapron, Chernokulsky, Donlon, Sizov, Soromotin, and Johannesen (2023), The Arctic Amplification and Its Impact: A Synthesis through Satellite Observations, *Remote Sensing 15, no. 5: 1354. https://doi.org/10.3390/rs15051354*

Forbes Bruce C., Kumpula Timo, Meschtyb Nina, Laptander Roza, Macias-Fauria Marc, Zetterberg Pentti, Verdonen Mariana, Skarin Anna, Kim Kwang-Yul, Boisvert Linette N., Stroeve Julienne C. and Bartsch Annett. 2016. Sea ice, rain-on-snow and tundra reindeer nomadism in Arctic Russia. Biol. Lett. 122016046620160466 http://doi.org/10.1098/rsbl.2016.0466

Lavergne, T., Kern, S., Aaboe, S., Derby, L., Dybkjaer, G., Garric, G., et al. (2022). A New Structure for the Sea Ice Essential Climate Variables of the Global Climate Observing System. Bull. Am. Meteorol. Soc. 103, E1502–E1521. doi: 10.1175/BAMS-D-21-0227.1.

Lucas, S.; Johannessen, J.A.; Cancet, M.; Pettersson, L.H.; Esau, I.; Rheinlænder, J.W.; Ardhuin, F.; Chapron, B.; Korosov, A.; Collard, F.; Herlédan, S.; Olason, E.; Ferrari, R.; Fouchet, E.; Donlon, C. (2023**).** Knowledge Gaps and

Impact of Future Satellite Missions to Facilitate Monitoring of Changes in the Arctic Ocean. *Remote Sens.* 2023, *15*, 2852. https://doi.org/10.3390/rs15112852

Ólason, E., Boutin, G., Korosov, A., Rampal, P., Williams, T., Kimmritz, M., et al. (2022). A New Brittle Rheology and Numerical Framework for Large-Scale Sea-Ice Models. J. Adv. Model. Earth Syst. 14, e2021MS002685. doi: 10.1029/2021MS002685.

Regan, H., C. Lique, et al. (2020) Response of Total and Eddy Kinetic Energy to the recent spin up of the Beaufort Gyre, *Journal of Physical Oceanography,* March 2020, https://doi.org/10.1175/JPO-D-19-0234.1

Rheinlænder, Jonathan W., Richard Davy, Einar Olason, Pierre Rampal, Clemens Spensberger, Timothy D. Williams, Anton Korosov, Thomas Spengler (2022), *Geophys. Res. Letter* 15. June 2022 https://doi.org/10.1029/2022GL099024

Xie, J., Bertino, L., Counillon, F., Lisæter, K. A., & Sakov, P. (2017). Quality assessment of the TOPAZ4 reanalysis in the Arctic over the period 1991–2013. Ocean Science, 13(1), 123–144. http://doi.org/10.5194/os-13-123-2017

4 ANNEXES

4.1 Annex: Arktalas Hoava Project participants and contact information

Personnel	Address/ e-mail	Phone
Nansen Environmental and Remote Sensing Center (NERSC)	**Jahnebakken 3, N-5007 Bergen, Norway**	**+4755205800**
Johnny A. Johannessen	Johnny.Johannessen@nersc.no	+47 93249414
Lasse H. Pettersson	Lasse.Pettersson@nersc.no	+47 93223563
Anton Korosov	Anton.Korosov@nersc.no	
Timothy Williams	Timothy.Williams@nersc.no	
Einar Ólason	Einar.Olason@nersc.no	
Igor Esau	Igor.Ezau@nersc.no	
Jonathan W. Rheinlænder	jonathan.rheinlaender@nersc.no	
Ricard Davy	Richard.davy@nersc.no	
IFREMER	**Zi Pointe du Diable, 29280 PLOUZANE, France**	
Bertrand Chapron	Bertrand.Chapron@ifremer.fr	+33 298224312
Camille Lique	camille.lique@ifremer.fr	
Fabrice Ardhuin	fabrice.ardhuin@ifremer.fr	
Angelina Cassianides	angelina.cassianides@ifremer.fr	
Ocean Data Lab -ODL	**870, route de Deolen, 29280 LOCMARIA PLOUZANE, France**	
Fabrice Collard	dr.fab@oceandatalab.com	
Sylvain Herlédan	sylvain.herledan@oceandatalab.com	
NOVELTIS	**153, rue du Lac F-31670 LABEGE, France**	
Mathilde Cancet	mcancet@mercator-ocean.fr	
Ramiro Ferrari	ramiro.ferrari@noveltis.fr	
Ergane Fouchet	ergane.fouchet@noveltis.fr	
Eric Jeansou	Eric.Jeansou@noveltis.fr	
Sylvain Lucas	sylvain.lucas@cnes.fr	

4.2 Annex: Key Arktalas Hoava project events

ID	Planned Date	Actual date	Venue	Purpose
KO	KO	09.07.2019	WebEx	Kick off meeting
PM-1	KO+3	5-6. 02.2020	NERSC, Bergen	Progress Meeting
PM-2	KO+6	01.07.2020	ESTEC	Progress Meeting
PM-3	KO+9	07.10.2020	WebEx	Progress Meeting
PM-4	KO+12	06.05.2021	Contractor	Progress Meeting
PM-5	KO+15	10.09.2021	WebEx	Progress Meeting with project partners
	KO+15	15-17.09.2021	WebEx	ESA Polar Science Cluster Collocation Meeting
PM6/ PM-7	KO+21	26-29. April 2022	UNIS/NERSC, Longyearbyen	Joint Progress meeting and Science workshop
		23-24 Nov. 2022	ESA-ESRIN, Frascati, Italy	ESA-EU Polar Science Cluster meeting
FM	KO+24	TBD Nov. 2023	TBD	Final Review
		2.-6. May 2023	UNIS, Longyearbyen	ESA SeaSAR 2023 workshop
		22-24 Nov. 2023	ESA-ESRIN, Frascati, Italy	ESA-EU Polar Science Cluster meeting

4.3 Annex: Arktalas Hoava Scientific Publications

Full versions of the following *Arktalas Hoavva* scientific publications follow:

1. Esau, I.; Pettersson, L.H.; Cancet, M.; Chapron, B.; Chernokulsky, A.; Donlon, C.; Sizov, O.; Soromotin, A.; Johannesen, J.A. **The Arctic Amplification and Its Impact: A Synthesis through Satellite Observations**. *Remote Sens.* **2023**, *15*, 1354. https://doi.org/10.3390/rs15051354
2. Collard, F., Marié, L., Nouguier, F., Kleinherenbrink, M., Ehlers, F., & Ardhuin, F. (2022). **Wind-wave attenuation in Arctic sea ice: A discussion of remote sensing capabilities.** *Journal of Geophysical Research: Oceans*, 127, e2022JC018654. https://doi.org/10.1029/2022JC018654
3. Boutin G, Williams T, HorvatC, Brodeau L. (2022). **Modelling the Arcticwave-affected marginal ice zone: acomparison with ICESat-2 observations.** *Phil.Trans. R. Soc. A380: 20210262.* https://doi.org/10.1098/rsta.2021.0262
4. Rheinlænder, J. W., Davy, R., Ólason, E., Rampal, P., Spensberger, C., Williams, T. D., Korosov, A. and Spengler, T. (2022). **Driving mechanisms of an extreme winter sea ice breakup event in the Beaufort Sea.** *Geophysical Research Letters*, 49, e2022GL099024. https://doi.org/10.1029/2022GL099024
5. H. Regan, C. Lique, C. Talandier and G. Meneghello (2020). **Response of Total and Eddy Kinetic Energy to the recent spin up of the Beaufort Gyre.** Published in *J. Physic. Oceangr.*, p. 575-594, 1. March 2020, https://doi.org/10.1175/JPO-D-19-0234.1
6. Cassianides, A., Lique, C., & Korosov, A. (2021). **Ocean eddy signature on SAR-derived sea ice drift and vorticity.** *Geophysical Research Letters*, 48, e2020GL092066. https://doi.org/10.1029/2020GL092066
7. Cancet, Mathilde , Florent H. Lyard, Ergane Fouchet (2023), **Impact of sea ice friction on ocean tides in the Arctic Ocean, modelling insights at various time and space scales**, *submitted to Ocean Modelling.*
8. Lucas, S.; Johannessen, J.A.; Cancet, M.; Pettersson, L.H.; Esau, I.; Rheinlænder, J.W.; Ardhuin, F.; Chapron, B.; Korosov, A.; Collard, F.; Herlédan, S.; Olason, E.; Ferrari, R.; Fouchet, E.; Donlon, C. (2023). **Knowledge Gaps and Impact of Future Satellite Missions to Facilitate Monitoring of Changes in the Arctic Ocean.** *Remote Sens.* 2023, *15*, 2852. https://doi.org/10.3390/rs15112852

Including eight scientific papers – totally 145 pages.

remote sensing

IMPACT FACTOR 5.349

CITESCORE 7.4

Review

The Arctic Amplification and Its Impact: A Synthesis through Satellite Observations

Igor Esau, Lasse H. Pettersson, Mathilde Cancet, Bertrand Chapron, Alexander Chernokulsky, Craig Donlon, Oleg Sizov, Andrei Soromotin and Johnny A. Johannesen

Special Issue

Earth Observations for Sustainable Development Goals

Edited by

Dr. Joan Masó, Dr. Ivette Serral and Dr. Alaitz Zabala Torres

MDPI

https://doi.org/10.3390/rs15051354

remote sensing

MDPI

Review

The Arctic Amplification and Its Impact: A Synthesis through Satellite Observations

Igor Esau [1,2,*], Lasse H. Pettersson [1], Mathilde Cancet [3], Bertrand Chapron [4], Alexander Chernokulsky [5], Craig Donlon [6], Oleg Sizov [7], Andrei Soromotin [8] and Johnny A. Johannesen [1]

1 Nansen Environmental and Remote Sensing Center, Jahnebakken 3, 5007 Bergen, Norway
2 Department of Physics and Technology, UiT—The Arctic University of Norway, 9037 Tromsø, Norway
3 NOVELTIS, 31670 Labège, France
4 Ifremer, 1625 Rte de Sainte-Anne, 29280 Plouzané, France
5 A.M. Obukhov Institute of Atmospheric Physics of the Russian Academy of Science, 3 Pyzhevsky, 119017 Moscow, Russia
6 Earth Surfaces and Interior Section (EOP-SME), Earth and Mission Science Division, European Space Agency/ESTEC, Keplerlaan 1, 2201 AZ Noordwijk, The Netherlands
7 Oil and Gas Research Institute of the Russian Academy of Sciences (OGRI RAS), 3 Gubkina Street, 119333 Moscow, Russia
8 Institute of Ecology and Natural Resources Management, Tyumen State University, Volodarskogo, 6, 625003 Tyumen, Russia
* Correspondence: igor.ezau@uit.no

Abstract: Arctic climate change has already resulted in amplified and accelerated regional warming, or the Arctic amplification. Satellite observations have captured this climate phenomenon in its development and in sufficient spatial details. As such, these observations have been—and still are—indispensable for monitoring of the amplification in this remote and inhospitable region, which is sparsely covered with ground observations. This study synthesizes the key contributions of satellite observations into an understanding and characterization of the amplification. The study reveals that the satellites were able to capture a number of important environmental transitions in the region that both precede and follow the emergence of the apparent amplification. Among those transitions, we find a rapid decline in the multiyear sea ice and subsequent changes in the surface radiation balance. Satellites have witnessed the impact of the amplification on phytoplankton and vegetation productivity as well as on human activity and infrastructure. Satellite missions of the European Space Agency (ESA) are increasingly contributing to amplification monitoring and assessment. The ESA Climate Change Initiative has become an essential provider of long-term climatic-quality remote-sensing data products for essential climate variables. Still, such synthesis has found that additional efforts are needed to improve cross-sensor calibrations and retrieval algorithms and to reduce uncertainties. As the amplification is set to continue into the 21st century, a new generation of satellite instruments with improved revisiting time and spectral and spatial resolutions are in high demand in both research and stakeholders' communities.

Keywords: European Space Agency; Climate Change Initiative; Arctic amplification; satellite observations; climate change monitoring

Citation: Esau, I.; Pettersson, L.H.; Cancet, M.; Chapron, B.; Chernokulsky, A.; Donlon, C.; Sizov, O.; Soromotin, A.; Johannesen, J.A. The Arctic Amplification and Its Impact: A Synthesis through Satellite Observations. *Remote Sens.* **2023**, *15*, 1354. https://doi.org/10.3390/rs15051354

Academic Editors: Joan Masó, Ivette Serral and Alaitz Zabala Torres

Received: 9 January 2023
Revised: 24 February 2023
Accepted: 25 February 2023
Published: 28 February 2023

1. Introduction

On 29 May 2020, a power plant oil reservoir near Norilsk, Russia collapsed, causing one of the largest oil spills and incidences of extensive land and water contamination in the Arctic. About 17,000 tons of diesel went into the river Ambarnaya and streamed down towards the large lake Pyasino (see Figure 1). Nobody was injured in this remote area, but the total cost of the disaster exceeded USD 2 billion. This accident became a rallying cry, among other such unpleasant reminders, of rapid Arctic warming and its adverse impact on the natural environment, infrastructure, and society in the region. Moreover, the

accident highlighted the indispensable role of satellite observations' disclosure of the true scale and extent of damages. The European Space Agency (ESA)'s Sentinel-2 platform has been used to complement the analysis, field photographs, and historical data covering the 1980–2020 daily air temperature and precipitation, permafrost observations, and modeling—all diverse materials that helped to attribute this accident to the Arctic amplification of global warming [1]. Its immediate cause, a collapsing pillar, was accidental and local. Yet this collapse occurred due to more persistent and large-scale climate factors, namely, accelerated permafrost thaw that followed the abnormally warm weather in May 2020. The permafrost thaw and weakened ground-bearing capacities were the result of preceding decades of climate change [2].

Figure 1. The Copernicus Sentinel-2 image of an oil (diesel) spill into the river Ambarnaya near Norilsk, Russia. The image, from 1 June 2020, was processed by the ESA and has been made available under CC BY-SA 3.0 IGO license at https://www.esa.int/ESA_Multimedia/Images/2020/06/Arctic_Circle_oil_spill (accessed on 8 January 2023).

Capturing the climate change over a relatively short period—the majority of remote-sensing data products have become available since 1979 [3]—satellite observations have proven to be crucial for the discovery and monitoring of important changes in the earth's climate system [4]. Particularly, Arctic climate studies and environmental monitoring have benefited from the high density of cross sections of polar-orbiting satellites [5]. Arguably, many climate phenomena would not have been detected by climate models and conventional observations alone [4], for example, the spatial pattern of sea ice retreat [6] and increasing biological productivity (greening) in the high northern latitudes [7]. One such impactful phenomenon is a climatic transition from multiyear to seasonal sea ice in the Arctic Ocean [8], which unlocked surface feedback leading to the emergence of the apparent amplification in the 21st century [9].

The longest time series (since 1966) of satellite observations exists for snow cover [10]. Figure 2 presents the temporal coverage for essential climate variables (ECVs) collected in the ESA Climate Change Initiative (CCI). The ESA CCI efforts are central for synthesis; ECVs are considered from the perspective of physical climatology of the Arctic amplification. ECVs provide reliable, traceable, observation-based evidence for a range of climate applications, including monitoring and attributing of climate change phenomena [11]. The ECV concept has been adopted by space agencies operating Earth observation satellites. At

present, ESA CCI comprises 23 parallel ECV projects, a dedicated climate-modeling project for the assessment of products, a portal (https://climate.esa.int/en/odp/#/dashboard (accessed on 8 January 2023)) providing the products, a toolbox to facilitate the combining and analysis of the products, and a visualization tool supporting outreach. Although climatic-quality ECV records require data fusion from many space-born sensors and missions, the ESA satellite missions were of critical importance for many ECVs. A timeline of all ESA satellite missions can be found in the online Earth Observation Handbook, in the CEOS database at http://database.eohandbook.com/measurements/overview.aspx (accessed on 26 November 2022). Starkweather et al. [12] provided a wider perspective on a value chain for the Arctic Observing Network that combines both satellite and ground-based (in situ) monitoring systems. The value chain traces the impact of satellite observations (in combination with other data sets and models) down to vital signs of climate change and societal impact.

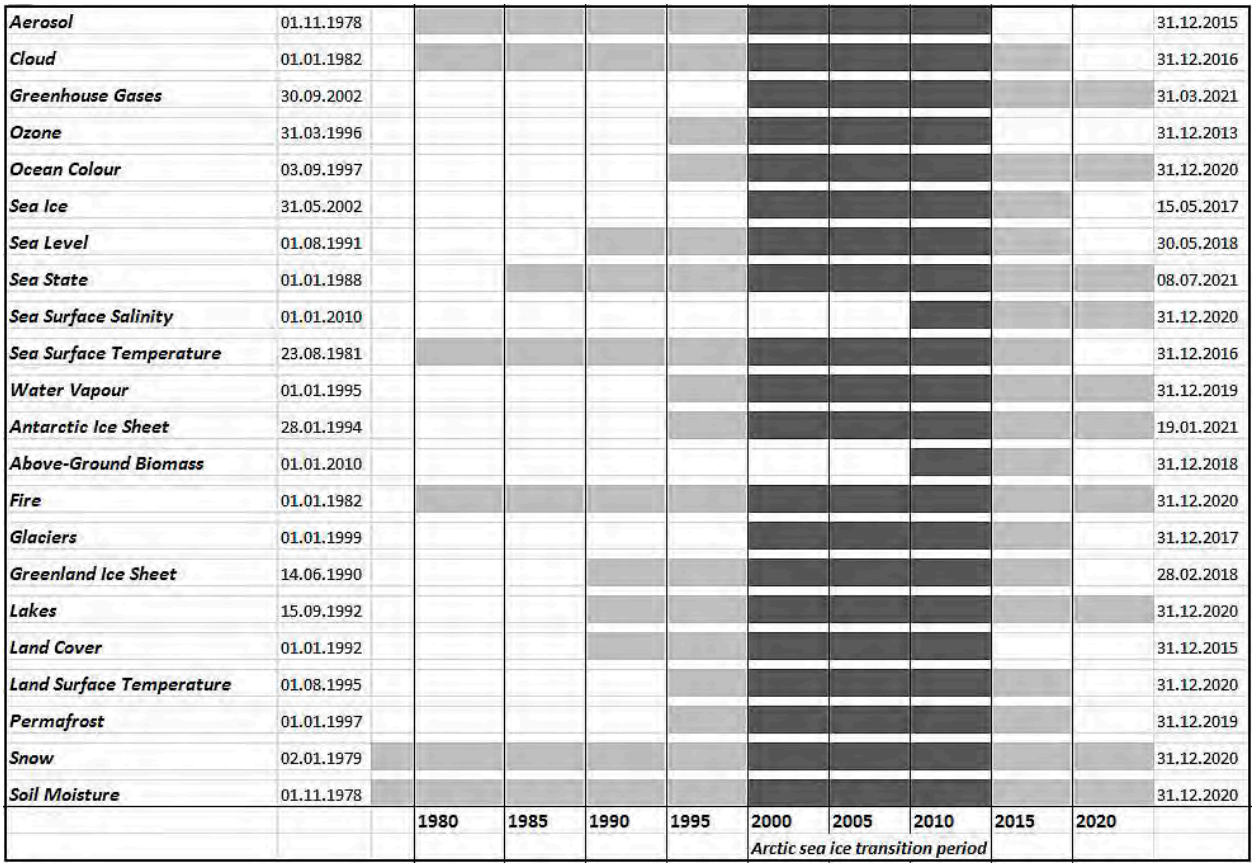

Figure 2. Temporal coverage of climate data records for ECVs in the ESA CCI. Dates and filled bars indicate availability of the data sets in the ESA CCI portal (https://climate.esa.int/ (accessed on 8 January 2023)) by the end of 2022. Dark shading indicates the period of apparent amplification emergence.

Polar-orbiting satellites have captured details of the major environmental transitions in the Arctic with a variety of space-born instruments. This has helped in the development of robust long-term ECV records, trend analysis, and the study of the amplification [13].

This study is a synthesis of the satellite contribution to the assessment of the Arctic amplification, which we will refer to as just the amplification. The amplification is defined as an accelerated and amplified regional climate change; it is primarily atmospheric and surface warming, but it is also related to a diverse set of influential climate phenomena [14,15]. We schematically illustrate the most important phenomena and their links to satellite observations in Figure 3. The paper is organized as follows. Section 2 presents the

relevant literature, data, and methods. Section 3 is focused on the synthesis and discussion of the satellite contributions into the understanding of the amplification. Section 4 outlines the broader impact of the amplification identified through satellite observations. Section 5 highlights the conclusions and recommendations of this study. It should be emphasized that we do not follow an unfortunate but popular trend of composing a meta-analysis solely on the basis of automatically relevant literature. On the contrary, this synthesis is guided by a new amplification paradigm that has crystallized in modeling studies (e.g., Previdi et al., 2021; Semenov, 2021). The focus on satellite observations makes our work complementary to the recent comprehensive reviews by Taylor et al. [9] and Wendisch et al. [16], which synthesize modeling results. At the same time, this synthesis is distinct from the recent comprehensive reviews of satellite observations by Duncan et al. [5] and earlier reviews by Comiso and Hall [13] and Wang et al. [17]. We consider satellite observations from the perspective of physical climatology.

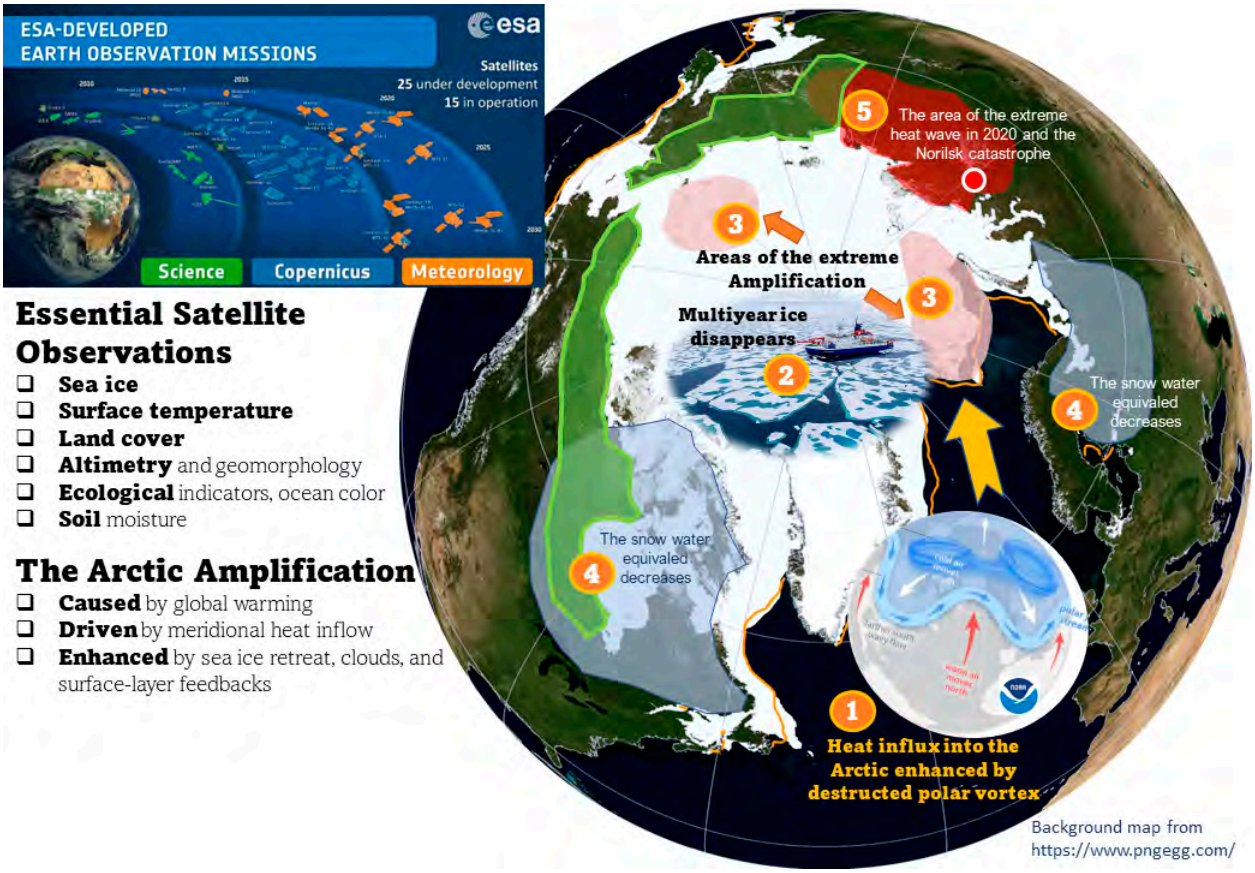

Figure 3. A schematic illustration of the ESA satellite fleet contributing to monitoring of the dynamic processes, physical feedback, and environmental impact related to the emergence of the apparent amplification.

2. Definition, Literature, Data, and Methods

Definition. Anthropogenic climate change is global. However, surface warming is uneven in space and time; the Arctic has experienced the regional amplification of this warming over the last three to five decades [18]. Moreover, the amplification in some limited Arctic areas, such as the northern Barents-Kara sea region, is exceptional and has no parallels elsewhere [19]. Although the amplification is an intuitive concept, it is not so unambiguous. Here, we rely on the amplification metrics found in recent studies [20–22]. The amplification can be defined through the difference, Δ_{AA}, and the ratio, R_{AA}, of air

temperature changes in the Arctic, ΔT_A, and over the northern hemisphere (0–90°N) or the northern extra-tropics (20–60°N), ΔT_H :

$$\Delta_{AA} = \Delta T_A - \Delta T_H, \quad (1)$$

$$R_{AA} = \frac{\Delta T_A}{\Delta T_H}. \quad (2)$$

The Arctic is typically defined as the region to the north of 60°N, 65°N, or 70°N (in this case, covering mostly the Arctic Ocean). Different definitions result in different values—the more limited the area of the Arctic is considered, the larger amplification indices are found [19,22]—but trends and variability of the phenomena are not significantly different. This similarity clearly indicates that the amplification patterns are localized in the high Arctic latitudes.

The amplification metrics are imperfect. A short-term trend of Δ_{AA}, i.e., $\frac{d\Delta_{AA}}{dt}$, would be a more justified measure of the regional temperature trends' divergence. This is, however, highly ambiguous against the backdrop of high Arctic climate variability, and it is hence used infrequently. A strong amplification ($R_{AA} \gg 1$) will be found during periods of transitional climate change, whereas approaching an equilibrium climate state will lead to $R_{AA} \approx 1$. Such behavior can be misleading. The averaging and aggregation of anomalies over longer periods (e.g., over 30 years) have been proposed to improve the statistical stability of the metrics [18,21,23]. As we will show, a longer averaging and aggregation impedes the identification of important physical transitions in the Arctic climate system that have a decisive impact on the amplification.

Literature. We are primarily interested in reviews and the synthesis of publications dealing with consistent long-term (climatic) satellite observations of temperature and closely related ECVs. We recommend the comprehensive review of Duncan et al. [5] to the reader interested in specific contributions from concrete instruments and satellite platforms. A detailed review of satellite temperature observations can be found in Comiso and Hall [13]. More recently, sea and ice surface temperatures from satellites (review and data sets) were published in [24]. A review of sea ice characteristics was published by Wang et al. [17]; a review of snow cover trends is found in Bormann et al. [25]; a review of phytoplankton dynamics is available in Ardyna and Arrigo [26]. Products and methods for monitoring changes in more complicated environmental indicators such as terrestrial vegetation cover [7] and permafrost [27] have also received considerable attention [28,29]. Several reviews have also attempted a holistic assessment of the Arctic environmental changes on the basis of satellite data products [30]. Data products covering two, three, and four decades of climate change combine data sets from successive satellite platforms/missions bearing similar instruments [28]. Table 1 lists some key recent reviews with a focus on satellite observations of Arctic climate change.

Table 1. List of key recent reviews focusing on satellite observations of Arctic climate change.

Reference	Key Notes and Brief Conclusions
	General reviews
[4]	Satellite observations are indispensable for climate monitoring.
[5]	Satellites plays a vital role in Arctic climate change assessment.
[31]	Satellites reveal climate change footprints in the Arctic energy budget.
[32]	Satellites reveal changes in the radiation balance.
[13,33]	Satellites disclose the amplified Arctic warming.
[9]	Satellites reveal interconnections in the amplification drivers, feedback, and geographical patterns.
[19,34,35]	Exceptional warming over Barents Sea is related to sea ice retreat and declining sea ice import.

Table 1. *Cont.*

	Specific reviews
	Dynamical factors of the amplification
[36]	Increase in ocean warm water inflow
[37]	Decrease in meridional heat transport since 2000
[38]	Decrease in middle atmosphere temperature inversion strength
	Local factors and feedback of the amplification
[39,40]	Increase in land surface temperatures with minimum trends in summer and maximum trends in autumn; atmospheric temperature inversions correlated with sea ice anomalies
[6,24]	Rise in Arctic sea surface temperatures
[19,41]	Surface air and sea surface temperatures correlated with sea ice cover
[17,42–44]	Satellites show disappearance of multiyear ice and reduction in ice thickness and volume
[45]	Increase in area of melting ponds on ice
[25,46]	General decrease in extent of snow cover and water equivalent, but geographical variations are significant
[47]	Arctic cloud cover undergoes multidirectional changes
[48]	Regional changes in TOA radiation fluxes are insignificant—implies weak atmosphere–surface coupling
[49–51]	Decrease in Arctic ice surface albedo
[52]	Increase in sea ice radiative forcing
[53]	Increase in cloud radiative forcing
	Environmental changes
[30]	Satellite observations reveal rapid changes in the Arctic environment; list of relevant satellite data sets provided
[7,28]	Satellite observations reveal complex changes in the Arctic environment
[27,29,54–56]	Satellite observations could be used to monitor permafrost thaw; permafrost becoming unstable in different regions
[57]	Growing season duration and increase in productivity of vegetation
[26]	Satellites reveal increasing marine biological production in the Arctic
[58–60]	Loss in Greenland ice sheet mass and height
	Impact on humans
[61,62]	Satellites reveal expanding human infrastructure and growing impact in the Arctic

Three prominent examples highlight the significance of satellite observations for amplification studies. One example is given by the Greenland ice sheet studies. An unprecedented loss of Greenland ice (100 to 255 Gt of ice per year) has been inferred from a synthetic data product for ice mass balance (elevation) monitoring [63]. The first data were collected in the late 1970s by the National Aeronautics and Space Administration (NASA)'s Geodetic and Earth Orbiting Satellite-3 (GEOS-3), NASA's Seasat, and the US Navy's Geosat oceanographic radar altimeters. These data were combined with observations from a fleet of missions that provided for different products, e.g., GRACE and GRACE-FO [60]. Another example is given by the University of Alabama in Huntsville (UAH)'s Microwave Sounding Unit (MSU) and Advanced Microwave Sounding Unit (AMSU) product that records the temperature of upper atmosphere data [64,65]. It combines data from NOAA satellite series and data from the TIROS-N (1978–1979), Aqua (2002–2009), and MetOP A (2007–2016) and B (2012–2016) satellites, which do not bear identical instrumentation. Yet another example refers to the Global Inventory Modeling and Mapping Studies Normalized

Difference Vegetation Index data set (GIMMS3g), which is widely used to assess long-term vegetation changes [66].

The ESA Copernicus Sentinel missions have opened a new era of polar satellite observations. The missions consist of a family of satellites designed for the operational monitoring of the Earth system with continuity up to 2030 and beyond. On-board sensors include both radar and multi-spectral imagers for land, ocean, sea ice, snow cover, ice sheets, glaciers, and atmospheric monitoring. Sentinel-1 is a polar-orbiting, all-weather, day-and-night radar imaging mission for land and ocean services. Sentinel-1A was launched on 3 April 2014, and Sentinel-1B on 25 April 2016. Sentinel-2 is a polar-orbiting, multi-spectral high-resolution imaging mission for land monitoring. Sentinel-2A was launched on 23 June 2015, and Sentinel-2B followed on 7 March 2017. Sentinel-3 is a polar-orbiting multi-instrument mission to measure sea surface topography, sea and land surface temperature, ocean color, and land color with high-end accuracy and reliability. Sentinel-3A was launched on 16 February 2016, and Sentinel-3B on 25 April 2018. Sentinel-5 is a polar-orbiting instrument aboard a MetOp Second Generation satellite with a focus on air quality and climate. Sentinel-5P has been orbiting since 13 October 2017. Sentinel-6 is a polar-orbiting mission carrying a radar altimeter to measure global sea surface heights, primarily for operational oceanography and for climate studies. The European earth's observation teams have identified several gaps and needs in the satellite monitoring of the polar regions. The most important characteristics are related to latency time and a lower revisit time [67]. Reductions in the revisit time to 3 h would enable polar navigation, enhanced weather forecasts, and the remediation of technogenic hazards.

Geostationary satellites continuously observe the same area as it moves through their field of view. Their contribution to amplification monitoring is, however, limited by large distortions in the field of view in high latitudes. Geostationary satellites are more for monitoring more distant impacts of the amplification in the sub-Arctic or mid-latitude continental areas, where they track snow cover changes.

Data. To date, several important climatic-quality data sets have been developed on the basis of remote-sensing data products. Since the accuracy of the data sets critically depends on high-quality satellite data, ESA CCI utilizes the Global Space-based Inter-Calibration System for bias intercalibration of level-1 data; this system calibrates geolocated measurements of radiances and other characteristics prior to the retrieval of geophysical variables [68]. The ESA CCI ESVs and the European Union's Earth Observation Program Copernicus Climate Change Service (C3S) have benefited from the systematic analysis of climatic-quality satellite data set requirements developed in several subsequent projects, e.g., in the Quality Assurance for Essential Climate Variables prototyping system [69]. An example of this production and validation system that was implemented for the derivation of long-term ice albedo products from MODIS data can be found in [70]. The main requirement for such climatic-quality data sets is that they should be free of multiyear fragmentation, be continuous in time, and be consistent in quality. A triple-collocation method has demonstrated promising results in several ESA CCI projects [71]. Geographically, the data sets should cover the whole Arctic or at least its important regions, e.g., the Barents Sea [72]. Our analysis of sea ice transitions suggests that the temporal coverage should include the critical years between 2000 and 2015.

At present, there is a large diversity in the long-term climatic-quality satellite data products available at different stages of their development [3]. Cross-product validation and calibration are still important issues for the remote-sensing community. The most actively used climatic-quality products in amplification studies are listed in Table 2.

Table 2. Actively used climatic-quality remote-sensing products complementing the essential climate variables from ESA CCI.

Product Name (Abbreviation)	Accessibility	Reference
	Multiple variable products	
MODIS data products	Moderate Resolution Imaging spectroradiometer https://modis.gsfc.nasa.gov/data/dataprod/ (accessed on 8 January 2023)	[30]
	Temperature	
UAH MSU/AMSU	University of Alabama-Huntsville (UAH) MSU/AMSU Mean Layer Atmospheric Temperatures, version 6 https://data.globalchange.gov/dataset/university-alabama-huntsville-uah-msu-amsu-mean-layer-atmospheric-temperatures-version-6 (accessed on 8 January 2023)	[65,73]
SST	Arctic Ocean—Sea and Ice Surface Temperature REPROCESSED https://data.marine.copernicus.eu/product/SEAICE_ARC_PHY_CLIMATE_L4_MY_011_016/description (accessed on 8 January 2023)	[24]
	Cloud and radiation budget characteristics	
CLARA-A2	Cloud, Albedo, and Surface Radiation data set from AVHRR data, second edition https://wui.cmsaf.eu/safira/action/viewDoiDetails?acronym=CLARA_AVHRR_V002 (accessed on 8 January 2023)	[74]
CERES EBAF	Clouds and the Earth's Radiant Energy System (CERES) Energy Balanced and Filled (EBAF) Top-of-Atmosphere (TOA) edition-4.1 data product https://asdc.larc.nasa.gov/project/CERES/CERES_EBAF-TOA_Edition4.1 (accessed on 8 January 2023)	[75]
PATMOS-x	NOAA's Pathfinder Atmospheres, Extended program (PATMOS-x), v6.0 https://doi.org/10.7289/V5X9287S (accessed on 8 January 2023)	[76]
APP-x	Extended Advanced Very High-Resolution Radiometer (AVHRR) Polar Pathfinder (APP-x) https://www.ncei.noaa.gov/data/avhrr-polar-pathfinder-extended/access/ (accessed on 8 January 2023)	[77,78]
	Sea ice and snow cover characteristics	
NOAA CDR – Rutgers	NOAA Snow Cover Extent Climate Data Record (CDR) Rutgers University Global Snow data set https://climate.rutgers.edu/snowcover/ (accessed on 8 January 2023)	[79]
EUMETSAT OSI SAF v2.0	https://osi-saf.eumetsat.int/about/access-data	[80]
Goddard Bootstrap (SB2) and NASA Team (NT1) data sets	National Snow and Ice Data Center (NSIDC): the NASA Team (http://nsidc.org/data/nsidc-0051 (accessed on 8 January 2023)) and Bootstrap SB2 (http://nsidc.org/data/nsidc-0079 (accessed on 8 January 2023))	[81]
PIOMAS	Polar Science Center sea ice data http://psc.apl.uw.edu/research/projects/arctic-sea-ice-volume-anomaly/data/ (accessed on 8 January 2023)	[82]

Table 2. *Cont.*

Product Name (Abbreviation)	Accessibility	Reference
	Land cover and vegetation productivity	
GIMMS3g	Global Inventory Modeling and Mapping Studies https://climatedataguide.ucar.edu/climate-data/ndvi-normalized-difference-vegetation-index-3rd-generation-nasagfsc-gimms (accessed on 8 January 2023)	[66,83,84]
MEaSUREs	MEaSUREs Global Record of Daily Landscape Freeze/Thaw Status, version 3 (NSIDC-0477) https://nsidc.org/data/nsidc-0477/versions/3 (accessed on 8 January 2023)	[85]

Methods. This synthesis study utilizes only results that have already been published in literature. We focus on the interannual climatic variability and climate change trends captured in long-term satellite data sets. Our methodological goal is narrowed towards understanding whether satellite observations have captured important transitions in the Arctic climate system—those transitions that have resulted in the emergence of the exceptional amplification in the 21st century [19,34]. Although the amplification was discovered several decades ago [86,87], also through satellite observations [13,88], its emergence in surface records and other environmental indicators remained debated [89–91]. Specifically, the extension of products from the Satellite Application Facility on Climate Monitoring (CM-SAF; www.cmsaf.eu) to the Arctic has increased the quality and diversity of amplification studies [80,92]. CM-SAF is a component of the EUMETSAT activities that provides remote-sensing products derived from meteorological satellites. CM-SAF remote-sensing products provide important data on key variables related to the Arctic amplification, such as surface temperatures, the extent of sea ice, and cloud cover. CM-SAF computes daily and monthly means of various cloud parameters with a horizontal resolution of 15 km. The computations are based on cloud products derived from the AVHRR instrument onboard polar-orbiting satellites and from the SEVIRI (Spinning Enhanced Visible and InfraRed Imager) instrument on the geostationary satellites.

3. The Synthesis

The current physical understanding of the amplification. Energy-balance models of the earth's climate system clearly relate the emergence of the apparent amplification to the changing heat capacity of the system, i.e., to the capacity to retain heat in the lower atmosphere and in the upper ocean/soil levels [93]. These models have revealed that the amplification emerges as the atmospheric fast mode in the meridional response to anthropogenic climate change. Enhanced heat transport towards the Arctic is a precursor driving sea ice melt and the eventual transition to a seasonally open-water Arctic Ocean. This indicates that the amplification can be seen as a response to the redistribution of heat sources and sinks on the planet [94]. In this way, accepting Manabe and Strickler's arguments [95], the amplification should not distort much of the top-of-the-atmosphere (TOA) radiation balance. On the contrary, a prominent effect on the surface energy balance is expected, as the surface is largely decoupled from the higher atmospheric layers in the stable Arctic atmosphere. Satellite observations clearly identify such a fingerprint of the dynamic Amplification drivers. Finally, both climate modeling and results of reanalysis studies found that the apparent amplification has accelerated when the local surface feedback was unlocked after the transition to seasonal sea ice cover [14,15,96]. This is when the surface recouples to the lower atmosphere. The fact that the amplification emerges in response to so many different drivers suggests that it is a robust global climate response independent of applied forcing and feedback details [9,14].

At present, the research community has created a physically consistent conceptual picture of the amplification [9]. The amplification is initiated by the atmospheric dynamics, but it is shaped and enhanced by interacting local physical processes and feedback. Climate simulations suggest the following chain of causality. Meridional atmospheric transport increases moist-static energy in the Arctic troposphere, which drives sea ice variability [97]. Initially, the atmospheric warming has little observable effect on the extent of sea ice and on surface temperatures, as multiyear ice has survived melting seasons [98]. By the year 2000, however, multiyear ice largely disappeared from the central Arctic and Eurasian shelf [42,44]. This outrunning thinning and reduction in multiyear ice was explained through a growth-thickness negative feedback mechanism [99]. Variability in the seasonal sea ice cover has increased [100]. This has unlocked mechanisms of summer heat accumulation in newly open surface waters with subsequent effects on autumn and winter temperatures [101]. The apparent amplification has been unlocked. Several specific physical feedback mechanisms trap further warming near the surface, enhancing its environmental impact. The most pronounced changes are then observed in the areas of the most recent sea ice and snow cover retreat, such as the marginal sea ice zone [19] and the forest–tundra interface [7]. A schematic illustration in Figure 3 provides a general overview of the dynamics and physics of the amplification under surveillance of the ESA satellite fleet.

Emergence and location of the apparent amplification. The current understanding maintains that the amplification developed for a long time in the free (lower) atmosphere, before it finally emerged onto surface climate records. Figure 4 displays this development in the UAH MSU TLT (lower atmosphere) data set. Time series of the Arctic and Hemispheric temperature anomalies, Δ_{AA}, began diverging in the 21st century, with the largest difference noted around 2005 and then again after 2015. The reanalysis data reveal that the contemporary amplification took off in 1990s [22]. Satellites (AVHRR data set) reveal the surface warming trends at latitudes above 64°N of $\sim 0.69 \pm 0.06$ °C dec^{-1} compared to ~ 0.17 °C/dec^{-1} globally from 1990–2010 [13]. The largest trends are found in the areas of active seasonal sea ice loss. The sea ice surface temperature and the sea surface temperature in the Arctic show smaller trends of 0.47 ± 0.06 °C dec^{-1} and 0.09 ± 0.01 °C dec^{-1}, correspondingly.

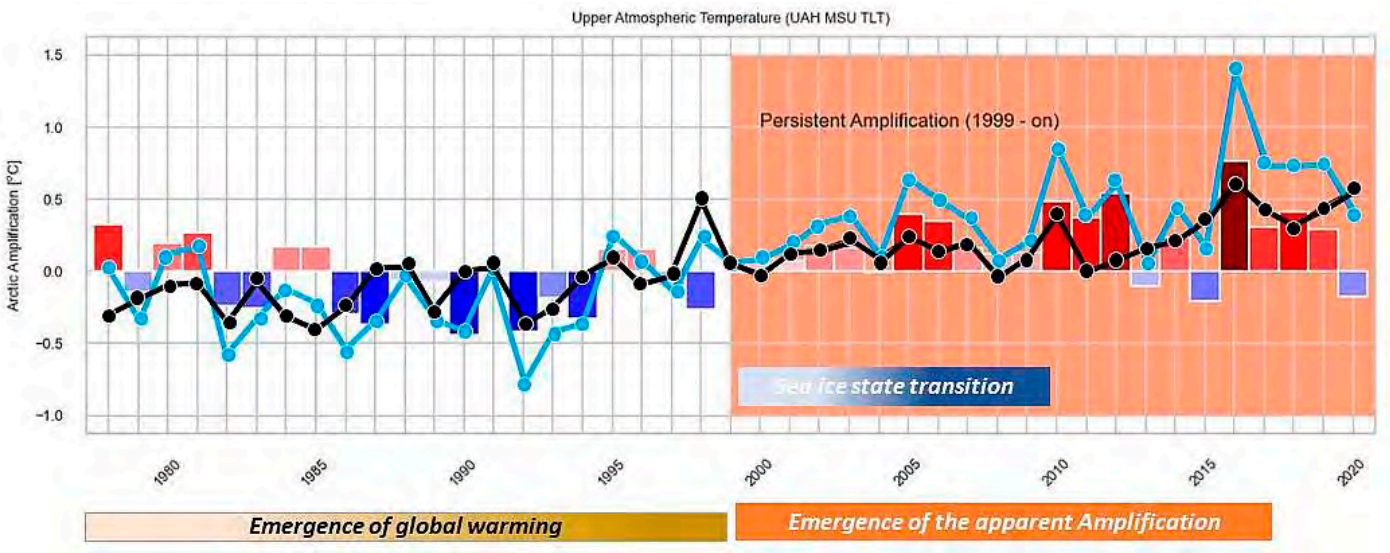

Figure 4. The amplification in the satellite observations (the lower troposphere UAH MSU TLT data set) with sketched periods of the apparent amplification emergence. The blue line shows the Arctic temperature anomalies; the black line shows the Northern Hemisphere temperature anomalies; the colored bars show the amplification (the difference Δ_{AA} between the lines).

Surface state transition caused by sea ice retreat. Monitoring of sea ice provides a spectacular example of satellites' contribution to the radical rethinking of Arctic climate

change [17,42]. A wide variety of satellite instruments provide data for sea ice monitoring [5,102]. Beginning with monitoring of the extent of sea ice [81,103], remote-sensing data products have gradually begun to provide for sea ice thickness since 2005 [44], as well as other derivative characteristics of the sea ice cover [42,102], including compactness and lead fraction [104,105]. Satellites with low spatial and high temporal resolution provide synoptic information about the Arctic sea ice cover, age, motion, and timing of retreat and advance.

Towards the end of the 20th century, global warming has been progressing without visible differences in its pace at low and high latitudes. The warming pace began to diverge only when sea ice had retreated over large areas in the Barents Sea and the Eastern Arctic. Satellites were able to capture a critical transition in both the extent and thickness of sea ice [106]. Between 2005 and 2007, the mean residual (October–November) sea ice thickness rapidly dropped by 1 m (about 50%), manifesting a transition from multiyear to seasonal ice cover [13], and the age-based sea ice volume decreased by around -411 km^3 yr^{-1} [43]. Changes in sea ice thickness contribute more this volume change than changes in sea ice area. The 15-year satellite record depicts an ice volume loss of 4305 km^3 and 7695 km^3 in winter (February–March) and autumn (October–November), respectively. These numbers suggest that 30% to 40% of the total sea ice volume and >70% of the multiyear ice volume have been lost already. The major transition from about 4×10^6 km^2 to less than 2×10^6 km^2 of multiyear sea ice occurred between 2005 and 2010. Figure 5 shows the changes in the sea ice extent (SIE) derived from the OSI SAF Sea Ice Index product. This transition is detected by combining data products from NASA Ice, Cloud, and land Elevation Satellite (NASA ICESat) over 2003–2008 and the European Space Agency Earth Explorer Cryosphere Satellite 2 (ESA CryoSAT-2) from 2010 onward. The gap from 2008–2010 was unfortunate, however, as it occurred in the middle of the main multiyear sea ice decline period [44]. Data from the QuikSCAT (1999–2009) and MetOP ASCAT (2009–2018) scatterometers indicate more than a 50% decline in multiyear sea ice coverage [44], with a rapid decline in the multiyear ice area and volume that happened over just a few years (see Figure 5). The most used climatic quality sea ice data sets agree on ice patterns and the overall extent and trends [81]. A disagreement remains when sea ice characteristics, especially ice concentration distributions, in the marginal ice zone and adjacent regions are considered.

The role of sea ice transition is further emphasized in an analysis of the seasonality of the trends. The amplification reveals a strong seasonal cycle, see Figure 6. The most significant changes develop when the surface freezes or melts, notably during September, October, and November (SON) due to the persistent shift in the melting/freezing onset. The mean SON trends in 12 reanalysis data sets are greater than +5 K from 1979–2017 [107]. The mean melting season (June, July, August) trends are less than +1 K from 1979–2017.

As sea ice retreats, the sea surface temperature (SST) in the Arctic begins increasing as well [6,108]. The mean August SST is the most appropriate representation of Arctic Ocean warming. The highest mean August SST (6–9 °C) is observed in the southern Chukchi and Barents Seas.

The warming of the Arctic SST is, however, in its initial stage. Yet the ocean impact is growing. Satellite-based analysis of sea ice loss suggests the rising influence of ocean fluxes [109]. One modeling study [110] attributed about 1 °C near-surface warming in winter to the thinning of sea ice, which corresponds to about 37% of the amplification in the marginal sea ice zone. Another study [111] argued that increasing ocean heat inflow leads to thermodynamic recoupling between the ocean and the atmosphere, and this might account for about 80% of the amplification by 2100.

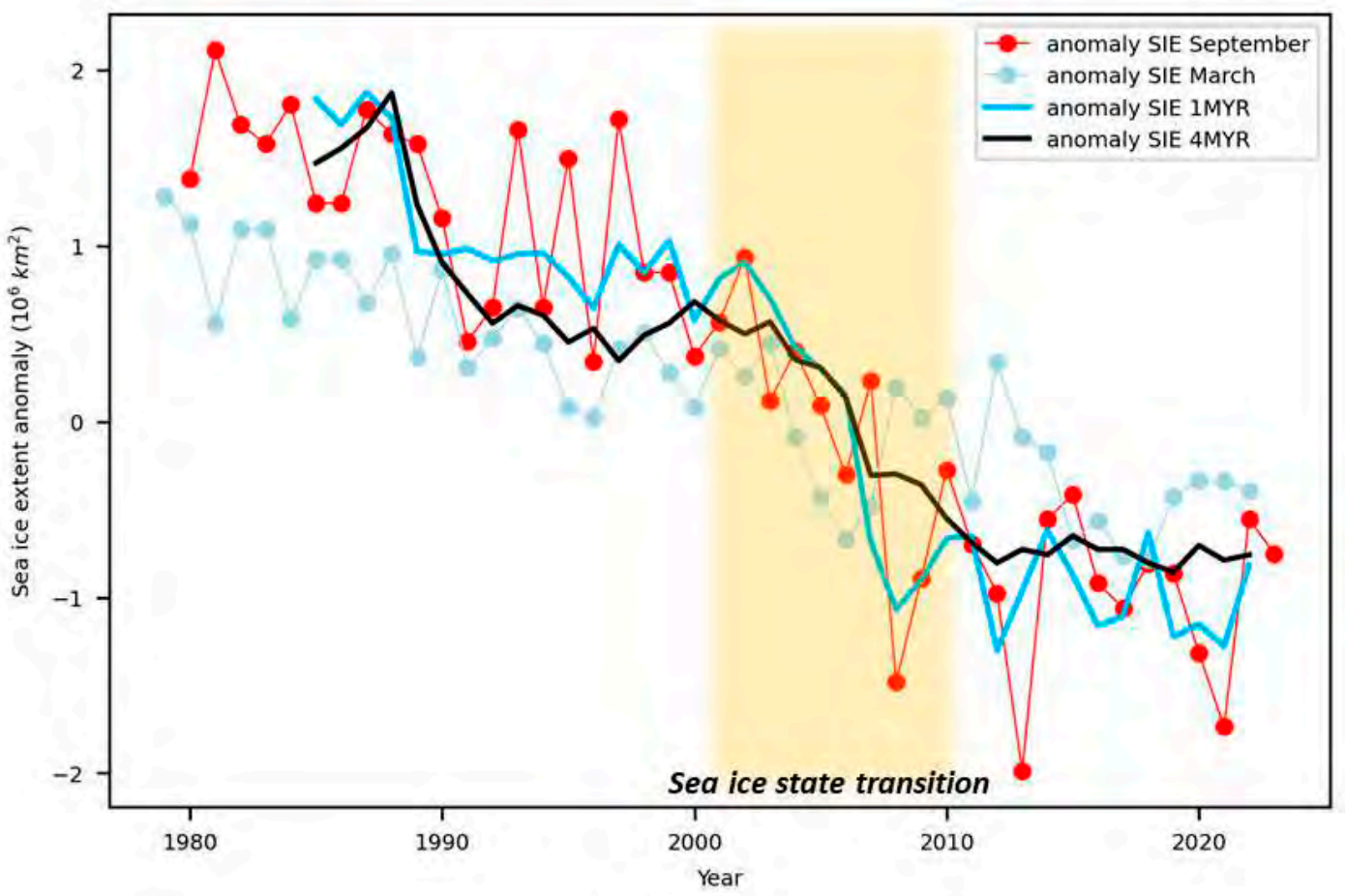

Figure 5. Changes in the Arctic sea ice extent (SIE). The total September and March SIE anomalies are taken from the OSI SAF Sea Ice Index v2.1 (available at https://osisaf-hl.met.no/v2p1-sea-ice-index, accessed on 5 January 2023) [80]; the reference period is 1989–2021. All data are based on passive microwave sensors (the SMMR, SSM/I, and SSMIS); the multiyear (older than one year, 1MYR) and old (older than 4 years, 4MYR) SIE anomalies are taken from NSIDC [112], see more details in [43]. SIE is defined as the area covered with more than 15% of sea ice.

Surface-state transitions caused by snow cover retreat. The longest satellite observations (since 1966) exist for snow cover [10,25]. The NOAA Climate Data Record (CDR), also known as the Rutgers snow cover data set, has been digitized from snow cover maps at a spatial resolution of 190.6 km at 60 N [79]. Since 2004, both the spatial resolution and quality of this record have been greatly enhanced by MODIS and VIIRS data streams (0.5 to 1 km resolution, respectively). The European Space Agency (ESA)'s GlobSnow product has an intermediate (25 km) resolution, which is generally adequate for homogeneous surfaces in the Arctic. The snow cover is in retreat in the Arctic, but trends remain controversial and dependent on the selected period and season. Estilow et al. [79] showed that the extent of hemispheric seasonal average snow cover increases in fall and winter but decreases in spring and summer. The snow cover duration is decreasing by 5–6 days per decade over the Northern Hemisphere. The snow water equivalent (SWE) determines the amount of heat needed to melt snow, and thus, it is important for the emergence of the amplification. Results for the SWE trends from the 36-year passive microwave record (1980–2015) suggest that the hemispheric SWE is decreasing. However, at regional scales, the trends are less certain and are highly variable between products. New satellite missions with the ability to retrieve snow water equivalents are needed to fill the gap in quantitative information. The Copernicus Global Land Cover service provides SWE for the northern hemisphere at a

5 km resolution (https://land.copernicus.eu/global/products/swe (accessed on 8 January 2023)).

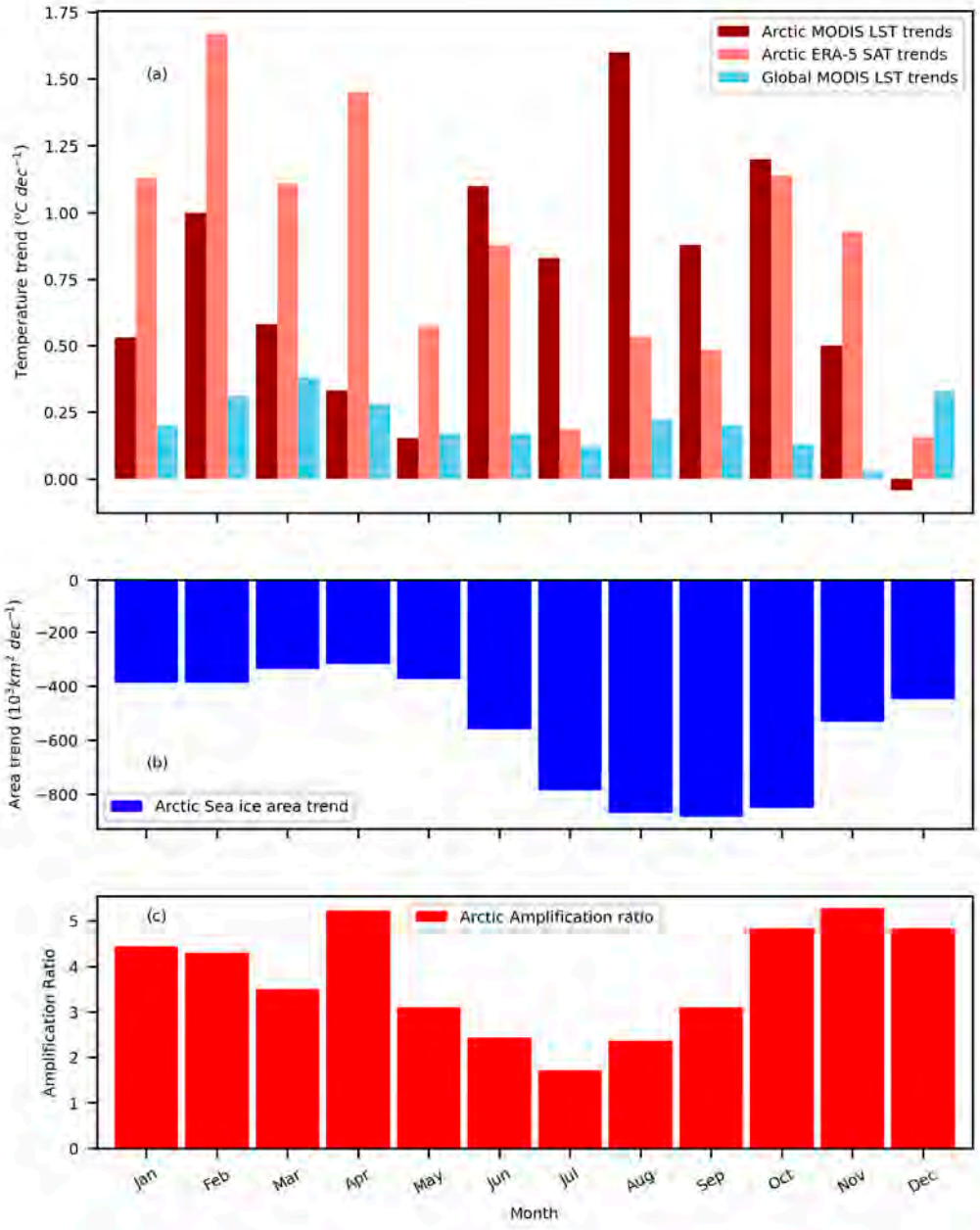

Figure 6. Monthly variations in Arctic climate trends. (**a**) Land temperature (LST) trends from MODIS LST data set and the surface air temperature trend from ERA-5 reanalysis from 2001–2020 [40]. (**b**) Sea ice area trends from 1979–2019 [113]. (**c**) Arctic amplification ratio from 1979–2021 averaged over three observational data sets (Berkeley Earth, Gistemp, HadCRUT5) and the ERA5 reanalysis [34].

Surface–atmospheric coupling effects. The Arctic is one of a few regions (other regions are collocated with ocean upwelling zones) where weak surface–atmospheric coupling controls the climate sensitivity [95].

Satellite observations can be used to estimate the characteristics of the vertical turbulent mixing, surface layer coupling, and effective heat capacity of the climate system [114]. However, such data products are still in their infancy. A promising algorithm looks at aerosol backscatter [115]. It utilizes a threshold at which the backscatter signal exceeds the clear atmosphere signal by a small arbitrary value or vertical gradients in a lidar backscatter profile. More sophisticated detection methods have been suggested as well [116]. The

CALIOP (Cloud-Aerosol Lidar with Orthogonal Polarization) instrument onboard the CALIPSO mission was also used [117,118]. Another potentially useful data set is provided by GPS Radio Occultations (GPS-RO) [119], which are more numerous and less sensitive to clouds. The GPS-RO algorithms typically define the boundary layer height as a level of the most negative moisture gradient [120]. During the winter months (December–February), when the total precipitable water in the troposphere is at a minimum, a fairly straightforward algorithm based on temperature inversions can be used [121]. The shallow Arctic boundary layer is a challenge for the GPS-RO retrieval. Ding et al. [122] showed that the 10-year retrieval has a low vertical resolution and accuracy, which could be critical for the detection of the boundary layer height in high latitudes. Temperature profile methods could be also used for the retrieval of the boundary layer height. In the Arctic, however, temperature inversions are of radiative origin and could be unrelated to vertical mixing. In addition, there is still no synthetic data product for lower atmosphere temperature inversions. The existing data sets, e.g., a 17-year time series (1980–1996) of clear-sky temperature inversions derived from High-Resolution Infrared Radiation Sounder (HIRS) data [38], do not cover the emergence period.

Turbulent fluxes are also important for the assessment of the surface energy budget, air–surface coupling and moisture, greenhouse gases, and aerosol exchange. The remote sensing of turbulent fluxes is a rapidly developing application of the earth's observations. Significant progress has been achieved in development of turbulent flux products over the global open ocean [71]. A corresponding development in the Arctic domain, however, has met with considerable difficulties. Turbulent fluxes here are influenced by sea ice, frequent overcast cloudiness, high wind speeds, low winter temperatures, and a small temperature contrast between the surface and cloud layers. Surface heterogeneity and the presence of sea ice leads, in particular, might greatly enhance the fluxes [123]. Qu et al. [124] derived turbulent fluxes from leads at different scales using a combination of surface temperatures and lead distribution from remote-sensing images (Landsat-8 TIRS and MODIS) and meteorological parameters from a reanalysis data set. A fetch-limited model applied to thermal images and wind data estimates the fluxes to be more than 40% larger than those of the homogeneous sea ice surface.

Arctic cloudiness effects. Arctic cloudiness is undoubtedly the major wildcard in amplification assessment and understanding [47]. The cloudiness effect is twofold. Clouds distract optical satellite surface observations and data retrievals, and clouds play an active and still poorly understood role in forcing the amplification on all scales. Strong connections have been found between cloud cover changes and dynamical patterns of the heat inflow into the Arctic [125]. Figure 7 compares interannual variations in the total cloud cover in the Arctic and its effect (forcing) on the longwave radiation balance at the surface, as obtained from two satellite data products. The recent decade has witnessed both enhanced cloud cover and its surface heat forcing.

Satellite observations are essential in studies of Arctic cloudiness and its impact [32,126,127]. Today, almost 40 years (1982 on) of satellite cloud observations are available [47]. Currently, four long-term climate data records (data sets) exist that are exclusively based on AVHRR data. One is a CM SAF Cloud, Albedo, and Surface Radiation data set from AVHRR data, second edition (CLARA-A2). It applies a hierarchical decision tree thresholding method to retrieve cloud properties [74]. The other data set—the NOAA's Pathfinder Atmospheres, Extended program (PATMOS-x)—is based on a naïve Bayesian method [76]. The third is the Extended Advanced Very High-Resolution Radiometer (AVHRR) Polar Pathfinder (APP-x) [77]. The fourth is the ESA Cloud CCI (version 3) 1982–2017, which uses neural network and optimal estimation techniques to provide cloud property retrievals [128,129].

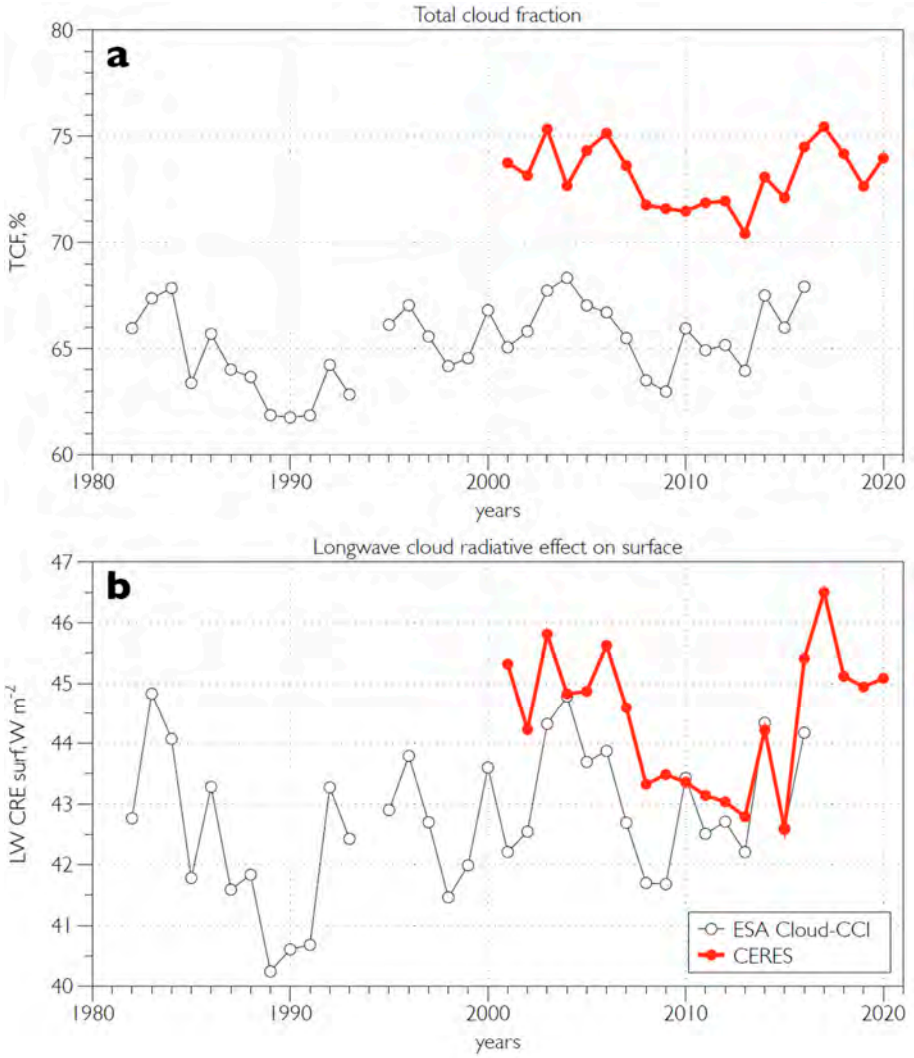

Figure 7. Variations in the total cloud cover (**a**) and the longwave cloud radiative effect on the surface (**b**) obtained from ESA Cloud-CCI and CERES data products.

Satellite cloud data products do not fully agree with each other. A study of 16 cloud climatologies showed that the annual mean total cloud fraction in the region north of 60°N is 0.70 ± 0.03 (over the ocean 0.74 ± 0.04; over land 0.67 ± 0.03) [130]. The average disagreement between MODIS and CALIOP over the whole Arctic reaches 13.1% during daytime and 26.7% during nighttime [131]. This MODIS–CALIOP disagreement has high seasonal dependence; it is the lowest in summer (showing a 10.7% difference in cloud fractions) and the largest in winter (28.0%). MODIS typically under-detects low-level (top height < 2 km) and high-level clouds (top height > 6 km). Very low and thin clouds (<0.3 km) over sea ice that are detected by MODIS are sometimes not observed or misclassified by CALIOP. Aside from this, MODIS cloud products perform better over open water than over ice [132]. The main reason for the discrepancies among observations is the difference in cloud detection algorithms, especially when clouds are detected over the ice/snow surface (during the whole year) or over regions with a presence of strong low-tropospheric temperature inversions (mostly in winter).

Arctic cloudiness is particularly challenging for climate models, causing major uncertainties and discrepancies in regional climate change projections. Most models project increasing low-level cloudiness in the region. Satellite observations confirm this tendency [114]. The Arctic was found to be more cloudy in spring (the decadal trend from 1984–2004 is 2.3% dec^{-1}) and summer (0.5% dec^{-1}) but less cloudy in winter (−3.4% dec^{-1}) [33].

More recent studies [133], however, found extensive positive low-level cloud fraction trends over the Arctic sea ice. The strongest trends are found for October and November. Amplitudes of these trends exceed +10% dec^{-1}.

The estimations of the TOA forcing sensitivity give -0.46 ± 0.90 W m^{-2} per each percentage of cloud cover change for shortwave radiation and $+0.14 \pm 0.087$ W m^{-2} per percentage for longwave radiation. The temperature responses to radiative changes vary from 0.25 W m^{-2} K^{-1} in the CLARA A1 data to 0.43 W m^{-2} K^{-1} in the CERES broadband planetary albedo data [53]. Hwang et al. [134] gave estimations of the radiative feedback using CERES/Terra data (2000–2014) of 1.88 ± 0.73 W m^{-2} K^{-1} and 2.38 ± 0.59 W m^{-2} K^{-1} for short- and long-wave radiation, respectively. They found that clouds reduce the albedo feedback by about 50%, from 1.13 ± 0.44 W m^{-2} K^{-1} in clear-sky periods to 0.49 ± 0.30 W m^{-2} K^{-1} in overcast periods. The TOA cloud feedback over 60–90°N using CERES data remains rather uncertain, ranging from –0.3 to 0.5 W m^{-2} K^{-1} [135]. Kay and L'Ecuyer [136,137] concluded that the clouds over the Arctic Ocean warm the surface by 10 W m^{-2} in annual average and cool the top of the atmosphere (TOA) by −12 W m^{-2}. Philipp et al. [114] analyzed clouds, radiation flux, and sea ice records covering 34 years of satellite observations. These data confirmed statistically significant anticorrelations between sea ice concentrations and the cloud fraction in autumn over melting zones. The net warming effect of clouds was found in late autumn through spring due to weak solar insolation. Thus, an increasing fraction of low-level clouds induces a surface warming trend up to +8.3 W m^{-2} dec^{-1}, causing a prolonged melting season and hindering perennial ice formation. Based on an assumption that the observed decrease in albedo is responsible for the full warming, Pistone et al. [50] obtained a feedback estimation of 0.31 ± 0.04 W m^{-2} K^{-1}.

Excessive cloud cover interferes differently with short- and long-wave radiation. In summertime, when short-wave radiation is available, a reduced cloud fraction allows for additional absorption of the solar energy at the surface and in the upper ocean. In total, Arctic clouds cool the atmosphere by 22 W m^{-2} [137]. The annual average cloud forcing has been changing at a rate of −2.11 W m^{-2} dec^{-1}, indicating a damping effect on the surface warming by clouds [33]. Cloud effects could, however, be offset by a changing surface albedo and radiation balance, as well as by a redistribution of the additional heat between atmospheric layers [51]. The net heating (the warming contribution to the amplification) effect of clouds is still uncertain and remains rather disputable [138]. However, recent additions to the satellite fleet (A-train with CloudSat and CALIPSO) have considerably advanced our knowledge of the Arctic clouds and their climatic impact [137].

Many important issues have been clarified in recent studies [47]. It was confirmed that reduced cloudiness supports the amplification well into the autumn season, when accumulated heat is released [139]. In the wintertime, enhanced low-level cloud fraction traps outgoing long-wave radiation. This trapping is known as cloud optical depth feedback [140]. Observations from the ISCCP, MODIS, and PATMOS-x platforms confirmed that this feedback increases surface warming [141]. The CERES EBAF data set suggests that cloudiness over the areas of sea ice retreat is enhanced, inducing positive radiation forcing [137,142]. Since clouds reduce surface heat loss in the winter season, they are capable of enhancing the amplification.

The Arctic energy budget. Satellite platforms are the most suitable for observing spectral radiance and the energy budget [31]. Therefore, the amplification has gained the largest boost in understanding from climatic-quality data sets of the radiative components of the TOA and surface energy budgets and forcing. The total Arctic energy budget is dominated by a heat deficit of 115.8 W m^{-2} at the top of the atmosphere (TOA) on the annual average [94]. This deficit is larger (−176.9 W m^{-2}) in January but reverts to a small energy gain (12.4 W m^{-2}) in July.

The TOA radiative forcing has been reconstructed using different sensors since the end of 1970s [31]. The CERES data set (2000–2018) indicates only a statistically insignificant Arctic TOA response of −0.19 ± 0.44 W m^{-2} K^{-1} (in high sea ice concentration (SIC) periods) to −0.15 ± 0.16 W m^{-2} K^{-1} (in low SIC periods) [48]. Thus, the TOA radiative

response in the amplification domain has remained nearly stable during the recent period, which is in agreement with model-drawn conclusions [14].

Changes in the regional surface albedo have a strong impact on the heat absorption and redistribution in the Arctic. The long-term darkening of the Arctic surface due to sea ice loss has been observationally confirmed; the mean surface albedo has been reduced from 0.52 to 0.48 since 1979 [50]. Over 28 years of homogenized satellite data (CLARA-A1-SAL product; 1982–2009), the mean albedo of the sea ice cover has been decreasing at 0.029 ± 0.011 dec^{-1} [49]. As sea ice and snow cover retreat, the total Arctic surface albedo has decreased over 1982–2014 at rates of 1.25 ± 0.34 (CLARA A1) and 1.51 ± 0.41 % dec^{-1} (APP-x) [143]. This has caused moderate changes in the radiative fluxes and forcing. Using the CLARA A1 data product, Cao et al. [53] found that sea ice loss has resulted in a 0.20 ± 0.05 W m^{-2} decrease in radiative forcing, yielding a sea ice albedo feedback strength of 0.25 W m^{-2} K^{-1} for the Northern Hemisphere and 0.19 W m^{-2} K^{-1} for the entire globe.

4. A Broader Impact of the Amplification

Impacts on extremes. Interest in the amplification is maintained by its impact on the marine environment, the biosphere, and the cryosphere. The amplification changes not only the mean values of ECVs but also induces a broad spectrum of weather extremes and environmental hazards [144]. Extremes are becoming new normals in the changing Arctic [8]. Amplified warming literally means more intensive and more frequent heat waves in the Arctic, such as those observed in 2012, 2016, 2019, and 2020 [145]. The effects of sea ice retreat, snow cover reduction, and soil carbon release could be felt worldwide [146], though they are perhaps not as straightforward as it has been previously suggested [147]. At the same time, there is no consensus on the impact of the amplification on mid-latitude weather extremes [148]. Synoptic activity in the mid-latitudes likely enhances the amplification; poleward winds are stronger in years of reduced sea ice concentration, increasing the atmospheric (surface oceanic) poleward heat flux by up to 25% and accelerating sea ice retreat [149]. However, the amplification likely has an insignificant impact on synoptic activity [150].

Impacts on ecosystems. The amplification impacts Arctic ecosystems (both their composition and productivity) strongly. The most informative data products systematically quantify changes from earlier baselines [90]. The longest running data product combines more than 40 years of satellite observations since 1981 in the Global Inventory Modeling and Mapping Studies (GIMMS) [66,83]. Vegetation indices in GIMMS isolate signals of vegetation productivity by emphasizing reflectance in different parts of the radiometric spectrum. However, the indices are not developed in the polar context [7]. The relevant issues here, for instance, are a low sun angle, an abundance of surface water, and a low or high surface contrast. Other climatic-quality products include: VIP3 (Vegetation Index and Phenology, version 3), LTDR4 (Long-Term Data Record, version 4), SPOT-VGT (Système Pour l'Observation de la Terre VEGETATION), and the MODIS data set [30]. These data products still have trend discontinuities, as sensor shifts potentially introduce uncertainties and artifacts in data records [151]. Spatial fragmentation of the pixel-based trends creates difficulties for regional trend aggregation [152], so that a trend detection methodology needs more attention [153]. Satellite products also suffer from inadequate sensitivity to detect changes; known problems are related to aliasing from decreasing snow cover and increasing leaf area, atmospheric contamination, orbital drift, and sensor replacements [83]. At present, the EU Sentinel missions [154] have significantly improved monitoring of the terrestrial ecosystem, introducing a 10–60 m spatial resolution and a potential revisit time of five days. The development of hyperspectral missions such as the EnMAP, FLEX, and HyspIRI is expected to deliver richer functionality and accuracy of information. In recent years, attempts to retrieve more diverse traits, such as plant heights, have been presented [155]. The retrieval combines C-band SAR and multispectral vegetation indices, especially through the acquisition strategy of Sentinel-1 and 2.

Remote sensing has already revealed longer growing seasons (up to 20 days longer over the past decade) and increased annual biological production (greening) of the northernmost bioclimatic zones of tundra and forest–tundra [156]. In total, seasonal biological productivity has increased for 42% of northern vegetation, which translates to a 21% gain in productivity between 1982 and 2014 [57]. Only 2.5% of northern vegetation shows browning, which corresponds to a 1.2% loss of productivity.

Impacts on marine biology. Sea ice retreat has improved illuminance, followed by increasing temperatures in upper, biologically productive layers. More stormy weather, higher waves, and enhanced inflow of Atlantic water enrich the productive layers with nutrients. Satellites are witnessing growing primary production, which extends further north and east in the marginal Arctic seas [26,157]. Areas of marine species, from algae and fish to birds and polar bears, have been moving northwards, with implications for the entire food web and leading to an increasing number of fishing vessels visiting Svalbard. Satellite platforms are the main tool to monitor marine ecosystems, providing for the onset and peaks of the annual spring and summer algae blooms as well as for their extent and phenology, both in open waters and under sea ice. Fishery fleet activity can be also monitored. The combined use of SAR and AIS data will provide information on changes in the catch pattern of the fishing fleet in Arctic waters. The ESA contribution has been politically recognized as an essential basis to sustain fisheries in the Arctic Ocean [158].

Impact on soils and permafrost. Following the amplification and land cover changes, warming begins to penetrate in active soil layers and permafrost [159]. The changes in permafrost could be monitored from space using direct and indirect methods. Indirect methods utilize diverse signatures left on terrestrial morphology, hydrology, and biology [29,160]. Such surface changes could be related to the occurrence of certain vegetation types [161] or to the disappearance or shrinkage of lakes [162]. The proxy data may be utilized to extend global permafrost products back to the 1980s or to even earlier periods.

A more direct approach utilizes the land surface temperature and its derivatives in connection with soil temperature modeling. The model complexity and remote-sensing contributions may vary. A number of auxiliary input parameters might be involved. A simple frost-and-thaw index approach was commonly used in earlier works, but later, a more computationally extensive approach began to dominate [163]. Permafrost monitoring with the MODIS LST input was applied by Marchand et al. [164]. This approach is followed in the GlobPermafrost project [56]. It estimates permafrost distribution using an equilibrium state model for the temperature at the top of the permafrost (TTOP model) for the 2000–2016 period. The Copernicus Sentinel-1 and -2 missions provide information on changing topography (land surface slumps, erosion related to thawing permafrost, surface depressions, shrubification), whereas missions carrying thermal sensors (Sentinel-3) assess changes in the land surface temperature. Information on snow conditions and land cover can be used as a proxy for soil properties. Both snow and soil regulate heat transfer and thus determine the impact of the amplification on the frozen soil beneath. Park et al. [54] inferred the extent of permafrost from satellite microwave data of the daily landscape freeze–thaw status over 30 years (1980–2009). The data set is presented in Kim et al. [85]. The extent of permafrost has been declining since 1980 at a rate of 0.33 million km^2 dec^{-1} ($p < 0.05$), but this decline has seemed to accelerate since 2004.

Impact on the Arctic ice sheets and glaciers. Due to the vast time scale difference, it is not a simple question as to whether the amplification has already imposed its impact on the Arctic ice sheets and glaciers. Satellite data reveal a robust decline in the Greenland ice mass since the 2000s. The IMBE team [58] published a data set that compares and combines 26 individual satellite measurements of changes in the Greenland ice sheet mass balance. The ice sheet remained nearly in balance in the 1990s, but annual ice losses have risen since then. The peak loss was recorded in 2011, when it reached 345 $\pm$ 66 billion tons. The total loss between 1992 and 2018 was 3902 $\pm$ 342 billion tons of ice, driving the mean sea level up by 10.8 $\pm$ 0.9 mm. Despite its significant ice sheet loss, Greenland and the surrounding seas do not exhibit a strong amplification, perhaps due to an increasing influx of ice in the

adjacent waters. A review by Cooper and Smith [60] synthesized remote-sensing methods and key findings for the Greenland ice sheet ablation zone. Observations for other, smaller glaciers have provided more diverse results [165].

Impacts on society and humans. Although still wild and remote, the Arctic is increasingly touched by human activity. The Sentinel-1 and -2 satellites have improved the mapping of Arctic settlements and infrastructure [61,62]. Local human disturbances around settlements, mining fields, and transport routes are gradually merging into a pan-Arctic network of modified land cover types. The slow recovery of soils and vegetation increases the footprints of any disturbances, even minimal artificial ones. High-resolution satellite imagery has helped in tracking human footprints over decades, e.g., in northern West Siberia, where the exploration of vast hydrocarbon deposits has been extensive since 1970s. Holistic, interdisciplinary studies of human-induced disturbances include the analysis of diverse satellite imagery and remote-sensing data products [166]. The extensive transformation of disturbed land patches has been documented.

Sizov et al. [167] gives an illustrative example of northern forest advance in northern West Siberia. They compared high-resolution satellite images taken over the last 50 years (1968–2018). The study clearly demonstrates the widespread advance of alternative ecosystems (forest) on damaged land patches that replace tundra ecosystems in their traditional ecotone (Figure 8). Generalizing this example, enhanced greening has been revealed in the MODIS NDVI data around the majority of Arctic towns [168].

Figure 8. Afforestation of a burned tundra area in northern West Siberia. The left image was taken by Corona/KH-4b, 21 August 1968, the right image by Resurs-P, 28 September 2016. Source: [168].

Following global economic and political trends regarding Arctic development, the Arctic population is experiencing significant changes [169]. The amplification creates both risks and opportunities. On the one hand, sea ice retreat, increasing land productivity, and less severe winters improve access to remote areas and resources in the Artic. On the other hand, an active soil layer and permafrost warming lead to weakened ground stability under infrastructure [2], destroyed roads, and other detrimental effects [170]. Satellites have monitored human-induced changes and effects since the 1960s. There are several important

issues for satellites to follow up on, namely, coastal erosion [61], the stability of settlements on the permafrost [171,172], and monitoring of the environmental pollution [173].

5. Conclusions and Perspectives

Responding to the global issue of anthropogenic climate change, the European Space Agency (ESA) has undertaken the Climate Change Initiative (CCI) to exploit the full potential of long-term global satellite observations. The ESA CCI essential climate variables (ECVs) cover more than 40 years of monitoring the earth from space and provide climatic-quality data sets for the investigation of climate phenomena in development [3]. Data sent by the ESA, NASA, and some other satellite platforms are utilized to create a variety of ECV records. Both the advantages and challenges of the ESA CCI projects are related to the need to fuse data information from different sensors working on different satellite platforms with different spatial, temporal, and spectral resolution. Nevertheless, since the emergence of profound climate change in the Arctic has been delayed by the transition of the sea ice state, ESA CCI climatic-quality records have captured the amplified and accelerated climate warming in the Arctic and its widespread influential effects and impacts. These linkages are summarized in Figure 9.

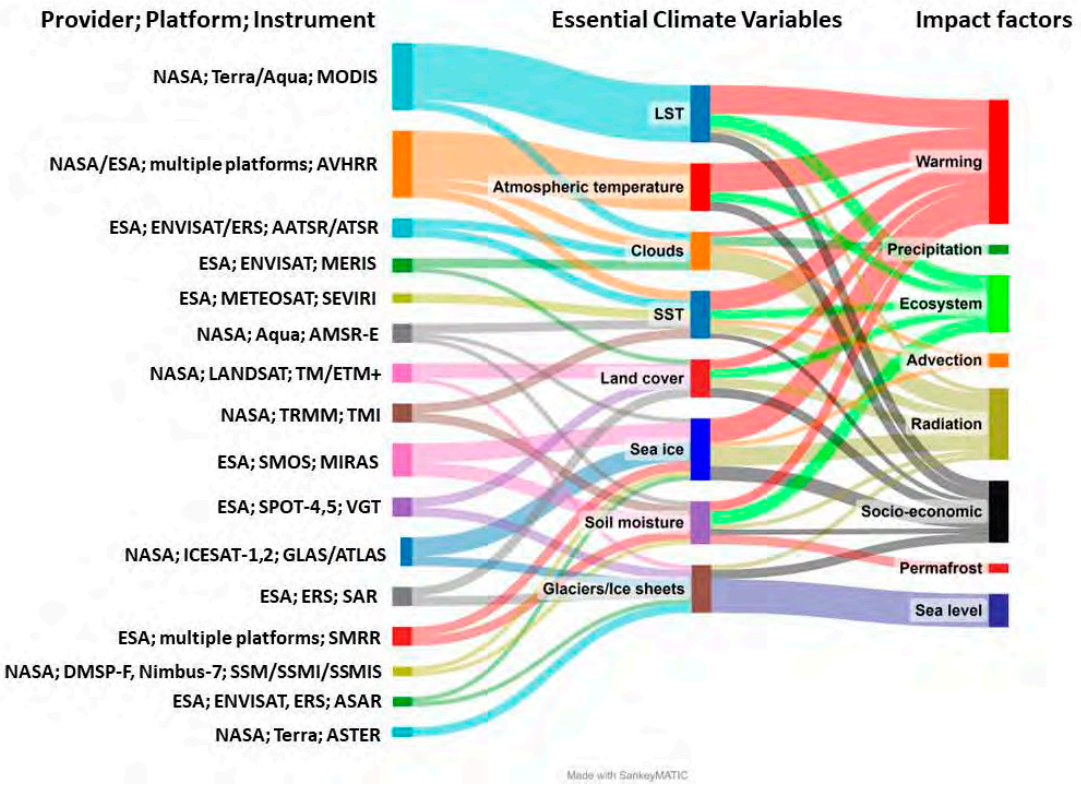

Figure 9. Primary satellite sensors contributing to the amplification ECVs in the ESA CCI program. The diagram combines presentations in several publications [5,12,68,80]. A complete description for each ECV is available at https://climate.esa.int/en/ (accessed on 8 January 2023).

Satellite observations are indispensable for crystallizing a new physical paradigm for the amplification. Although this paradigm benefits from model sensitivity and process studies, such modeling efforts would not be feasible without satellite information in native resolution on the characteristics of sea ice, snow cover, clouds, vegetation, albedo, and TOA radiative fluxes—all of these characteristics are poorly reproduced in unconstrained model runs. Specifically, satellite observations have been essential in revealing the link between sea ice cover and the apparent (surface layer) amplification. They revealed the spatial

relocation of the amplification core from the northern continents to the marginal sea ice zone (e.g., the Barents-Kara Sea region) as soon as multiyear sea ice cover had disappeared.

This synthesis draws a broadly consistent picture of the amplification and its impacts derived from the ESA CCI ECVs and other collections of climatic-quality remote-sensing data products. At the same time, we have to agree with a critical judgement of satellite observations: "*While suitable for detecting overall change, the current capability [of satellite observations] is inadequate for systematic monitoring and for improving process-based and large-scale understanding of the integrated components the cryosphere, biosphere, hydrosphere, and atmosphere*" [5]. There is future potential in multi-sensor/data and synergetic applications of satellite and in situ data to be used in combination with numerical modeling. Those still-existing gaps in ECVs for amplification monitoring will be reduced by new ESA satellite missions [67].

Perspectives on the future amplification. The amplification is a robust response to climate forcing. Historical observations and climate reconstructions have revealed periods of amplified and accelerated temperature trends in the Arctic's past [174]. Model simulations suggest that the amplification will proceed into the future. At the same time, the amplification will not develop as a steady process. Will it vanish as the Earth's climate system approaches its new, warmer equilibrium? Climate models suggest that it will decrease already by the end of the 21st century [175], owing largely to the disappearance of summer sea ice in the Arctic and the equilibration of the global radiation response in the climate system [176]. Other studies disagree with this projection [177]. They expect R_{AA} between 2.5 and 3.5 by the end of the 21st century. CMIP6 climate models project the amplification's continued presence throughout the 21st century, with R_{AA} of about 2.4 (2 to 4 for individual models). As such, the Arctic's annual mean temperature and precipitation could reach about 11.5 $\pm$ 3.4 °C and 49 $\pm$ 19% over the 2081–2100 period (with respect to a 1995–2014 baseline) under the SSP5-8.5 scenario or 4.0 $\pm$ 2.5 °C and 17 $\pm$ 11% under the SSP1-2.6 scenario. It remains unclear whether the period of the most accelerated warming will be limited to the transition to a seasonally ice-free Arctic Ocean, or whether the Arctic warming pace will be still increasing in an open-water Arctic [178].

Satellite observations contribute not only to the monitoring of the amplification but also to the entire value chain that comprises data, information, knowledge, and wisdom [179]. Remote-sensing products of climate quality become integrated into body of knowledge and are used in holistic informed decision making. The ESA CCI is significant in providing data for societal benefits [180]. There is, however, more work to be done. First, more diverse long-term climate quality data products are needed. Diversification of ECV products must be complemented by studies of consistency between different products, and intercalibration should be performed if necessary. This will help to create a model-independent assessment of Arctic climate change and also of spatial and temporal scales that are still unresolved in climate models and analyses. Second, there is a need to improve the processing and cross-platform calibration of long-term climate quality data products, so that the statistical analysis of time records, specifically trends, would become more reliable. Year-round sampling capabilities and sampling of the land sea interface need to be considerably advanced. Specifically, regular atmospheric vertical profile information is still undersampled. Finally, there is a need for a standard protocol for such calibration, which would ensure the quality of long-term data sets. It is important to bring consistency to diverse data products, which at present are increasing the uncertainties of future climate projections.

Author Contributions: Conceptualization, I.E., B.C. and J.A.J.; methodology, I.E., B.C., L.H.P. and A.C.; formal analysis, I.E., L.H.P., A.C. and A.S.; resources, J.A.J. and C.D.; data curation, O.S., M.C., A.S., A.C. and I.E.; writing, I.E. and A.C.; supervision, J.A.J., B.C. and C.D.; project administration, J.A.J.; funding acquisition, J.A.J. and C.D. All authors have read and agreed to the published version of the manuscript.

Funding: This work was supported by the European Space Agency (contract no. 4000127401/19/NL/LF—"ARKTALAS Hoavva").

Data Availability Statement: All data sets should be requested from original references.

Conflicts of Interest: The authors declare no conflict of interest.

References

1. Rajendran, S.; Sadooni, F.N.; Al-Kuwari, H.A.S.; Oleg, A.; Govil, H.; Nasir, S.; Vethamony, P. Monitoring Oil Spill in Norilsk, Russia Using Satellite Data. *Sci. Rep.* **2021**, *11*, 3817. [CrossRef]
2. Hjort, J.; Karjalainen, O.; Aalto, J.; Westermann, S.; Romanovsky, V.E.; Nelson, F.E.; Etzelmüller, B.; Luoto, M. Degrading Permafrost Puts Arctic Infrastructure at Risk by Mid-Century. *Nat. Commun.* **2018**, *9*, 5147. [CrossRef]
3. Hegglin, M.I.; Hollmann, R.; Ardhuin, F.; Bartsch, A.; Bastos, A.; Bennett, V.; Boutin, J.; Brockmann, C.; Buchwitz, M.; Chuvieco, E.; et al. Consistency of Satellite Climate Data Records for Earth System Monitoring. *Bull. Am. Meteorol. Soc.* **2020**, *101*, E1948–E1971. [CrossRef]
4. Yang, J.; Gong, P.; Fu, R.; Zhang, M.; Chen, J.; Liang, S.; Xu, B.; Shi, J.; Dickinson, R. The Role of Satellite Remote Sensing in Climate Change Studies. *Nat. Clim. Chang.* **2013**, *3*, 875–883. [CrossRef]
5. Duncan, B.N.; Ott, L.E.; Abshire, J.B.; Brucker, L.; Carroll, M.L.; Carton, J.; Comiso, J.C.; Dinnat, E.P.; Forbes, B.C.; Gonsamo, A.; et al. Space-Based Observations for Understanding Changes in the Arctic-Boreal Zone. *Rev. Geophys.* **2020**, *58*, e2019RG000652. [CrossRef]
6. Jia, C.; Minnett, P.J. High Latitude Sea Surface Temperatures Derived from MODIS Infrared Measurements. *Remote Sens. Environ.* **2020**, *251*, 112094. [CrossRef]
7. Myers-smith, I.H.; Kerby, J.T.; Phoenix, G.K.; Bjerke, J.W.; Epstein, H.E.; Assmann, J.J.; John, C.; Andreu-hayles, L.; Angers-blondin, S.; Beck, P.S.A.; et al. Complexity Revealed in the Greening of the Arctic. *Nat. Clim. Chang.* **2020**, *10*, 106–117. [CrossRef]
8. Landrum, L.; Holland, M.M. Extremes Become Routine in an Emerging New Arctic. *Nat. Clim. Chang.* **2020**, *10*, 1108–1115. [CrossRef]
9. Taylor, P.C.; Boeke, R.C.; Boisvert, L.N.; Feldl, N.; Henry, M.; Huang, Y.; Langen, P.L.; Liu, W.; Pithan, F.; Sejas, S.A.; et al. Process Drivers, Inter-Model Spread, and the Path Forward: A Review of Amplified Arctic Warming. *Front. Earth Sci.* **2022**, *9*, 1391. [CrossRef]
10. Robinson, D.A.; Dewey, K.F.; Heim, R.R. Global Snow Cover Monitoring: An Update. *Bull. Am. Meteorol. Soc.* **1993**, *74*, 1689–1696. [CrossRef]
11. Bojinski, S.; Verstraete, M.; Peterson, T.C.; Richter, C.; Simmons, A.; Zemp, M. The Concept of Essential Climate Variables in Support of Climate Research, Applications, and Policy. *Bull. Am. Meteorol. Soc.* **2014**, *95*, 1431–1443. [CrossRef]
12. Starkweather, S.; Shapiro, H.; Vakhutinsky, S.; Druckenmiller, M. *15-Year Retrospective Analysis on AON the Observational Foundation of the Arctic Report Card—A 15-Year Retrospective Analysis on the Arctic Observing Network (AON) and Insights for the Future System*; NOAA Arctic: Washington, DC, USA, 2020. [CrossRef]
13. Comiso, J.C.; Hall, D.K. Climate Trends in the Arctic as Observed from Space. *WIREs Clim. Chang.* **2014**, *5*, 389–409. [CrossRef]
14. Previdi, M.; Smith, K.L.; Polvani, L.M. Arctic Amplification of Climate Change: A Review of Underlying Mechanisms. *Environ. Res. Lett.* **2021**, *16*, 093003. [CrossRef]
15. Semenov, V.A. Modern Arctic Climate Research: Progress, Change of Concepts, and Urgent Problems. *Izv. Atmos. Ocean. Phys.* **2021**, *57*, 18–28. [CrossRef]
16. Wendisch, M.; Brückner, M.; Crewell, S.; Ehrlich, A.; Notholt, J.; Lüpkes, C.; Macke, A.; Burrows, J.P.; Rinke, A.; Quaas, J.; et al. Atmospheric and Surface Processes, and Feedback Mechanisms Determining Arctic Amplification: A Review of First Results and Prospects of the (AC)3 Project. *Bull. Am. Meteorol. Soc.* **2022**, *104*, E208–E242. [CrossRef]
17. Wang, Y.; Bi, H.; Huang, H.; Liu, Y.; Liu, Y.; Liang, X.; Fu, M.; Zhang, Z. Satellite-Observed Trends in the Arctic Sea Ice Concentration for the Period 1979–2016. *J. Oceanol. Limnol.* **2019**, *37*, 18–37. [CrossRef]
18. England, M.R.; Eisenman, I.; Lutsko, N.J.; Wagner, T.J.W. The Recent Emergence of Arctic Amplification. *Geophys. Res. Lett.* **2021**, *48*, e2021GL094086. [CrossRef]
19. Isaksen, K.; Nordli, Ø.; Ivanov, B.; Køltzow, M.A.Ø.; Aaboe, S.; Gjelten, H.M.; Mezghani, A.; Eastwood, S.; Førland, E.; Benestad, R.E.; et al. Exceptional Warming over the Barents Area. *Sci. Rep.* **2022**, *12*, 9371. [CrossRef]
20. Francis, J.A.; Vavrus, S.J. Evidence Linking Arctic Amplification to Extreme Weather in Mid-Latitude. *Geophys. Res. Lett.* **2012**, *39*, L06801. [CrossRef]
21. Johannessen, O.M.; Kuzmina, S.I.; Bobylev, L.P.; Miles, M.W. Surface Air Temperature Variability and Trends in the Arctic: New Amplification Assessment and Regionalisation. *Tellus Ser. A Dyn. Meteorol. Oceanogr.* **2016**, *68*, 28234. [CrossRef]
22. Davy, R.; Chen, L.; Hanna, E. Arctic Amplification Metrics. *Int. J. Climatol.* **2018**, *38*, 4384–4394. [CrossRef]
23. Bekryaev, R.V.; Polyakov, I.V.; Alexeev, V.A. Role of Polar Amplification in Long-Term Surface Air Temperature Variations and Modern Arctic Warming. *J. Clim.* **2010**, *23*, 3888–3906. [CrossRef]
24. Nielsen-Englyst, P.; Høyer, J.L.; Kolbe, W.M.; Dybkjær, G.; Lavergne, T.; Tonboe, R.T.; Skarpalezos, S.; Karagali, I. A Combined Sea and Sea-Ice Surface Temperature Climate Dataset of the Arctic, 1982–2021. *Remote Sens. Environ.* **2023**, *284*, 113331. [CrossRef]

25. Bormann, K.J.; Brown, R.D.; Derksen, C.; Painter, T.H. Estimating Snow-Cover Trends from Space. *Nat. Clim. Chang.* **2018**, *8*, 924–928. [CrossRef]
26. Ardyna, M.; Arrigo, K.R. Phytoplankton Dynamics in a Changing Arctic Ocean. *Nat. Clim. Chang.* **2020**, *10*, 892–903. [CrossRef]
27. Nitze, I.; Grosse, G.; Jones, B.M.; Romanovsky, V.E.; Boike, J. Remote Sensing Quantifies Widespread Abundance of Permafrost Region Disturbances across the Arctic and Subarctic. *Nat. Commun.* **2018**, *9*, 5423. [CrossRef] [PubMed]
28. Beamish, A.; Raynolds, M.K.; Epstein, H.; Frost, G.V.; Macander, M.J.; Bergstedt, H.; Bartsch, A.; Kruse, S.; Miles, V.; Tanis, C.M.; et al. Recent Trends and Remaining Challenges for Optical Remote Sensing of Arctic Tundra Vegetation: A Review and Outlook. *Remote Sens. Environ.* **2020**, *246*, 111872. [CrossRef]
29. Trofaier, A.M.; Westermann, S.; Bartsch, A. Progress in Space-Borne Studies of Permafrost for Climate Science: Towards a Multi-ECV Approach. *Remote Sens. Environ.* **2017**, *203*, 55–70. [CrossRef]
30. Jenkins, L.K.; Barry, T.; Bosse, K.R.; Currie, W.S.; Christensen, T.; Longan, S.; Shuchman, R.A.; Tanzer, D.; Taylor, J.J. Satellite-Based Decadal Change Assessments of Pan-Arctic Environments. *Ambio* **2020**, *49*, 820–832. [CrossRef]
31. Liang, S.; Wang, D.; He, T.; Yu, Y. Remote Sensing of Earth's Energy Budget: Synthesis and Review. *Int. J. Digit. Earth* **2019**, *12*, 737–780. [CrossRef]
32. Riihelä, A.; Key, J.R.; Meirink, J.F.; Kuipers Munneke, P.; Palo, T.; Karlsson, K.-G. An Intercomparison and Validation of Satellite-Based Surface Radiative Energy Flux Estimates over the Arctic. *J. Geophys. Res. Atmos.* **2017**, *122*, 4829–4848. [CrossRef]
33. Wang, X.; Key, J.; Liu, Y.; Fowler, C.; Maslanik, J.; Tschudi, M. Arctic Climate Variability and Trends from Satellite Observations. *Adv. Meteorol.* **2012**, *2012*, 505613. [CrossRef]
34. Rantanen, M.; Karpechko, A.Y.; Lipponen, A.; Nordling, K.; Hyvärinen, O.; Ruosteenoja, K.; Vihma, T.; Laaksonen, A. The Arctic Has Warmed Nearly Four Times Faster than the Globe since 1979. *Commun. Earth Environ.* **2022**, *3*, 168. [CrossRef]
35. Lind, S.; Ingvaldsen, R.B.; Furevik, T. Arctic warming hotspot in the northern Barents Sea linked to declining sea-ice import. *Nat. Clim. Chang.* **2018**, *8*, 634–639. [CrossRef]
36. Ricker, R.; Kauker, F.; Schweiger, A.; Hendricks, S.; Zhang, J.; Paul, S. Evidence for an Increasing Role of Ocean Heat in Arctic Winter Sea Ice Growth. *J. Clim.* **2021**, *34*, 5215–5227. [CrossRef]
37. Yang, X.-Y.; Fyfe, J.C.; Flato, G.M. The Role of Poleward Energy Transport in Arctic Temperature Evolution. *Geophys. Res. Lett.* **2010**, *37*. [CrossRef]
38. Liu, Y.; Key, J.R.; Schweiger, A.; Francis, J. Characteristics of Satellite-Derived Clear-Sky Atmospheric Temperature Inversion Strength in the Arctic, 1980–1996. *J. Clim.* **2006**, *19*, 4902–4913. [CrossRef]
39. Sobrino, J.A.; Julien, Y.; García-Monteiro, S. Surface Temperature of the Planet Earth from Satellite Data. *Remote Sens.* **2020**, *12*, 218. [CrossRef]
40. Wang, Y.; Hessen, D.O.; Samset, B.H.; Stordal, F. Evaluating Global and Regional Land Warming Trends in the Past Decades with Both MODIS and ERA5-Land Land Surface Temperature Data. *Remote Sens. Environ.* **2022**, *280*, 113181. [CrossRef]
41. Li, M.; Ke, C.Q.; Shen, X.; Cheng, B.; Li, H. Investigation of the Arctic Sea Ice Volume from 2002 to 2018 Using Multi-Source Data. *Int. J. Climatol.* **2021**, *41*, 2509–2527. [CrossRef]
42. Bi, H.; Liang, Y.; Wang, Y.; Liang, X.; Zhang, Z.; Du, T.; Yu, Q.; Huang, J.; Kong, M.; Huang, H. Arctic Multiyear Sea Ice Variability Observed from Satellites: A Review. *J. Oceanol. Limnol.* **2020**, *38*, 962–984. [CrossRef]
43. Liu, Y.; Key, J.R.; Wang, X.; Tschudi, M. Multidecadal Arctic Sea Ice Thickness and Volume Derived from Ice Age. *Cryosph.* **2020**, *14*, 1325–1345. [CrossRef]
44. Kwok, R. Arctic Sea Ice Thickness, Volume, and Multiyear Ice Coverage: Losses and Coupled Variability (1958-2018). *Environ. Res. Lett.* **2018**, *13*, 105005. [CrossRef]
45. Feng, J.; Zhang, Y.; Cheng, Q.; Tsou, J.Y. Pan-Arctic Melt Pond Fraction Trend, Variability, and Contribution to Sea Ice Changes. *Glob. Planet. Chang.* **2022**, *217*, 103932. [CrossRef]
46. Pulliainen, J.; Luojus, K.; Derksen, C.; Mudryk, L.; Lemmetyinen, J.; Salminen, M.; Ikonen, J.; Takala, M.; Cohen, J.; Smolander, T.; et al. Patterns and Trends of Northern Hemisphere Snow Mass from 1980 to 2018. *Nature* **2020**, *581*, 294–298. [CrossRef]
47. Devasthale, A.; Sedlar, J.; Tjernström, M.; Kokhanovsky, A. A Climatological Overview of Arctic Clouds. In *Physics and Chemistry of the Arctic Atmosphere*; Springer: Cham, Switzerland, 2020; pp. 331–360.
48. Hwang, J.; Choi, Y.; Su, H.; Jiang, J.H. Invariability of Arctic Top-of-Atmosphere Radiative Response to Surface Temperature Changes. *Earth Space Sci.* **2020**, *7*, e2020EA001316. [CrossRef]
49. Riihelä, A.; Manninen, T.; Laine, V. Observed Changes in the Albedo of the Arctic Sea-Ice Zone for the Period 1982–2009. *Nat. Clim. Chang.* **2013**, *3*, 895–898. [CrossRef]
50. Pistone, K.; Eisenman, I.; Ramanathan, V. Observational Determination of Albedo Decrease Caused by Vanishing Arctic Sea Ice. *Proc. Natl. Acad. Sci. USA* **2014**, *111*, 3322–3326. [CrossRef]
51. Marcianesi, F.; Aulicino, G.; Wadhams, P. Arctic Sea Ice and Snow Cover Albedo Variability and Trends during the Last Three Decades. *Polar Sci.* **2021**, *28*, 100617. [CrossRef]
52. Seong, N.; Kim, H.-C.; Choi, S.; Jin, D.; Jung, D.; Sim, S.; Woo, J.; Kim, N.; Seo, M.; Lee, K.; et al. Evaluation of Sea Ice Radiative Forcing According to Surface Albedo and Skin Temperature over the Arctic from 1982–2015. *Remote Sens.* **2022**, *14*, 2512. [CrossRef]
53. Cao, Y.; Liang, S.; Chen, X.; He, T. Assessment of Sea Ice Albedo Radiative Forcing and Feedback over the Northern Hemisphere from 1982 to 2009 Using Satellite and Reanalysis Data. *J. Clim.* **2015**, *28*, 1248–1259. [CrossRef]

54. Park, H.; Kim, Y.; Kimball, J.S. Widespread Permafrost Vulnerability and Soil Active Layer Increases over the High Northern Latitudes Inferred from Satellite Remote Sensing and Process Model Assessments. *Remote Sens. Environ.* **2016**, *175*, 349–358. [CrossRef]
55. Philipp, M.; Dietz, A.; Buchelt, S.; Kuenzer, C. Trends in Satellite Earth Observation for Permafrost Related Analyses-a Review. *Remote Sens.* **2021**, *13*, 1217. [CrossRef]
56. Obu, J.; Westermann, S.; Bartsch, A.; Berdnikov, N.; Christiansen, H.H.; Dashtseren, A.; Delaloye, R.; Elberling, B.; Etzelmüller, B.; Kholodov, A.; et al. Northern Hemisphere Permafrost Map Based on TTOP Modelling for 2000–2016 at 1 Km2 Scale. *Earth-Sci. Rev.* **2019**, *193*, 299–316. [CrossRef]
57. Park, T.; Ganguly, S.; Tømmervik, H.; Euskirchen, E.S.; Høgda, K.-A.; Karlsen, S.R.; Brovkin, V.; Nemani, R.R.; Myneni, R.B. Changes in Growing Season Duration and Productivity of Northern Vegetation Inferred from Long-Term Remote Sensing Data. *Environ. Res. Lett.* **2016**, *11*, 084001. [CrossRef]
58. The IMBIE team Mass Balance of the Greenland Ice Sheet from 1992 to 2018. *Nature* **2020**, *579*, 233–239. [CrossRef]
59. Mottram, R.; Simonsen, S.B.; Høyer Svendsen, S.; Barletta, V.R.; Sandberg Sørensen, L.; Nagler, T.; Wuite, J.; Groh, A.; Horwath, M.; Rosier, J.; et al. An Integrated View of Greenland Ice Sheet Mass Changes Based on Models and Satellite Observations. *Remote Sens.* **2019**, *11*, 1407. [CrossRef]
60. Cooper, M.; Smith, L. Satellite Remote Sensing of the Greenland Ice Sheet Ablation Zone: A Review. *Remote Sens.* **2019**, *11*, 2405. [CrossRef]
61. Bartsch, A.; Pointner, G.; Nitze, I.; Efimova, A.; Jakober, D.; Ley, S.; Högström, E.; Grosse, G.; Schweitzer, P. Expanding Infrastructure and Growing Anthropogenic Impacts along Arctic Coasts. *Environ. Res. Lett.* **2021**, *16*, 115013. [CrossRef]
62. Bartsch, A.; Pointner, G.; Ingeman-Nielsen, T.; Lu, W. Towards Circumpolar Mapping of Arctic Settlements and Infrastructure Based on Sentinel-1 and Sentinel-2. *Remote Sens.* **2020**, *12*, 2368. [CrossRef]
63. Sasgen, I.; Wouters, B.; Gardner, A.S.; King, M.D.; Tedesco, M.; Landerer, F.W.; Dahle, C.; Save, H.; Fettweis, X. Return to Rapid Ice Loss in Greenland and Record Loss in 2019 Detected by the GRACE-FO Satellites. *Commun. Earth Environ.* **2020**, *1*, 8. [CrossRef]
64. Spencer, R.W.; Christy, J.R.; Braswell, W.D. UAH Version 6 Global Satellite Temperature Products: Methodology and Results. *Asia-Pac. J. Atmos. Sci.* **2017**, *53*, 121–130. [CrossRef]
65. Christy, J.R.; Spencer, R.W.; Braswell, W.D.; Doty, K.G. NOAA CDR Program. *NOAA Climate Data Record (CDR) of MSU and AMSU-A Mean Layer Temperatures, UAH Version 6.0*, NOAA National Centers for Environmental Information: Washington, DC, USA, 2017. [CrossRef]
66. Guay, K.C.; Beck, P.S.A.; Berner, L.T.; Goetz, S.J.; Baccini, A.; Buermann, W. Vegetation Productivity Patterns at High Northern Latitudes: A Multi-Sensor Satellite Data Assessment. *Glob. Chang. Biol.* **2014**, *20*, 3147–3158. [CrossRef]
67. Lancheros, E.; Camps, A.; Park, H.; Sicard, P.; Mangin, A.; Matevosyan, H.; Lluch, I. Gaps Analysis and Requirements Specification for the Evolution of Copernicus System for Polar Regions Monitoring: Addressing the Challenges in the Horizon 2020–2030. *Remote Sens.* **2018**, *10*, 1098. [CrossRef]
68. Hollmann, R.; Merchant, C.J.; Saunders, R.; Downy, C.; Buchwitz, M.; Cazenave, A.; Chuvieco, E.; Defourny, P.; de Leeuw, G.; Forsberg, R.; et al. The ESA Climate Change Initiative: Satellite Data Records for Essential Climate Variables. *Bull. Am. Meteorol. Soc.* **2013**, *94*, 1541–1552. [CrossRef]
69. Nightingale, J.; Boersma, K.; Muller, J.-P.; Compernolle, S.; Lambert, J.-C.; Blessing, S.; Giering, R.; Gobron, N.; De Smedt, I.; Coheur, P.; et al. Quality Assurance Framework Development Based on Six New ECV Data Products to Enhance User Confidence for Climate Applications. *Remote Sens.* **2018**, *10*, 1254. [CrossRef]
70. Kharbouche, S.; Muller, J.-P. Sea Ice Albedo from MISR and MODIS: Production, Validation, and Trend Analysis. *Remote Sens.* **2018**, *11*, 9. [CrossRef]
71. Bentamy, A.; Piollé, J.F.; Grouazel, A.; Danielson, R.; Gulev, S.; Paul, F.; Azelmat, H.; Mathieu, P.P.; von Schuckmann, K.; Sathyendranath, S.; et al. Review and Assessment of Latent and Sensible Heat Flux Accuracy over the Global Oceans. *Remote Sens. Environ.* **2017**, *201*, 196–218. [CrossRef]
72. Smedsrud, L.H.; Esau, I.; Ingvaldsen, R.B.; Eldevik, T.; Haugan, P.M.; Li, C.; Lien, V.S.; Olsen, A.; Omar, A.M.; Otterå, O.H.; et al. The role of the barents sea in the arctic climate system. *Rev. Geophys.* **2013**, *51*, 415–449. [CrossRef]
73. Santer, B.D.; Solomon, S.; Pallotta, G.; Mears, C.; Po-Chedley, S.; Fu, Q.; Wentz, F.; Zou, C.Z.; Painter, J.; Cvijanovic, I.; et al. Comparing Tropospheric Warming in Climate Models and Satellite Data. *J. Clim.* **2017**, *30*, 373–392. [CrossRef]
74. Karlsson, K.-G.; Anttila, K.; Trentmann, J.; Stengel, M.; Fokke Meirink, J.; Devasthale, A.; Hanschmann, T.; Kothe, S.; Jääskeläinen, E.; Sedlar, J.; et al. CLARA-A2: The Second Edition of the CM SAF Cloud and Radiation Data Record from 34 Years of Global AVHRR Data. *Atmos. Chem. Phys.* **2017**, *17*, 5809–5828. [CrossRef]
75. Loeb, N.G.; Doelling, D.R.; Wang, H.; Su, W.; Nguyen, C.; Corbett, J.G.; Liang, L.; Mitrescu, C.; Rose, F.G.; Kato, S. Clouds and the Earth's Radiant Energy System (CERES) Energy Balanced and Filled (EBAF) Top-of-Atmosphere (TOA) Edition-4.0 Data Product. *J. Clim.* **2018**, *31*, 895–918. [CrossRef]
76. Heidinger, A.K.; Foster, M.J.; Walther, A.; Zhao, X. (Tom) The Pathfinder Atmospheres–Extended AVHRR Climate Dataset. *Bull. Am. Meteorol. Soc.* **2014**, *95*, 909–922. [CrossRef]
77. Wang, X.; Key, J.R. Arctic Surface, Cloud, and Radiation Properties Based on the AVHRR Polar Pathfinder Dataset. Part II: Recent Trends. *J. Clim.* **2005**, *18*, 2575–2593. [CrossRef]

78. Wang, X.; Liu, J.; Yang, B.; Bao, Y.; Petropoulos, G.P.; Liu, H.; Hu, B. Seasonal Trends in Clouds and Radiation over the Arctic Seas from Satellite Observations during 1982 to 2019. *Remote Sens.* **2021**, *13*, 3201. [CrossRef]
79. Estilow, T.W.; Young, A.H.; Robinson, D.A. A Long-Term Northern Hemisphere Snow Cover Extent Data Record for Climate Studies and Monitoring. *Earth Syst. Sci. Data* **2015**, *7*, 137–142. [CrossRef]
80. Lavergne, T.; Macdonald Sørensen, A.; Kern, S.; Tonboe, R.; Notz, D.; Aaboe, S.; Bell, L.; Dybkjær, G.; Eastwood, S.; Gabarro, C.; et al. Version 2 of the EUMETSAT OSI SAF and ESA CCI Sea-Ice Concentration Climate Data Records. *Cryosphere* **2019**, *13*, 49–78. [CrossRef]
81. Comiso, J.C.; Meier, W.N.; Gersten, R. Variability and Trends in the Arctic Sea Ice Cover: Results from Different Techniques. *J. Geophys. Res. Ocean.* **2017**, *122*, 6883–6900. [CrossRef]
82. Schweiger, A.J.; Wood, K.R.; Zhang, J. Arctic Sea Ice Volume Variability over 1901–2010: A Model-Based Reconstruction. *J. Clim.* **2019**, *32*, 4731–4752. [CrossRef]
83. Piao, S.; Wang, X.; Park, T.; Chen, C.; Lian, X.; He, Y.; Bjerke, J.W.; Chen, A.; Ciais, P.; Tømmervik, H.; et al. Characteristics, Drivers and Feedbacks of Global Greening. *Nat. Rev. Earth Environ.* **2020**, *1*, 14–27. [CrossRef]
84. Pinzon, J.; Tucker, C. A Non-Stationary 1981–2012 AVHRR NDVI3g Time Series. *Remote Sens.* **2014**, *6*, 6929–6960. [CrossRef]
85. Kim, Y.; Kimball, J.S.; Glassy, J.; Du, J. An Extended Global Earth System Data Record on Daily Landscape Freeze–Thaw Status Determined from Satellite Passive Microwave Remote Sensing. *Earth Syst. Sci. Data* **2017**, *9*, 133–147. [CrossRef]
86. Holland, M.M.; Bitz, C.M. Polar Amplification of Climate Change in Coupled Models. *Clim. Dyn.* **2003**, *21*, 221–232. [CrossRef]
87. Serreze, M.C.; Barry, R.G. Processes and Impacts of Arctic Amplification: A Research Synthesis. *Glob. Planet. Chang.* **2011**, *77*, 85–96. [CrossRef]
88. Comiso, J.C. Warming Trends in the Arctic from Clear Sky Satellite Observations. *J. Clim.* **2003**, *16*, 3498–3510. [CrossRef]
89. Serreze, M.C.; Francis, J.A. The Arctic Amplification Debate. *Clim. Chang.* **2006**, *76*, 241–264. [CrossRef]
90. Box, J.E.; Colgan, W.T.; Christensen, T.R.; Schmidt, N.M.; Lund, M.; Parmentier, F.J.W.; Brown, R.; Bhatt, U.S.; Euskirchen, E.S.; Romanovsky, V.E.; et al. Key Indicators of Arctic Climate Change: 1971-2017. *Environ. Res. Lett.* **2019**, *14*, 45010. [CrossRef]
91. Screen, J.A.; Deser, C.; Simmonds, I. Local and Remote Controls on Observed Arctic Warming. *Geophys. Res. Lett.* **2012**, *39*. [CrossRef]
92. Babar, B.; Graversen, R.; Boström, T. Evaluating CM-SAF Solar Radiation CLARA-A1 and CLARA-A2 Datasets in Scandinavia. *Sol. Energy* **2018**, *170*, 76–85. [CrossRef]
93. Lohmann, G. Temperatures from Energy Balance Models: The Effective Heat Capacity Matters. *Earth Syst. Dyn.* **2020**, *11*, 1195–1208. [CrossRef]
94. Mayer, M.; Tietsche, S.; Haimberger, L.; Tsubouchi, T.; Mayer, J.; Zuo, H. An Improved Estimate of the Coupled Arctic Energy Budget. *J. Clim.* **2019**, *32*, 7915–7934. [CrossRef]
95. Jeevanjee, N.; Held, I.; Ramaswamy, V. Manabe's Radiative–Convective Equilibrium. *Bull. Am. Meteorol. Soc.* **2022**, *103*, E2559–E2569. [CrossRef]
96. Thackeray, C.W.; Hall, A. An Emergent Constraint on Future Arctic Sea-Ice Albedo Feedback. *Nat. Clim. Chang.* **2019**, *9*, 972–978. [CrossRef]
97. Olonscheck, D.; Mauritsen, T.; Notz, D. Arctic Sea-Ice Variability Is Primarily Driven by Atmospheric Temperature Fluctuations. *Nat. Geosci.* **2019**, *12*, 430–434. [CrossRef]
98. Bliss, A.C.; Anderson, M.R. Arctic Sea Ice Melt Onset Timing From Passive Microwave-Based and Surface Air Temperature-Based Methods. *J. Geophys. Res. Atmos.* **2018**, *123*, 9063–9080. [CrossRef]
99. Bitz, C.M.; Roe, G.H. A Mechanism for the High Rate of Sea Ice Thinning in the Arctic Ocean. *J. Clim.* **2004**, *17*, 3623–3632. [CrossRef]
100. Brennan, M.K.; Hakim, G.J.; Blanchard-Wrigglesworth, E. Arctic Sea-Ice Variability During the Instrumental Era. *Geophys. Res. Lett.* **2020**, *47*, e2019GL086843. [CrossRef]
101. Serreze, M.C.; Barrett, A.P.; Stroeve, J.C.; Kindig, D.N.; Holland, M.M. The Emergence of Surface-Based Arctic Amplification. *Cryosphere* **2009**, *3*, 11–19. [CrossRef]
102. Johannessen, O.M.; Bobylev, L.P.; Shalina, E.V.; Sandven, S. (Eds.) *Sea Ice in the Arctic*; Springer Polar Sciences; Springer International Publishing: Cham, Switzerland, 2020; ISBN 978-3-030-21300-8.
103. Ivanova, N.; Pedersen, L.T.; Tonboe, R.T.; Kern, S.; Heygster, G.; Lavergne, T.; Sørensen, A.; Saldo, R.; Dybkjær, G.; Brucker, L.; et al. Inter-Comparison and Evaluation of Sea Ice Algorithms: Towards Further Identification of Challenges and Optimal Approach Using Passive Microwave Observations. *Cryosphere* **2015**, *9*, 1797–1817. [CrossRef]
104. Ólason, E.; Rampal, P.; Dansereau, V. On the Statistical Properties of Sea-Ice Lead Fraction and Heat Fluxes in the Arctic. *Cryosphere* **2021**, *15*, 1053–1064. [CrossRef]
105. Zhang, Y.; Cheng, X.; Liu, J.; Hui, F. The Potential of Sea Ice Leads as a Predictor for Summer Arctic Sea Ice Extent. *Cryosphere* **2018**, *12*, 3747–3757. [CrossRef]
106. Wagner, P.M.; Hughes, N.; Bourbonnais, P.; Stroeve, J.; Rabenstein, L.; Bhatt, U.; Little, J.; Wiggins, H.; Fleming, A. Sea-Ice Information and Forecast Needs for Industry Maritime Stakeholders. *Polar Geogr.* **2020**, *43*, 160–187. [CrossRef]
107. Marquardt Collow, A.B.; Cullather, R.I.; Bosilovich, M.G. Recent Arctic Ocean Surface Air Temperatures in Atmospheric Reanalyses and Numerical Simulations. *J. Clim.* **2020**, *33*, 4347–4367. [CrossRef]

108. Minnett, P.J.; Alvera-Azcárate, A.; Chin, T.M.; Corlett, G.K.; Gentemann, C.L.; Karagali, I.; Li, X.; Marsouin, A.; Marullo, S.; Maturi, E.; et al. Half a Century of Satellite Remote Sensing of Sea-Surface Temperature. *Remote Sens. Environ.* **2019**, *233*, 111366. [CrossRef]
109. Kumar, A.; Yadav, J.; Mohan, R. Spatio-Temporal Change and Variability of Barents-Kara Sea Ice, in the Arctic: Ocean and Atmospheric Implications. *Sci. Total Environ.* **2021**, *753*, 142046. [CrossRef]
110. Lang, A.; Yang, S.; Kaas, E. Sea Ice Thickness and Recent Arctic Warming. *Geophys. Res. Lett.* **2017**, *44*, 409–418. [CrossRef]
111. Chemke, R.; Polvani, L.M.; Kay, J.E.; Orbe, C. Quantifying the Role of Ocean Coupling in Arctic Amplification and Sea-Ice Loss over the 21st Century. *NPJ Clim. Atmos. Sci.* **2021**, *4*, 46. [CrossRef]
112. Tschudi, M.; Meier, W.N.; Stewart, J.S.; Fowler, C.; Maslanik, J. *EASE-Grid Sea Ice Age, Version 4 [Data Set]*; NASA National Snow and Ice Data Center Distributed Active Archive Center: Boulder, CO, USA, 2019.
113. Matveeva, T.A.; Semenov, V.A. Regional Features of the Arctic Sea Ice Area Changes in 2000–2019 versus 1979–1999 Periods. *Atmosphere* **2022**, *13*, 1434. [CrossRef]
114. Philipp, D.; Stengel, M.; Ahrens, B. Analyzing the Arctic Feedback Mechanism between Sea Ice and Low-Level Clouds Using 34 Years of Satellite Observations. *J. Clim.* **2020**, *33*, 7479–7501. [CrossRef]
115. Luo, T.; Yuan, R.; Wang, Z. Lidar-Based Remote Sensing of Atmospheric Boundary Layer Height over Land and Ocean. *Atmos. Meas. Tech.* **2014**, *7*, 173–182. [CrossRef]
116. Dang, R.; Yang, Y.; Hu, X.M.; Wang, Z.; Zhang, S. A Review of Techniques for Diagnosing the Atmospheric Boundary Layer Height (ABLH) Using Aerosol Lidar Data. *Remote Sens.* **2019**, *11*, 1590. [CrossRef]
117. McGrath-Spangler, E.L.; Denning, A.S. Global Seasonal Variations of Midday Planetary Boundary Layer Depth from CALIPSO Space-Borne LIDAR. *J. Geophys. Res. Atmos.* **2013**, *118*, 1226–1233. [CrossRef]
118. Kim, M.-H.; Yeo, H.; Park, S.; Park, D.-H.; Omar, A.; Nishizawa, T.; Shimizu, A.; Kim, S.-W. Assessing CALIOP-Derived Planetary Boundary Layer Height Using Ground-Based Lidar. *Remote Sens.* **2021**, *13*, 1496. [CrossRef]
119. Von Engeln, A.; Teixeira, J. A Planetary Boundary Layer Height Climatology Derived from ECMWF Reanalysis Data. *J. Clim.* **2013**, *26*, 6575–6590. [CrossRef]
120. Ao, C.O.; Waliser, D.E.; Chan, S.K.; Li, J.L.; Tian, B.; Xie, F.; Mannucci, A.J. Planetary Boundary Layer Heights from GPS Radio Occultation Refractivity and Humidity Profiles. *J. Geophys. Res. Atmos.* **2012**, *117*, 1–18. [CrossRef]
121. Ganeshan, M.; Wu, D.L. An Investigation of the Arctic Inversion Using COSMIC RO Observations. *J. Geophys. Res. Atmos.* **2015**, *120*, 9338–9351. [CrossRef]
122. Ding, F.; Iredell, L.; Theobald, M.; Wei, J.; Meyer, D. PBL Height From AIRS, GPS RO, and MERRA-2 Products in NASA GES DISC and Their 10-Year Seasonal Mean Intercomparison. *Earth Space Sci.* **2021**, *8*, e2021EA001859. [CrossRef]
123. Esau, I.N. Amplification of Turbulent Exchange over Wide Arctic Leads: Large-Eddy Simulation Study. *J. Geophys. Res. Atmos.* **2007**, *112*, D08109. [CrossRef]
124. Qu, M.; Pang, X.; Zhao, X.; Zhang, J.; Ji, Q.; Fan, P. Estimation of Turbulent Heat Flux over Leads Using Satellite Thermal Images. *Cryosph.* **2019**, *13*, 1565–1582. [CrossRef]
125. Chernokulsky, A.; Esau, I. Cloud Cover and Cloud Types in the Eurasian Arctic in 1936–2012. *Int. J. Climatol.* **2019**, *39*, 5771–5790. [CrossRef]
126. Lenaerts, J.T.M.; Van Tricht, K.; Lhermitte, S.; L'Ecuyer, T.S. Polar Clouds and Radiation in Satellite Observations, Reanalyses, and Climate Models. *Geophys. Res. Lett.* **2017**, *44*, 3355–3364. [CrossRef]
127. Karlsson, K.-G.; Devasthale, A. Inter-Comparison and Evaluation of the Four Longest Satellite-Derived Cloud Climate Data Records: CLARA-A2, ESA Cloud CCI V3, ISCCP-HGM, and PATMOS-X. *Remote Sens.* **2018**, *10*, 1567. [CrossRef]
128. Stengel, M.; Stapelberg, S.; Sus, O.; Schlundt, C.; Poulsen, C.; Thomas, G.; Christensen, M.; Carbajal Henken, C.; Preusker, R.; Fischer, J.; et al. Cloud Property Datasets Retrieved from AVHRR, MODIS, AATSR and MERIS in the Framework of the Cloud_cci Project. *Earth Syst. Sci. Data* **2017**, *9*, 881–904. [CrossRef]
129. Stengel, M.; Stapelberg, S.; Sus, O.; Finkensieper, S.; Würzler, B.; Philipp, D.; Hollmann, R.; Poulsen, C.; Christensen, M.; McGarragh, G. Cloud_cci Advanced Very High Resolution Radiometer Post Meridiem (AVHRR-PM) Dataset Version 3: 35-Year Climatology of Global Cloud and Radiation Properties. *Earth Syst. Sci. Data* **2020**, *12*, 41–60. [CrossRef]
130. Chernokulsky, A.; Mokhov, I.I. Climatology of Total Cloudiness in the Arctic: An Intercomparison of Observations and Reanalyses. *Adv. Meteorol.* **2012**, *2012*, 542093. [CrossRef]
131. Chan, M.A.; Comiso, J.C. Arctic Cloud Characteristics as Derived from MODIS, CALIPSO, and CloudSat. *J. Clim.* **2013**, *26*, 3285–3306. [CrossRef]
132. Liu, Y.; Ackerman, S.A.; Maddux, B.C.; Key, J.R.; Frey, R.A. Errors in Cloud Detection over the Arctic Using a Satellite Imager and Implications for Observing Feedback Mechanisms. *J. Clim.* **2010**, *23*, 1894–1907. [CrossRef]
133. Boccolari, M.; Parmiggiani, F. Trends and Variability of Cloud Fraction Cover in the Arctic, 1982–2009. *Theor. Appl. Climatol.* **2018**, *132*, 739–749. [CrossRef]
134. Hwang, J.; Choi, Y.S.; Kim, W.M.; Su, H.; Jiang, J.H. Observational Estimation of Radiative Feedback to Surface Air Temperature over Northern High Latitudes. *Clim. Dyn.* **2018**, *50*, 615–628. [CrossRef]
135. Zhang, R.; Wang, H.; Fu, Q.; Pendergrass, A.G.; Wang, M.; Yang, Y.; Ma, P.; Rasch, P.J. Local Radiative Feedbacks Over the Arctic Based on Observed Short-Term Climate Variations. *Geophys. Res. Lett.* **2018**, *45*, 5761–5770. [CrossRef]

136. Kay, J.E.; L'Ecuyer, T. Observational Constraints on Arctic Ocean Clouds and Radiative Fluxes during the Early 21st Century. *J. Geophys. Res. Atmos.* **2013**, *118*, 7219–7236. [CrossRef]
137. Kay, J.E.; L'Ecuyer, T.; Chepfer, H.; Loeb, N.; Morrison, A.; Cesana, G. Recent Advances in Arctic Cloud and Climate Research. *Curr. Clim. Chang. Rep.* **2016**, *2*, 159–169. [CrossRef]
138. Pithan, F.; Mauritsen, T. Arctic Amplification Dominated by Temperature Feedbacks in Contemporary Climate Models. *Nat. Geosci.* **2014**, *7*, 181–184. [CrossRef]
139. Palm, S.P.; Strey, S.T.; Spinhirne, J.; Markus, T. Influence of Arctic Sea Ice Extent on Polar Cloud Fraction and Vertical Structure and Implications for Regional Climate. *J. Geophys. Res.* **2010**, *115*, D21209. [CrossRef]
140. Goosse, H.; Kay, J.E.; Armour, K.C.; Bodas-Salcedo, A.; Chepfer, H.; Docquier, D.; Jonko, A.; Kushner, P.J.; Lecomte, O.; Massonnet, F.; et al. Quantifying Climate Feedbacks in Polar Regions. *Nat. Commun.* **2018**, *9*, 1919. [CrossRef] [PubMed]
141. Terai, C.R.; Klein, S.A.; Zelinka, M.D. Constraining the Low-Cloud Optical Depth Feedback at Middle and High Latitudes Using Satellite Observations. *J. Geophys. Res. Atmos.* **2016**, *121*, 9696–9716. [CrossRef]
142. Sledd, A.; L'Ecuyer, T. How Much Do Clouds Mask the Impacts of Arctic Sea Ice and Snow Cover Variations? Different Perspectives from Observations and Reanalyses. *Atmosphere* **2019**, *10*, 12. [CrossRef]
143. Zhang, R.; Wang, H.; Fu, Q.; Rasch, P.J.; Wang, X. Unraveling Driving Forces Explaining Significant Reduction in Satellite-Inferred Arctic Surface Albedo since the 1980s. *Proc. Natl. Acad. Sci. USA* **2019**, *116*, 23947–23953. [CrossRef]
144. Walsh, J.E.; Ballinger, T.J.; Euskirchen, E.S.; Hanna, E.; Mård, J.; Overland, J.E.; Tangen, H.; Vihma, T. Extreme Weather and Climate Events in Northern Areas: A Review. *Earth-Sci. Rev.* **2020**, *209*, 103324. [CrossRef]
145. Dobricic, S.; Russo, S.; Pozzoli, L.; Wilson, J.; Vignati, E. Increasing Occurrence of Heat Waves in the Terrestrial Arctic. *Environ. Res. Lett.* **2020**, *15*, 024022. [CrossRef]
146. Vincent, W.F. Arctic Climate Change: Local Impacts, Global Consequences, and Policy Implications. In *The Palgrave Handbook of Arctic Policy and Politics*; Springer International Publishing: Cham, Switzerland, 2020; pp. 507–526.
147. Smith, D.M.; Eade, R.; Andrews, M.B.; Ayres, H.; Clark, A.; Chripko, S.; Deser, C.; Dunstone, N.J.; García-Serrano, J.; Gastineau, G.; et al. Robust but Weak Winter Atmospheric Circulation Response to Future Arctic Sea Ice Loss. *Nat. Commun.* **2022**, *13*, 727. [CrossRef]
148. Cohen, J.; Zhang, X.; Francis, J.; Jung, T.; Kwok, R.; Overland, J.; Ballinger, T.J.; Bhatt, U.S.; Chen, H.W.; Coumou, D.; et al. Divergent Consensuses on Arctic Amplification Influence on Midlatitude Severe Winter Weather. *Nat. Clim. Chang.* **2020**, *10*, 20–29. [CrossRef]
149. Alkama, R.; Koffi, E.N.; Vavrus, S.J.; Diehl, T.; Francis, J.A.; Stroeve, J.; Forzieri, G.; Vihma, T.; Cescatti, A. Wind Amplifies the Polar Sea Ice Retreat. *Environ. Res. Lett.* **2020**, *15*, 124022. [CrossRef]
150. Blackport, R.; Screen, J.A. Insignificant Effect of Arctic Amplification on the Amplitude of Midlatitude Atmospheric Waves. *Sci. Adv.* **2020**, *6*, eaay2880. [CrossRef] [PubMed]
151. Tian, F.; Fensholt, R.; Verbesselt, J.; Grogan, K.; Horion, S.; Wang, Y. Evaluating Temporal Consistency of Long-Term Global NDVI Datasets for Trend Analysis. *Remote Sens. Environ.* **2015**, *163*, 326–340. [CrossRef]
152. Metcalfe, D.B.; Hermans, T.D.G.; Ahlstrand, J.; Becker, M.; Berggren, M.; Björk, R.G.; Björkman, M.P.; Blok, D.; Chaudhary, N.; Chisholm, C.; et al. Patchy Field Sampling Biases Understanding of Climate Change Impacts across the Arctic. *Nat. Ecol. Evol.* **2018**, *2*, 1443–1448. [CrossRef]
153. Forkel, M.; Carvalhais, N.; Verbesselt, J.; Mahecha, M.; Neigh, C.; Reichstein, M. Trend Change Detection in NDVI Time Series: Effects of Inter-Annual Variability and Methodology. *Remote Sens.* **2013**, *5*, 2113–2144. [CrossRef]
154. Dash, J.; Ogutu, B.O. Recent Advances in Space-Borne Optical Remote Sensing Systems for Monitoring Global Terrestrial Ecosystems. *Prog. Phys. Geogr. Earth Environ.* **2016**, *40*, 322–351. [CrossRef]
155. Bartsch, A.; Widhalm, B.; Leibman, M.; Ermokhina, K.; Kumpula, T.; Skarin, A.; Wilcox, E.J.; Jones, B.M.; Frost, G.V.; Höfler, A.; et al. Feasibility of Tundra Vegetation Height Retrieval from Sentinel-1 and Sentinel-2 Data. *Remote Sens. Environ.* **2020**, *237*, 111515. [CrossRef]
156. Post, E.; Forchhammer, M.C.; Bret-Harte, M.S.; Callaghan, T.V.; Christensen, T.R.; Elberling, B.; Fox, A.D.; Gilg, O.; Hik, D.S.; Hoye, T.T.; et al. Ecological Dynamics Across the Arctic Associated with Recent Climate Change. *Science* **2009**, *325*, 1355–1358. [CrossRef]
157. Frey, K.E.; Comiso, J.C.; Cooper, L.W.; Grebmeier, J.M.; Stock, L.V. Arctic Ocean Primary Productivity: The Response of Marine Algae to Climate Warming and Sea Ice Decline. *Arct. Rep. Card* **2020**. [CrossRef]
158. Bohlmann, U.M.; Koller, V.F. ESA and the Arctic—The European Space Agency's Contributions to a Sustainable Arctic. *Acta Astronaut.* **2020**, *176*, 33–39. [CrossRef]
159. Biskaborn, B.K.; Smith, S.L.; Noetzli, J.; Matthes, H.; Vieira, G.; Streletskiy, D.A.; Schoeneich, P.; Romanovsky, V.E.; Lewkowicz, A.G.; Abramov, A.; et al. Permafrost Is Warming at a Global Scale. *Nat. Commun.* **2019**, *10*, 264. [CrossRef]
160. Jorgenson, M.T.; Grosse, G. Remote Sensing of Landscape Change in Permafrost Regions. *Permafr. Periglac. Process.* **2016**, *27*, 324–338. [CrossRef]
161. Stow, D.A.; Hope, A.; McGuire, D.; Verbyla, D.; Gamon, J.; Huemmrich, F.; Houston, S.; Racine, C.; Sturm, M.; Tape, K.; et al. Remote Sensing of Vegetation and Land-Cover Change in Arctic Tundra Ecosystems. *Remote Sens. Environ.* **2004**, *89*, 281–308. [CrossRef]
162. Smith, L.C.; Sheng, Y.; MacDonald, G.M.; Hinzman, L.D. Disappearing Arctic Lakes. *Science* **2005**, *308*, 1429. [CrossRef] [PubMed]

163. Riseborough, D.; Shiklomanov, N.; Etzelmuller, B.; Gruber, S.; Marchenko, S. Recent Advances in Permafrost Modelling. *Permafr. Periglac. Process.* **2008**, *19*, 137–156. [CrossRef]
164. Marchand, N.; Royer, A.; Krinner, G.; Roy, A.; Langlois, A.; Vargel, C. Snow-Covered Soil Temperature Retrieval in Canadian Arctic Permafrost Areas, Using a Land Surface Scheme Informed with Satellite Remote Sensing Data. *Remote Sens.* **2018**, *10*, 1703. [CrossRef]
165. Du, J.; Watts, J.D.; Jiang, L.; Lu, H.; Cheng, X.; Duguay, C.; Farina, M.; Qiu, Y.; Kim, Y.; Kimball, J.S.; et al. Remote Sensing of Environmental Changes in Cold Regions: Methods, Achievements and Challenges. *Remote Sens.* **2019**, *11*, 1952. [CrossRef]
166. Kumpula, T.; Pajunen, A.; Kaarlejärvi, E.; Forbes, B.C.; Stammler, F. Land Use and Land Cover Change in Arctic Russia: Ecological and Social Implications of Industrial Development. *Glob. Environ. Chang.* **2011**, *21*, 550–562. [CrossRef]
167. Sizov, O.S.; Tsymbarovich, P.R.; Ezhova, E.V.; Soromotin, A.V.; Prikhodko, N.V. Assessment of the Post-Pyrogenic Dynamics of Tundra Vegetation in the Northern Part of Western Siberia over the Past 50 Years (1968–2018) Based on Detailed and High Resolution Remote Sensing Data. *Sovrem. Probl. Distantsionnogo Zo. Zemli Kosmosa* **2020**, *17*, 137–153. [CrossRef]
168. Esau, I.; Miles, V.V.; Davy, R.; Miles, M.W.; Kurchatova, A. Trends in Normalized Difference Vegetation Index (NDVI) Associated with Urban Development in Northern West Siberia. *Atmos. Chem. Phys.* **2016**, *16*, 9563–9577. [CrossRef]
169. Vaguet, Y.; Ourng, C.; Moriconi-Ebrard, F. Is the Arctic Really a Frontier? Settlement Dynamics within Various Arctic Limits Based on the Arcticapolis Geohistorical Database. *Espac. Popul. Sociétés* **2021**, 1. [CrossRef]
170. Yu, Q.; Epstein, H.E.; Engstrom, R.; Shiklomanov, N.; Strelestskiy, D. Land Cover and Land Use Changes in the Oil and Gas Regions of Northwestern Siberia under Changing Climatic Conditions. *Environ. Res. Lett.* **2015**, *10*, 124020. [CrossRef]
171. Melnikov, V.P.; Osipov, V.I.; Brouchkov, A.V.; Falaleeva, A.A.; Badina, S.V.; Zheleznyak, M.N.; Sadurtdinov, M.R.; Ostrakov, N.A.; Drozdov, D.S.; Osokin, A.B.; et al. Climate Warming and Permafrost Thaw in the Russian Arctic: Potential Economic Impacts on Public Infrastructure by 2050. *Nat. Hazards* **2022**, *112*, 231–251. [CrossRef]
172. Ramage, J.; Jungsberg, L.; Wang, S.; Westermann, S.; Lantuit, H.; Heleniak, T. Population Living on Permafrost in the Arctic. *Popul. Environ.* **2021**, *43*, 22–38. [CrossRef]
173. Nyland, K.E.; Gunn, G.E.; Shiklomanov, N.I.; Engstrom, R.N.; Streletskiy, D.A. Land Cover Change in the Lower Yenisei River Using Dense Stacking of Landsat Imagery in Google Earth Engine. *Remote Sens.* **2018**, *10*, 1226. [CrossRef]
174. Miller, G.H.; Alley, R.B.; Brigham-Grette, J.; Fitzpatrick, J.J.; Polyak, L.; Serreze, M.C.; White, J.W.C. Arctic Amplification: Can the Past Constrain the Future? *Quat. Sci. Rev.* **2010**, *29*, 1779–1790. [CrossRef]
175. Andrews, T.; Gregory, J.M.; Webb, M.J. The Dependence of Radiative Forcing and Feedback on Evolving Patterns of Surface Temperature Change in Climate Models. *J. Clim.* **2015**, *28*, 1630–1648. [CrossRef]
176. Alexeev, V.A.; Langen, P.L.; Bates, J.R. Polar Amplification of Surface Warming on an Aquaplanet in "Ghost Forcing" Experiments without Sea Ice Feedbacks. *Clim. Dyn.* **2005**, *24*, 655–666. [CrossRef]
177. Haine, T.W.N.; Martin, T. The Arctic-Subarctic Sea Ice System Is Entering a Seasonal Regime: Implications for Future Arctic Amplification. *Sci. Rep.* **2017**, *7*, 4618. [CrossRef] [PubMed]
178. Graff, L.S.; Iversen, T.; Bethke, I.; Debernard, J.B.; Seland, Ø.; Bentsen, M.; Kirkevåg, A.; Li, C.; Olivié, D.J.L. Arctic Amplification under Global Warming of 1.5 and 2 °C in NorESM1-Happi. *Earth Syst. Dyn.* **2019**, *10*, 569–598. [CrossRef]
179. Virapongse, A.; Pearlman, F.; Pearlman, J.; Murambadoro, M.D.; Kuwayama, Y.; Glasscoe, M.T. Ten Rules to Increase the Societal Value of Earth Observations. *Earth Sci. Inform.* **2020**, *13*, 233–247. [CrossRef]
180. Plummer, S.; Lecomte, P.; Doherty, M. The ESA Climate Change Initiative (CCI): A European Contribution to the Generation of the Global Climate Observing System. *Remote Sens. Environ.* **2017**, *203*, 2–8. [CrossRef]

JGR Oceans

RESEARCH ARTICLE
10.1029/2022JC018654

Special Section:
The Arctic: An AGU Joint Special Collection

Wind-Wave Attenuation in Arctic Sea Ice: A Discussion of Remote Sensing Capabilities

Fabrice Collard[1], Louis Marié[2], Frédéric Nouguier[2], Marcel Kleinherenbrink[3], Frithjof Ehlers[3], and Fabrice Ardhuin[2]

[1]OceanDataLab, Locmaria-Plouzané, France, [2]Univ. Brest, CNRS, Ifremer, IRD, Laboratoire d'Océanographie Physique et Spatiale, Brest, France, [3]TU Delft, Delft, The Netherlands

Key Points:

- Wave patterns in sea ice can be found in radar and optical remote sensing data
- We provide a quantitative estimation of wave height, wavelength and direction from ICESat-2 and Sentinel-2 data
- Wavelengths and directions in full-focus SAR altimetry and CFOSAT SWIM are consistent with other sensors

Correspondence to:
F. Ardhuin,
ardhuin@ifremer.fr

Citation:
Collard, F., Marié, L., Nouguier, F., Kleinherenbrink, M., Ehlers, F., & Ardhuin, F. (2022). Wind-wave attenuation in Arctic sea ice: A discussion of remote sensing capabilities. *Journal of Geophysical Research: Oceans*, *127*, e2022JC018654. https://doi.org/10.1029/2022JC018654

Received 20 MAR 2022
Accepted 6 JUN 2022

Abstract Wind-generated waves strongly interact with sea ice and impact air-sea exchanges, operations at sea, and marine life. Unfortunately, the dissipation of wave energy is not well quantified and its possible effect on upper ocean mixing and ice drift is still mysterious. As the Arctic is opening up and wave energy increases, the limited amount of *in situ* observations is a clear limitation to our scientific understanding. Both radar and optical remote sensing has revealed the frequent presence of waves in ice, and could be used more systematically to investigate wave-ice interactions. Here we show that, in cloud-free conditions, Sentinel-2 images exhibit brightness modulations in ice-covered water, consistent with the presence of waves measured a few hours later by the ICESat-2 laser altimeter. We show that a full-focus SAR processing of Sentinel-3 radar altimeter data also reveals the presence and wavelengths of waves in sea ice, within minutes of Sentinel-2 imagery. The SWIM instrument on CFOSAT is another source of quantitative evidence for the direction and wavelengths of waves in ice, when ice conditions are spatially homogeneous. In the presence of sea ice, a quantitative wave height measurement method is not yet available for all-weather near-nadir radar instruments such as altimeters and SWIM. However, their systematic colocation with optical instruments on Sentinel-2 and ICESat-2, which are less frequently able to observe waves in sea ice, may provide the empirical transfer functions needed to interpret and calibrate the radar data, greatly expanding the available data on wave-ice interactions.

Plain Language Summary Waves generated by winds over the ocean propagate in ice-covered regions where they can be strongly attenuated and can contribute to breaking up the ice and pushing the ice around. Wavy patterns are clearly visible in remote sensing data collected by different instruments including the ICESat-2 laser altimeter, Sentinel-1 imaging radar, the Sentinel-2 optical imager, Sentinel-3 radar altimeter, and CFOSAT wave-measuring instrument SWIM. Here, we show examples of such patterns and propose a quantitative interpretation of ICESat-2 and Sentinel-2 that is consistent with waves generated by storms in the Barents Sea that are observed to travel under the ice over hundreds of kilometers. For Sentinel-3 and SWIM, a quantification of wave heights will have to be validated, possibly based on data from the other two instruments. This may strongly expand the quantity of available information for scientific investigations and operational applications.

1. Introduction

The evolving ice cover in the Arctic is becoming more exposed to wind-generated waves that now develop over larger open water regions and grow to larger heights and wavelengths (Stopa et al., 2016; Thomson & Rogers, 2014). When these waves reach the ice edge, they are strongly attenuated by sea ice but the components of the sea state with the longest periods may still break up the ice far from the ice edge, over hundreds of kilometers (Collins et al., 2015). Wave attenuation contributes to ice drift (Thomson, Lund, et al., 2021), under-ice mixing, ice formation (Sutherland & Dumont, 2018), or melting (Horvat & Tziperman, 2017). Whereas numerical wave models have made considerable progress in ice-free waters, the forecasting of wave conditions in ice-covered regions is limited by a poor knowledge of wave attenuation. The investigation of wave-ice interactions has been the topic of a growing number of field experiments (Squire, 2020; Wadhams et al., 1986). Many of these experiments have focused near the ice edge where access from ships is possible (Doble et al., 2011; Thomson et al., 2018) and where the attenuation is strongest. However, the spatial heterogeneity of the ice field and the generally low values of wave heights makes the measurement analysis difficult and prone to contamination by noise (Thomson, Hoseková, et al., 2021). Still, *in situ* experiments have been critical in identifying ice type as an

important factor in wave attenuation (Rogers et al., 2016), and ruling out wave scattering as the dominant mechanism of wave attenuation (Ardhuin et al., 2016). Remote sensing from airplanes or satellites can provide unique measurements of waves, far into the ice field, giving maps of surface elevation (Sutherland & Gascard, 2016) or vertical orbital velocities (Ardhuin et al., 2015) that provide a quantitative estimate of local wave heights, wavelengths, and directions.

Using the most extensive waves-in-ice data set to date, provided by the Sentinel-1 wave mode, a wide range of attenuation rates was found for waves entering sea ice from the ice-free ocean (Stopa, Sutherland, & Ardhuin, 2018). These different attenuations are probably caused by different ice properties, in particular ice thickness and floe sizes. Ardhuin et al. (2020) confirmed the importance of floe size, with a much stronger attenuation for floe sizes much larger than the wind-wave wavelength. These analyses have been performed in the Southern Ocean where 5 m resolution Synthetic Aperture Radar (SAR) imagery is routinely collected with the Wave Mode of Sentinel-1 (Hasselmann et al., 2012).

The main limitation of these high-quality wave-mode SAR images is their sparse acquisition: one can only guess what kind of waves and ice are present between two images that are 20 km by 20 km across but separated by 100 km. The coarser 10 m resolution Interferometric Wide swath mode (IW) is more seldom used over sea ice but provides continuous images that allow following waves 500 km or more into the sea ice (Stopa, Ardhuin, et al., 2018). Even coarser images, with an azimuth resolution of 43 m, are most often acquired by Sentinel-1 over the Arctic, using the Extended Wide Swath mode (EW), which is prioritized to get the widest coverage of sea ice. Because only waves with wavelengths larger than about 4 SAR pixels can be resolved, the EW mode can detect only swells with relatively large wavelengths. In practice SAR measurements of waves in sea ice can be very accurate with a sharp contrast for wave heights larger than 50 cm in wave-mode and IW mode Sentinel 1 data (Ardhuin et al., 2017), which is sufficient to measure the strong attenuations near the ice edges. For smaller wave heights, it can be difficult to separate the wave signature from the signatures of ice heterogeneities, in particular in the presence of leads where ice is not broken up by the wave field.

The recent analysis of ICESat-2 laser altimeter data by Horvat et al. (2020) shows that there are ice-height variations induced by ocean waves in many satellite passes, which may provide an interesting source of cross-validation of both techniques for studying waves in ice. While looking for different sources of data to help in the interpretation of ICESat-2 data we also found wave patterns in Sentinel-2 optical imagery, and Sentinel-3 Synthetic Aperture Radar Altimeter reprocessed with Full-Focus SAR (FF-SAR) as described by Kleinherenbrink et al. (2020) and Altiparmaki et al. (2022). These different remote sensing techniques are influenced by waves in different ways, be it the change in surface elevation, slope, or line-of-sight velocity, as summarized in Figure 1.

The goal of the present paper is to discuss the complementarity of data from SAR, ICESat-2, and other satellite instruments for the detection and measurement of wave properties in sea ice, in particular across the ice edge where waves-ice interactions are expected to be strongest. We have thus looked at two cases, one on 23 March 2019 to the East of Spitzbergen, taken from Horvat et al. (2020) for which Sentinel-1 and Sentinel-2 data are also available. The second case is in the same region, on 12 March 2021, and is also covered by Sentinel-3 and th Chn-a-Franc Ocan SatllCFOSAT. Discussions and conclusions follow in Section 4.

2. Case of 23 March 2019

As illustrated in Figure 2, a storm swept through the Barents Sea, from the West, on March 22, with a band of high winds exceeding 20 m/s from Spitzbergen to Norway, dying out after 19:00 UTC according to the ECMWF operational analyses and forecasts that we also use in our wave model. These high winds generated swells with wave heights exceeding 6 m that persisted until March 23 at 14:00 UTC.

Wave properties were estimated using a configuration of the WAVEWATCH III model (The WAVEWATCH III® Development Group, 2019) that uses a 12 km resolution polar stereographic grid. Forcing uses winds from ECMWF operational forecasts and analyses, and sea ice concentration from the Ifremer product derived from the SSM/I satellite radiometer. For the ice thickness we have used a simple constant thickness h_i with $0.25 \leq h_i \leq 1.0$ m to give a plausible range of wave attenuation that is broadly consistent with thin ice estimations from remote sensing data (Kaleschke et al., 2012). The parameterizations of wave-ice interactions and ice break-up are adapted from Boutin et al. (2018) with the parameter settings adjusted by Ardhuin et al. (2020).

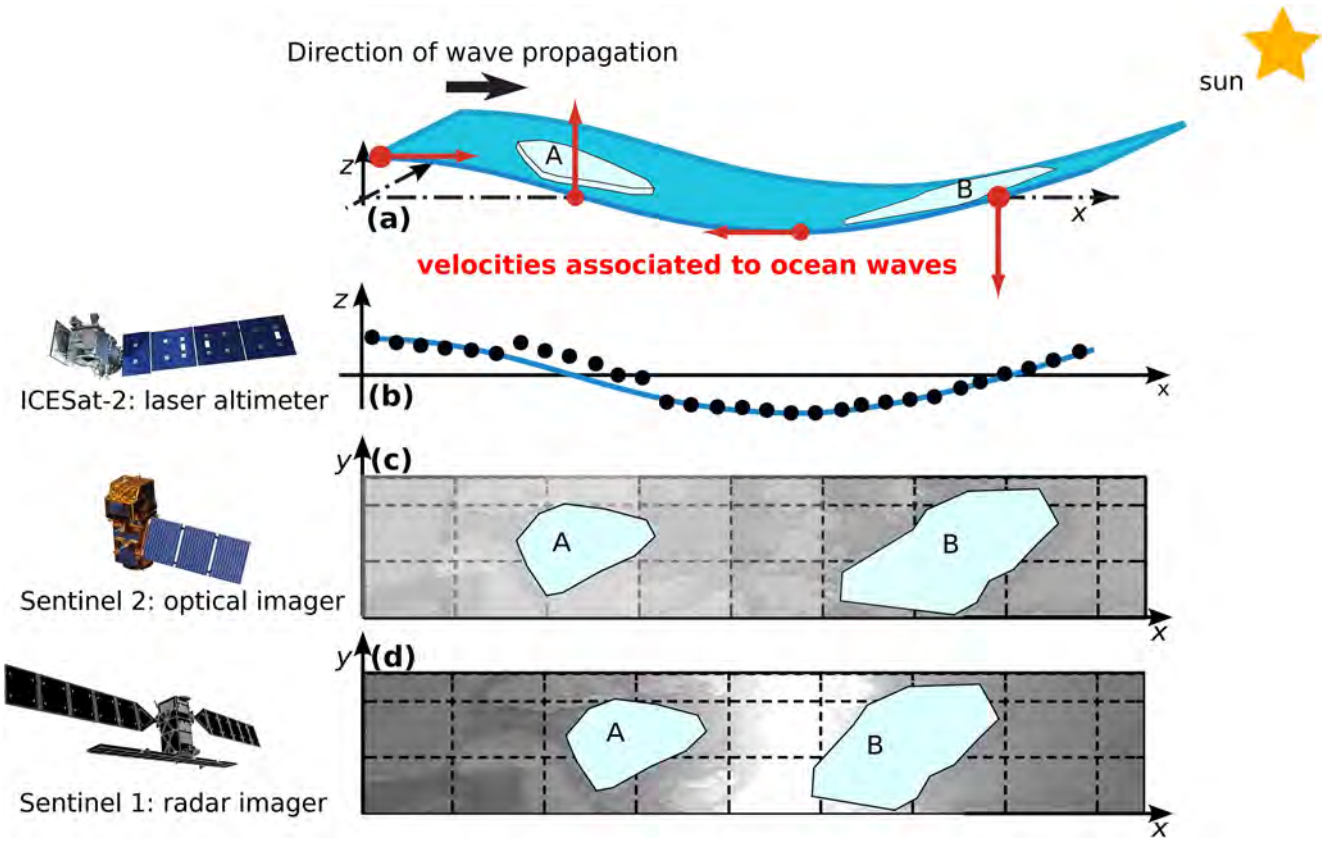

Figure 1. How different remote sensing techniques detect or measure waves in the presence of sea ice? (b) We expect that waves introduce vertical displacement, which change the range-measurements of ICESat-2 laser altimeter, which includes the water level and ice freeboard (Sutherland & Gascard, 2016), (c) introduce a surface brightness variation, possibly due to the sloping surface as discussed in Section 2.2, and picked up by optical imagers if the sun is low enough over the horizon, and (d) the vertical velocities of the ice produce a constructive velocity bunching effect in SAR imagery (Ardhuin et al., 2017; Lyzenga et al., 1985).

2.1. Quantitative Information on Waves in Ice From ICESat-2

Horvat et al. (2020) reported the detection of waves in sea ice on 23 March 2019, along the track of ICESat-2 shown in Figure 3. ICESat-2 beams have a 13 m diameter footprint and are thus capable of sampling relatively short waves. Here, we use the same data set, namely Level-3a ATL07 ice elevation (Kwok et al., 2021), with a pass near 4:00 UTC. Due to cloud cover, ice elevation is not available all the way to the ice edge but starts around 77.6°N. It is often the case that on-ice winds tend to blow the cloud cover from the relatively warm open water over the ice.

Beyond the presence of waves in sea ice that gives characteristic ice elevation profiles, with examples shown in Figure 3e–3g, it would be interesting to quantify wave heights, periods, and directions. ICESat-2 ice elevation data are provided for 6 beams arranged in 3 pairs, with a 90 m separation within each pair and a separation of the different pairs by about 3.3 km. As a result, the ice elevation samples only very few waves, in particular when the angle between the satellite track and wave propagation direction gets close to 90°. As a result there is a large uncertainty on the wave height, which may be estimated as 4 times the standard deviation of ice elevation. Here we find 1.5, 1.1, and 0.4 m for the 3 segments shown in Figure 3. The evolution of wave height along the ICESat-2 track is compared in Figure 4 to the two model simulations with ice thicknesses of 0.25 and 1 m.

Besides wave heights, the clear coherence within pairs of beams makes it possible to estimate mean wave direction (Yu et al., 2021). Because the sea ice prevents the formation of a local wind-sea and strongly dissipates swells propagating over longer distances, the wave spectrum is generally narrow in directions (Ardhuin et al., 2016). Assuming that the directional wave spectrum is narrow, for any band of latitude of the order of 0.1° (about 12 km along-track), we estimated the latitudinal shift dy that maximizes the correlation between the ice elevations measured by two beams in a pair. As we know the track separation in longitude dx, the ratio $-dy/dx$ is the tangent of the

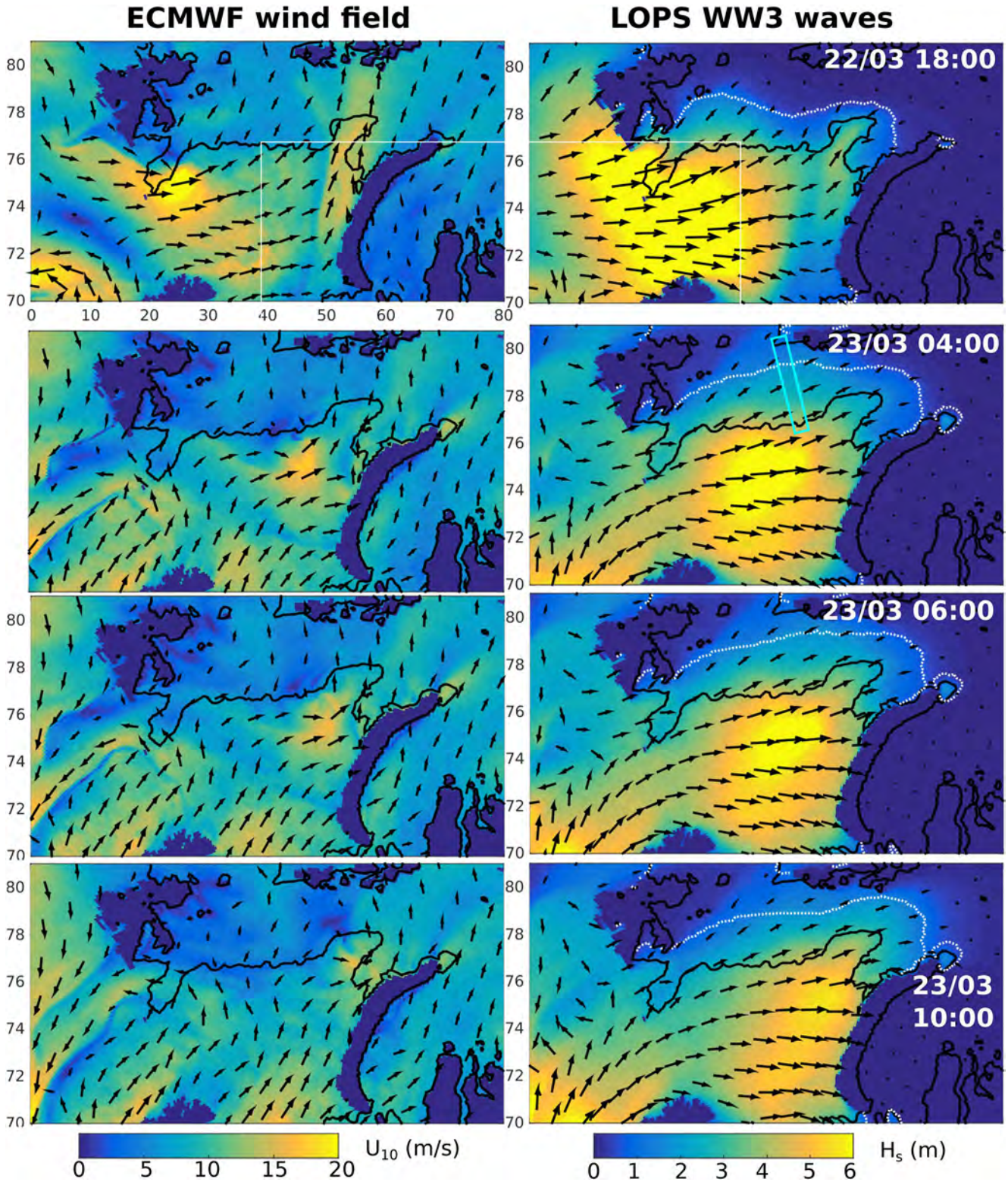

Figure 2. Wind and wave conditions from 18:00 UTC on 22 March 2019 (top panels) to 10:00 UTC on 23 March (bottom panels). In each panel the black line marks the location of the ice edge. Wind speed and directions are given by ECMWF IFS Operational analyses and forecasts, and waves are given by our wave model, here using an ice thickness $h_i = 0.25$ m. The wave model also predicts ice break-up, with the 200 m contour of floe diameter shown with the dotted white line. The cyan rectangle on the second line is the transect in which model data was compared to ICESat-2 data.

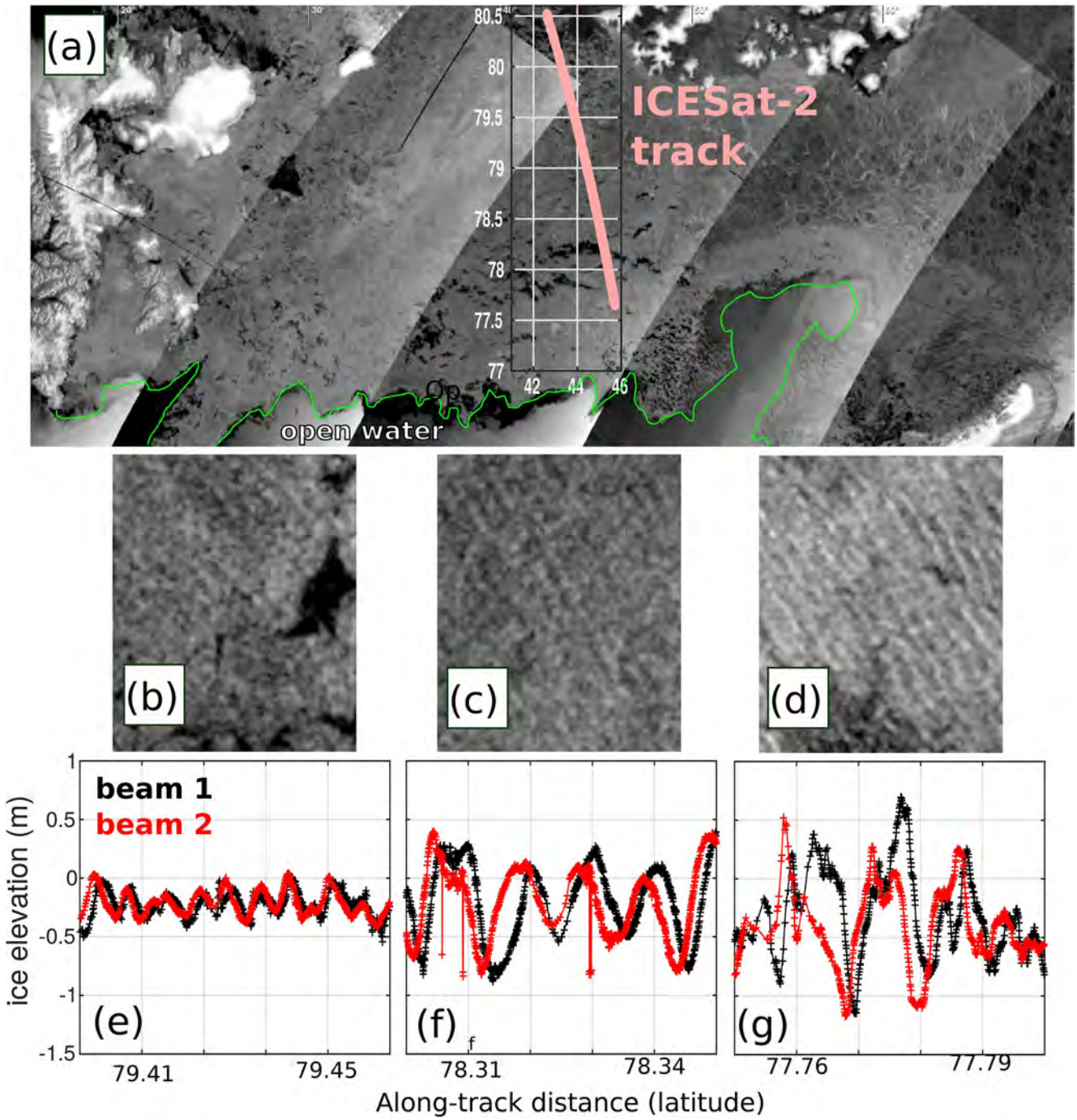

Figure 3. Wave signatures in Sentinel-1 and ICESat-2 on 23 March 2019. (a) The portion of ICESat-2 track where wave signals are detected in the Level3a ATL07 ice elevation product is show in pink, overlaid on the mosaic of Sentinel-1 Extended Wide Swath mode (EW) intensity. Svalbard is to the left and Novaya Zemlya to the bottom right. The ice edge is the green line. (b–d) are pieces of the Sentinel one images, each extending 0.05° in latitude, along the ICESat-2 tracks, with surface elevations shown in the bottom panels (e–g). Ice elevations are only shown for the first pair of ICESat-2 beams.

iso-phase patterns in the elevation data, which we take to be aligned with the wave crests. These mean directions are shown in Figure 4, where the squared correlation coefficients are above 0.8. The general trend is that wave directions veer from a west-south-westerly directions of 240–250 near the ice edge, to a more southerly direction around 225° as they approach 80°N. This is consistent with the general result that the mean wave direction tends to turn toward the direction that gives the shortest distance to the ice edge, because wave attenuation is lower

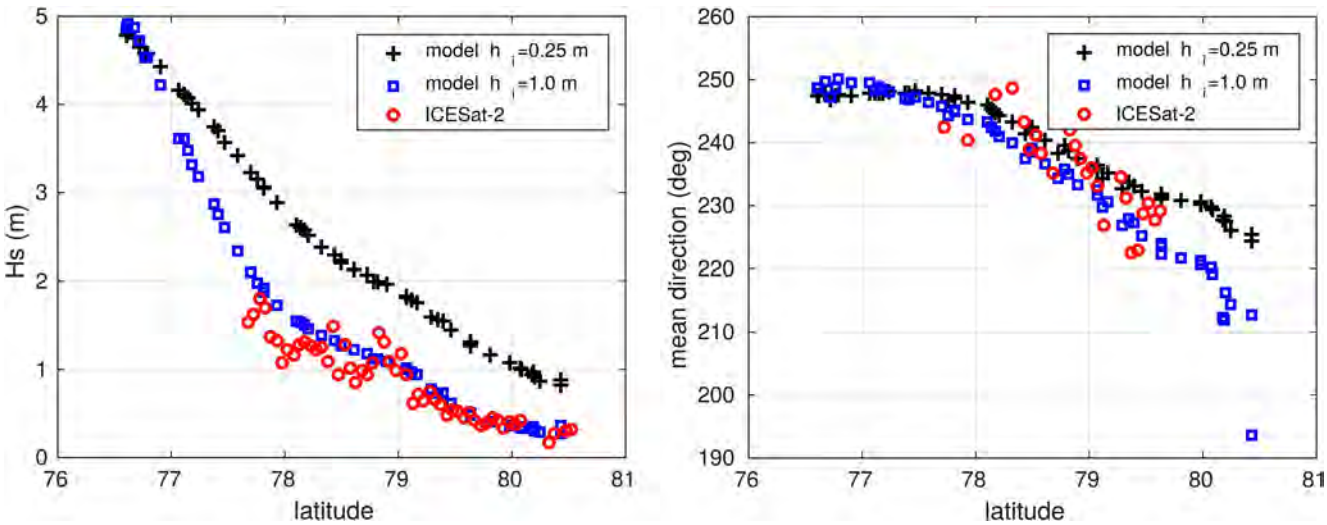

Figure 4. Wave heights and mean wave directions (from, nautical convention) along the ICESat-2 track at 4:00 UTC on 23 March 2019, according to two different model simulations or taken as the average of the 6 wave heights estimated for each of the six ICESat-2 laser beams.

for shorter propagation distances across the ice. This is also why the model with the stronger dissipation has a different mean direction as waves get farther into the ice.

Once the direction is known, we may convert the apparent along-track wavenumber k_a that is the projection of the actual wavenumbers on the satellite track, into the actual wavenumber k,

$$k = k_a / \cos(\theta_w - \theta_t). \quad (1)$$

Using these wavenumbers k, the main difficulty in defining a mean wavelength, that can be compared to the modeled mean period, is that the ice elevation contains also large-scale variations in freeboard between ice and water. These freeboard variations contribute to the ice height at long wavelengths. In our case, this effect gives a positive bias for the mean wavelength for latitudes under 78° (not shown). Further in the ice, the elevation spectrum appears to have lower variance at low frequencies and gives a mean wavelength around 310 m that is consistent with the modeled mean period of 15 s, using the Airy wave dispersion relation that is applicable for these long waves and thin ice conditions. Alternatively, one may use a peak wavelength to avoid contamination by large-scale freeboard variations.

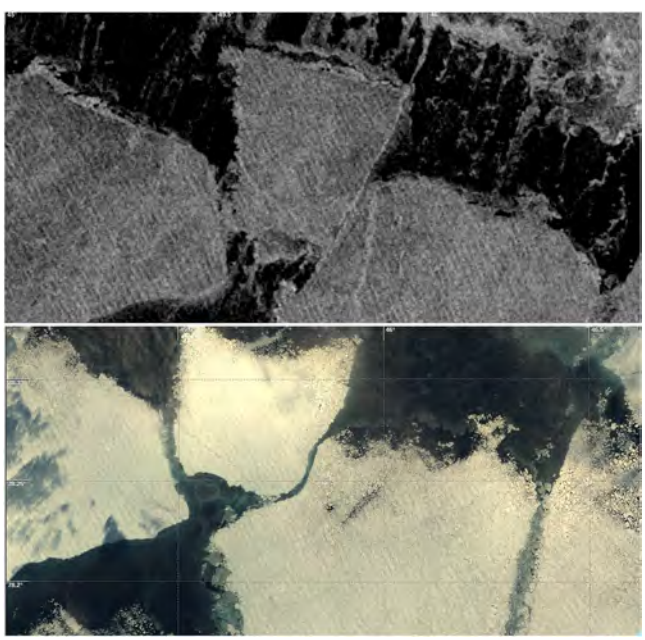

Figure 5. Same ice floes observed by Sentinel 1 at 9:00 UTC and Sentinel 2 at 11:07 UTC on 23 March 2019, around 78.15°N, 46.00°E. The Sentinel two image is a true color composite using bands B02, B03, and B04.

For this same event, additional information is provided by Sentinel 2 with an image acquired at 11:07 UTC on the same day. The same ice floes and leads are clearly identifiable in both Sentinel-1 and Sentinel-2 imagery, as shown in Figure 5. The 10 m resolution of S2 imagery allows to see that what could look like a solid 8-km long floe is actually shattered in many floes with sizes under 50 m. These small floes have not yet moved much with respect to one another. Stripes in the image brightness clearly correspond to waves with a direction and wavelength that is very similar to what was found in the S1 image and in the ICESat-2 data.

2.2. Interpreting Wave Patterns in Sentinel-2 Two Imagery

The image intensity in optical imagery is generally a function of the sun and sensor orientation and the surface bidirectional reflectance distribution function. For the scene shown in Figure 5, the sun zenithal angle is $\theta_{\text{Sun}} = 79.4°$ (i.e., 10.6° above the horizon), with a sun azimuth of 215°, and the instrument zenith angle is around $\theta_d = 10.0°$. For observation zenith angles smaller

than 30°, snow on sea ice can be considered a Lambertian scatterer (Dirmhirn & Eaton, 1975). In this limit, the specific intensity leaving a horizontal snow-covered sea ice surface toward the detector, in azimuth ϕ_d and zenith angle θ_d, in W m^{-2} sr^{-1}, is given by

$$I(\theta_d, \phi_d) = \frac{1}{\pi} I_{\text{Sun}} \rho \cos(\theta_{\text{Sun}}),$$

where I_{Sun} is the Sun irradiance, in W m^{-2}, ρ is the (dimensionless) surface reflectance, and θ_{Sun} is the sun zenith angle. The effects of detector characteristics, Sun irradiance, and nominal Sun zenith angle are taken into account by the L1c processor, to yield the Top-Of-Atmosphere estimate of the reflectance ρ_{L1c}.

These corrections do not take into account the sloping of the ice surface as it is tilted by underlying waves. As a result, the sun zenith angle should be replaced by angle θ_l between the vector locally normal to the ice or snow surface and the vector pointing from the surface to the Sun, giving rise to modulations of the L1c TOA reflectance as

$$\rho_{\text{L1c}} = \rho_{\text{true}} \frac{\cos(\theta_l)}{\cos(\theta_{\text{Sun}})}.$$

We can use small slope approximations for the unit vector normal to the ice/snow surface $(-\partial\zeta/\partial x, -\partial\zeta/\partial y, 1)$ and take the dot product with the unit vector pointing to the sun $(\cos\phi_{\text{Sun}}\sin\theta_{\text{Sun}}, \sin\phi_{\text{Sun}}\sin\theta_{\text{Sun}}, \cos\theta_{\text{Sun}})$.

From the definition of θ_l we have

$$\cos\theta_l = \cos\theta_{\text{Sun}} - \sin\theta_{\text{Sun}} (\cos\phi_{\text{Sun}}\partial\zeta/\partial x + \sin\phi_{\text{Sun}}\partial\zeta/\partial y) \quad (2)$$

which oscillates around the value $\cos\theta_{\text{Sun}}$. As a result, the TOA reflectance given in the image oscillates around the value ρ_{true}. In general the variance of the normalized oscillations $<\cos^2\theta_l>/\cos^2\theta_{\text{Sun}} - 1$ can be decomposed into a modulation spectrum $E_m(k_x, k_y)$. This modulation spectrum is related to the surface elevation power spectral density $E(k_x, k_y)$, usually called "wave spectrum,"

$$E_m(k_x, k_y) = M^2 E(k_x, k_y) + N(k_x, k_y) \quad (3)$$

where $N(k_x, k_y)$ is a non-wave contribution to the image and the modulation transfer function M is given by

$$M = k \tan\theta_{\text{Sun}} \cos(\phi_{\text{Sun}} - \phi_w) \quad (4)$$

where ϕ_w is the wave propagation azimuth and the wavenumber vector is $(k_x = k\cos\phi_w, k_y = k\sin\phi_w)$. If there are no waves propagating in the azimuth perpendicular to that of the Sun, we may invert this relationship to estimate the wave spectrum $E(k_x, k_y)$, and from it the significant wave height,

$$H_s = 4\sqrt{\iint E(k_x, k_y)\, k\mathrm{d}k\mathrm{d}\phi_w}$$

In practice, the main difficulty is to separate the wave-induced changes in apparent reflectivity from heterogeneities in the image caused by water-ice contrasts at the edges of ice floes, variations in ice roughness, or different ice thicknesses.

In the example shown in Figure 6, we have chosen a 4 km by 4 km region of relatively uniform brightness (without large leads, clouds, or changes in ice reflectance). Filtering scales smaller than 100 m makes it easier to separate the swell spectral peak (dashed box) from other features. Assuming that the filtering did not significantly reduce the variance of our wave signal, we integrate the wave spectrum over the dashed box region. For this range of wave numbers the root mean square variation in $\rho_{\text{L1c}}/\rho_{\text{true}}$ is 0.009. Using the transfer function and integrating the surface elevation variance gives a significant wave height of 0.35 m (0.40 m when the image is filtered at 50 m), that is of the order of the values expected at 11 UTC at the location of Figure 5, with a strong reduction compared to the 4 UTC values, due to the general propagation of the swells toward the East. The wave field can be followed at least 200 km into the ice with an estimated significant wave height decreasing to 0.2 m (Figure 7).

Given the 1 s time difference between the acquisition of the B02 and B04 bands (Kudryavtsev et al., 2017), we can use the wave phase difference between the two bands to remove the 180° ambiguity on wave propagation,

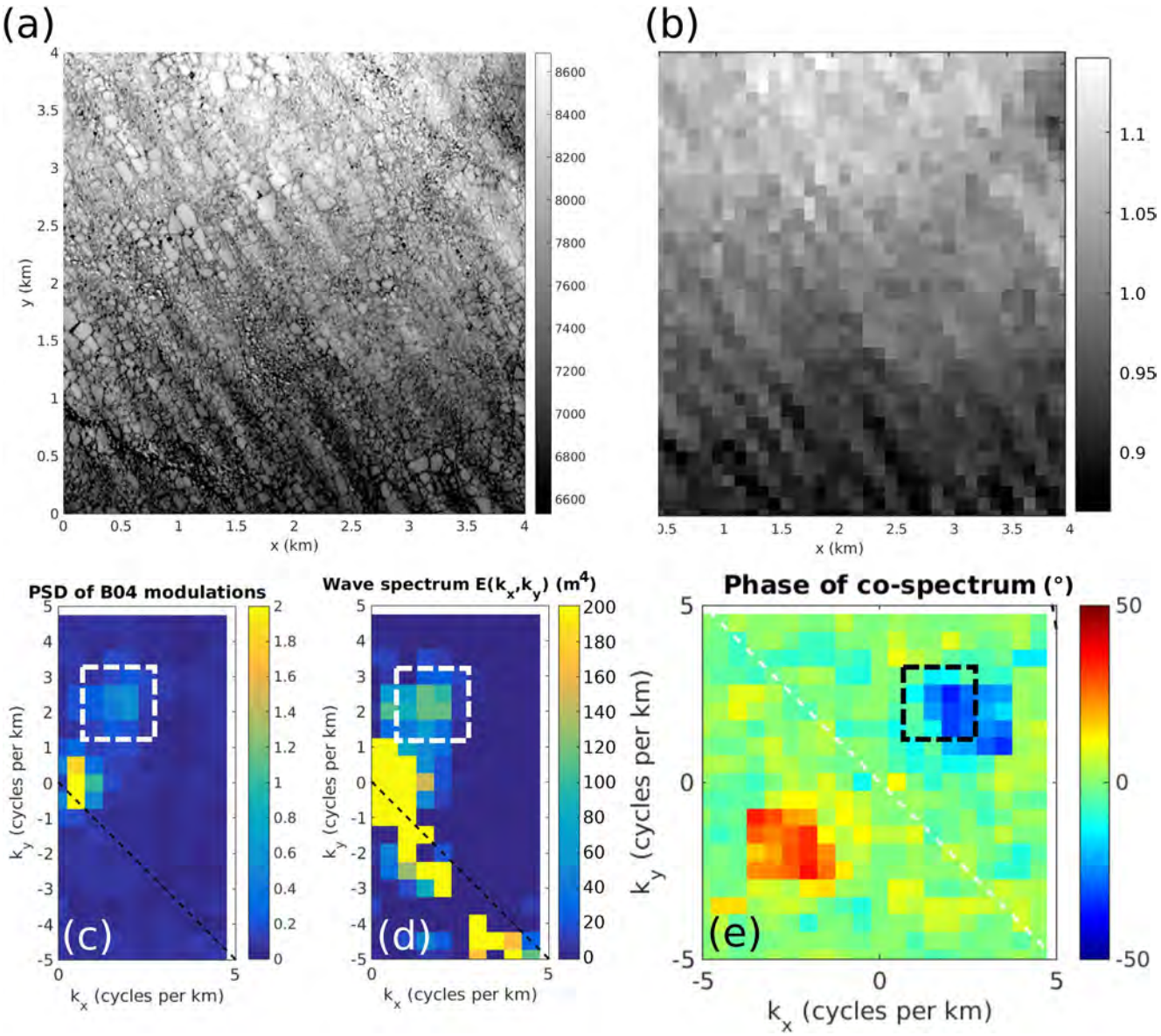

Figure 6. Processing of S2 B04 and B02 bands to obtain a wave spectrum. (a) Original image (b) subsampled image, normalized by the median image value (c) double-sided Power Spectral Density E_m of image modulation (d) single-sided Wave spectrum (e) phase of the co-spectrum of B04 and B02 images. The dashed box in panels (c–e) corresponds to the "wave partition" region of the spectral space where we expect wave signatures, and is the only place where the wave spectrum is expected to be correct. The non-wave contributions to the image $N(k_x, k_y)$ were estimated to be a constant equal to the median value of the modulation spectrum. The dashed line that goes through the origin is the blind azimuth, perpendicular to the sun azimuth for which waves produce no pattern in the image.

unless there are waves with similar energy levels propagating in opposite directions (Ardhuin et al., 2021). Further use of the wave phase to estimate surface currents is limited by the image sub-pixel co-registration accuracy (Yurovskaya et al., 2019), and the necessary averaging over a large area to reduce the phase noise. That phase noise would be lower for shorter wavelengths but these are not present in the ice.

3. Case of 12 March 2021

Instead of a local storm, we now look for off-ice winds and cloud-free conditions at the ice edge, in which case the waves are remotely generated swells. Also, after March 2019, spectra from CFOSAT's SWIM instrument are available (Hauser et al., 2017), providing measurements of wave spectra over open water. Finally we will also use Sentinel 3 data, in particular with FF-SAR processing that is capable of resolving wind-generated waves. Figure 8

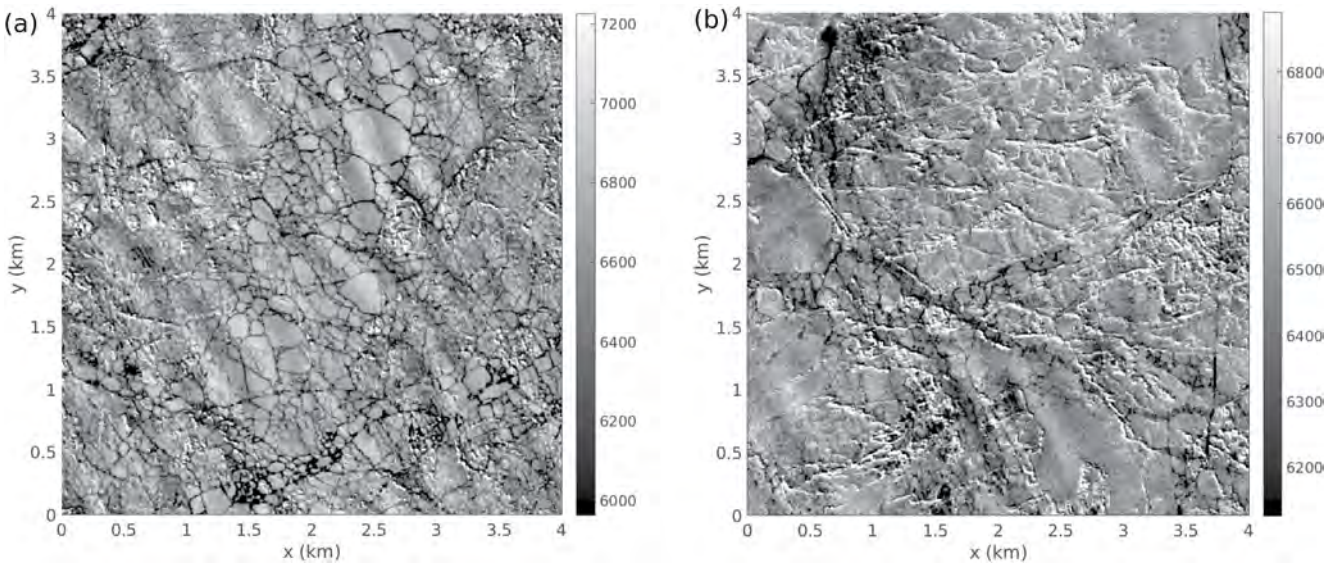

Figure 7. Other examples of wave patterns in sea ice at 11:07 UTC on 23 March 2019, (a) at 78.79°N, 50.12°E with an estimated wave height of 0.36 m (b) at 79.07°N, 50.80°E with an estimated wave height of 0.20 m.

shows a mosaic of Sentinel 2 imagery acquired around Svalbard at 11:08 UTC on 12 March 2021, and an example of colocated swell signatures in Sentinel 3 SRAL and Sentinel 2 MSI imagery.

Swells arrived in the region from a strong mid-Atlantic storm that peaked on 10 March with wave heights exceeding 14 m, and propagated to the Barents Sea through the gap between Iceland and the Faroe islands. These long swells with amplitudes around 1 m were superimposed on a local wind sea generated by a strong north-easterly wind system that expanded from the central Arctic into the Barents sea on 11 and 12 March. These winds led to a shift of the ice edge toward the south.

The ice cover East of Svalbard is characterized by a relatively straight East-West ice edge around 35°E and a bulging ice tongue around 20°E that often extends to Bear Island to the south (Figure 8a). This ice tongue was stretched to the south-west by the wind, which blew most of the clouds away and made it possible to see the ice. This ice tongue happens to be under a Sentinel 3B track that coincided within 10 min of the Sentinel two imagery. The more compact ice around 35°E was sampled later in the day by both Sentinel 3A (at 16:50) ICESat-2 at 18:14 and two CFOSAT passes at 6:50 and 14:40.

Observing waves close to the ice edge is challenging for all sensors. Optical imagery is obviously affected by clouds. The few bands of clouds and their shadows that are present over the ice tongue, around 75.5°N, 20°E, make it difficult to apply the technique presented in the previous section. Using a relatively homogenous piece of ice ($9 < x < 12$ km and $1 < y < 4$ km in Figure 8c) gives a wave height of about 0.44 m and a peak wavelength of 250 m. Heterogeneities in the optical image also include leads that are more numerous near the ice edge in the case of off-ice winds.

3.1. Wave Patterns in Sentinel-3 FF-SAR Imagery

Standard altimeter measurements, that provide significant wave heights in ice-free regions as the only sea state parameter, give a very limited picture of the complex sea state with swells and an opposing wind sea. Here, we show the first fully focused SAR (FF-SAR) processing of altimeter data in wave-impacted sea ice (Figure 8b). Level 1a data from Sentinel-3B are FF-SAR processed using the Delft Altimeter Toolbox (Kleinherenbrink et al., 2020). A Gaussian filter is applied in the along-track direction after which the waveforms are subsampled at 22 m along-track to ensure a better spectral response than standard multilooking approach. The waveforms are retracked using a threshold. Any drifts and jumps in the range are compensated for to align the leading edge of the waveforms, to ensure proper cross-track projection of the waveform bins. Then a normalization procedure is applied comparable to Altiparmaki et al. (2022) to compute the SAR contrast that is, the ratio

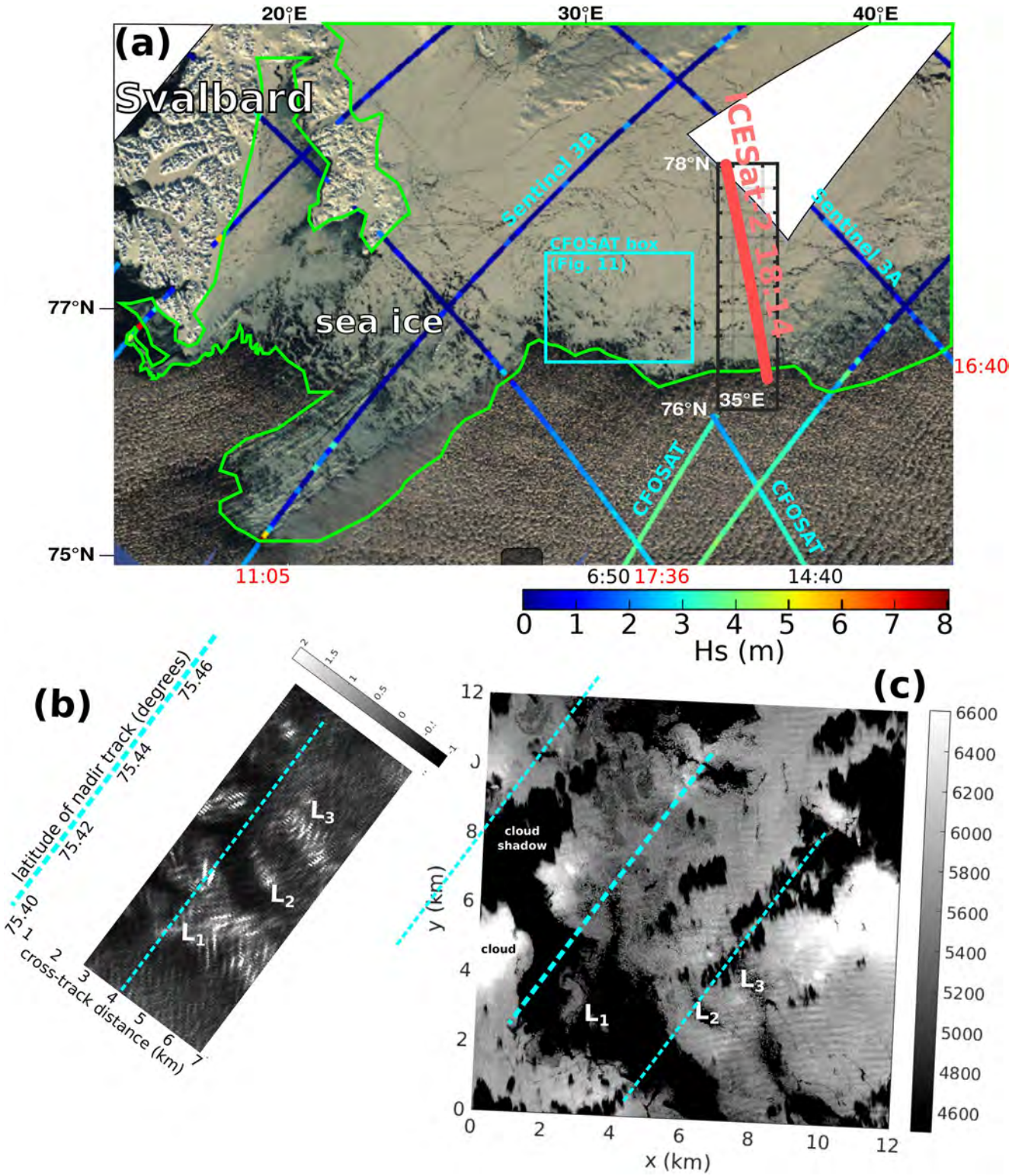

Figure 8.

of the high-resolution backscatter variations with respect to the low-resolution backscatter variations. For the low-resolution backscatter variations σ_{lpf}, we apply a two-dimensional Gaussian filter, which should filter the swell signals, but should capture the quickly changing backscatter from leads and sea ice. The normalized backscatter is then given as

$$\sigma_{\text{N}}(n,m) = \frac{\sigma(n,m) - \sigma_{\text{lpf}}(n,m)}{\sigma_{\text{lpf}}(n,m)}, \tag{5}$$

where $\sigma(n, m)$ is the backscatter in the waveform tail at bin n and along-track waveform m. Finally, the waveform bins are projected on the ground as a function of cross-track distance x using the relation

$$x(n) = \sqrt{(H + (n - n_{\text{ref}})\,\Delta r)^2 - H^2}, \tag{6}$$

where $n - n_{\text{ref}}$ is the relative waveform bin from the leading edge, Δr is the altimeter sampling distance, and H is the platform altitude.

As in ice-free conditions, swells give four peaks in the wave spectrum due to the left-right ambiguity of the measurement geometry and the similar signature of waves propagating in opposite directions. The bright regions marked "L1," "L2," and "L3" are different leads, regions of flat water or ice, that appear very bright in the radar image and dark in the optical image. Although Figure 8c was strongly saturated to show the wave patterns, leads are brighter and clearly distinct from cloud shadows. We note that the vertical wave patterns in both L1 and L3 are brighter than the horizontal wave pattern. The vertical bright stripes are actually east-west wave crests and trough patterns that are on the right hand side of the track and, given the measurement geometry that cannot distinguish left and right, are folded on the left hand side of our Figure 8b. However, we may use the knowledge of the swell direction to unfold the image, as done in Figure 9, now putting the stronger contrast of leads L1 and L3 on the right side of the track.

Just like in the case of ice-free water, the pattern in the FF-SAR is expected to come from a combination of velocity-bunching that is common to all SAR images (Ardhuin et al., 2015; Lyzenga et al., 1985), and range-bunching that is specific to near-nadir radar measurements (Peral et al., 2015). Given the general low slope of swell waves in sea ice, the nonlinear contributions to bunching are relatively weak and it may be possible to retrieve a wave spectrum from the image spectrum. However, the strong changes in backscattered radar power associated with leads create heterogeneities in the image that are similar to those in usual SAR imagery.

3.2. Wave Patterns in CFOSAT SWIM Data

The SWIM instrument is a wave spectrometer that measures the backscatter power as a function of range, with high resolution in range and averaging over 18 km in the perpendicular direction (Hauser et al., 2017, 2021). These measurements are made with beams that rotate in azimuth while keeping a fixed incidence angle. Here, we use data from the beam centered on the incidence angle of 6°. Due to the large-scale averaging across the beam, only the features that are exactly perpendicular to the azimuth contribute to the measured signal (Jackson et al., 1985). This is the principle of the wave spectrometer that is capable of resolving waves in their perpendicular direction thanks to a high resolution in range, and selecting only one wave direction (with 180° ambiguity) thanks to the very large-scale averaging in the perpendicular direction.

Over the oceans, the modulations in radar backscatter have been shown to correspond to waves, and the wave directional spectrum can be retrieved by combining wavenumber spectra obtained for different azimuths (Hauser et al., 2021; Le Merle et al., 2021). Over sea ice, the backscatter variation as a function of incidence angle and local ice slope is a priori very different, and also the backscatter can vary due to variations in ice properties and

Figure 8. Wave signatures in Sentinel-2, Sentinel-3B, and ICESat-2 on 12 March 2021. (a) The portion of ICESat-2 track where wave signals are detected in the Level3a ATL07 ice elevation product is show in pink, overlaid on the mosaic of Sentinel 2 imagery. Svalbard is to the left. The ice edge is the green line. Wave heights from nadir altimeters on CFOSAT, Sentinel 3A, and Sentinel 3B are shown in colors, with the time of the tracks indicated on the edge of the image. (b) Fully focused Sentinel 3B waveforms showing the signature of leads (bright regions, three of them are marked L_1, L_2, and L_3). Swell patterns with wavelengths around 250 m are visible in both leads and sea ice, with 2 main orientations due to the left-right ambiguity in the cross-track direction. (c) Sentinel-2 B04 image showing leads, clouds, and cloud shadows, and a clear swell signature with a 250 m wavelength. In (b and c), the nadir ground track of Sentinel 3B is shown with the thick dashed cyan line, and the thinner lines indicate the location of pixels 4 km from nadir, on both sides of the track, corresponding the lines.

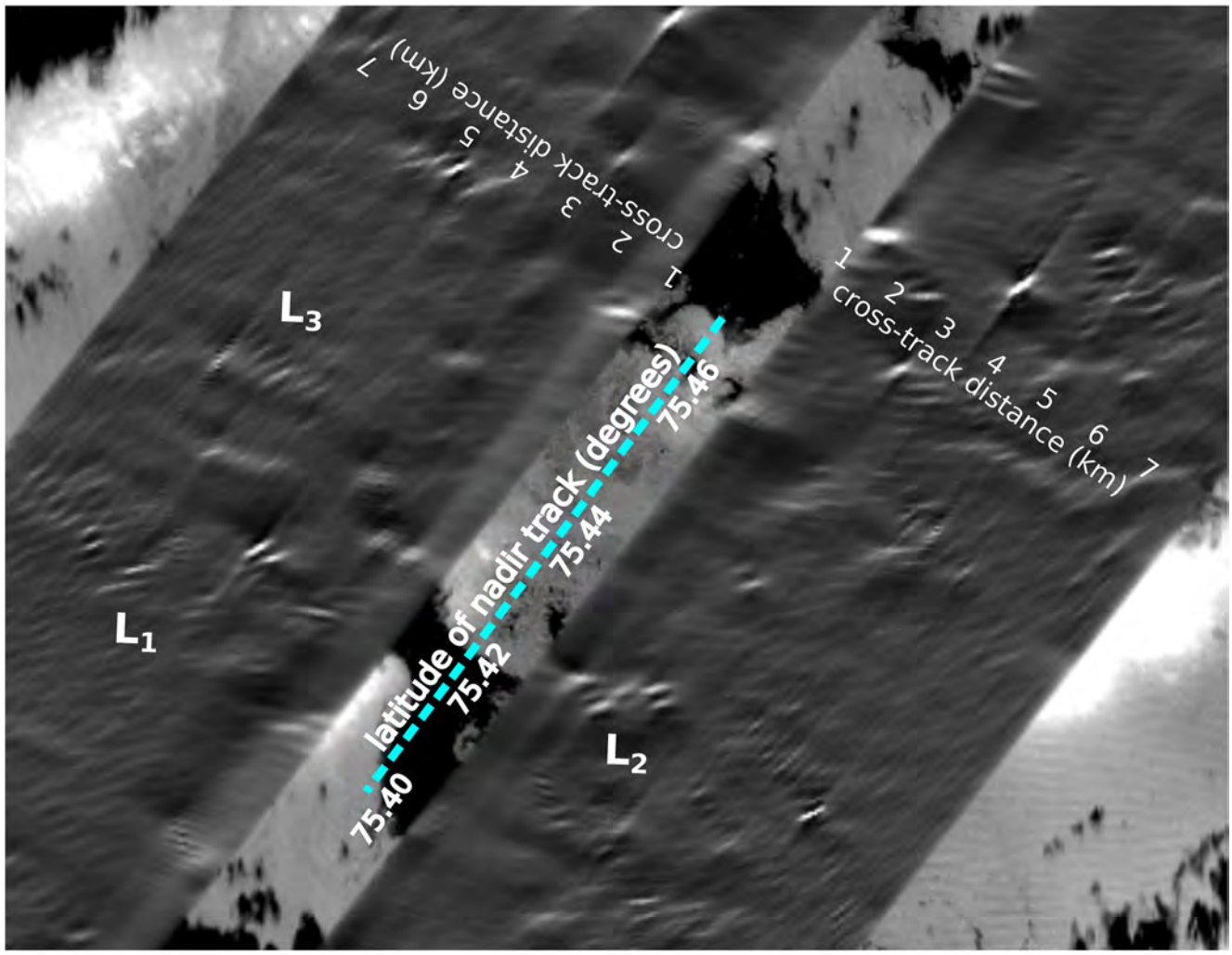

Figure 9. Unfolded Sentinel-3 radar backscatter from Full-Focus SAR (FF-SAR) processing using Fourier analysis to separate near-horizontal features from near-vertical features in Figure 8b, and inverse Fourier transform that generates a left-side image with near-horizontal features and a right-side image with what was near-vertical when folded to the left which now appears also near-horizontal. The background image is Sentinel-2.

the presence of leads. The analysis presented here is, to the best of our knowledge, the first attempt at interpreting SWIM radar modulations over sea ice.

CFOSAT SWIM data used are the L2S products V1.0 from IWWOC processing center at Ifremer. The fluctuation spectra are estimated after mean speckle noise removal and non-wave signature low wavenumber filter. Additional filtering is used over sea ice by looking at the variability of spectral coefficients estimated on successive 2.56 km segments within the 18 km diameter footprint. Spectral coefficients for which the standard deviation exceed two times the mean value over all segments are discarded.

Figure 10a shows a 7 km by 8 km piece of Sentinel-2 image around 76.7°N, 30°E with a dominant wave propagation direction around 37° clockwise from North. Figure 10b shows a wider area from the same image, now also including the 1D spectra from SWIM shown as an overlaid color strip with warmer colors corresponding to higher power spectral density, and each strip occupies the same length as the ground ranges of the SWIM footprint (note that the footprint also covers the same distance in the perpendicular direction). To facilitate the interpretation, the strip that is in the magenta box, with an azimuth 37° clockwise from North, is plotted in Figure 10c with a more usual power spectral density as a function of wavenumbers. The overlaid spectra from the Sentinel-2 and Sentinel-1 images have a similar shape with a peak wavenumber around 0.022 rad/m. Although not exactly colocated in time and space, the ICESat-2 data also shares similar wavelengths when assuming that the wave

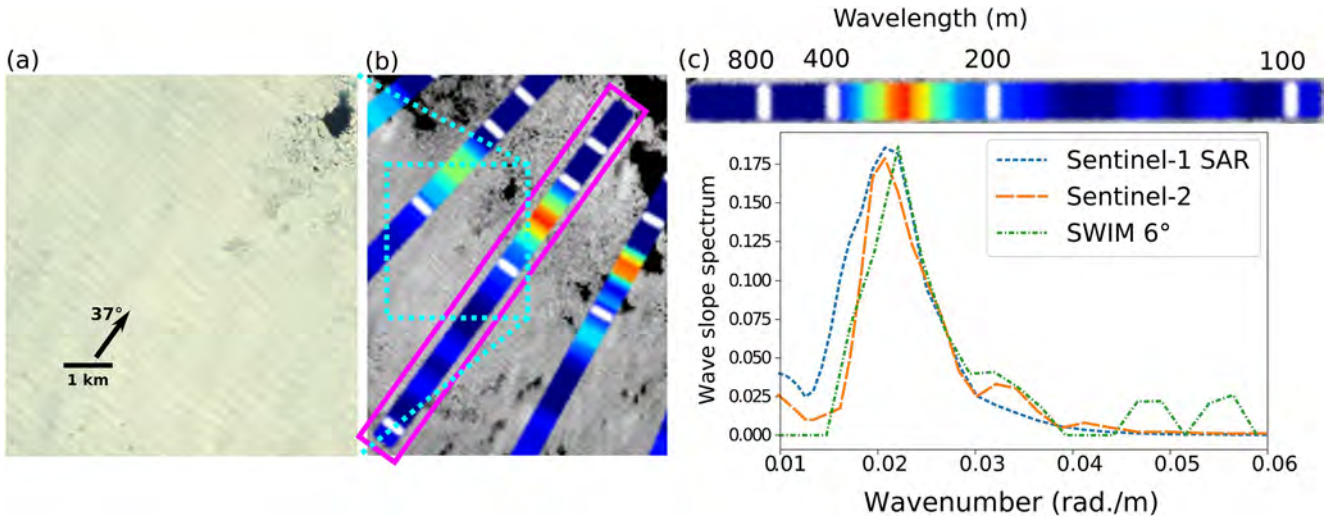

Figure 10. (a) and (b) Wave patterns around 76.7°N, 30°E on 12 March 2021, and CFOSAT-SWIM spectrum in azimuth 37° using the 6° incidence beam, compared to the spectra of Sentinel-1 and Sentinel-2 images in the same region. In (b) SWIM modulation spectra from the 6° incidence beam are overlaid as colored strips. The white marks in the colored strip correspond to wavelengths 800, 400, 200, and 100 m. (c) SWIM spectrum for the azimuth 37° clockwise from North in strip form as a the usual power spectral density as a function of wavenumber, compared with spectra in the same direction from Sentinel-1 and Sentinel-2 imagery. ICESat-2 data was averaged from the three strong beams over the latitude range 77.75°–77.9° using Fourier transforms over 0.05° in latitude. The wavenumber was multiplied by the proper projection from the satellite track to the 37° azimuth, common to the other data sets.

propagation azimuth is 37°. The higher energy at high wavenumbers in ICESat-2 is probably induced by noise, and it is much more pronounced for the weak beams (not shown).

Looking at SWIM spectra for all directions shows that SWIM detects peaks at the expected wavelengths and directions of the swell (Figure 11). However, peaks in the modulation spectrum are also present at a wide range of scales for directions perpendicular to the wave propagation. These peaks that cannot be associated with waves are highlighted with magenta arrows. The background Sentinel-2 image suggests that the regions where non-wave signatures are present are the regions where leads have scales that overlap with the usual range of wavelengths. In that case it is impossible to separate radar backscatter variations coming from a patchy ice cover with the modulation caused by waves.

4. Discussion and Conclusion

Wave patterns in Arctic sea ice have been found in all radar and optical measurements near the ice edge. These observations can provide useful observation for understanding the interactions of waves and sea ice. Previous works have insisted on the variability of wave attenuation and more measurements of wave attenuation are needed to better understand the processes at play. In this context, the frequent detection of waves in sea ice in ICESat-2 data (Horvat et al., 2020) can provide a very useful data set for waves in Arctic sea ice, allowing for a quantitative measurement of wave height, wavelength and direction, and the attenuation of waves along the altimeter track. Because the altimeter track does not often coincide with the wave direction the data may require some ancillary numerical modeling for its interpretation: the apparent reduction in wave height may be caused by open water gradients in the wave field and not by ice-induced effects.

The less frequent appearance of wave patterns in Sentinel-2 imagery, which requires a near-grazing sun illumination in addition to the absence of clouds, provides further information. In particular the size of floes can be estimated, at least qualitatively, which is key to interpret the wave attenuation. Also, having a two-dimensional image may help in resolving gradients in sea state long the ice edge that should contain both different attenuation histories and a signature of waves-current interactions near the ice edge (von Appen et al., 2018). Difficulties in the interpretation of wave signature in optical imagery will remain due to the presence of clouds and the heterogeneities in the ice cover.

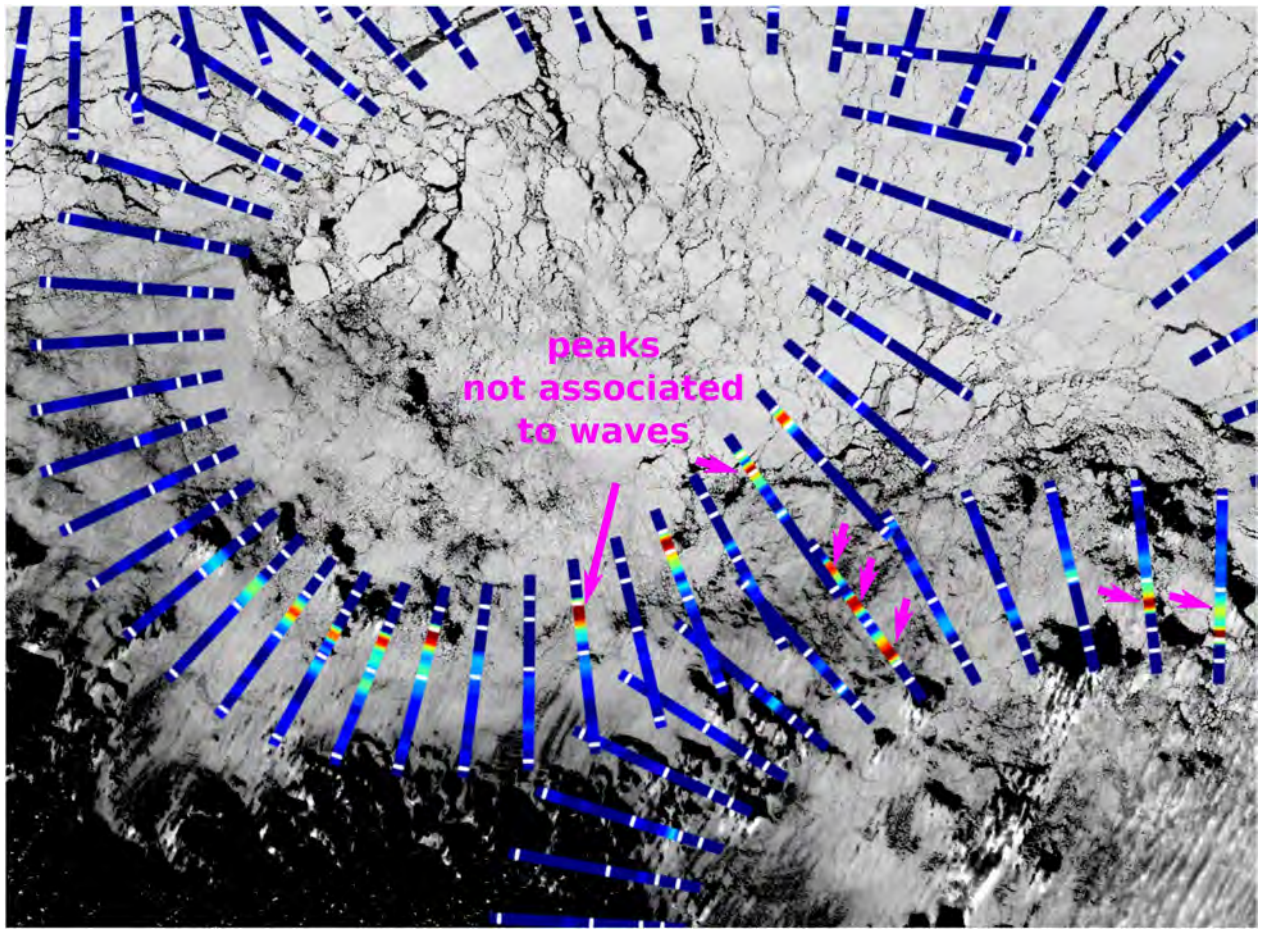

Figure 11. Same as Figure 10b, but over a wider area, corresponding to the cyan box in Figure 8.

Finally, wave-resolving radar data over sea ice are more readily obtained but their quantitative analysis is not so straightforward (Ardhuin et al., 2017). The novel capability provided by FF-SAR processing is clearly an interesting source of data that can be obtained from recent altimeter missions (Cryosat-2, Sentinel-3, and Sentinel-6-Michael-Freilich), as well as planned missions, including the dual frequency altimeter Cristal.

We have presented observations of wave patterns in sea ice using three types of satellite radars, Sentinel-1 SAR imagery, Sentinel-3 FF-SAR altimetry, and SWIM modulation spectra, and two types of optical observations, ICESat-2 lidar ice height measurements and Sentinel-2 imagery. Only the Sentinel-1 SAR has been previously validated in detail (Ardhuin et al., 2017) and used for science applications (Ardhuin et al., 2018; Stopa, Ardhuin, et al., 2018). Here, we have expanded on the previous detection of waves in ice by Horvat et al. (2020) to show that a quantitative analysis of wave heights, directions, and wavelengths was possible from ICESat-2 data. We have also exhibited and interpreted wave signatures in Sentinel-2, Sentinel-3 FF-SAR, and SWIM data. The quantitative interpretation of the last two measurements will require further work in developing a forward model that represents range bunching, velocity bunching, and possibly other effects. Taken together, there is a great potential for a synergistic use of these 5 data sources, some of which allow exact colocation in space with time differences of only a few minutes. Building colocated data sets of waves in ice observations can certainly help to reach a more quantitative understanding of the radar measurements, leading to science applications on the understanding of wave-ice interactions as well as practical applications to marine safety and Earth System modeling.

Data Availability Statement

ICESat-2 data was obtained from NASA National Snow and Ice Data Center Distributed Active Archive Center, Boulder, Colorado, https://doi.org/10.5067/ATLAS/ATL07.005, and CFOSAT modulation spectra data was obtained from Ifremer at https://data-cersat.ifremer.fr/projects/iwwoc/.

Acknowledgments
We acknowledge the use of Copernicus Sentinel 1, 2, and 3 data, obtained from the Copernicus Science Hub https://scihub.copernicus.eu. F.C. was supported by ESA through the ARKTALAS contract AO/1-9595/18/NL/LF. We thank Bertrand Chapron for fruitful discussions.

References

Altiparmaki, O., Kleinherenbrink, M., Naeije, M., Slobbe, C., & Visser, P. (2022). Sar altimetry data as a new source for swell monitoring. *Geophysical Research Letters*, *49*(7), e2021GL096224. https://doi.org/10.1029/2021GL096224

Ardhuin, F., Alday, M., & Yurovskaya, M. (2021). Total surface current vector and shear from a sequence of satellite images: Effect of waves in opposite directions. *Journal of Geophysical Research: Oceans*, *126*(7), e2021JC017342. https://doi.org/10.1029/2021JC017342

Ardhuin, F., Boutin, G., Stopa, J., Girard-Ardhuin, F., Melsheimer, C., Thomson, J., et al. (2018). Wave attenuation through an Arctic marginal ice zone on 12 october, 2015: 2: Numerical modeling of waves and associated ice break-up. *Journal of Geophysical Research: Oceans*, *123*(8), 5652–5668. https://doi.org/10.1002/2018JC013784

Ardhuin, F., Chapron, B., Collard, F., Smith, M., Stopa, J., Thomson, J., et al. (2017). Measuring ocean waves in sea ice using SAR imagery: A quasi-deterministic approach evaluated with sentinel-1 and in situ data. *Remote Sensing of Environment*, *189*, 211–222. https://doi.org/10.1016/j.rse.2016.11.024

Ardhuin, F., Collard, F., Chapron, B., Girard-Ardhuin, F., Guitton, G., Mouche, A., & Stopa, J. (2015). Estimates of ocean wave heights and attenuation in sea ice using the sar wave mode on Sentinel-1A. *Geophysical Research Letters*, *42*(7), 2317–2325. https://doi.org/10.1002/2014GL062940

Ardhuin, F., Otero, M., Merrifield, S., Grouazel, A., & Terrill, E. (2020). Ice breakup controls dissipation of wind waves across southern ocean sea ice. *Geophysical Research Letters*, *47*(13), e2020GL087699. https://doi.org/10.1029/2020GL087699

Ardhuin, F., Sutherland, P., Doble, M., & Wadhams, P. (2016). Ocean waves across the Arctic: Attenuation due to dissipation dominates over scattering for periods longer than 19 s. *Geophysical Research Letters*, *43*(11), 5775–5783. https://doi.org/10.1002/2016GL068204

Boutin, G., Ardhuin, F., Dumont, D., Sévigny, C., Girard-Ardhuin, F., & Accensi, M. (2018). Floe size effects on wave-ice interactions: Theoretical background, implementation and applications. *Journal of Geophysical Research: Oceans*, *123*(7), 4779–4805. https://doi.org/10.1029/2017JC013622

Collins, C., Rogers, W. E., Marchenko, A., & Babanin, A. V. (2015). In situ measurements of an energetic wave event in the Arctic marginal ice zone. *Geophysical Research Letters*, *42*(6), 1863–1870. https://doi.org/10.1002/2015GL063063

Dirmhirn, I., & Eaton, F. D. (1975). Some characteristics of the albedo of snow. *Journal of Applied Mechanics*, *14*(3), 375–379. https://doi.org/10.1175/1520-0450(1975)014<0375:SCOTAO>2.0.CO;2

Doble, M. J., Skourup, H., Wadhams, P., & Geiger, C. A. (2011). The relation between Arctic sea ice surface elevation and draft: A case study using coincident AUV sonar and airborne scanning laser. *Journal of Geophysical Research*, *116*, COOE03. https://doi.org/10.1029/2011JC007076

Hasselmann, K., Chapron, B., Aouf, L., Ardhuin, F., Collard, F., Engen, G., et al. (2012). The ERS SAR wave mode: A breakthrough in global ocean wave observations. In *Ers missions: 20 years of observing earth* (pp. 165–198). European Space Agency.

Hauser, D., Tison, C., Amiot, T., Delaye, L., Corcoral, N., & Castillan, P. (2017). SWIM: The first spaceborne wave scatterometer. *IEEE Transactions on Geoscience and Remote Sensing*, *55*(5), 3000–3014. https://doi.org/10.1109/tgrs.2017.2658672

Hauser, D., Tourain, C., Hermozo, L., Alraddawi, D., Aouf, L., Chapron, B., et al. (2021). New observations from the SWIM radar on-board CFOSAT: Instrument validation and ocean wave measurement assessment. *IEEE Transactions on Geoscience and Remote Sensing*, *59*(1), 5–26. https://doi.org/10.1109/tgrs.2020.2994372

Horvat, C., Blanchard-Wrigglesworth, E., & Petty, A. (2020). Observing waves in sea ice with ICESat-2. *Geophysical Research Letters*, *47*(10), e2020GL087629. https://doi.org/10.1029/2020GL087629

Horvat, C., & Tziperman, E. (2017). The evolution of scaling laws in the sea ice floe size distribution. *Journal of Geophysical Research: Oceans*, *122*(9), 7630–7650. https://doi.org/10.1002/2016jc012573

Jackson, F. C., Walton, W. T., & Baker, P. L. (1985). Aircraft and satellite measurement of ocean wave directional spectra using scanning-beam microwave radars. *Journal of Geophysical Research*, *90*(C1), 987–1004. https://doi.org/10.1029/jc090ic01p00987

Kaleschke, L., Tian-Kunze, X., Maaß, N., Mäkynen, M., & Drusch, M. (2012). Sea ice thickness retrieval from SMOS brightness temperatures during the arctic freeze-up period. *Geophysical Research Letters*, *39*(5), L05501. https://doi.org/10.1029/2012gl050916

Kleinherenbrink, M., Naeije, M., Slobbe, C., Egido, A., & Smith, W. (2020). Observations of polar ice fields. *Remote Sensing of Environment*, *237*, 111589. https://doi.org/10.1016/j.rse.2019.111589

Kudryavtsev, V., Yurovskaya, M., Chapron, B., Collard, F., & Donlon, C. (2017). Sun glitter imagery of surface waves. part 1: Directional spectrum retrieval and validation. *Journal of Geophysical Research: Oceans*, *122*(2), 1369–1383. https://doi.org/10.1002/2016JC012425

Kwok, R., Petty, A. A., Cunningham, G., Markus, T., Hancock, D., Ivanoff, A., et al. (2021). *Atlas/icesat-2 l3a sea ice height, version 5*. Tech. Rep. No. 2007/5. NASA National Snow and Ice Data Center Distributed Active Archive Center. https://doi.org/10.5067/ATLAS/ATL07.005

Le Merle, E., Hauser, D., Peureux, C., Aouf, L., Schippers, P., Dufour, C., & Dalphinet, A. (2021). Directional and frequency spread of surface ocean waves from swim measurements. *Journal of Geophysical Research: Oceans*, *126*(7), e2021JC017220. https://doi.org/10.1029/2021JC017220

Lyzenga, D. R., Shuchman, R. A., Lyden, J. D., & Rufenach, C. L. (1985). SAR imaging of waves in water and ice: Evidence for velocity bunching. *Journal of Geophysical Research*, *90*(C1), 1031–1036. https://doi.org/10.1029/jc090ic01p01031

Peral, E., Rodriguez, E., & Esteban-Fernandez, D. (2015). Impact of surface waves on SWOT's projected ocean accuracy. *Remote Sensing*, *7*(11), 14509–14529. https://doi.org/10.3390/rs71114509

Rogers, W. E., Thomson, J., Shen, H. H., Doble, M. J., Wadhams, P., & Cheng, S. (2016). Dissipation of wind waves by pancake and frazil ice in the autumn beaufort sea. *Journal of Geophysical Research*, *121*(11), 7991–8007. https://doi.org/10.1002/2016JC012251

Squire, V. A. (2020). Ocean wave interactions with sea ice: A reappraisal. *Annual Review of Fluid Mechanics*, *52*(1), 37–60. https://doi.org/10.1146/annurev-fluid-010719-060301

Stopa, J. E., Ardhuin, F., & Girard-Ardhuin, F. (2016). Wave climate in the Arctic 1992-2014: Seasonality and trends. *The Cryosphere*, *10*(4), 1605–1629. https://doi.org/10.5194/tc-10-1605-2016

Stopa, J. E., Ardhuin, F., Thomson, J., Smith, M. M., Kohout, A., Doble, M., & Wadhams, P. (2018). Wave attenuation through an arctic marginal ice zone on 12 october, 2015: 1. Measurement of wave spectra and ice features from sentinel 1A. *Journal of Geophysical Research: Oceans*, *123*(5), 3619–3634. https://doi.org/10.1029/2018JC013791

Stopa, J. E., Sutherland, P., & Ardhuin, F. (2018). Strong and highly variable push of ocean waves on southern ocean sea ice. *Proceedings of the National Academy of Sciences*, *115*(23), 5861–5865. https://doi.org/10.1073/pnas.1802011115

Sutherland, P., & Dumont, D. (2018). Marginal ice zone thickness and extent due to wave radiation stress. *Journal of Physical Oceanography*, *48*(8), 1885–1901. https://doi.org/10.1175/JPO-D-17-0167.1

Sutherland, P., & Gascard, J. C. (2016). Airborne remote sensing of ocean wave directional wavenumber spectra in the marginal ice zone. *Geophysical Research Letters*, *43*(10), 4659–4664. https://doi.org/10.1002/grl.53444

The WAVEWATCH III® Development Group. (2019). *User manual and system documentation of WAVEWATCH III® version 6.07 (Tech. Note No. 333)*. (p. 465 + Appendices). NOAA/NWS/NCEP/MMAB.

Thomson, J., Ackley, S., Girard-Ardhuin, F., Ardhuin, F., Babanin, A., Boutin, G., et al. (2018). Overview of the arctic sea state and boundary layer physics program. *Journal of Geophysical Research: Oceans*, *123*(12), 8674–8687. https://doi.org/10.1002/2018JC013766

Thomson, J., Hoseková, L., Meylan, M. H., Kohout, A. L., & Kumar, N. (2021). Spurious rollover of wave attenuation rates in sea ice caused by noise in field measurements. *Journal of Geophysical Research: Oceans*, *47*(3), e2020JC016606. https://doi.org/10.1029/2020JC016606

Thomson, J., Lund, B., Hargrove, J., Smith, M. M., Horstmann, J., & MacKinnon, J. A. (2021). Wave-driven flow along a compact marginal ice zone. *Geophysical Research Letters*, *48*(3), e2020GL090735. https://doi.org/10.1029/2020GL090735

Thomson, J., & Rogers, W. E. (2014). Swell and sea in the emerging Arctic Ocean. *Geophysical Research Letters*, *41*(9), 3136–3140. https://doi.org/10.1002/2014GL059983

von Appen, W.-J., Wekerle, C., Hehemann, L., Schourup-Kristensen, V., Konrad, C., & Iversen, M. H. (2018). Observations of a subme-soscale cyclonic filament in themarginal ice zone. *Geophysical Research Letters*, *45*, 6141–6149. https://doi.org/10.1029/2018GL077897

Wadhams, P., Squire, V. A., Ewing, J. A., & Pascal, R. W. (1986). The effect of the marginal ice zone on the directional wave spectrum of the ocean. *Journal of Physical Oceanography*, *16*(2), 358–376. https://doi.org/10.1175/1520-0485(1986)016<0358:teotmi>2.0.co;2

Yu, Y., Sandwell, D. T., Gille, S. T., & Boas, A. B. V. (2021). Assessment of ICESat-2 for the recovery of ocean topography. *Geophysical Journal International*, *226*(1), 456–467. https://doi.org/10.1093/gji/ggab084

Yurovskaya, M., Kudryavtsev, V., Chapron, B., & Collard, F. (2019). Ocean surface current retrieval from space: The sentinel-2 multispectral capabilities. *Remote Sensing of Environment*, *234*, 111468. https://doi.org/10.1016/j.rse.2019.111468

PHILOSOPHICAL TRANSACTIONS A

royalsocietypublishing.org/journal/rsta

Research

Cite this article: Boutin G, Williams T, Horvat C, Brodeau L. 2022 Modelling the Arctic wave-affected marginal ice zone: a comparison with ICESat-2 observations. *Phil. Trans. R. Soc. A* **380**: 20210262. https://doi.org/10.1098/rsta.2021.0262

Received: 11 March 2022
Accepted: 20 July 2022

One contribution of 17 to a theme issue 'Theory, modelling and observations of marginal ice zone dynamics: multidisciplinary perspectives and outlooks'.

Subject Areas:
oceanography, glaciology, geophysics

Keywords:
sea ice, waves, modelling

Author for correspondence:
G. Boutin
e-mail: guillaume.boutin@nersc.no

Electronic supplementary material is available online at https://doi.org/10.6084/m9.figshare.c.6135624.

THE ROYAL SOCIETY PUBLISHING

Modelling the Arctic wave-affected marginal ice zone: a comparison with ICESat-2 observations

G. Boutin[1], T. Williams[1], C. Horvat[2] and L. Brodeau[3]

[1]Nansen Environmental and Remote Sensing Center, N-5007 Bergen, Norway
[2]Institute at Brown for Environment and Society, Brown University, Providence, RI 02912, USA
[3]CNRS, Institut de Géophysique de l'Environnement, 38 058 Grenoble, France

GB, 0000-0002-1689-9351; CH, 0000-0001-6512-0335; LB, 0000-0001-8745-7510

We evaluate marginal ice zone (MIZ) extent in a wave–ice 25 km-resolution coupled model, compared with pan-Arctic wave-affected sea-ice regions derived from ICESat-2 altimetry over the period December 2018–May 2020. By using a definition of the MIZ based on the monthly maximum of the wave height, we suggest metrics to evaluate the model taking into account the sparse coverage of ICESat-2. The model produces MIZ extents comparable to observations, especially in winter. A sensitivity study highlights the need for strong wave attenuation in thick, compact ice but weaker attenuation as sea ice forms, as the model underestimates the MIZ extent in autumn. This underestimation may be due to limited wave growth in partially covered ice, overestimated sea-ice concentration or the absence of other processes affecting floe size. We discuss our results in the context of other definitions of the MIZ based on floe size and sea-ice concentration, as well as the potential impact of wave-induced fragmentation on ice dynamics, found to be minor at the climate scales investigated here.

This article is part of the theme issue 'Theory, modelling and observations of marginal ice zone dynamics: multidisciplinary perspectives and outlooks'.

1. Introduction

The regions lying between open ocean and compact sea ice are collectively referred to as marginal ice zones (MIZs). In both hemispheres, MIZs are areas of particular importance for atmosphere–ocean–sea-ice processes (e.g. [1,2]), including interactions between waves and sea ice.

Sea ice inhibits wave generation and attenuates the waves propagating from open ocean. As a consequence, the presence of waves in sea ice has been suggested as a definition of the MIZ [3], since the distance over which waves propagate is approximately the extent over which open-ocean processes affect sea ice, mostly through the fracture of the ice by these waves. Once broken, sea ice is more sensitive to melt (lateral melt in particular [4–7]), less resistant to deformation [8] and more permissive to waves [9]. To properly assess the effect of waves on sea ice, we seek to properly estimate the extent over which waves are present in the ice and cause its fracture and to understand the key quantities that modulate this extent. Such an understanding is particularly crucial in a warming world, as reduced summer sea-ice extent and delayed autumn refreezing increases available fetch and permits the generation of more frequent and energetic waves in the Arctic [10]. Increasingly energetic waves also interact with thinner and more fragile Arctic sea ice [11,12], which is more susceptible to wave-induced fracture.

A number of dedicated modelling studies (e.g. [7,13–17]) and field campaigns (e.g. [18,19]) have recently attempted to characterize the impact of waves on sea ice. Modelling studies have mostly focused on two aspects: (i) wave attenuation in ice (e.g. [13,15,20,21]) and (ii) feedbacks of wave-induced ice break-up on sea ice and the ocean, such as enhanced lateral melting [7,16,17], lower ice strength [22,23] and sub-mesoscale eddy generation [5]. However, a major limitation of these modelling studies is that they are conducted at climate scales and therefore lack comparison against data that span large areas and long time periods (longer than a few weeks), which are not available via field campaigns. Indeed, most wave attenuation studies evaluate their models against only one or a few wave events (e.g. [14,15,20]), meaning that most wave attenuation parametrizations available in numerical models have not been evaluated in pan-Arctic/Antarctic simulations on climate time scales. Being able to evaluate wave attenuation over monthly time scales is all the more important given that dominant wave attenuation processes are known to strongly depend on ice properties such as the ice thickness, the floe size and the ice type [24–26], which vary strongly over time and between regions.

The lack of climate-scale evaluation of different modelling studies derives from an absence of observational datasets on wave–ice interactions (i.e. wave properties in ice and sea-ice floe size) covering large geographical areas (regional to global) over long time periods (more than a few days). Recently progress has been made by exploiting long-period moorings [27] and spaceborne radar or optical imagery [28–30]. A major advance has been made possible by satellite altimetry and particularly the recent launch of ICESat-2 (IS-2). The high (cm-scale) horizontal resolution of IS-2 measurements means that it can be used to directly measure waves in both open water and sea ice at long time scales and across the polar regions. IS-2 data have been used to estimate a wave-affected fraction (WAF) in both hemispheres, a quantity related to the extent of ice affected by waves [31]. Here, we will relate this WAF to quantities available as model output, as a method for understanding conclusions of previous modelling studies [23] investigating the effect of sea-ice break-up on sea-ice dynamics.

In this study, we evaluate the extent of ice affected by waves in the neXtSIM–WAVEWATCH III [32–34] coupled wave–sea-ice model [23] against the wave-affected marginal ice zone (wMIZ) estimated from IS-2 data in [31]. We introduce a method for evaluating standard wave and sea-ice model output against WAF values retrieved from IS-2. We assess the ability of our model to

reproduce the wMIZ extent and discuss physical parameters affecting the results. We also discuss how the wMIZ extent compares with that based on floe size, which can also be observed from satellite altimetry [29,35], as well as the potential impact of wave-induced break-up on sea-ice dynamics.

2. Methods

(a) ICESat-2 wave-in-ice data

The IS-2 dataset and retrieval method are described in detail in [31]. Briefly, IS-2 sea-ice height data are analysed for regions with high, wave-like variations. IS-2 tracks are divided into segments with a mean length of approximately 17 m. In [31] the segments were distinguished with a negative height anomaly from the others and considered to be wave affected. Then, the WAF was computed as the length of negative IS-2 heights divided by the length of all heights, for all segments binned monthly on a 100 km (or 25 km) polar stereographic grid over the period from October 2018 to the present. The main limitation of this method is that it only detects waves with large amplitudes (of at least 0.54 m) to ensure that a negative height anomaly is not due to sea-ice or sea-level variability. Even though validation against *in situ* data would be required to fully assess the uncertainties associated with wave detection using IS-2, recent studies [36,37] have demonstrated IS-2's ability to capture wave signature in its data. The authors of [31] suggested that their method of filtering segments to determine whether they are wave affected is rather conservative and hence is more likely to exclude true wave observations than to include noise (due to ice roughness for instance). This statement is confirmed in [36], where spectral analysis was used to retrieve wave signatures in IS-2 data and the results were compared against those of [31]. Summer retrievals, however, should be considered carefully, as melt ponds can be mistaken for sea surface points, leading to overestimates of sea-level height and false positive segments in the wave detection algorithm.

WAF values are reported only when more than 1000 segments are recorded in a given month in each bin, making the 25 km grid significantly noisier than the 100 km grid (figure 1*a* compared with figs S1 and S5 in the supplementary material of [31]). Yet given that waves rarely propagate more than 100 km into the ice cover, we choose to work with the 25 km dataset and address missing values below.

As in [31], we consider a grid cell to be 'wave affected' if the WAF exceeds a certain threshold, which we impose to limit the impact of noise. We qualitatively pick 0.1 as the threshold, as it eliminates a large part of the noise and shows a month-to-month variability of the wMIZ extent similar to that obtained using the 100 km version of the dataset and the threshold of 0.075 described in [31] (figure 1*b*). We use a higher threshold of 0.25 to delimit areas more confidently affected by waves. The observed wMIZ extent is relatively insensitive to further increases in this threshold. We also define a second high-confidence area by filtering out all cells with fewer than 30 000 segments observed monthly. This restriction reduces the total observed area by approximately 30% in the winter and 15% in the summer (figure 1*c*), and includes almost entirely observations of 'no waves' (WAF < 0.1), as most of the cells that remain are found at latitudes higher than 75° N.

(b) Coupled wave–ice model

We use the coupled wave–ice model developed in [23]. The wave model is WAVEWATCH III (hereafter referred to as WW3 [34]), and the sea-ice model is neXtSIM [33,38]. The model resolution is 25 km, the same as in the IS-2 dataset, and the model domain includes all the Arctic covered by the IS-2 dataset. We exclude closed seas (Hudson Bay and Baltic Sea) and the Canadian Archipelago from our analysis (see figure 1*a*), as we do not expect our model with a 25 km resolution to resolve wave growth and propagation in these areas.

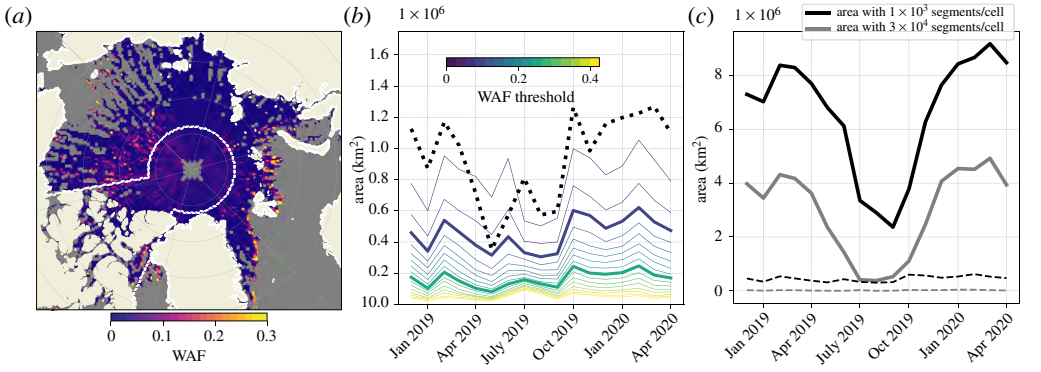

Figure 1. (*a*) Wave-affected fraction as defined in [31] in the Arctic for November 2019, using the 25 km dataset. The white contour around the pole and encompassing the Canadian Archipelago represents the part of the domain that is excluded for the model evaluation. (*b*) wMIZ extent evolution from the 25 km dataset using different WAF thresholds. The dotted line represents the wMIZ extent using the 100 km dataset and a WAF threshold of 0.075, as in [31]. (*c*) Evolution of total area covered by the dataset if we ignore cells with fewer than 1000 segments in a month (black solid line) or if we ignore cells with fewer than 30 000 segments in a month (grey solid line). The dashed lines represent the area with detected waves (WAF $\geq$ 0.1) in both cases (cells with more than 1000 segments in black and those with more than 30 000 segments in grey). (Online version in colour.)

The main difference between the model used in this study and that of [23] is that the sea-ice rheology in neXtSIM has been updated from the Maxwell elasto-brittle rheology [32] to the brittle Bingham–Maxwell (BBM) rheology [33]. The BBM rheology introduces a plastic threshold that prevents convergence unless ice is strongly damaged or undergoes strong external compressive stress. The potential impact of this change is discussed in §3e. The other differences from [23] are related to the model set-up and are described in detail in §S1 of the electronic supplementary material.

We define a reference simulation, denoted by REF, where we do not activate processes (lateral melting, link between damage and fragmentation; see [23]) related to the impact of waves on sea-ice properties, other than to update the floe size in the sea-ice model. This means that in REF, WW3 sends information about whether fragmentation occurs, as explained in [23], and neXtSIM updates the floe size. This floe size has no impact on sea-ice thermodynamics, drift or damage, and is sent back to WW3 where it is used to compute wave attenuation. Floe size in neXtSIM is only affected by wave-induced break-up and floe size growth mechanisms (refreezing and floe welding; see [23]).

We also run sensitivity experiments to investigate the effects of the values of the inelastic dissipation of wave energy through the B parameter as defined in [15] (eqn (20)), the roughness length z_0 associated with the contribution of turbulent friction to wave energy dissipation [39] (eqns (B3)–(B5)), the flexural strength of sea ice σ_{flex} [15] (eqn (12)), and the link between wave-induced fragmentation and damage [23]. Simulation names and the associated parameter values are summarized in table 1.

(c) Other datasets

To evaluate simulated wave heights in open water, we use a wave-height dataset focusing on the Arctic compiled by Heorton *et al*. [40]. It provides daily estimates of wave height using the CryoSat-2 altimeter. These estimates are binned daily and averaged on a 100 km polar stereographic grid covering 2011–2019. For this comparison, we average daily simulated wave heights interpolated to the coarser observational grid.

Table 1. Model parameters associated with each simulation described in §2b. In bold are the values that differ from the reference simulation.

name	link frag. and damage	z_0 (m)	B (N m^2 s$^{1/3}$)	σ_{flex} (MPa)
REF	no	10^{-4}	3×10^7	0.6
DMG	**yes**	10^{-4}	3×10^7	0.6
LFXST	**yes**	10^{-4}	3×10^7	**0.247**
NIDIS	**yes**	10^{-2}	**0**	0.6

For evaluation of sea-ice properties, we follow the methods of [41] and use the observations described therein: CS2-SMOS sea-ice thickness [42], OSI-SAF SSMIS sea-ice concentration [43] and the low-resolution 48 h OSI-SAF sea-ice drift [44].

3. Results

(a) Evaluation of modelled ocean wave height and sea-ice properties

We first examine open-ocean wave conditions, with the results presented in figure S1 of the electronic supplementary material. Overall the model reproduces the observed wave energies, in particular with low significant wave-height bias in key Arctic regions of interest such as the Greenland, Barents and Bering Seas (figure S1*b*,*c*, electronic supplementary material). Wave heights tend to be underestimated within the Arctic Basin, such as in the Kara, Beaufort, Chukchi and East Siberian Seas, which are only ice free (and therefore usable for this comparison) for a short part of the year (approximately June to October). Wave heights are generally quite low in these regions, even when they are ice free (figure S1a, electronic supplementary material).

We also evaluate bulk sea-ice properties against observations, with the results summarized in table S2 of the electronic supplementary material. We find good agreement between the model and observed drift, but near-uniform overestimation of sea-ice extent except from July to August 2019. Most of this consistent bias is found in the Greenland Sea, with sea ice extending too far east (by 1–2 grid cells) and more compact than in observations (see figure S2, electronic supplementary material). As a result, the model is likely to overestimate wave attenuation and underestimate the wMIZ extent in this region. Conversely, in summer, overestimation of wave height in ice may arise from an overestimation of the available fetch. Sea-ice thicknesses are underestimated, mainly in the central Arctic (not shown), where waves are not expected to be found, at least in winter.

(b) Comparison of modelled wMIZ extent against ICESat-2

As described in §2a, we seek to define a model wMIZ that can be compared with the region where the IS-2 WAF is higher than 0.1. The WAF provides information about the frequency of detection of waves with amplitude higher than 0.54 m (1.08 m wave height). In [31] this threshold was estimated on average for the Arctic and Antarctic. It depends on local properties such as the variability of sea-ice thickness and sea level. Assuming a Rayleigh distribution of the wave height, which seems reasonable as wave spectra in ice are generally narrow, a sea state with a significant wave height of $H_s = 1.5$ m should have approximately 37% of individual waves exceeding 1.08 m. This is a significant amount of waves that should be identified by IS-2 and should significantly increase the WAF value for a given grid cell [31]. Thus, a consistent modelled definition of the wMIZ is the ice-covered area (i.e. with sea-ice concentration higher than 15%) with values of H_s higher than approximately 1.5 m at least once in the month.

This definition is simple, but the maximum H_s may give an upper bound on the extent observed by ICESat-2 as the sparse coverage of the altimeter is unlikely to capture the maximum value of the wave height at any given location. To estimate the sensitivity of our results to this

wMIZ definition, we also use a definition of the wMIZ that considers the 90th percentile of wave heights in a month, a more conservative estimate of the modelled wMIZ. We also consider the uncertainty associated with the modelled H_s, as well as the detection threshold. Assuming a wave attenuation rate of the order of 10^{-5} (m/m), which is an upper bound on measured in-ice attenuation rates (attenuation being stronger at the ice edge [21]), the wave height decrease in a 25 km grid cell should be of the order of 0.25 m. The uncertainties linked to the detection threshold are difficult to estimate in the absence of extensive evaluation of the WAF retrieval method, but we address this issue in two ways. First, we assume an uncertainty of approximately 10 cm in this threshold, mostly due to variations of what Horvat *et al*. [31] call ν (linked to local surface properties, it is 20 cm on average but can be as low as 10 cm as found in [31]), resulting in an approximately 20 cm uncertainty for the minimum wave height that can be detected. Adding this uncertainty to that of the modelled wave height and rounding it up, we compare the observed wMIZ to the area with a monthly maximum value of the modelled H_s higher than 1.50 ± 0.5 m. Second, given that recent studies have shown clear wave signals in the IS-2 data for wave heights as low as 0.50 m (fig. 3*e* in [37]), we define the upper bound of the wMIZ extent as the area with a monthly maximum of H_s higher than 0.50 m. This area is affected by waves that could be detected using the method of [31], assuming very little 'noise' (e.g. ice roughness) in the data, and is used to give an idea of the sensitivity of the wMIZ extent to lower wave heights.

Maps of 2019 wMIZ extents are shown in figure 2, representing model behaviour for winter, summer and autumn. The modelled wMIZ extent in winter (figure 2*a*) captures most of the observed locations with a WAF exceeding 0.1 in the vicinity of the ice edge, though a number of points with high WAF values, over 0.25, are not captured farther in the ice pack of the Arctic Basin. A similar pattern holds in April and May, though there are fewer observations of waves close to the ice edge and more of them in pack ice not captured by the model (not shown). From June to August (figure 2*b*), the model fails to capture most of the observations of waves. This means either that the model underestimates wave heights in ice or that the data are very noisy in this period, as suggested in [31]. In November, the model performs well on the Atlantic sector, but the wMIZ extent in the Beaufort and Chukchi Seas is still underestimated, even when using the upper bound of the wMIZ extent.

The evolution of integrated wMIZ extent is shown in figure 3*a* (in orange) along with the wMIZ extent estimated using the binned 100 km IS-2 dataset in [31]. The magnitudes of the modelled and observed extents are very different, with the modelled wMIZ extent being generally twice as large as the observed wMIZ extent in winter. This is a consequence of the modelled wMIZ being a continuous area, while the wMIZ in the IS-2 dataset is more discrete, due to the non-continuous sparse coverage of the altimeter. This difference in magnitudes is even greater when using the 25 km dataset (figure 1*b*), as it contains more cells with fewer than 1000 segments per month. Note that in our analysis, we only sample model cells where IS-2 data are available, the problem being that wave observations by IS-2 are often scattered points between cells with no (or not enough) detected waves. The reasons behind this behaviour are discussed later in this section. Trying to extrapolate a continuous wMIZ from IS-2 observations is not straightforward given the difficulty in assessing uncertainties when computing the WAF. However, it is encouraging that the modelled wMIZ generally shows the same key features as the observed one: a decrease from winter to spring, a sharp rise in the autumn, and a rather stable extent in winter. Using the 90th percentile of H_s (in blue) gives a similar evolution of the wMIZ extent overall, but the wMIZ extent is smaller by 20% than when using the monthly maximum of H_s. The results also show little sensitivity to the H_s threshold value in the 1–2 m range, which gives us confidence in the robustness of our wMIZ definition. Assuming IS-2 can detect waves with an H_s down to 50 cm highly increases the wMIZ extent, by 50% in winter and a lot more in spring and summer. It also enhances the month-to-month variability of the wMIZ extent, showing for instance a secondary peak after April 2019 similar to the observed wMIZ extent. Thus, the upper bound of the wMIZ extent seems to capture part of the observed wMIZ variability.

We next investigate some quantitative metrics for the modelled wMIZ extent. Define A_{10} as the area that belongs to the modelled wMIZ but not to the observed one, A_{01} as the area that

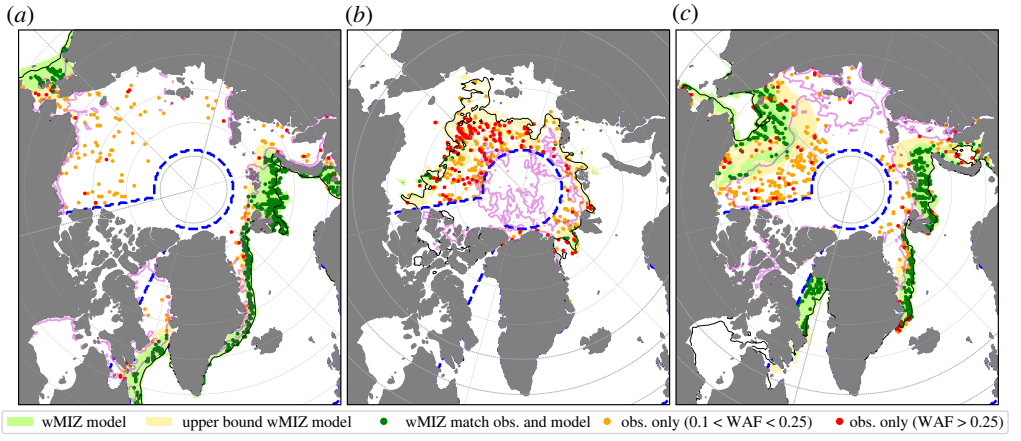

Figure 2. (*a–c*) Comparison of the wMIZ between the model (using REF and the maximum H_s for each month) and IS-2, for the months of February (*a*), August (*b*) and November (*c*) 2019. The blue dashed line corresponds to the domain where we perform the quantitative analysis, ignoring the Canadian Archipelago, the Baltic Sea and Hudson Bay. The green and yellow shaded areas correspond to the modelled wMIZ using the criteria that the monthly maximum value of H_s in ice is higher than 1.50 m and 0.50 m, respectively. Points with detected waves (WAF $>$ 0.1) within the wMIZ are in darker green. Red (orange) points show wave observations with WAF $>$ 0.25 (0.1 $<$ WAF $<$ 0.25) that are not encompassed by the modelled wMIZ. The thin solid black contour represents the area with an averaged total sea-ice concentration above 15%. The magenta contour represents the area with an averaged sea-ice concentration above 80%, ignoring newly formed ice in the model (see §A.2 of [38] for its definition). (Online version in colour.)

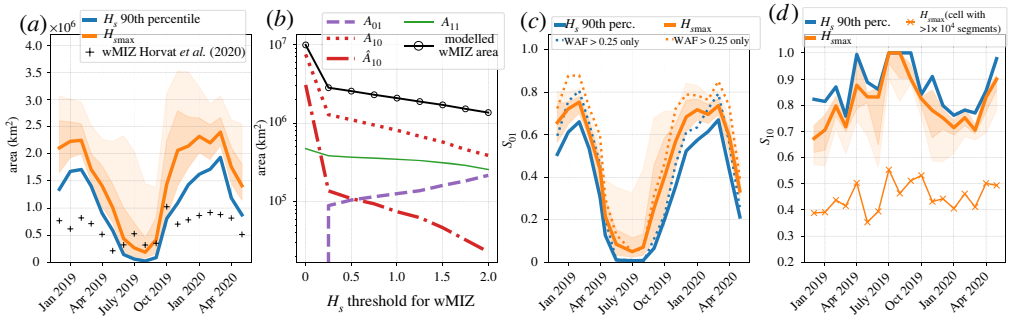

Figure 3. (*a*) wMIZ extent evolution depending on the definition of the wMIZ. The black line represents the wMIZ extent from IS-2 computed from the 100 km dataset as in [31]. The darker orange shaded area illustrates the sensitivity of the wMIZ extent for the maximum value of H_s being 1 m (upper bound) and 2 m (lower bound). The lighter orange shaded area illustrates this sensitivity for a maximum value of H_s as low as 0.5 m. (*b*) Extent of model match (A_{11}) and mismatch (A_{10}, A_{01} and $\hat{A}_{10}$; see their definitions in §3b) with observations and MIZ area for different H_s values used as a threshold for the wMIZ definition using the 90th percentile of H_s for each month. For the computation of A_{10} and $\hat{A}_{10}$, i.e. areas with waves in the model but not in observations, model cells are sampled only if IS-2 observations are available (i.e. no missing values in IS-2 dataset). (*c*) Time evolution of S_{01}, the fraction of the wave-affected area as observed from IS-2 that is captured by the modelled wMIZ using maximum H_s (orange) and the 90th percentile of H_s (blue), both with an H_s threshold of 1.5 m. The upper and lower bounds of the orange shaded areas are the same as for (*a*). Dotted lines correspond to the same quantities but when only the high-confidence wave-affected area (WAF $>$ 0.25) is considered in S_{01}. (*d*) Same as (*c*) but this time for S_{10}, the percentage of the modelled wMIZ surface area that matches the observed wMIZ area from IS-2. The upper and lower bounds of the darker orange shaded area are reversed compared to (*b*). The lighter orange shaded area still represents the sensitivity using a maximum value of H_s as low as 0.5 m, and S_{10} is computed using $\hat{A}_{10}$. The thin solid line with crosses represents the evolution of S_{10}, with $\hat{A}_{10}$ computed using cells with more than 10 000, instead of 30 000, segments. (Online version in colour.)

belongs to the observed wMIZ but not to the modelled one, and A_{11} as the area where the model and observation agree that a given location belongs to the wMIZ. A classical way of assessing the ability of a model to capture an extent is to use A_{11} and the errors A_{10} and A_{01} to assign a model score [45]. In our case, we are challenged by the fact that an absence of detected waves is not necessarily indicative of a region without waves, particularly if an area has few wave events in each month. Thus, the IS-2 dataset can provide a large number of false negatives, and a low WAF value (i.e. no waves detected) is less predictive of wave state than a high WAF value. This is visible in figures 1*a* and 2, where areas with a high density of detected waves (WAF > 0.1) are interspersed with missing values and locations with WAF $= 0$.

A consequence is that the A_{10} mismatch area can be significantly larger than the matching area A_{11}, as the modelled wMIZ extent necessarily encompasses a large number of missing values or locations with no detected waves (figure 1*a*). This is illustrated in figure 3*b*, which shows the dependence of A_{11}, A_{10} and A_{01}, along with the wMIZ extent, on the threshold value applied to H_s to define the wMIZ. We can see that A_{10} follows similar behaviour to the wMIZ extent, being much larger than A_{11}. To reduce the number of false negatives leading to a large A_{10}, we test the effect of increasing the level of confidence in the 'no waves' observations by only considering cells with a WAF of more than 30 000 segments (instead of 1000). This reduces the coverage by about 66%, as seen in figure 1*c*, but allows us to define a more conservative version of A_{10}, which we call $\hat{A}_{10}$. We see that $\hat{A}_{10}$ is of the same order of magnitude as A_{11} (figure 3*b*) and increases dramatically when the wMIZ extent becomes very large. This is because as the wMIZ extent keeps increasing, it ends up encompassing large areas of pack ice with very few waves observed. The area $\hat{A}_{10}$ can therefore be useful for investigating potential overestimation of the wMIZ extent in a simulation.

The monotonic increase of A_{01} in figure 3*a* illustrates a second challenge in quantitative evaluation of the wMIZ extent. It is due to the high values of WAF that are not captured by the model in the central Arctic pack ice, particularly from May to November [31], visible in figure 2*b*,*c*. It is unlikely that the model in its current configuration would be able to capture these waves, whether these observations are due to noise (false positives) or to wave generation in openings in pack ice [27]. This is because (i) the prediction of the exact location of such openings without assimilating sea-ice deformation is not possible owing to the chaotic nature of the crack formation process [46]; and (ii) the model resolution is likely too coarse to properly resolve wave growth in leads. Indeed, in WW3, wave generation in partially ice-covered cells is scaled by the concentration, but at 25 km resolution, the drop in sea-ice concentration due to divergence is not large enough (generally less than 0.1) to allow for noticeable wave growth in the pack, even though recent observations suggest that this may happen in the Beaufort Sea [27].

We propose separate evaluations of the ability of the model to capture the areas with observed waves, so as not to extend the wMIZ into areas where the IS-2 dataset is confident that there are no waves. First, we compute the fraction of observations captured by the modelled wMIZ by computing the evolution of $S_{01} = A_{11}/(A_{11} + A_{01})$ for REF (figure 3*c*). This metric only samples points with wave observations in the IS-2 dataset and checks whether they are captured by the modelled wMIZ. The model shows a clear seasonal pattern, performing well in the winter and less well in the summer. From December to March, we find that the modelled wMIZ captures about 70% of observations, with little dependence (about 10% maximum) on the definition of the wMIZ. This result varies little with the choice of the H_s threshold (± 50 cm). If we only account for observations of the WAF with values over 0.25 (dotted lines), where we are highly confident that there are waves, this score is as high as 90% in the 2019 winter (80% using the maximum value or 90th percentile of H_s). This percentage is lower in 2020 but remains around 80%. This gives us confidence that the model does not underestimate wave activity in the winter, at least in the vicinity of the ice edge, as is visible in figure 2*a*. The model's ability to capture observations drops from April to August (figure 2*c*), but increases again from September onwards. The results in summer are sensitive to the use of either the maximum value or the 90th percentile of H_s for each month (from 0 to 20% of observations captured by the wMIZ), which highlights the

stronger sensitivity of the modelled wMIZ to the factors affecting H_s magnitude in this season. The reasons behind this underestimation of the wave height in ice from spring to autumn are investigated further in §3c. The main limitation of S_{01} is that it does not inform us whether the model overestimates the wMIZ. For example, a modelled wMIZ encompassing the whole Arctic would include all cells with observed waves, hence getting the perfect score $S_{01} = 1$. The second step of our evaluation should therefore aim to estimate potential overestimations of the modelled wMIZ. We suggest using $S_{10} = A_{11}/(\hat{A}_{10} + A_{11})$, presented for REF in figure 3*d*. The higher S_{10} is, the lower the proportion of observations of 'no waves' in the modelled wMIZ relative to the number of cells with observed waves within the modelled wMIZ. Changing the number of segments to filter out cells when computing $\hat{A}_{10}$ has some effect on the magnitude of S_{10} but little on its qualitative evolution for numbers above 10 000 segments per month (also visible in figure 3*d*). This means that to evaluate different simulations, one can compare the values of S_{10} obtained for each of them, but their interpretation (i.e. whether the modelled wMIZ extent is overestimated or not) requires a qualitative assessment first (as made with figure 2 for REF). Here, we analyse the evolution of S_{10} knowing the qualitative evolution of the wMIZ extent from figure 2, and values of S_{10} using the same methodology applied to other simulations can inform us of the behaviour of these simulations compared to REF (see §3c). We find that S_{10} varies between 0.6 and 1 and shows a seasonal cycle opposite to S_{01} (figure 3*d*). In winter, where the wMIZ extent seems reasonable in figure 2*a*, S_{10} is found to be around 0.7. Therefore, we estimate that a value of S_{10} in the range of 0.6–0.7 means that the modelled wMIZ extent is reasonable, and lower values would mean that the wMIZ extent likely is overestimated. Given that the winter sea-ice extent in the model tends to be overestimated, particularly in the Greenland Sea, a good wave attenuation in the model should lead to a rather underestimated wMIZ extent. In summer, S_{10} reaches values above 0.9, as the model seems to underestimate the wMIZ extent rather than overestimate it (figure 2*b*). In general, the model is not too sensitive to the choice of the H_s threshold, and using a more conservative wMIZ extent by taking the 90th percentile is found to increase S_{10} by about 0.1 (15% better than REF). Overall, none of these choices has a significant impact on our results.

(c) Sensitivity of the modelled wMIZ to model parameters

To investigate what the important factors are in simulating the wMIZ, we compute the quantities S_{01} and S_{10} for the different sensitivity simulations described in §2b. The results are compiled in table 2, and the wMIZ extent for each simulation is shown in figure 4*a*. We also use this sensitivity experiment to investigate the reasons behind the underestimation of the autumn wMIZ extent in REF. This underestimation could be due to false positives in the observations of waves by IS-2. This is likely to be the case in summer (June–August), as the number of segments per cell tends to be lower and melt ponds could be mistaken for ocean surface points when computing the WAF [31]. Because of this high uncertainty in the summer data, we ignore the period June–August in our analysis and focus on September–November (autumn). For this period, moorings measurements support the idea that waves around 1 m high can be found far in pack ice in the Beaufort Sea [27], giving some credit to the high WAF values retrieved from IS-2 in this area.

We first look at DMG to check that activating the link between damage and fragmentation has little impact on the wMIZ extent. This is needed as this link is activated in other simulations investigating the sensitivity of other parameters compared to REF (table 2). The impacts of activating this link are described in detail in [23] and could affect wave attenuation by making the ice thicker in the wMIZ after a long period, but we find that differences between DMG and REF are negligible for both the extent metrics, S_{10} and S_{01}.

The NIDIS simulation changes the attenuation process by removing inelastic dissipation, which is efficient at attenuating waves with longer wave periods (greater than 10 s) and in broken ice [15]. Inelastic dissipation assumes that sea ice is a viscoelastic solid flexing repeatedly under the wave action, which dissipates energy. Its effect vanishes when the floe size becomes smaller than the wavelength of the waves [15]. To compensate for this loss of attenuation compared to REF, we increase turbulent friction by increasing the roughness length (table 1;

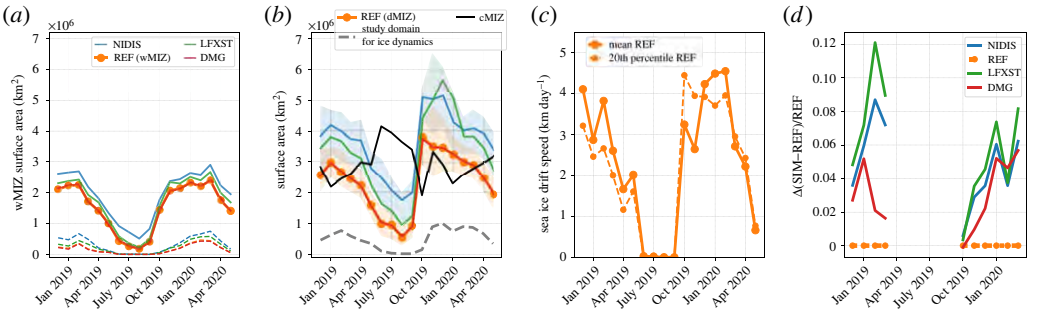

Figure 4. (*a*) Evolution of the wMIZ extent (solid lines) for the different simulations of the sensitivity study. Dashed lines represent the part of the wMIZ extent with sea-ice concentration (ignoring newly formed ice) above 0.8. (*b*) Solid lines are similar to (*a*) but for the dMIZ extent evolution, defined as the area with D_{max} lower than 100 m on average for each month. The orange and blue shaded areas represent the sensitivity of the dMIZ to the floe size threshold between 30 m and 300 m for REF and NIDIS, respectively. The solid black line represents the cMIZ extent evolution when ignoring the newly formed ice category [38]. The grey dashed line represents the evolution of the area used for the estimation of wave impact on ice dynamics (a monthly averaged $D_{max} \leq 100$ m and sea-ice concentration higher than 0.8 when ignoring newly formed ice). (*c*) Evolution of the monthly average (solid dotted line) and 20th percentile (dashed dotted line) of the ice drift velocity in this area. (*d*) Difference in the 20th percentile of the ice drift velocity in the DMG, LFXST and NIDIS simulations relative to REF in this area. (Online version in colour.)

Table 2. Values of S_{01} and S_{10} for the different sensitivity experiments and for the winter period (December to March, 2018–2019 and 2019–2020), spring (April to May, 2019 and 2020) and autumn (September to November 2019). Values in brackets in the S_{01} column correspond to the score accounting only for locations with WAF values above 0.25. Values in brackets in the S_{10} column correspond to the score using a monthly maximum H_s of 0.5 m to define the upper bound of the modelled wMIZ extent. The period from June to August is not considered here because of the likely high level of noise in the IS-2 observations.

	December–March		April–May		September–November	
simulation	S_{01}	S_{10}	S_{01}	S_{10}	S_{01}	S_{10}
REF	0.70 (0.80)	0.73 (0.63)	0.39 (0.50)	0.86 (0.72)	0.41 (0.50)	0.83 (0.74)
DMG	0.70 (0.80)	0.73 (0.63)	0.39 (0.50)	0.86 (0.73)	0.40 (0.50)	0.84 (0.73)
LFXST	0.72 (0.82)	0.67 (0.51)	0.43 (0.54)	0.83 (0.66)	0.44 (0.53)	0.79 (0.69)
NIDIS	0.73 (0.83)	0.58 (0.39)	0.45 (0.56)	0.77 (0.55)	0.51 (0.62)	0.80 (0.60)

see [39]). In winter, NIDIS does slightly better than REF at capturing cells with observed waves ($S_{01} = 0.73$ vs 0.70 in REF), but at the cost of overestimating the wMIZ extent, with a value of S_{10} dropping below 0.6, which is approximately 20% less than S_{10} for REF. The wMIZ extent increases by about 15% compared to REF (figure 4*a*). This increase of the wMIZ extent in NIDIS results in an increase of S_{10}, as the additional wMIZ area compared to REF mostly encompasses regions with few waves observed by IS-2 and hence most likely overestimates H_s in these locations (figure 5*a*). Moreover, this increase of the wMIZ mostly corresponds to areas in the Greenland and Barents Seas, where we would expect an underestimation of the wMIZ given that the model consistently overestimates the ice extent in these regions. This increase is particularly visible when considering the upper bound of the wMIZ extent (using the threshold $H_s = 0.5$ m). Using this definition of the wMIZ extent, S_{10} decreases by 35% between REF and NIDIS. In autumn, however, NIDIS captures more of the waves detected in the Beaufort and Chukchi Seas (figure 5*c*), and the wMIZ extent does not appear to be overestimated, at least when using $H_s = 1.5$ m as a threshold. This is visible in the S_{10} values, which are roughly similar for REF and NIDIS, while S_{01} in NIDIS is equal to 0.51, 20% higher than in REF

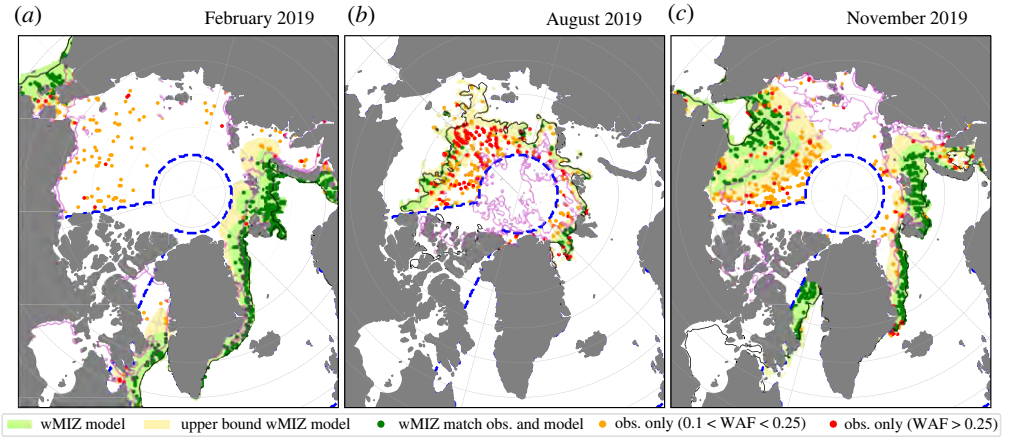

Figure 5. Same as figure 2 but for the NIDIS simulation. (Online version in colour.)

(0.41). The comparison between REF and NIDIS suggests that inelastic dissipation may not be a dominant mechanism in autumn, when sea ice in the MIZ is forming and consolidating. In winter, however, inelastic dissipation, or in general an attenuation process efficient at attenuating long waves in unbroken ice, seems necessary to obtain enough wave attenuation in thick pack ice, such as north of the Barents and Greenland Seas. This is particularly visible as few wave observations are found beyond the contour of sea-ice concentration higher than 0.8 in February (figure 2*a*).

The overestimation of the wave attenuation from inelastic dissipation in REF in autumn could also originate from an overestimation of the floe size. This is likely to be the case in our model, as we ignore the effects of processes other than waves [30] and assume that ice forms as an unbroken, continuous, thin ice sheet [23]. Lowering the flexural strength (LFXST) tends to increase the wMIZ extent, as it reduces the wave attenuation by making it easier for waves to break the ice, reducing the amount of inelastic dissipation in the model. The value of the flexural strength in REF was taken from [21], where it was shown to give approximately the right extent of broken ice after a wave event in the Beaufort Sea, while the value in LFXST is the one used in a number of other studies and originally suggested in [12]. Changes in S_{10} and S_{01} in winter and autumn are relatively small, which means that lowering the flexural strength has little impact on the wMIZ extent. However, if we consider the upper bound of the winter wMIZ, we find a relative decrease of S_{10} by 15% between REF and LFXST, suggesting that waves with lower heights are able to propagate significantly farther when the flexural strength is reduced. This suggests that the flexural strength value used in [21] (taken in the upper range of what is known of the flexural strength of sea ice) and in REF gives a better wMIZ extent overall, at least for a conservative approach.

As neither the inelastic dissipation nor the flexural strength fully explains this underestimation of the autumn wMIZ, we look more closely at the sea-ice properties. The sea-ice evaluation (§3a and table S2 in the electronic supplementary material) shows that the autumn sea-ice extent in the Beaufort and Chukchi Seas is slightly overestimated, but also that sea-ice concentration shows a clear positive bias (figure S2, electronic supplementary material), which likely explains part of the underestimated wMIZ extent. This is supported by the finding [27] that waves measured in pack ice are mostly locally generated, which requires the presence of open water that the model seems not to capture. However, this overestimation of sea-ice concentration could be partly compensated for by underestimation of the ice thickness at the end of summer, which should have the opposite effect. Adjusting the modelled ice extent and thickness in a specific region is not straightforward, particularly in a simulation with prescribed oceanic and atmospheric conditions. The best way to address this issue would be to use data assimilation, as in [41], but this is beyond the scope of the

present study. Note that we also investigated the sensitivity of our simulation to the wind speed by increasing $\beta_{\max}$, a non-dimensional wave growth parameter that controls the input of energy from the wind to the waves, but found very little impact within a reasonable range of values.

(d) Comparison with a floe size-defined MIZ

We now investigate how the wMIZ definition would compare with a floe size-based definition. Such definitions of the MIZ have been suggested in other studies [13,14,23], generally using the maximum floe size $D_{\max}$ as a metric. Using the same coupled system as here, Boutin *et al*. [23] investigated the impact of waves on sea-ice dynamics in a MIZ defined as the area with a $D_{\max}$ lower than 100 m. This maximum floe size is defined in neXtSIM as the 90th percentile of the areal floe size distribution, and mostly depends on the wavelength of the incoming waves [23]. It varies between 10 m (broken thin ice) and 1000 m (unbroken ice).

Here, we use the same definition as in [23], using the area where the monthly averaged value of the maximum floe size ($D_{\max}$) is lower than 100 m, and refer to this area as the dMIZ. We also look at the sensitivity of this definition in the 30–300 m range; 30 m corresponds roughly to the smallest floe size that can undergo flexural failure for an ice thickness less than 2 m [47], while 300 m corresponds to the maximum floe size associated with long waves (with periods of around 14 s) and is an upper bound for the dMIZ used in different studies (e.g. [22]). For all the simulations, the dMIZ extent is very similar to the wMIZ extent investigated before (figure 4*b*), with the exception of the months of September to November, where the area of broken ice exceeds the wMIZ extent by about 33% for REF. This is similar to the observed wMIZ, which also shows a clear peak in October. This similarity is not unexpected, as floe size in the current set-up is mostly influenced by wave break-up, and it is likely that more differences would emerge if other processes were also affecting the floe size. The dMIZ shows a rather high sensitivity to the choice of the value of $D_{\max}$, particularly in the range of 30–100 m, even if the qualitative evolution of the dMIZ extent remains unchanged. The dMIZ also shows greater sensitivity to the flexural strength wave attenuation (NIDIS vs REF) than the wMIZ, particularly in the autumn. This greater sensitivity of the dMIZ to the flexural strength is quite logical, as this latter quantity is used to determine whether break-up occurs [14,15]. We have some confidence in our fragmentation criterion (described in [15]), as Voermans *et al*. [48] note that it is consistent with observations. From our evaluation of the wMIZ, where REF performed better than LFXST, we suggest that the dMIZ in REF is a more reasonable estimate than LFXST.

The greater sensitivity of the dMIZ to wave attenuation processes than the wMIZ (when looking at REF and NIDIS) is possible because the wMIZ extent is constrained by the minimum H_s detected by IS-2, but waves with $H_s \simeq 0.3$ m can still break the ice [21], and observations do not allow us to constrain the attenuation for these waves. This is a key limitation of using the simple wave-detection approach to IS-2 data when it comes to constraining the modelled wave impact on ice in a model.

While we do not expect the model to predict $D_{\max}$ precisely, as the floe size distribution in the model is poorly constrained because of the limited observations available, it is still possible to interpret the meaning of average $D_{\max}$ values. The area defined by $D_{\max}$ lower than 300 m roughly corresponds to the area where the minimum value of $D_{\max}$ is lower than 100 m (figures S4 and S5, electronic supplementary material), meaning that fragmentation has occurred at least once in the month. It gives an upper bound on the ice-covered area impacted by waves, which is larger than the wMIZ extent, particularly in autumn. The area where $D_{\max}$ is lower than 100 m on average over the month corresponds to regions that are regularly undergoing wave-induced fragmentation, while the MIZ extent defined using $D_{\max}$ lower than 30 m is very similar to the wMIZ defined using the 90th percentile of H_s for each month (figure 3*a*).

We also compare the wMIZ and the dMIZ with the classical definition of the MIZ based on the concentration (cMIZ), i.e. the area with a sea-ice concentration between 0.15 and 0.8 [49,50] (figure 4*b*), which is a useful metric for climate model evaluation [51]. Here, we take the upper bound of the cMIZ to be 0.8, ignoring the fraction occupied by the 'newly formed ice' category

[38]. This ice type is meant to represent thin forming ice (frazil, nylas etc.), which may not be captured by satellite observations [52]. More importantly, this not-consolidated ice has no internal stress and its strength is therefore not affected by wave-induced ice break-up in the model [23]. As noted in [31], the wMIZ in REF mostly overlaps with the cMIZ (figure 2*a*,*c*), except in limited areas where the wMIZ encompasses more compact ice with a concentration higher than 0.8, mostly in the Greenland Sea and north of the Barents Sea. It is only when the wMIZ (and hence the dMIZ) extent is overestimated in winter (in NIDIS) that these areas of pack ice affected by waves become really significant (up to 25% of the wMIZ, instead of around 15% maximum in REF).

(e) Impact on sea-ice dynamics

One of the main goals of waves-in-ice modelling is to assess the potential of waves to affect sea-ice evolution, as was done with the model presented here and the sea-ice dynamics in [23], the latter focusing only on the Barents Sea in October 2015. The impact on ice deformation and drift compared to a reference uncoupled simulation was found to be significant in the aftermath of storm events, as areas of compact ice that had been fragmented were more mobile due to lower ice strength. However, on average over the whole 40-day period, the impact on the average drift was small (7%) and limited to a small region.

Here, we compare the simulations DMG, LFXST and NIDIS, in which fragmentation lowers the ice strength of compact ice, with REF (figure 4*d*). For a fair comparison between these four simulations, we define a fixed geographical area for each month that is independent of the simulation. We take it to be the area where $D_{\max}$ in REF is lower than 300 m and the monthly average concentration is higher than 0.8 (ignoring the forming ice as defined in [38], as it has no ice strength), as it gives a reasonable estimate of where fragmentation happens at least once during the month. This area is small, representing about one-third of the wMIZ extent in winter and quickly dropping to almost zero between April and October/November (figure 4*b*). We therefore limit our analysis to the months from October to March.

We find little difference in the average sea-ice drift in the selected area between the different simulations (not shown). A greater difference is visible when looking at the 20th percentile of drift speed, which is of the same order of magnitude as the average drift speed. This is consistent with [23], i.e. the impact was mostly an increase in mobility of fragmented ice when the drift is slow. The greatest increase in the drift speed for this percentile is found for LFXST, with drift velocities 12% higher than in REF, likely because a lower ice strength increases the amount of ice break-up. However, the increase in ice drift does not exceed 6% in DMG, where the wave attenuation and ice break-up are the same as in REF. Overall, the impact is therefore not significant on the sea-ice evolution in the model. This does not contradict [23]: waves can affect sea-ice mobility, but their impact remains limited in time and space. The fact that we still find an increase in low drift speed means that the updated neXtSIM rheology [33] used here compared to [23], with more resistance to convergence, does not prevent waves from affecting sea-ice deformation.

4. Discussion and conclusion

We have compared the wMIZ extent in a coupled wave–sea-ice model with observations from IS-2, showing satisfying results for our reference simulation. We have suggested two quantitative metrics, S_{01} and S_{10}, for assessing whether the modelled wMIZ extent is underestimated or overestimated. These metrics, S_{10} in particular, have to be considered in combination with a qualitative assessment of the wMIZ. Using our methodology, values of S_{10} above 0.66, such as for REF in winter, mean that the model does not overestimate the extent. Our method of comparing a wave–ice model with WAF observations provides a simple but robust way to evaluate model performance over a full year and for the whole Arctic. However, quantitative interpretation of the WAF remains largely uncertain and limits its use to assessing whether a modelled wMIZ is underestimated or overestimated. This is useful for investigating wave impact on sea ice in coupled models but limited when it comes to understanding wave attenuation, for

instance. The retrieval of wave spectra information, currently in development [36], should make comparison with other types of data easier [37]. Combining IS-2 data with remote sensing of floe size [30] and analysis of mooring measurements [27] in ice could also contribute to increasing our understanding of the WAF and wave–ice interactions in general.

Our results suggest the need for a modelled mechanism to dissipate wave energy in compact, thick, solid ice. Sea-ice models including floe size distributions should therefore be careful to have strong wave attenuation in the winter so as to not strongly overestimate the impact of waves in this season. A consequence of strong attenuation in pack ice in winter is that even when the wMIZ extent peaks due to large open-ocean waves, the amount of thick, compact ice affected by waves in the Arctic remains small. This is likely not the case in the Southern Ocean, where large wave events and long-period waves are much more frequent [19,36]. This has recently been shown in [36], wherewaves in IS-2 data were detected far beyond the in-ice extent of the cMIZ.

A consequence for sea-ice dynamics is that taking wave-induced fragmentation into account when computing the ice strength differs little from using classical concentration-based parametrizations [53]. However, in [23] Boutin *et al*. assumed that the recovery time scale of ice strength after a fragmentation event is the same as for brittle fracture in the pack ice, but wave break-up is likely to create a larger number of cracks in the sea ice and may have a longer-lasting effect. Another limitation of their approach is that it neglects the impact of floe–floe interactions on internal stress, which can be significant [54].

Data accessibility. The ICESat-2 dataset is publicly available at https://doi.org/10.1594/PANGAEA.918199. Scripts and modified routines will be available on GitHub after publication of this paper. The processed model outputs are available at https://ige-meom-opendap.univ-grenoble-alpes.fr/thredds/catalog/meomopendap/extract/SASIP/model-outputs/WW3-neXtSIM/catalog.html. The CS2SMOS sea-ice thickness product is available at ftp://ftp.awi.de/sea_ice/product/ (last accessed January 2022). The low-resolution daily sea-ice drift product and sea-ice concentration products from OSI-SAF can be found at ftp://osisaf.met.no/archive/ice/ (last accessed January 2022). The data are provided in the electronic supplementary material [55].

Authors' contributions. G.B.: conceptualization, investigation, methodology, validation and writing—original draft; T.W.: software, validation and writing—original draft; C.H.: conceptualization, data curation, methodology and, writing—original draft; L.B.: resources and software.

All authors gave final approval for publication and agreed to be held accountable for the work performed therein.

Conflict of interest declaration. We declare we have no competing interests.

Funding. This work was funded by the SASIP project, supported by Schmidt Futures—a philanthropic initiative that seeks to improve societal outcomes through the development of emerging science and technologies—and the European Space Agency (contract no. 4000127401/19/NL/LF—'ARKTALAS Hoavva').

References

1. Dumont D. 2021 Marginal ice zone dynamics: history, definitions and research perspectives. *Phil. Trans. R. Soc. A* **380**, 20210253. (doi:10.1098/rsta.2021.0253)
2. Andreas EL, Horst TW, Grachev AA, Persson POG, Fairall CW, Guest PS, Jordan RE. 2010 Parametrizing turbulent exchange over summer sea ice and the marginal ice zone. *Q. J. R. Meteorol. Soc.* **136**, 927–943. (doi:10.1002/qj.618)
3. Wadhams P. 1986 The seasonal ice zone. In *The geophysics of sea ice* (ed. N Untersteiner), pp. 825–991. NATO ASI Series. Boston, MA: Springer.
4. Steele M. 1992 Sea ice melting and floe geometry in a simple ice-ocean model. *J. Geophys. Res. Oceans* **97**, 17 729–17 738. (doi:10.1029/92JC01755)
5. Horvat C, Tziperman E, Campin JM. 2016 Interaction of sea ice floe size, ocean eddies, and sea ice melting. *Geophys. Res. Lett.* **43**, 8083–8090. (doi:10.1002/2016GL069742)
6. Asplin MG, Galley R, Barber DG, Prinsenberg SJ. 2012 Fracture of summer perennial sea ice by ocean swell as a result of Arctic storms. *J. Geophys. Res.* **117, C06025**. (doi:10.1029/2011JC007221)

7. Bateson AW, Feltham DL, Schröder D, Hosekova L, Ridley JK, Aksenov Y. 2020 Impact of sea ice floe size distribution on seasonal fragmentation and melt of Arctic sea ice. *Cryosphere* **14**, 403–428. (doi:10.5194/tc-14-403-2020)
8. Vichi M *et al.* 2019 Effects of an explosive polar cyclone crossing the Antarctic marginal ice zone. *Geophys. Res. Lett.* **46**, 5948–5958. (doi:10.1029/2019GL082457)
9. Collins CO III, Rogers WE, Marchenko AV, Babanin AV. 2015 In situ measurements of an energetic wave event in the Arctic marginal ice zone. *Geophys. Res. Lett.* **42**, 1863–1870. (doi:10.1002/2015GL063063)
10. Thomson J, Rogers WE. 2014 Swell and sea in the emerging Arctic ocean. *Geophys. Res. Lett.* **41**, 3136–3140. (doi:10.1002/2014GL059983)
11. Kwok R. 2018 Arctic sea ice thickness, volume, and multiyear ice coverage: losses and coupled variability (1958–2018). *Environ. Res. Lett.* **13**, 105005. (doi:10.1088/1748-9326/aae3ec)
12. Timco G, Weeks W. 2010 A review of the engineering properties of sea ice. *Cold Reg. Sci. Technol.* **60**, 107–129. (doi:10.1016/j.coldregions.2009.10.003)
13. Dumont D, Kohout AL, Bertino L. 2011 A wave-based model for the marginal ice zone including a floe breaking parameterization. *J. Geophys. Res.* **116**, 1–12. (doi:10.1029/2010JC006682)
14. Williams TD, Bennetts LG, Squire VA, Dumont D, Bertino L. 2013 Wave-ice interactions in the marginal ice zone. Part 2: numerical implementation and sensitivity studies along 1D transects of the ocean surface. *Ocean Model.* **71**, 92–101. (doi:10.1016/j.ocemod.2013.05.011)
15. Boutin G, Ardhuin F, Dumont D, Sévigny C, Girard-Ardhuin F, Accensi M. 2018 Floe size effect on wave-ice interactions: possible effects, implementation in wave model, and evaluation. *J. Geophys. Res. Oceans* **123**, 4779–4805. (doi:10.1029/2017JC013622)
16. Roach LA, Horvat C, Dean SM, Bitz CM. 2018 An emergent sea ice floe size distribution in a global coupled ocean-sea ice model. *J. Geophys. Res. Oceans* **123**, 4322–4337. (doi:10.1029/2017JC013692)
17. Roach LA, Bitz CM, Horvat C, Dean SM. 2019 Advances in modeling interactions between sea ice and ocean surface waves. *J. Adv. Model. Earth Syst.* **11**, 4167–4181. (doi:10.1029/2019MS001836)
18. Thomson J *et al.* 2018 Overview of the Arctic Sea State and Boundary Layer Physics program. *J. Geophys. Res.: Oceans* **123**, 8674–8687. (doi:10.1002/2018JC013766)
19. Kohout AL, Smith M, Roach LA, Williams G, Montiel F, Williams MJ. 2020 Observations of exponential wave attenuation in Antarctic sea ice during the PIPERS campaign. *Ann. Glaciol.* **61**, 196–209. (doi:10.1017/aog.2020.36)
20. Kohout AL, Meylan MH. 2008 An elastic plate model for wave attenuation and ice floe breaking in the marginal ice zone. *J. Geophys. Res.* **113**, C09016. (doi:10.1029/2007JC004434)
21. Ardhuin F, Boutin G, Stopa J, Girard-Ardhuin F, Melsheimer C, Thomson J, Kohout A, Doble M, Wadhams P. 2018 Wave attenuation through an Arctic marginal ice zone on October 12, 2015: 2. Numerical modeling of waves and associated ice break-up. *J. Geophys. Res. Oceans* **123**, 5652–5668. (doi:10.1002/2018JC013784)
22. Williams TD, Rampal P, Bouillon S. 2017 Wave-ice interactions in the neXtSIM sea-ice model. *Cryosphere* **11**, 2117–2135. (doi:10.5194/tc-11-2117-2017)
23. Boutin G, Williams T, Rampal P, Olason E, Lique C. 2021 Wave–sea-ice interactions in a brittle rheological framework. *Cryosphere* **15**, 431–457. (doi:10.5194/tc-15-431-2021)
24. Squire VA. 2007 Of ocean waves and sea-ice revisited. *Cold Reg. Sci. Technol.* **49**, 110–133. (doi:10.1016/j.coldregions.2007.04.007)
25. Nose T, Waseda T, Kodaira T, Inoue J. 2019 Satellite retrieved sea ice concentration uncertainty and its effect on modelling wave evolution in marginal ice zones. *Cryosphere Discuss.* **2019**, 1–42. (doi:10.5194/tc-2019-285)
26. Horvat C. 2022 Floes, the marginal ice zone and coupled wave-sea-ice feedbacks. *Phil. Trans. R. Soc. A* **380**, 20210252. (doi:10.1098/rsta.2021.0252)
27. Cooper VT, Roach LA, Thomson J, Brenner SD, Smith MM, Meylan MH, Bitz CM. 2022 Wind waves in sea ice of the western Arctic and a global coupled wave-ice model. *Phil. Trans. R. Soc. A* **380**, 20210258. (doi:10.1098/rsta.2021.0258)
28. Ardhuin F, Collard F, Chapron B, Girard-Ardhuin F, Guitton G, Mouche A, Stopa J. 2015 Estimates of ocean wave heights and attenuation in sea ice using the SAR wave mode on Sentinel-1A. *Geophys. Res. Lett.* **42**, 2317–2325. (doi:10.1002/2014GL062940)

29. Horvat C, Roach LA, Tilling R, Bitz CM, Fox-Kemper B, Guider C, Hill K, Ridout A, Shepherd A. 2019 Estimating the sea ice floe size distribution using satellite altimetry: theory, climatology, and model comparison. *Cryosphere* **13**, 2869–2885. (doi:10.5194/tc-13-2869-2019)
30. Hwang B, Wang Y. 2022 Multi-scale satellite observation of Arctic sea ice: a new insight into the life cycle of the floe size distribution. *Phil. Trans. R. Soc. A* **380**, 20210259. (doi:10.1098/rsta.2021.0259)
31. Horvat C, Blanchard-Wrigglesworth E, Petty A. 2020 Observing waves in sea ice with ICESat-2. *Geophys. Res. Lett.* **47**, e2020GL087629. (doi:10.1029/2020GL087629)
32. Rampal P, Dansereau V, Ólason E, Williams TD, Korosov A, Samaké A. 2019 On the multi-fractal scaling properties of sea ice deformation. *Cryosphere* **13**, 2457–2474. (doi:10.5194/tc-13-2457-2019)
33. Olason E, Boutin G, Korosov A, Rampal P, Williams T, Kimmritz M, Dansereau V, Samaké A. 2022 A new brittle rheology and numerical framework for large-scale sea-ice models. *J. Adv. Model. Earth Syst* **14**, e2021MS002685. (doi:10.1029/2021MS002685)
34. The WAVEWATCH III® Development Group (WW3DG). 2019 *User manual and system documentation of WAVEWATCH III version 6.07*. Technical Note 33. College Park, MD: NOAA/NWS/NCEP/MMAB.
35. Tilling RL, Ridout A, Shepherd A. 2018 Estimating Arctic sea ice thickness and volume using CryoSat-2 radar altimeter data. *Adv. Space Res.* **62**, 1203–1225. (doi:10.1016/j.asr.2017.10.051)
36. Brouwer J *et al.* 2022 Altimetric observation of wave attenuation through the Antarctic marginal ice zone using ICESat-2. *Cryosphere* **16**, 2325–2353. (doi:10.5194/tc-16-2325-2022)
37. Collard F, Marié L, Nouguier F, Kleinherenbrink M, Ehlers F, Ardhuin F. 2022 Wind-wave attenuation in Arctic sea ice: a discussion of remote sensing capabilities. *J. Geophys. Res. Oceans* **127**, e2022JC018654. (doi:10.1029/2022JC018654)
38. Rampal P, Dansereau V, Olason E, Bouillon S, Williams T, Korosov A, Samaké A. 2019 On the multi-fractal scaling properties of sea ice deformation. *Cryosphere* **13**, 2457–2474. (doi:10.5194/tc-13-2457-2019)
39. Stopa JE, Ardhuin F, Girard-Ardhuin F. 2016 Wave climate in the Arctic 1992–2014: seasonality and trends. *Cryosphere* **10**, 1605–1629. (doi:10.5194/tc-10-1605-2016)
40. Heorton H, Tsamados M, Armitage T, Ridout A, Landy J. 2021 Cryosat-2 significant wave height in polar oceans derived using a semi-analytical model of synthetic aperture radar 2011–2019. *Remote Sens.* **13**, 4166. (doi:10.3390/rs13204166)
41. Williams T, Korosov A, Rampal P, Ólason E. 2021 Presentation and evaluation of the Arctic sea ice forecasting system neXtSIM-F. *Cryosphere* **15**, 3207–3227. (doi:10.5194/tc-15-3207-2021)
42. Ricker R, Hendricks S, Kaleschke L, Tian-Kunze X, King J, Haas C. 2017 A weekly Arctic sea-ice thickness data record from merged Cryosat-2 and SMOS satellite data. *Cryosphere* **11**, 1607–1623. (doi:10.5194/tc-11-1607-2017)
43. Lavelle J, Tonboe R, Jensen M, Howe E. 2017 *Product user manual for OSI SAF global sea ice concentration*. Technical Report SAF/OSI/CDOP2/DMI/SCI/RP/225. Copenhagen, Denmark: Danish Meteorological Institute.
44. Lavergne T, Eastwood S. 2010 *Low resolution sea ice drift product user's manual*. Technical Report SAF/OSI/CDOP/met.no/TEC/MA/128. Oslo, Norway: Norwegian Meteorological Institute.
45. Goessling HF, Tietsche S, Day JJ, Hawkins E, Jung T. 2016 Predictability of the Arctic sea ice edge. *Geophys. Res. Lett.* **43**, 1642–1650. (doi:10.1002/2015GL067232)
46. Korosov A, Rampal P, Ying Y, Ólason E, Williams T. 2022 Towards improving short-term sea ice predictability using deformation observations. *Cryosphere Discuss.* **2022**, 1–20. (doi:10.5194/tc-2022-46)
47. Mellor M. 1983 *Mechanical behavior of sea ice*. Monograph 83-1. Hanover, NH: Cold Regions Research and Engineering Laboratory.
48. Voermans JJ *et al.* 2020 Experimental evidence for a universal threshold characterizing wave-induced sea ice break-up. *Cryosphere* **14**, 4265–4278. (doi:10.5194/tc-14-4265-2020)
49. Strong C, Rigor IG. 2013 Arctic marginal ice zone trending wider in summer and narrower in winter. *Geophys. Res. Lett.* **40**, 4864–4868. (doi:10.1002/grl.50928)
50. Rolph RJ, Feltham DL, Schröder D. 2020 Changes of the Arctic marginal ice zone during the satellite era. *Cryosphere* **14**, 1971–1984. (doi:10.5194/tc-14-1971-2020)

51. Horvat C. 2021 Marginal ice zone fraction benchmarks sea ice and climate model skill. *Nat. Commun.* **12**, 2221. (doi:10.1038/s41467-021-22004-7)
52. Ólason E, Rampal P, Dansereau V. 2021 On the statistical properties of sea-ice lead fraction and heat fluxes in the Arctic. *Cryosphere* **15**, 1053–1064. (doi:10.5194/tc-15-1053-2021)
53. Hibler III WD. 1979 A dynamic thermodynamic sea ice model. *J. Phys. Oceanogr.* **9**, 815–846. (doi:10.1175/1520-0485(1979)009<0815:ADTSIM>2.0.CO;2)
54. Herman A. 2022 Granular effects in sea ice rheology in the marginal ice zone. *Phil. Trans. R. Soc. A* **380**, 20210260. (doi:10.1098/rsta.2021.0260)
55. Boutin G, Williams T, Horvat C, Brodeau L. 2022 Modelling the Arctic wave-affected marginal ice zone: a comparison with ICESat-2 observations. Figshare. (doi:10.6084/m9.figshare.c.6135624)

Geophysical Research Letters

RESEARCH LETTER
10.1029/2022GL099024

Driving Mechanisms of an Extreme Winter Sea Ice Breakup Event in the Beaufort Sea

Jonathan W. Rheinlænder[1,2], Richard Davy[1], Einar Ólason[1], Pierre Rampal[3], Clemens Spensberger[4], Timothy D. Williams[1], Anton Korosov[1], and Thomas Spengler[4]

[1]Nansen Environmental and Remote Sensing Center and Bjerknes Centre for Climate Research, Bergen, Norway, [2]Department of Earth Science, University of Bergen, and Bjerknes Centre for Climate Research, Bergen, Norway, [3]Institut de Géophysique de l'Environnement, Université Grenoble Alpes/CNRS/IRD/G-INP, Grenoble, France, [4]Geophysical Institute, University of Bergen, and Bjerknes Centre for Climate Research, Bergen, Norway

Abstract The thick multiyear sea ice that once covered large parts of the Arctic is increasingly being replaced by thinner and weaker first-year ice, making it more vulnerable to breakup by winds. We use the neXtSIM sea ice model to investigate the driving mechanisms behind a large breakup event in the Beaufort Sea during winter 2013. Our simulations are the first to successfully reproduce the timing, location, and propagation of sea ice leads associated with wind-driven breakup and highlight the importance of accuracy of the atmospheric forcing, sea ice rheology, and changes in sea ice thickness. We found that the breakup resulted in enhanced export of multiyear ice from the Beaufort Sea. Overall, this leads to a relatively thinner and weaker simulated ice cover that potentially preconditions earlier breakup in spring and accelerates sea ice loss. Finally, our simulations indicate that large breakup events could become more frequent as Arctic sea ice continues to thin.

Plain Language Summary The loss of thick multiyear sea ice in the Arctic leads to weaker sea ice that is more easily broken up by strong winds. As a consequence, extreme sea ice breakup events may become more frequent, even during the middle of winter when the sea ice cover is frozen solid. This can lead to an earlier onset of the melt season and potentially accelerate Arctic sea ice loss. Such extreme breakup events are generally not captured by climate models, potentially limiting our confidence in projections of Arctic sea ice. We investigated the driving forces behind sea ice breakup events during winter and how they change in a future climate. Our sea ice model is the first to reproduce such breakup events and reveals that the combination of strong winds and thin sea ice is a key factor for these breakups. We found that winter breakups have a large effect on local heat and moisture transfer and cause enhanced sea ice production, but also increase the overall movement of the sea ice cover, making it more vulnerable. Finally, we show that if the Arctic sea ice continues to thin, these extreme breakup events could become even more frequent.

Key Points:

- An extreme winter breakup event in the Beaufort Sea is accurately simulated with the neXtSIM sea ice model
- High-resolution and skillful atmospheric forcing, as well as appropriate sea ice rheology, are necessary to simulate such breakups
- In the model, thinning Beaufort Sea ice is more vulnerable to breakup, which may accelerate loss of multiyear ice

Supporting Information:

Supporting Information may be found in the online version of this article.

Correspondence to:

J. W. Rheinlænder,
jonathan.rheinlaender@nersc.no

Citation:

Rheinlænder, J. W., Davy, R., Ólason, E., Rampal, P., Spensberger, C., Williams, T. D., et al. (2022). Driving mechanisms of an extreme winter sea ice breakup event in the Beaufort Sea. *Geophysical Research Letters*, *49*, e2022GL099024. https://doi.org/10.1029/2022GL099024

Received 4 APR 2022
Accepted 9 JUN 2022

Author Contributions:

Conceptualization: Jonathan W. Rheinlænder, Richard Davy, Pierre Rampal, Thomas Spengler
Data curation: Jonathan W. Rheinlænder, Clemens Spensberger, Timothy D. Williams
Formal analysis: Jonathan W. Rheinlænder, Anton Korosov
Funding acquisition: Richard Davy, Einar Ólason
Investigation: Jonathan W. Rheinlænder
Project Administration: Richard Davy, Einar Ólason
Resources: Clemens Spensberger, Timothy D. Williams, Anton Korosov

1. Introduction

Arctic sea ice is thinning (Meier, 2017) in conjunction with the decrease in the area covered by thick multiyear ice (MYI) (Kwok, 2018), which is replaced by thinner first-year ice (FYI) that is more mobile and less dynamically stable (Rampal et al., 2009; J. Zhang et al., 2012). This makes the ice cover more vulnerable to intense winds breaking up the sea ice. In the Beaufort Sea in particular, the loss of MYI may contribute to the earlier onset of the melt season in recent years (Johnson & Eicken, 2016).

When sea ice breaks up, it exposes the underlying warmer ocean within narrow, linear openings in the ice cover known as leads. This has important consequences for air-sea exchange, ocean eddy generation and dynamics, sea ice production, and Arctic Ocean properties in general (Cohanim et al., 2021; Graham et al., 2019; Nguyen et al., 2009), especially during the winter months when heat fluxes over sea ice are generally small (Andreas & Cash, 1999). In addition, breakup in winter weakens the ice cover, potentially preconditioning the minimum ice extent in summer (Y. Zhang et al., 2018; Babb et al., 2019) and thus creating a positive feedback to Arctic amplification (Dai et al., 2019). Therefore, extreme breakup events are of crucial interest for understanding the seasonal and long-term evolution of Arctic sea ice, which in turn affect weather, ecosystems, and local communities in polar regions and beyond (Forbes et al., 2016; Vihma, 2014).

Supervision: Richard Davy, Einar Ólason
Validation: Jonathan W. Rheinlænder, Timothy D. Williams, Anton Korosov
Visualization: Jonathan W. Rheinlænder
Writing – original draft: Jonathan W. Rheinlænder, Richard Davy, Einar Ólason, Pierre Rampal, Timothy D. Williams
Writing – review & editing: Jonathan W. Rheinlænder, Einar Ólason, Pierre Rampal, Clemens Spensberger, Thomas Spengler

Several studies have investigated the impact of storms on Arctic sea ice cover (e.g., J. Zhang et al., 2013; Graham et al., 2019; Wang et al., 2016). However, when it comes to modeling individual breakup events, and accurately reproducing the spatial distribution of leads, there have been few successful attempts (Ólason, Rampal, & Dansereau, 2021; Wang et al., 2016), and breakup events are not well captured in current sea ice and climate models (Spreen et al., 2017). This presents a critical gap in our understanding of atmosphere-ocean-ice interaction processes and limits the credibility of future projections of the climate in polar and subpolar regions (Notz & Stroeve, 2016).

This paper is the first step toward filling this gap by presenting simulations using the next-generation sea ice model—neXtSIM (Ólason, Rampal, & Dansereau, 2021; Rampal et al., 2016, 2019; Samaké et al., 2017)—focusing on a large breakup event that occurred in the Beaufort Sea during February and March 2013. This event was captured by the Visible Infrared Imaging Radiometer Suite of the Suomi NPP satellite (Beitsch et al., 2014) and coincided with a high-pressure system centered over the northwest Beaufort Sea (Figure 1a). The objective of this study is to identify the key factors driving such wintertime sea ice breakup events, and provide a first estimate of the consequences of these events for the Arctic sea ice volume budget.

2. neXtSIM Model Setup

All simulations presented here are performed with the stand-alone version of neXtSIM, which is a finite element sea ice model using a moving Lagrangian mesh (Bouillon & Rampal, 2015; Rampal et al., 2016). The spatial resolution of the mesh is about 10 km, covering the central Arctic. Sea ice mechanics are reproduced using the Brittle Bingham-Maxwell (BBM) rheology based on a damage propagation mechanism (Dansereau et al., 2016; Girard et al., 2011; Ólason, Boutin, et al., 2021). This allows for realistic reproduction of cracks and leads in the ice cover (Ólason, Rampal, & Dansereau, 2021; Rampal et al., 2019), making the neXtSIM ideal for simulating breakup events. Other relevant model settings are listed in Table S1 of Supporting Information S1.

The model is forced by hourly atmospheric fields from the polar-optimized version of the Weather Research and Forecasting (WRF) model version 3.9.1 (Polar-WRF; Hines et al., 2015; Powers et al., 2012). The WRF output is a dynamical downscaling of the European Centre for Medium Range Weather Forecasts (ECMWF) operational analysis with interior nudging toward the ECMWF analysis. We tested four different horizontal resolutions (10, 20, 40, and 80 km) to investigate the role of atmospheric resolution on simulating the 2013 breakup event. These are referred to as WRF10, WRF20, WRF40, and WRF80. To test the impact of not using a polar-specific atmospheric model, we also used the standard global reanalysis from ERA5 (Hersbach et al., 2020) with a horizontal resolution of 31 km (Figure S2 in Supporting Information S1). All neXtSIM simulations are initialized with sea ice fields from CS2/SMOS (Ricker et al., 2017) and are integrated from 13 February to 13 March 2013, encompassing the anticyclone passage.

2.1. Lead Fraction Definition

neXtSIM uses three ice categories; *new ice* (frazil ice formed in open water), *young ice* ($\lesssim$25 cm), and *old ice* ($\gtrsim$25 cm) and thus explicitly represents the thin and newly formed ice in leads (Rampal et al., 2019). When leads form in winter they quickly refreeze and become a mixture of open water and thin ice (Beitsch et al., 2014). Based on this, we define a lead fraction as the combined fraction of open water and young ice. A grid cell is then considered a lead when the lead fraction exceeds 5%, thereby excluding the thicker pack ice. This approach is comparable to previous lead detection algorithms (e.g., Röhrs & Kaleschke, 2012; Ólason, Rampal, & Dansereau, 2021).

To evaluate the accuracy of the model in capturing the breakup, we compare our results to satellite observations of leads (Arcleads derived from the Moderate Resolution Imaging Spectroradiometer; Willmes & Heinemann, 2015), ice drift from the Ocean and Sea Ice Satellite Application Facility (OSISAF; Lavergne et al., 2010), and sea ice deformation from RADARSAT data (Figure S1 in Supporting Information S1).

3. Simulating the 2013 Sea Ice Breakup Event

Satellite observations show that a fracture was already present by mid-February at Point Barrow in the western Beaufort Sea within an area covered by FYI (Figure 1b). Over the next few days, large pieces of sea ice started to break off and were transported toward the Chukchi Sea. On 23 February, an extensive arch-shaped fracture

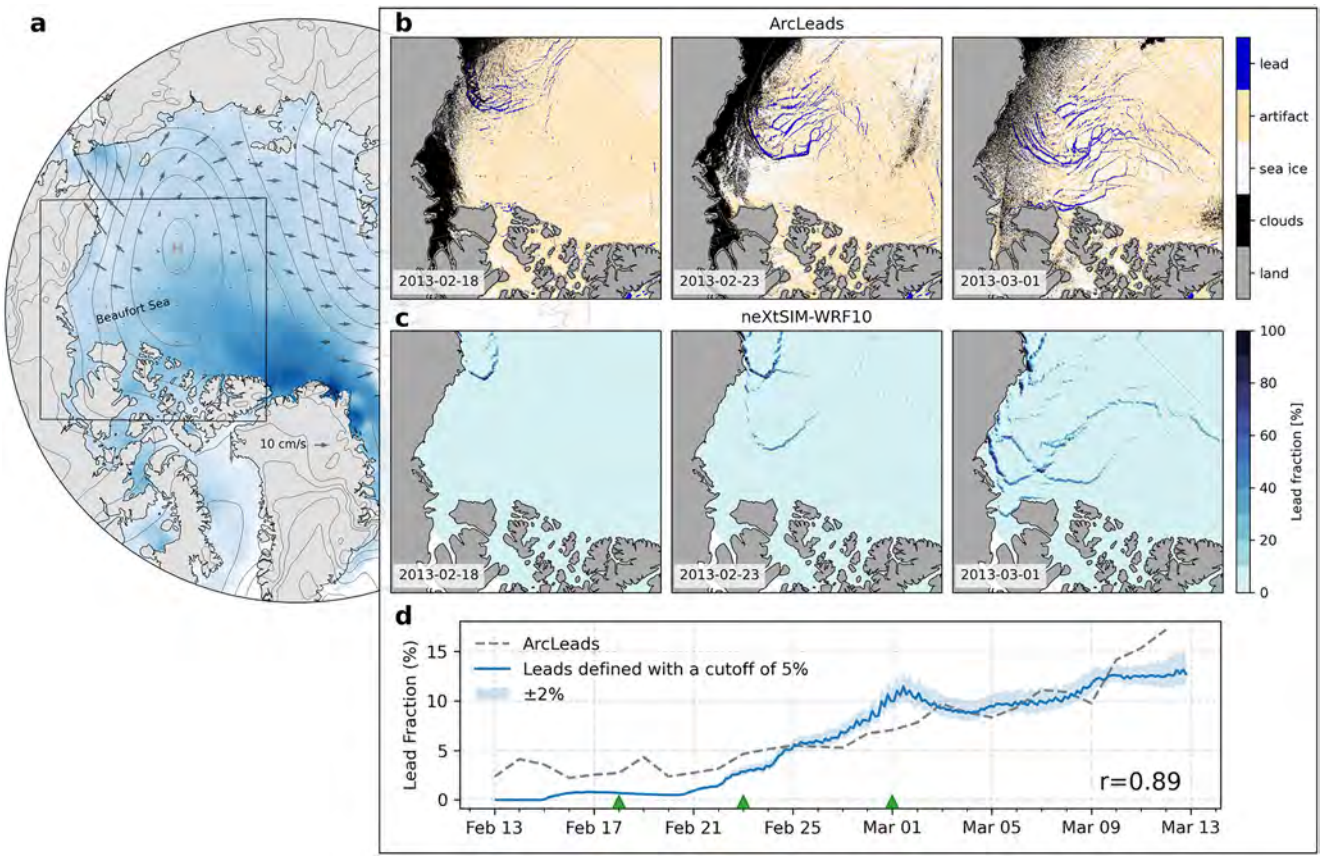

Figure 1. (a) Schematic map of the Beaufort Sea with the observed winter sea ice thickness from CS2/SMOS (shading), ice flow from neXtSIM (arrows), and mean sea-level pressure from ERA5 (solid and gray lines) all shown on 23 February 2013. (b) Daily categorical lead map following Willmes and Heinemann (2015) based on the Moderate Resolution Imaging Spectroradiometer imagery. (c) Simulated lead fraction using WRF10 as the atmospheric forcing. (d) Time series of lead area fraction in the Beaufort Sea for the model (blue) and Arcleads (gray-dashed line). Leads are defined as areas where the lead fraction exceeds 5%. The shading shows the sensitivity to using a threshold value of 3% and 7%, respectively. The r-value is the correlation coefficient between the observed and modeled lead fraction. Both (b and c) for 18, 23 February and 1 March 2013 are marked by green triangles in (d).

about 1,000 km long and ~4 km wide had formed, extending across nearly the entire Beaufort Sea with secondary fractures on the leeward side. By the end of February, the fracturing had expanded toward Banks Island in the east, at which point the ice cover was broken up and consisted of a myriad of free-drifting ice floes. The model shows remarkably good agreement with the observations, both in terms of the spatial pattern (Figure 1c) and the evolution of the lead area fraction in the Beaufort Sea (Figure 1d). In particular, the model captures the characteristic arch-shaped wave of fractures with the first opening close to Point Barrow in mid-February, propagating east toward Banks Island (see also Supporting Information Movie 1).

The simulated breakup pattern is due to a combination of the wind forcing (controlled by the location and strength of the anticyclone) and the coastal geometry. This makes the quality of the atmospheric forcing very important for simulating the breakup. By examining the internal stress state of the sea ice (not shown), we find that the fractures form due to a combination of high shear and comparatively low normal stresses. This is associated with westward winds blowing nearly parallel to the Alaskan coast (Figure 2a), causing sea ice to break tangentially to the coast (as also seen by Lewis & Hutchings, 2019). Once the wind speed exceeds a critical value (about 10 m s^{-1}), the ice breaks and fractures spread eastward in a step-like manner matching the timing of the anticyclone passage (Figure 2b). This critical threshold likely depends on multiple factors, including ice thickness and concentration, wind direction, and sea ice floe size distribution (Rampal et al., 2009; Stern et al., 2018). Overall, the simulated sea ice drift associated with the breakup is remarkably close to the observed drift from OSISAF (Figure 2c), especially in the pack ice (RMSE = 4.9 cm s^{-1}).

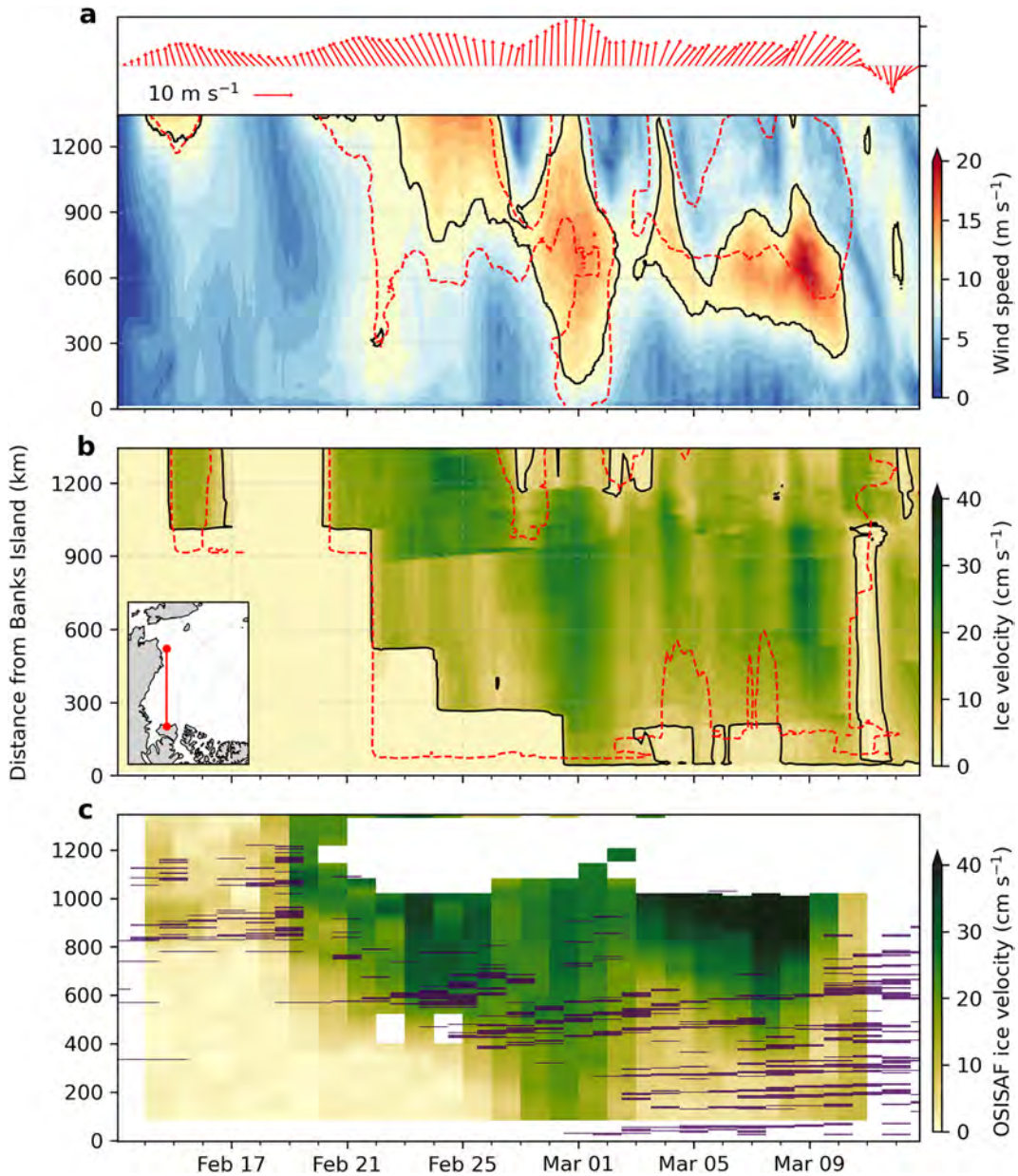

Figure 2. Time series during the breakup event of (a) wind speed and direction (red arrows; up = away from Banks Island), (b) sea ice velocity and lead propagation indicated by the 5-cm s^{-1} ice velocity contour, and (c) observed ice velocity from OSISAF and lead propagation from Arcleads data (purple lines). All variables are calculated along the transect indicated in (b) running from the western Beaufort Sea (close to Point Barrow) to Banks Island. Black lines in (a and b) represent the 10-m s^{-1} wind speed and 5-cm s^{-1} ice velocity, respectively. The red-dashed line corresponds to the WRF80 experiment.

Another important factor for the fidelity of the simulated breakup is the new BBM rheology (Ólason, Boutin, et al., 2021) employed in neXtSIM. Fracturing and threshold mechanics seen in both observations and the simulation are characteristics of the brittle nature of sea ice mechanics (Rampal et al., 2019; Schulson, 2009). In comparison, this is not adequately resolved in traditional elastic-viscous-plastic (EVP) models that typically require a horizontal resolution of about 1 km—between one and two orders of magnitude higher than what is used in the latest CMIP6 climate models—to represent sea ice deformation features at smaller scales (Hutter et al., 2019, 2022; Spreen et al., 2017; Wang et al., 2016). This can be seen from the neXtSIM simulation performed using the modified EVP rheology (mEVP; Figure S1 in Supporting Information S1). Compared to BBM, the mEVP simulates a much smoother sea ice deformation field and does not capture the fracture

propagation (although it does capture some arching at Point Barrow). We expect very high resolution (EVP) models to perform substantially better than the mEVP results shown here, but such experiments are costly and were not attempted here. The role of resolution in reproducing small-scale features in (E)VP models is being actively investigated in the community as well as that of modifying parameters and parameterizations within sea ice models (e.g., J. Zhang, 2021; Bouchat et al., 2022; Hutter et al., 2022).

3.1. Impact of Atmospheric Resolution on Sea Ice Breakup

Regional atmospheric properties, such as weather dynamics and horizontal gradients, are generally more skillfully reproduced at a higher resolution (Lindsay et al., 2014). To test how the simulated breakup is affected by the resolution of the atmospheric forcing, we performed additional experiments with different resolutions of the Polar-WRF model (Figure S2 and S3 in Supporting Information S1). Doing this, we find that using high-resolution forcing (WRF10 or WRF20) yields the characteristic progressive wave of fractures toward Banks Island, which matches the timing of the observed sequence of lead openings quite well (Figures 2b and 2c). Whereas the ice immediately breaks much further east, closer to Banks Island when using the low-resolution forcing.

The improved breakup pattern seen in WRF10 is due to the fact that the location of the anticyclone and associated winds is better reproduced at a higher resolution. In comparison, the lower resolution forcing (WRF40 and WRF80) exhibits stronger winds, exceeding 10 m s^{-1} in the central Beaufort due to an offset in the anticyclone track, causing the ice to break up prematurely (Figure S3 in Supporting Information S1). Hence, despite these relatively modest differences in the location and strength of the anticyclone between the high- and low-resolution forcing, we obtain major differences in the simulated breakup pattern. This underlines the nonlinear, threshold-like response of the ice to the atmospheric forcing.

The difference in the simulated wind fields is, however, not purely due to the resolution itself, but is also related to how the atmospheric dynamics behave at these higher resolutions. We demonstrate this by using the global ERA5 reanalysis, which despite its relatively high resolution of 31 km performed similarly to WRF80 (Figure S2 and S3 in Supporting Information S1). This suggests that not only the resolution but also proper tuning of the atmospheric model (e.g., improved parameterizations optimized for polar regions) is an important factor for simulating sea ice deformation (Hines et al., 2015).

4. Thinning Sea Ice Accelerates Wind-Induced Breakup

Following the minimum extent in 2012, the Beaufort Sea ice cover was exceptionally thin and weak in winter 2013 (Parkinson & Comiso, 2013), which may have preconditioned the breakup. Long-term sea ice thinning could therefore be expected to weaken the sea ice cover further and increase deformation rates (Rampal et al., 2009). To test this, we ran three sensitivity experiments with the initial sea ice thickness (SIT) set at 50% (0.5 × SIT), 150% (1.5 × SIT), and 200% (2.0 × SIT) of that of the control experiment (Figure S4 in Supporting Information S1). The average thickness in the Beaufort Sea for these three scenarios is 0.69 m, 2.01 m, and 2.75 m, respectively (compared to 1.37 m in the control experiment). Thus, for 0.5 × SIT, the winter ice cover mostly consists of thin FYI, which is projected to occur before the end of 2100 by CMIP6 models (Figure S4 in Supporting Information S1). The remaining two cases reflect sea ice conditions prior to the 2000s, when the Beaufort Sea ice cover was considerably thicker (Rothrock et al., 2008).

When the sea ice is thinner, it breaks up more easily and becomes more mobile, while for thicker sea ice, the threshold for initiating breakup is higher. This is because thicker sea ice has a higher mechanical strength compared to thin ice, limiting its fragmentation (Rampal et al., 2009). This relationship between thickness and mobility is reflected in the ratio between sea ice drift and wind speeds (Figure 3a), which increases with thinner ice (e.g., Maeda et al., 2020). In neXtSIM, the mechanical strength is a combination of Coulomb shear failure and a resistance to ridging proportional to ice thickness to the power 3/2 following Hopkins (1998). As a result, the modeled ice cover is more damaged when the sea ice is thin (SIT × 0.5) with more leads (lead fraction increases by ∼3%; Figure 3b), while for thicker ice (SIT × 1.5 and SIT × 2.0), stronger winds (>14 m s^{-1}) are required to break the ice and there is a large reduction in the drift speed. The start of the breakup also occurs progressively later with increasing thickness (21 February for 1.5 × SIT and around 1 March for 2.0 × SIT, Figure 3b), a direct consequence and illustration of thicker sea ice being more resistant to breakups. We caution, however, that the

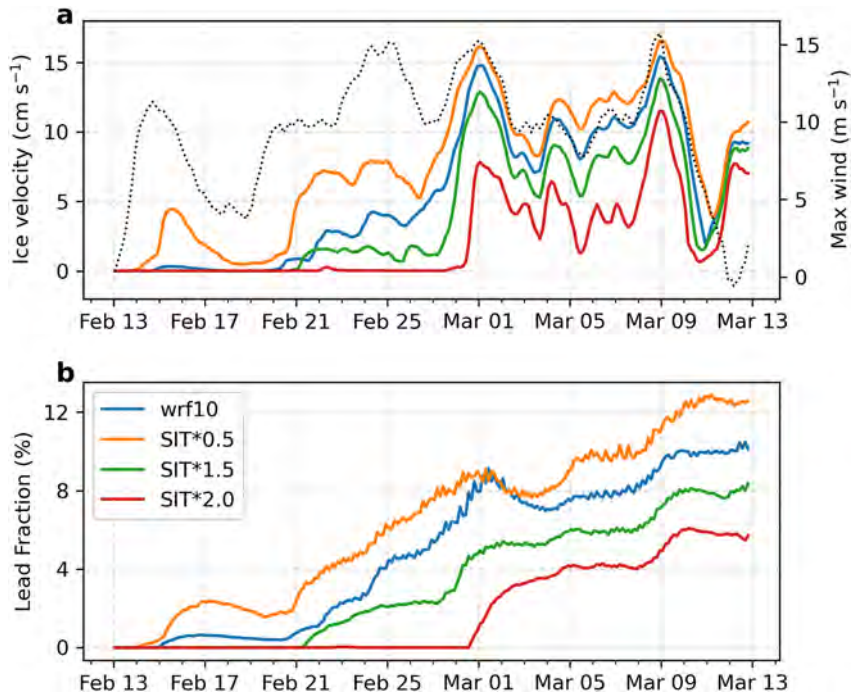

Figure 3. Time series of (a) mean sea ice velocities in the Beaufort Sea and maximum winds (gray-dashed line) in the along-transect direction (inset in Figure 2b). (b) Average lead fraction shown as a % of the total Beaufort Sea area. The area is outlined in Figure 4a.

sensitivity of the simulated failure to changes in ice thickness is likely to be more complicated in reality as the model may not fully reflect the true relationship between ice strength and ice thickness.

5. Local Impact on Ice Thickness and Volume

Opening of leads exposes the relatively warm ocean to the cold atmosphere, resulting in stronger heat and moisture transfers from the ocean to the atmosphere. Locally, heat fluxes in excess of 300 W m^{-2} are found in open leads (Figure S5 in Supporting Information S1), similar to those found in observations (Andreas & Cash, 1999). The enhanced ocean heat loss promotes new ice growth within the leads, which can be seen in the thickness distribution between 0 and 1 m (Figure 4a). During the breakup, the median thickness increases from 1.29 to 1.45 m (16 cm), corresponding to a net increase of 111 km^3 in ice volume (Table S2 in Supporting Information S1). Overall, this is comparable to earlier estimates from Babb et al. (2019) and thickness observations by Richter-Menge and Farrell (2013) obtained during winter 2013.

Changes in ice volume occur due to ice growth (thermodynamics) and ice advection (dynamics). First, we consider the thermodynamic impact of the breakup by estimating the ice growth in the Beaufort Sea for the leads and pack ice separately (see "Methods"). The total thermodynamic ice growth from 13 February to 13 March is 344 km^3 (Figure 4b) and is dominated by sea ice growth in the pack ice (80%). Thus, the formation of new ice in leads yields a ∼20% increase (67 km^3) in the Beaufort ice volume. This gives an average growth rate of ∼20 cm day^{-1} within leads (Figure S6 in Supporting Information S1), which is similar to growth rates observed in open water during winter (e.g., Skogseth et al., 2009).

The impact of changes in ice dynamics on the sea ice mass budget is illustrated in Figure 4d. As the ice cover becomes more fractured and mobile, more ice is also advected through the Beaufort Sea as a consequence of the strong (westward) winds and enhanced drift speeds (Figure 3a). During the event, there is a net sea ice export of 233 km^3, implying that 2/3 of the ice formed by thermodynamic processes is transported out of the region. Note that as the model underestimates the free ice drift (Figure 2c), the simulated export is likely a conservative estimate. This indicates that extreme winter breakup events may result in a thinner and thus weaker sea ice cover compared to years without any breakups. This can be illustrated by turning off the ice dynamics in the model,

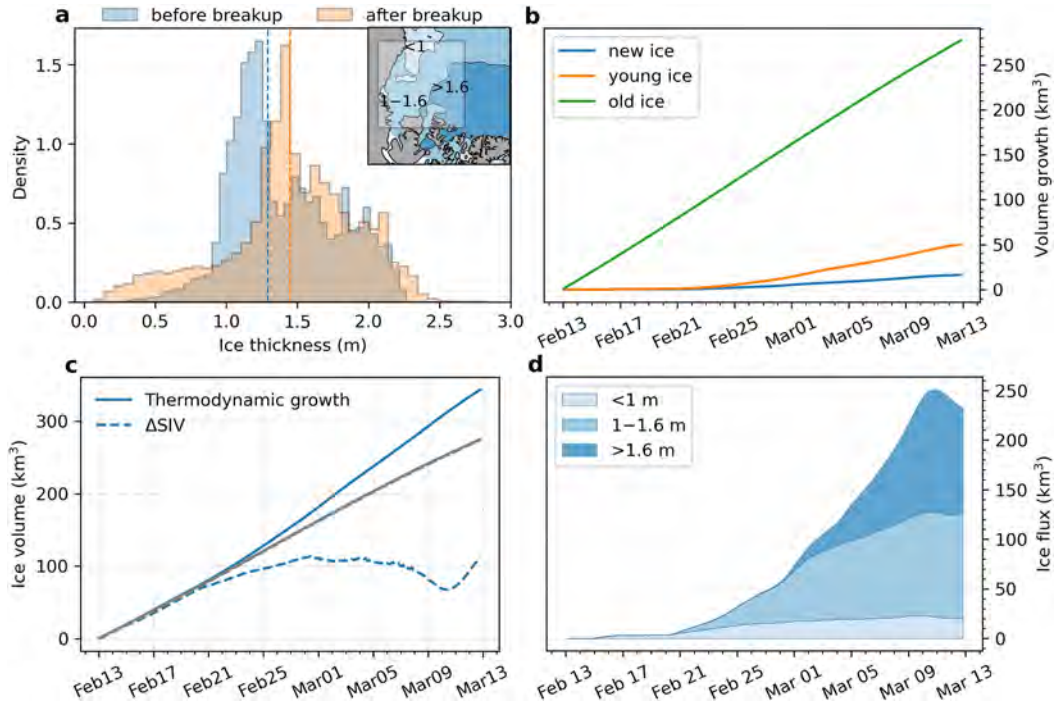

Figure 4. (a) Histograms of the normalized sea ice thickness in the Beaufort Sea before (blue) and after (orange) the breakup event. (b) Cumulative thermodynamic ice growth in the Beaufort Sea, calculated for new ice (blue line), young ice (orange line), and old ice (green line). (c) Total thermodynamic ice growth (solid line) and ice volume change (ΔSIV; dashed line) in the Beaufort Sea for WRF10 (blue) and no_motion (gray). In no_motion, the sea ice dynamics are turned off. (d) Time series of sea ice volume flux, where positive values correspond to an export out of the Beaufort Sea. The total flux is split into contributions from newly formed sea ice (SIT < 1 m), first-year ice (1 > SIT < 1.6 m), and multiyear ice (SIT > 1.6 m). The spatial distribution of the thickness classes is shown in (a) for February 13.

thereby preventing the breakup from occurring (no_motion in Figure 4c). In this case, due to the reduced ice export, there is much larger increase in ice volume (ΔSIV = 277 km^3), which is purely from the thermodynamic growth of pack ice.

During the initial stage of the breakup, it is predominantly FYI (<1.6 m thick) located in the central and southwestern Beaufort that is being exported westward into the Chukchi Sea (see inset in Figure 4a). When the fractures reach Banks Island on 1 March, the thicker and older ice (>1.6 m) is mobilized and subsequently transported to the Canadian Basin. This pattern is largely consistent with the climatological mean sea ice drift in the Beaufort Sea, following the anticyclonic motion of the Beaufort Gyre (Howell et al., 2016). Toward the end of the breakup, the sea ice flux decreases due to a reversal of the wind direction to the southeast (Figure 2a), enhancing transport of MYI located north of Greenland into the Beaufort Sea, where it replenishes the dynamic sea ice loss. Similarly, airborne observations from late March 2013 show a larger amount of MYI in the north central Beaufort Sea and the central Canada Basin compared to the previous year (Richter-Menge & Farrell, 2013).

6. Discussion and Conclusions

6.1. Challenges Simulating Extreme Breakup Events

In this study, we were able to successfully capture the main features of the 2013 breakup and show that it has a significant impact on the evolution of ice volume in the Beaufort Sea during winter. When it comes to the long-term and wider impacts of the breakup, there are some notable limitations of the current study, in part due to the lack of atmospheric and oceanic feedbacks in the model. Opening of leads has considerable influence on the overlying atmosphere (Lüpkes et al., 2008), which in turn has potential implications for the wider Arctic (Mioduszewski et al., 2018). For example, oceanic heat loss within leads causes near-surface temperature to increase by more than 20°C, which could enhance turbulent convection in the atmospheric boundary layer,

driving further breakup and sea ice production. The resulting changes in surface roughness, for example, from enhanced ridging or reduced concentration, could amplify this effect, but is not properly captured when using a constant and uniform atmospheric drag coefficient (Martin et al., 2016). On the other hand, low-level clouds that further increase downward long-wave radiation are often found over leads (Beitsch et al., 2014; Graham et al., 2019), thereby reducing surface heat loss and inhibiting thermodynamic ice growth.

At the ice-ocean interface, the opening of leads can trigger eddy generation through increased buoyancy fluxes that in turn affect large-scale sea ice dynamics and drift (Cohanim et al., 2021). The increase in drift speeds promotes a significant increase in ocean mixing and drives enhanced bottom melt by mixing up warmer water from below (J. Zhang et al., 2013; Graham et al., 2019). Most of these processes and feedbacks occur on small spatial and temporal scales, which are currently beyond the capabilities of CMIP-style models (Hutter et al., 2022), thus highlighting the need for developing sub-grid-scale parameterizations to account for such processes in future climate simulations.

6.2. Potential Implications for Arctic Sea Ice Loss

Although we cannot directly assess the long-term impact from a single modeled event, our findings suggest that sea ice breakup in winter could lead to an overall reduction in Arctic sea ice in the long term. This is supported by Graham et al. (2019) who show that Arctic winter storms may precondition the sea ice cover for a faster summer melt by promoting enhanced lateral melt rates in deformed sea ice. Similarly, Babb et al. (2019) showed that enhanced sea ice export from the Beaufort Sea in winter results in a thinner and weaker ice cover by the start of the melting season, which could promote an earlier breakup of sea ice in spring. This would accelerate the ice-albedo feedback and a further loss of Arctic sea ice (Dai et al., 2019). However, despite the breakup in winter 2013, the Arctic sea ice volume actually increased that year (Tilling et al., 2015), implying that other factors are also important for controlling year-to-year variations in the Arctic sea ice mass budget (e.g., Screen et al., 2011).

As sea ice in the Beaufort Sea continues to thin (Kwok, 2018), our model results suggest that it becomes more vulnerable to wind-driven breakup during winter months. This could affect ice motion further upstream and potentially increase advection of MYI across the Beaufort Sea (Hutchings & Rigor, 2012; Richter-Menge & Farrell, 2013). Here, it becomes more exposed to summer melt (Babb et al., 2019; Kwok & Cunningham, 2010), thereby reducing the survivability of the remaining MYI in the Arctic. If the frequency of extreme weather events (particularly extreme anticyclones) also increases in the future (Walsh et al., 2020), this could lead to more breakup and further amplify the loss of MYI. Ultimately, these findings highlight that winter breakup events may lead to a faster reduction in Arctic sea ice volume than currently projected by coupled climate models (Davy & Outten, 2020).

Acknowledgments
This work was supported by the Bjerknes Centre for Climate Research through the AOI project, the European Space Agency (Grant Nos. AO/1-9595/18/NL/LF and contract no. 4000132195/20/I-NB—"Digital Twin Earth Precursors—Oceans"; contract no. 4000127401/19/NL/LF—"ARKTALAS Hoavva"), and the Research Council of Norway ("ARIA", Grant No. 302934). The model simulations were performed on resources provided by UNINETT Sigma2—the National Infrastructure for High Performance Computing and Data Storage in Norway. The authors thank A. Komarov from Environment and Climate Change Canada for help with accessing Radarsat-2 data and S. Willmes for providing the Arcleads data set. Finally, we wish to thank J. Hutchings and D. Ringeisen for reviewing the manuscript and inspiring discussions that greatly helped improve the paper.

Data Availability Statement

The neXtSIM model output is available at https://zenodo.org/record/5639492#.YYJJLZso9M8. Scripts for data analysis and plotting can be found at https://zenodo.org/record/6607546#.YpjbcTlBxM8 with the https://doi.org/10.5281/zenodo.6607546. The ERA-5 data (Hersbach et al., 2020) were downloaded from the Copernicus Climate Change Service Climate Data Store (C3S) https://cds.climate.copernicus.eu/cdsapp#!/dataset/reanalysis-era5-single-levels?tab=overview. The Arcleads data set (Willmes & Heinemann, 2015) was obtained from https://meteo.uni-trier.de/v2/arcleads.php. The OSISAF data are freely available at MET-Norway (https://osisaf-hl.met.no/).

References

Andreas, E. L., & Cash, B. A. (1999). Convective heat transfer over wintertime leads and polynyas. *Journal of Geophysical Research*, *104*(C11), 25721–25734. https://doi.org/10.1029/1999jc900241

Babb, D. G., Landy, J. C., Barber, D. G., & Galley, R. J. (2019). Winter sea ice export from the Beaufort Sea as a preconditioning mechanism for enhanced summer melt: A case study of 2016. *Journal of Geophysical Research: Oceans*, *124*(9), 6575–6600. https://doi.org/10.1029/2019jc015053

Beitsch, A., Kaleschke, L., & Kern, S. (2014). Investigating high-resolution AMSR2 sea ice concentrations during the February 2013 fracture event in the Beaufort Sea. *Remote Sensing*, *6*(5), 3841–3856. https://doi.org/10.3390/rs6053841

Bouchat, A., Hutter, N., Chanut, J., Dupont, F., Dukhovskoy, D., Garric, G., et al. (2022). Sea ice rheology experiment (SIREx), part I: Scaling and statistical properties of sea-ice deformation fields. *Journal of Geophysical Research: Oceans*, *127*(4). https://doi.org/10.1029/2021jc017667

Bouillon, S., & Rampal, P. (2015). Presentation of the dynamical core of neXtSIM, a new sea ice model. *Ocean Modelling*, *91*, 23–37. https://doi.org/10.1016/j.ocemod.2015.04.005

Cohanim, K., Zhao, K. X., & Stewart, A. L. (2021). Dynamics of eddies generated by sea ice leads. *Journal of Physical Oceanography*, *51*(10), 3071–3092. https://doi.org/10.1175/JPO-D-20-0169.1

Dai, A., Luo, D., Song, M., & Liu, J. (2019). Arctic amplification is caused by sea-ice loss under increasing CO 2. *Nature Communications*, *10*(1), 1–13. https://doi.org/10.1038/s41467-018-07954-9

Dansereau, V., Weiss, J., Saramito, P., & Lattes, P. (2016). A Maxwell elasto-brittle rheology for sea ice modelling. *The Cryosphere*, *10*(3), 1339–1359. https://doi.org/10.5194/tc-10-1339-2016

Davy, R., & Outten, S. (2020). The arctic surface climate in CMIP6: Status and developments since CMIP5. *Journal of Climate*, *33*(18), 8047–8068. https://doi.org/10.1175/JCLI-D-19-0990.1

Forbes, B. C., Kumpula, T., Meschtyb, N., Laptander, R., MacIas-Fauria, M., Zetterberg, P., et al. (2016). Sea ice, rain-on-snow and tundra reindeer nomadism in Arctic Russia. *Biology Letters*, *12*(11), 20160466. https://doi.org/10.1098/rsbl.2016.0466

Girard, L., Bouillon, S., Weiss, J., Amitrano, D., Fichefet, T., & Legat, V. (2011). A new modeling framework for sea-ice mechanics based on elasto-brittle rheology. *Annals of Glaciology*, *52*(57), 123–132. https://doi.org/10.3189/172756411795931499

Graham, R. M., Itkin, P., Meyer, A., Sundfjord, A., Spreen, G., Smedsrud, L. H., et al. (2019). Winter storms accelerate the demise of sea ice in the Atlantic sector of the Arctic Ocean. *Scientific Reports*, *9*(1), 1–16. https://doi.org/10.1038/s41598-019-45574-5

Hersbach, H., Bell, B., Berrisford, P., Hirahara, S., Horányi, A., Muñoz-Sabater, J., et al. (2020). The ERA5 global reanalysis. *Quarterly Journal of the Royal Meteorological Society*, *146*(730), 1999–2049. https://doi.org/10.1002/qj.3803

Hines, K. M., Bromwich, D. H., Bai, L., Bitz, C. M., Powers, J. G., & Manning, K. W. (2015). Sea ice enhancements to polar WRF. *Monthly Weather Review*, *143*(6), 2363–2385. https://doi.org/10.1175/MWR-D-14-00344.1

Hopkins, M. A. (1998). Four stages of pressure ridging. *Journal of Geophysical Research*, *103*(C10), 21883–21891. https://doi.org/10.1029/98JC01257

Howell, S. E. L., Brady, M., Derksen, C., & Kelly, R. E. J. (2016). Recent changes in sea ice area flux through the Beaufort Sea during the summer. *Journal of Geophysical Research: Oceans*, *121*(4), 2659–2672. https://doi.org/10.1002/2015jc011464

Hutchings, J. K., & Rigor, I. G. (2012). Role of ice dynamics in anomalous ice conditions in the Beaufort Sea during 2006 and 2007. *Journal of Geophysical Research*, *117*(C8), C00E04. https://doi.org/10.1029/2011JC007182

Hutter, N., Bouchat, A., Dupont, F., Dukhovskoy, D., Koldunov, N., Lee, Y., et al. (2022). Sea ice rheology experiment (SIREx), part II: Evaluating linear kinematic features in high-resolution sea-ice simulations. *Journal of Geophysical Research: Oceans*, *127*(4). https://doi.org/10.1029/2021jc017666

Hutter, N., Zampieri, L., & Losch, M. (2019). Leads and ridges in Arctic sea ice from RGPS data and a new tracking algorithm. *The Cryosphere*, *13*(2), 627–645. https://doi.org/10.5194/tc-13-627-2019

Johnson, M., & Eicken, H. (2016). Estimating Arctic sea-ice freeze-up and break-up from the satellite record: A comparison of different approaches in the Chukchi and Beaufort Seas. *Elementa: Science of the Anthropocene*, *2016*(4), 000124. https://doi.org/10.12952/journal.elementa.000124

Kwok, R. (2018). Arctic sea ice thickness, volume, and multiyear ice coverage: Losses and coupled variability (1958-2018). *Institute of Physics Publishing*, *13*(No. 10), 105005. https://doi.org/10.1088/1748-9326/aae3ec

Kwok, R., & Cunningham, G. F. (2010). Contribution of melt in the Beaufort Sea to the decline in Arctic multiyear sea ice coverage: 1993-2009. *Geophysical Research Letters*, *37*(20). https://doi.org/10.1029/2010GL044678

Lavergne, T., Eastwood, S., Teffah, Z., Schyberg, H., & Breivik, L. A. (2010). Sea ice motion from low-resolution satellite sensors: An alternative method and its validation in the Arctic. *Journal of Geophysical Research*, *115*(10), 2009JC005958. https://doi.org/10.1029/2009JC005958

Lewis, B. J., & Hutchings, J. K. (2019). Leads and associated sea ice drift in the beaufort sea in winter. *Journal of Geophysical Research: Oceans*, *124*(5), 3411–3427. https://doi.org/10.1029/2018jc014898

Lindsay, R., Wensnahan, M., Schweiger, A., & Zhang, J. (2014). Evaluation of seven different atmospheric reanalysis products in the arctic. *Journal of Climate*, *27*(7), 2588–2606. https://doi.org/10.1175/JCLI-D-13-00014.1

Lüpkes, C., Vihma, T., Birnbaum, G., & Wacker, U. (2008). Influence of leads in sea ice on the temperature of the atmospheric boundary layer during polar night. *Geophysical Research Letters*, *35*(3), 3805. https://doi.org/10.1029/2007gl032461

Maeda, K., Kimura, N., & Yamaguchi, H. (2020). Temporal and spatial change in the relationship between sea-ice motion and wind in the arctic. *Polar Research*, *39*. https://doi.org/10.33265/polar.v39.3370

Martin, T., Tsamados, M., Schroeder, D., & Feltham, D. L. (2016). The impact of variable sea ice roughness on changes in Arctic Ocean surface stress: A model study. *Journal of Geophysical Research: Oceans*, *121*(3), 1931–1952. https://doi.org/10.1002/2015JC011186

Meier, W. (2017). Losing Arctic sea ice: Observations of the recent decline and the long-term context. In D. Thomas (Ed.), *Sea ice* (Third Edit ed., pp. 290–303). Wiley Blackwell.

Mioduszewski, J., Vavrus, S., & Wang, M. (2018). Diminishing Arctic Sea ice promotes stronger surface winds. *Journal of Climate*, *31*(19), 8101–8119. https://doi.org/10.1175/jcli-d-18-0109.1

Nguyen, A. T., Menemenlis, D., & Kwok, R. (2009). Improved modeling of the Arctic halocline with a subgrid-scale brine rejection parameterization. *Journal of Geophysical Research*, *114*(C11), C11014. https://doi.org/10.1029/2008jc005121

Notz, D., & Stroeve, J. (2016). Observed Arctic sea-ice loss directly follows anthropogenic CO2 emission. *Science*, *354*(6313), 747–750. https://doi.org/10.1126/science.aag2345

Ólason, E., Boutin, G., Korosov, A., Rampal, P., Williams, T., Kimmritz, M., et al. (2021). *A new brittle rheology and numerical framework for large-scale sea-ice models*. JAMES. https://www.essoar.org/doi/10.1002/essoar.10507977.4

Ólason, E., Rampal, P., & Dansereau, V. (2021). On the statistical properties of sea-ice lead fraction and heat fluxes in the arctic. *The Cryosphere*, *15*(2), 1053–1064. https://doi.org/10.5194/tc-15-1053-2021

Parkinson, C. L., & Comiso, J. C. (2013). On the 2012 record low Arctic sea ice cover: Combined impact of preconditioning and an August storm. *Geophysical Research Letters*, *40*(7), 1356–1361. https://doi.org/10.1002/grl.50349

Powers, J. G., Manning, K. W., Bromwich, D. H., Cassano, J. J., & Cayette, A. M. (2012). A decade of Antarctic science support through amps. *Bulletin of the American Meteorological Society*, *93*(11), 1699–1712. https://doi.org/10.1175/bams-d-11-00186.1

Rampal, P., Bouillon, S., Ólason, E., & Morlighem, M. (2016). NeXtSIM: A new Lagrangian sea ice model. *The Cryosphere*, *10*(3), 1055–1073. https://doi.org/10.5194/tc-10-1055-2016

Rampal, P., Dansereau, V., Olason, E., Bouillon, S., Williams, T., Korosov, A., & Samaké, A. (2019). On the multi-fractal scaling properties of sea ice deformation. *The Cryosphere*, *13*(9), 2457–2474. https://doi.org/10.5194/tc-13-2457-2019

Rampal, P., Weiss, J., & Marsan, D. (2009). Positive trend in the mean speed and deformation rate of Arctic sea ice, 1979–2007. *Journal of Geophysical Research*, *114*(C5), C05013. https://doi.org/10.1029/2008jc005066

Richter-Menge, J. A., & Farrell, S. L. (2013). Arctic sea ice conditions in spring 2009–2013 prior to melt. *Geophysical Research Letters*, *40*(22), 5888–5893. https://doi.org/10.1002/2013gl058011

Ricker, R., Hendricks, S., Kaleschke, L., Tian-Kunze, X., King, J., & Haas, C. (2017). A weekly Arctic sea-ice thickness data record from merged CryoSat-2 and SMOS satellite data. *The Cryosphere*, *11*(4), 1607–1623. https://doi.org/10.5194/tc-11-1607-2017

Röhrs, J., & Kaleschke, L. (2012). An algorithm to detect sea ice leads by using AMSR-E passive microwave imagery. *The Cryosphere*, *6*(2), 343–352. https://doi.org/10.5194/TC-6-343-2012

Rothrock, D. A., Percival, D. B., & Wensnahan, M. (2008). The decline in arctic sea-ice thickness: Separating the spatial, annual, and interannual variability in a quarter century of submarine data. *Journal of Geophysical Research*, *113*(C5), C05003. https://doi.org/10.1029/2007jc004252

Samaké, A., Rampal, P., Bouillon, S., & Ólason, E. (2017). Parallel implementation of a Lagrangian-based model on an adaptive mesh in C++: Application to sea-ice. *Journal of Computational Physics*, *350*, 84–96. https://doi.org/10.1016/J.JCP.2017.08.055

Schulson, E. M. (2009). Fracture of ice and other Coulombic materials. In *Mechanics of natural solids* (pp. 177–202). https://doi.org/10.1007/978-3-642-03578-4_8

Screen, J. A., Simmonds, I., & Keay, K. (2011). Dramatic interannual changes of perennial Arctic sea ice linked to abnormal summer storm activity. *Journal of Geophysical Research*, *116*(D15), D15105. https://doi.org/10.1029/2011JD015847

Skogseth, R., Nilsen, F., & Smedsrud, L. H. (2009). Supercooled water in an Arctic polynya: Observations and modeling. *Journal of Glaciology*, *55*(189), 43–52. https://doi.org/10.3189/002214309788608840

Spreen, G., Kwok, R., Menemenlis, D., & Nguyen, A. T. (2017). Sea-ice deformation in a coupled ocean–sea-ice model and in satellite remote sensing data. *The Cryosphere*, *11*(4), 1553–1573. https://doi.org/10.5194/tc-11-1553-2017

Stern, H. L., Schweiger, A. J., Stark, M., Zhang, J., Steele, M., & Hwang, B. (2018). Seasonal evolution of the sea-ice floe size distribution in the Beaufort and Chukchi seas. *Elementa: Science of the Anthropocene*, *6*. https://doi.org/10.1525/ELEMENTA.305

Tilling, R. L., Ridout, A., Shepherd, A., & Wingham, D. J. (2015). Increased Arctic sea ice volume after anomalously low melting in 2013. *Nature Geoscience*, *8*(8), 643–646. https://doi.org/10.1038/ngeo2489

Vihma, T. (2014). Effects of Arctic sea ice decline on weather and climate: A review. *Surveys in Geophysics*, *35*(5), 1175–1214. https://doi.org/10.1007/s10712-014-9284-0

Walsh, J. E., Ballinger, T. J., Euskirchen, E. S., Hanna, E., Mård, J., Overland, J. E., et al. (2020). *Extreme weather and climate events in northern areas: A review* (Vol. 209). Elsevier B.V. https://doi.org/10.1016/j.earscirev.2020.103324

Wang, Q., Danilov, S., Jung, T., Kaleschke, L., & Wernecke, A. (2016). Sea ice leads in the Arctic Ocean: Model assessment, interannual variability and trends. *Geophysical Research Letters*, *43*(13), 7019–7027. https://doi.org/10.1002/2016gl068696

Willmes, S., & Heinemann, G. (2015). Pan-arctic lead detection from MODIS thermal infrared imagery. *Annals of Glaciology*, *56*(69), 29–37. https://doi.org/10.3189/2015AoG69A615

Zhang, J. (2021). Sea ice properties in high-resolution sea ice models. *Journal of Geophysical Research: Oceans*, *126*(1), e2020JC016686. https://doi.org/10.1029/2020JC016686

Zhang, J., Lindsay, R., Schweiger, A., & Rigor, I. (2012). Recent changes in the dynamic properties of declining Arctic sea ice: A model study. *Geophysical Research Letters*, *39*(20), 2012GL053545. https://doi.org/10.1029/2012gl053545

Zhang, J., Lindsay, R., Schweiger, A., Steele, M., Lindsay, R., Schweiger, A., & Steele, M. (2013). The impact of an intense summer cyclone on 2012 Arctic sea ice retreat. *Geophysical Research Letters*, *40*(4), 720–726. https://doi.org/10.1002/grl.50190

Zhang, Y., Cheng, X., Liu, J., & Hui, F. (2018). The potential of sea ice leads as a predictor for summer Arctic sea ice extent. *The Cryosphere*, *12*(12), 3747–3757. https://doi.org/10.5194/tc-12-3747-2018

Response of Total and Eddy Kinetic Energy to the Recent Spinup of the Beaufort Gyre

HEATHER REGAN, CAMILLE LIQUE, AND CLAUDE TALANDIER

Univ. Brest, CNRS, IRD, Ifremer, Laboratoire d'Océanographie Physique et Spatiale, IUEM, Brest, France

GIANLUCA MENEGHELLO

Department of Earth, Atmospheric and Planetary Sciences, Massachusetts Institute of Technology, Cambridge, Massachusetts

(Manuscript received 23 September 2019, in final form 26 November 2019)

ABSTRACT

The Beaufort Gyre in the Arctic Ocean has spun up over the past two decades in response to changes of the wind forcing and sea ice conditions, accumulating a significant amount of freshwater. Here a simulation performed with a high-resolution, eddy-resolving model is analyzed in order to provide a detailed description of the total and eddy kinetic energy and their response to this spinup of the gyre. On average, and in contrast to the typical open ocean conditions, the levels of mean and eddy kinetic energy are of the same order of magnitude, and the eddy kinetic energy is only intensified along the boundary and in the subsurface. In response to the strong anomalous atmospheric conditions in 2007, the gyre spins up and the mean kinetic energy almost doubles, while the eddy kinetic energy does not increase significantly for a long time period. This is because the isopycnals are able to flatten and the gyre expands outwards, reducing the potential for baroclinic instability. These results have implications for understanding the mechanisms at play for equilibrating the Beaufort Gyre and the variability and future changes of the Arctic freshwater system.

1. Introduction

The Beaufort Gyre is an anticyclonic upper-ocean circulation feature that is the largest reservoir of freshwater in the Arctic (Haine et al. 2015; Carmack et al. 2016). Variability of freshwater export from the Arctic has the potential to influence the North Atlantic circulation and climate (Jahn and Holland 2013), for example, through contributing to Great Salinity Anomalies there (e.g., Belkin et al. 1998; Dickson et al. 1988), and affecting deep water formation (Arzel et al. 2008). The potential role of the gyre freshwater reservoir in modulating this export has motivated the recent effort to pin down the functioning of the Beaufort Gyre. This is particularly timely as we know the gyre is not in steady state. Satellite altimetry has indicated that the gyre has spun up during the 2000s (Giles et al. 2012), with hydrographic observations demonstrating that there was an associated increase in freshwater content of over 5400 km^3 (around one-third of the content in 2003) between 2003 and 2010 (Krishfield et al. 2014). Characterization of the gyre from recent satellite observations of sea surface height (SSH) has indicated a gyre expansion at a rate of 53 000 $km^2\,yr^{-1}$ toward the northwest from 2003 to 2014, resulting in the 2014 annual-mean gyre being almost double its 2003 area, with elevated gyre intensity between 2008 and 2012 (Regan et al. 2019).

Our current understanding of Beaufort Gyre dynamics mostly comes from simple process models (Davis et al. 2014; Lique et al. 2015; Manucharyan and Spall 2016; Meneghello et al. 2018a; Doddridge et al. 2019) and can be summarized as a three-way balance. At the surface, winds associated with the anticyclonic Beaufort Sea high drive Ekman pumping, and its resulting intensity is largely determined by the difference between the ice and ocean surface velocities (a process known as the ice–ocean governor; Meneghello et al. 2018b). The remaining input of energy induces downwelling and deepening of the halocline, which, in simple process models, is balanced by an eddy flux acting to flatten the isopycnals and stabilize the gyre

Corresponding author: Heather Regan, heather.regan@ifremer.fr

DOI: 10.1175/JPO-D-19-0234.1

(e.g., Manucharyan and Spall 2016). This balance is thought to occur on a long time scale (from a few years to a few decades; Doddridge et al. 2019; Johnson et al. 2018; Manucharyan et al. 2017) and suggests a link between small scale features and changes to the large scale circulation. The focus of this paper is to investigate the validity of the three-way balance in a realistic model, and in particular to quantify the response of the total and eddy kinetic energy to the recent spinup of the gyre.

Based on observations from a limited amount of temperature and salinity profiles collected by ice-tethered profilers (ITPs; Toole et al. 2011), Zhao et al. (2016) found that the number of eddies within the western Canada Basin increased in 2013–14 compared to the previous decade, and they hypothesized that this increase might be the consequence of the gyre spinup, resulting from more active baroclinic instability of the Beaufort Gyre. Moreover, the gyre changes could increase the number of eddies since expansion could increase interactions with shelf waters, boundary currents and topography (Zhao et al. 2016), although the presence of a continental slope may also help to stabilize the gyre, impeding the development of baroclinic instability at the edge of the gyre, and thus eddy generation, instead deepening the halocline (Manucharyan and Isachsen 2019). Therefore, determining the response of the eddy field to a gyre spinup is nontrivial. This has not been done before, largely because state-of-the-art numerical simulations do not resolve the small Rossby radius in the Arctic (~10 km; Nurser and Bacon 2014) and thus the evolution of the eddy field in the Arctic remains largely unknown.

Arctic eddies are generated from a variety of mechanisms and on different scales, and their presence was discussed in the literature before their role for Beaufort Gyre dynamics was established. Eddies were first observed in the Canada Basin in the 1970s (Newton et al. 1974; Manley and Hunkins 1985). They serve to transport heat and salt (Hunkins 1981), and can play an important role in the biological pump in the Beaufort Sea (Watanabe et al. 2014). The prevalent mesoscale eddies in the Canada Basin, with diameters around 10 km, are concentrated in the stratified halocline (Timmermans et al. 2008; Zhao et al. 2014). There is a higher density in the southern portion of the basin (Plueddemann et al. 1998; Zhao et al. 2016) where anticyclonic flow is the strongest (Armitage et al. 2017). The depth, size, and core properties of eddies suggest that there are multiple source regions and formation mechanisms (Zhao et al. 2014), to include eddies arising from baroclinic instabilities in the basin interior and in boundary currents, such as the inflow of Pacific Water into the Arctic basin via the Alaskan Coastal Current (Manley and Hunkins 1985) or the Beaufort shelfbreak jet (Plueddemann et al. 1998; Pickart et al. 2013; Spall et al. 2008; Watanabe and Hasumi 2009), and mixed layer instabilities at surface fronts (Brannigan et al. 2017). Examining the distribution of eddy kinetic energy (EKE) provides a first step toward determining the relative contributions of those different instabilities to the mesoscale activity in the Arctic. In the open ocean, surface EKE has been estimated for decades based on satellite observations of SSH (e.g., Le Traon 1991). In the Arctic, ice cover has thus far prevented us to estimate surface EKE, and the recent SSH dataset developed by Armitage et al. (2016) remains at too low spatial (~25 km) and temporal (monthly) resolution to resolve the mesoscale features in the region.

In this paper we use a high-resolution, eddy-resolving Arctic model to investigate the total KE and EKE fields in the Canada Basin, and their links with the dynamics of the Beaufort Gyre in a period of strong spinup. The remainder of this paper is structured as follows. Section 2 briefly presents the numerical model and simulation analyzed in this study. In section 3, we provide a 3D description of the gyre and its temporal variations, and compare the model outputs to available observations. A detailed description of the temporal and spatial variations of the levels of total and eddy kinetic energy is given in section 4, followed by a discussion of the mechanisms at play to explain their variations in section 5. Conclusions are given in section 6.

2. Methods

In this study we make use of the regional Arctic–North Atlantic high-resolution model configuration named CREG12 (Canadian Regional; Dupont et al. 2015). A 5-day mean of model sea surface salinity (SSS) of the Arctic portion of the domain is shown in Fig. 1. CREG12 is a seamless regional extraction (i.e., the ''north-fold'' discontinuity of the global grid is removed) of the ORCA12 configuration developed jointly by the Drakkar consortium and Mercator-Océan (Barnier et al. 2006; Tréguier et al. 2014), encompassing the Arctic and parts of the North Atlantic down to 27°N. It is based on the NEMO 3.6 (Madec 2016) and LIM 3.5 (Rousset et al. 2015) numerical models for the ocean and sea ice components, respectively. The configuration has a high vertical (75 levels) and horizontal (3–4 km) resolution in the Arctic Ocean, meaning that baroclinic eddies are resolved everywhere in the Arctic except on the shallow shelves (Dupont et al. 2015). Parameterizations include a Laplacian mixing of temperature and salinity along isopycnals, a horizontal biharmonic viscosity, and a

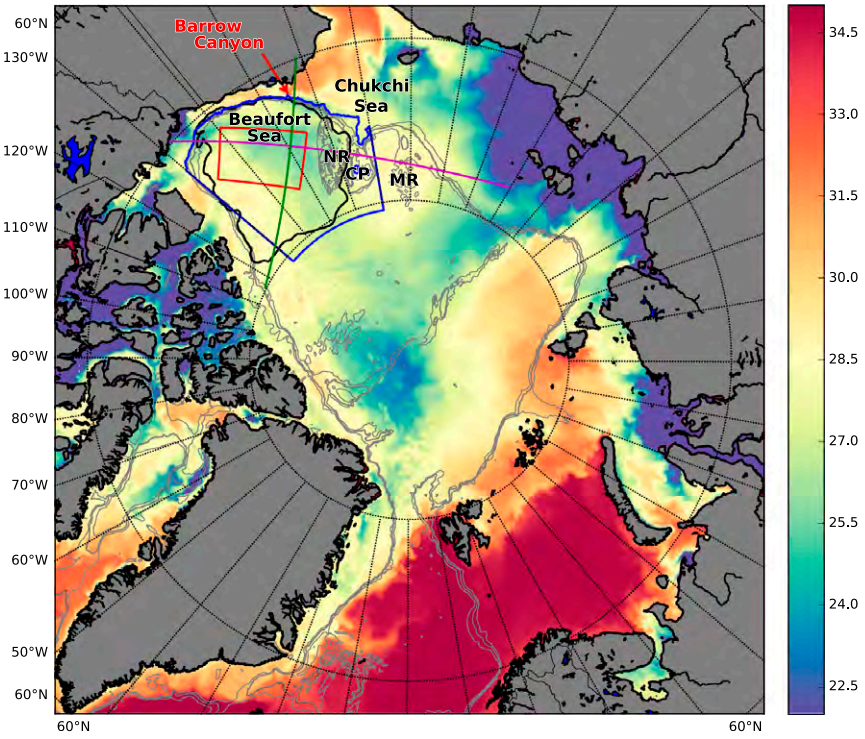

FIG. 1. Map of modeled sea surface salinity (SSS; psu) from the 5-day average centered on 3 Aug 2007. The corresponding gyre area defined as the largest closed sea surface height contour is shown in black. Key locations and regions used for computations are also shown: green (section A) and magenta (section B) lines indicate locations of cross sections through the center of the 1990–2014 mean gyre at 74.74°N, 209.38°E. Also shown are the BG box (blue box), a region defined as 70.5°–80.5°N, 190°–230°E, and limited by the 300-m bathymetry contour, and the central gyre (red box). Bathymetry contours are shown at 500, 1000, and 1500 m. The Beaufort Sea and Chukchi Sea are labeled, as are the Northwind Ridge (NR), Chukchi Plateau (CP), Mendeleev Ridge (MR), and Barrow Canyon.

turbulence closure scheme (TKE) for vertical mixing. The representation of tidal mixing effects is included in the new comprehensive parameterization of mixing by breaking internal tides and lee waves (de Lavergne et al. 2019).

Initial conditions are taken from the *World Ocean Atlas 2009* climatology for temperature and salinity while the ocean is at rest. The initial sea ice thickness and concentration are taken from a long ORCA12 simulation performed by the Drakkar group. Along the lateral open boundaries, monthly climatological conditions (comprising 3D velocities, temperature and salinity, and sea ice thickness and concentration) are taken from the same ORCA12 simulation. In particular, the transport of volume, heat and freshwater through the Bering Strait are comparable to the observational estimates from Woodgate et al. (2015). Regarding the atmospheric forcing, we use the latest version of the Drakkar Forcing Set (DFS 5.2), which is an updated version of the forcing set described in Brodeau et al. (2010). Inputs from the river and ice sheet runoff are based on the Dai and Trenberth (2002) climatological dataset, which has been recently corrected to include the large and increasing contribution from Greenland (Hu et al. 2019).

The simulation covers the period 1979–2014, and we only analyze the following the period of 1990–2014, in order to allow for the adjustment of the ocean and sea ice conditions. All analysis is carried out on 5-day mean model outputs unless otherwise stated.

3. Variability of the Beaufort Gyre

We first evaluate the capacity of the model simulation to reproduce the spatiotemporal variability of the Beaufort Gyre as captured by available observational datasets. We make use of the altimetry-derived Dynamic Ocean Topography (DOT) dataset produced by Armitage et al. (2016, 2017), spanning 2003–14 with monthly temporal resolution and 0.75° × 0.25° resolution in longitude and latitude, respectively. Following the method of Regan et al. (2019),

we define the gyre in both the observations and the model output as follows, noting that model SSH is equivalent to observed DOT, albeit referenced to a different constant level. First, the maximum SSH within the box defined by 140°–280°E, 68°–81.5°N is deemed the gyre center. When the gyre is present, its SSH at the center exceeds that of individual eddies, so this method identifies the center of the gyre rather than an individual anticyclonic eddy (verified by visual inspection). Then the gyre area in the model is defined as the largest closed SSH contour around this maximum.

Based on this detection algorithm of the gyre, we find that the model successfully reproduces both the location of the Beaufort Gyre and its shift over 2003–14 (Figs. 2a,b). The annual-mean gyre extent varies between the deep basin with a western limit over the Northwind Ridge in 2003, to a bathymetry-bounded large gyre reaching the Mendeleev Ridge to the west and the continental slope north of the Canadian Arctic Archipelago to the east in 2014. The northward extent also generally varies in line with DOT observations. Quantitatively, some differences between the model and altimetry data do exist. Some are expected due to the differing resolutions of the two products; for example, more spatial variability might be expected in the model which is at a higher resolution. The increase of the gyre area and the shift of its center toward the northwest is also less linear in the model than in the observations, with the gyre area in the model being, for instance, roughly as large in 2005 as in 2012 (Fig. 2b). One should note that the maps shown Figs. 2a and 2b are based on the detection of the gyre from annual-mean SSH, and thus the variations captured here slightly differ from the variability visible in Figs. 2c and 2d, which are based on monthly mean SSH fields. Nonetheless, the seasonal and interannual variability of the gyre area is well represented, with a correlation coefficient of 0.64 between the two time series after removing the linear trend (Fig. 2d). The mismatch in gyre area between the simulation and the observations in 2007 and 2008 is partly due to the 81.5°N northern limit of the satellite data before 2011.

The model also accurately simulates the maximum SSH variability when compared to the DOT variability from observations (Fig. 2c), with a correlation coefficient of 0.63 after detrending. This parameter was found to be a good proxy for the intensity of the gyre (Regan et al. 2019), and thus also reflects the variations of the freshwater content stored within the gyre (e.g., Proshutinsky et al. 2009). Indeed, when compared against the freshwater content estimated from summertime CTD and mooring data from the Beaufort Gyre Exploration Project (BGEP; Proshutinsky et al. 2020) averaged over a box bounded by 190°–230°E, 70.5°–80.5°N (excluding the regions shallower than 300 m), hereafter termed the ''BG box,'' the documented increase in freshwater content occurring after 2007 is also captured well (Fig. 2e). A good representation of the integrated freshwater content suggests that the model is able to accurately represent the variations of both the salinity in the halocline and the depth of the isohalines (see also Figs. 3e–h).

Both the time series of the freshwater content and the maximum SSH (and thus the gyre intensity) suggest that a regime shift occurs in 2007–08, with a spinup phase occurring from 2003 to 2007, and a stabilization after 2008, consistent with the modeling results of J. Zhang et al. (2016). In the following, we will contrast these two periods (referred to as ''spinup'' for 2003–07 and ''post-spinup'' for 2008–14) when examining the energetics of the gyre, and compare them to the long term average (1990–2014). The variability of the gyre is partly driven by the surface forcing (Fig. 2g; Meneghello et al. 2017; Regan et al. 2019); the rapid shift occurring in 2007–08, which has been linked to short-lived anomalous surface forcing (e.g., Zhong et al. 2019b), is also discussed in section 5.

While the observational datasets provide an accurate description of some aspects of the spatiotemporal variability of the Beaufort Gyre, models outputs are required to obtain a full 3D description of the gyre. To investigate its vertical structure, we use two sections that intersect at the 1990–2014 mean center of the gyre, referred to as sections A (south–north) and B (east–west), as shown in Fig. 1. The increase in SSH occurring from 1990 to 2014, associated with freshwater convergence within the gyre, is accompanied by a deepening of the halocline in the center of the gyre (Figs. 3a–d; corresponding bathymetry shown in Figs. 3i,j). Note that in the cold Arctic, isohalines and isopycnals are roughly equivalent. The mirroring of SSH and isohalines on time scales longer than a season is expected as the Beaufort Gyre dynamics can be examined considering the system as a fresh layer overlying a stationary Atlantic layer (e.g., Davis et al. 2014), that is thus governed by the dynamics of a 1.5-layer reduced gravity model. The deepening in the gyre center was indeed seen in simple process models (e.g., Manucharyan and Spall 2016). However, the model mean salinity section here demonstrates a clear asymmetry across the gyre that was not captured in those idealized models (Figs. 3e,f) but is present in the MIMOC climatology (Schmidtko et al. (2013), plotted along sections A and B in Figs. 3g and 3h). Overall the model reproduces well the depth of the halocline and the steep salinity gradient across it, although the

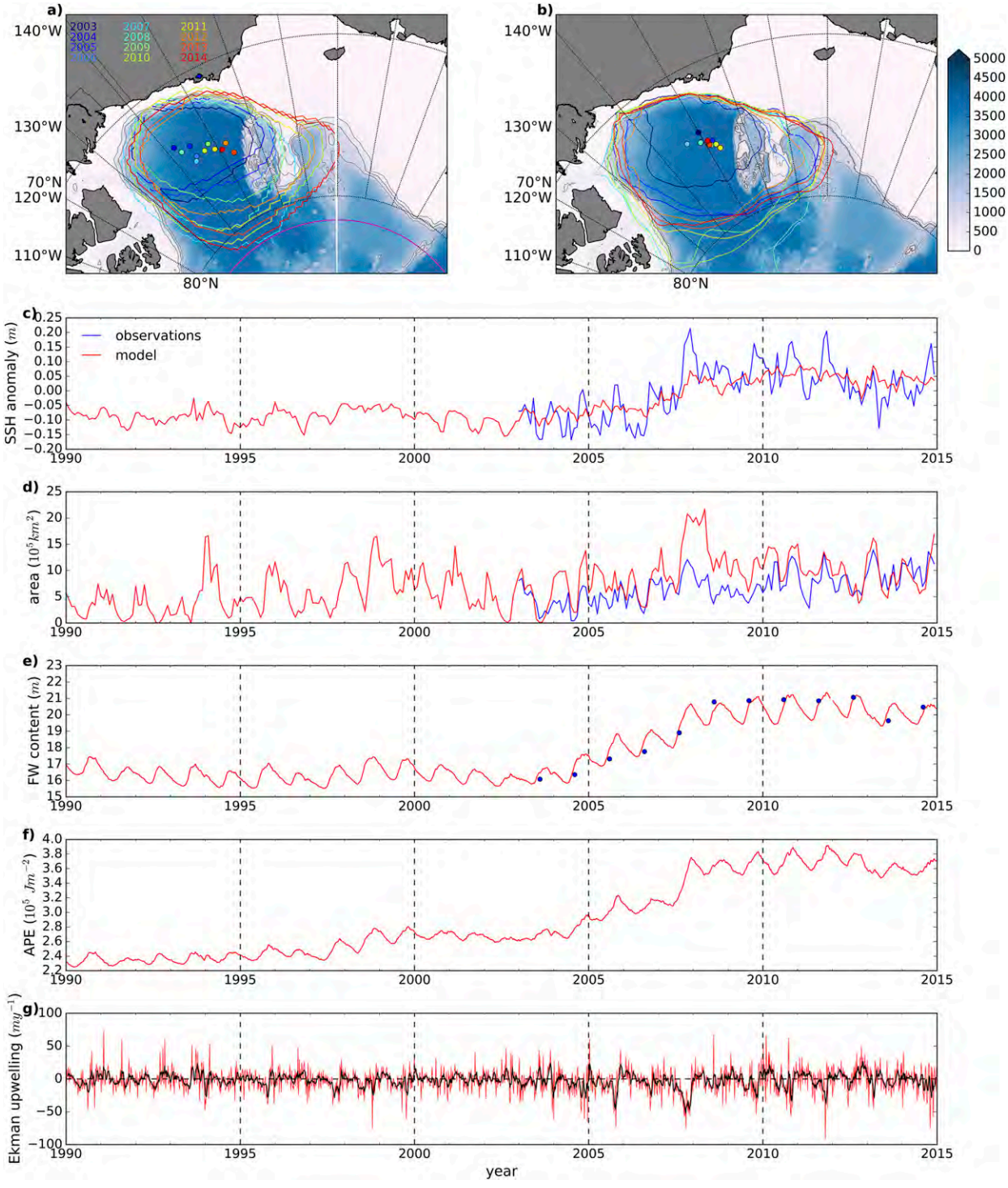

FIG. 2. Annual-mean gyre extent from 2003 to 2014 in (a) DOT observations from Armitage et al. (2016, 2017) and (b) the model, overlaid onto GEBCO bathymetry and model bathymetry, respectively. The center of the gyre in each year is also shown with a dot. (c) Anomaly from the 2003–14 mean of the monthly maximum height of the gyre SSH (red) and observed DOT (blue). (d) Monthly gyre area in the model (red) and observations (blue). (e) Average freshwater (FW) content relative to 34.8 psu in the BG box from the model (red) and the BGEP (blue dots). (f) Vertically integrated APE from the base of the halocline to the surface, based on the method by Polyakov et al. (2018). (g) Average Ekman pumping within the BG box (red, with 30-day running mean shown in black), estimated from the surface ocean stress from the model.

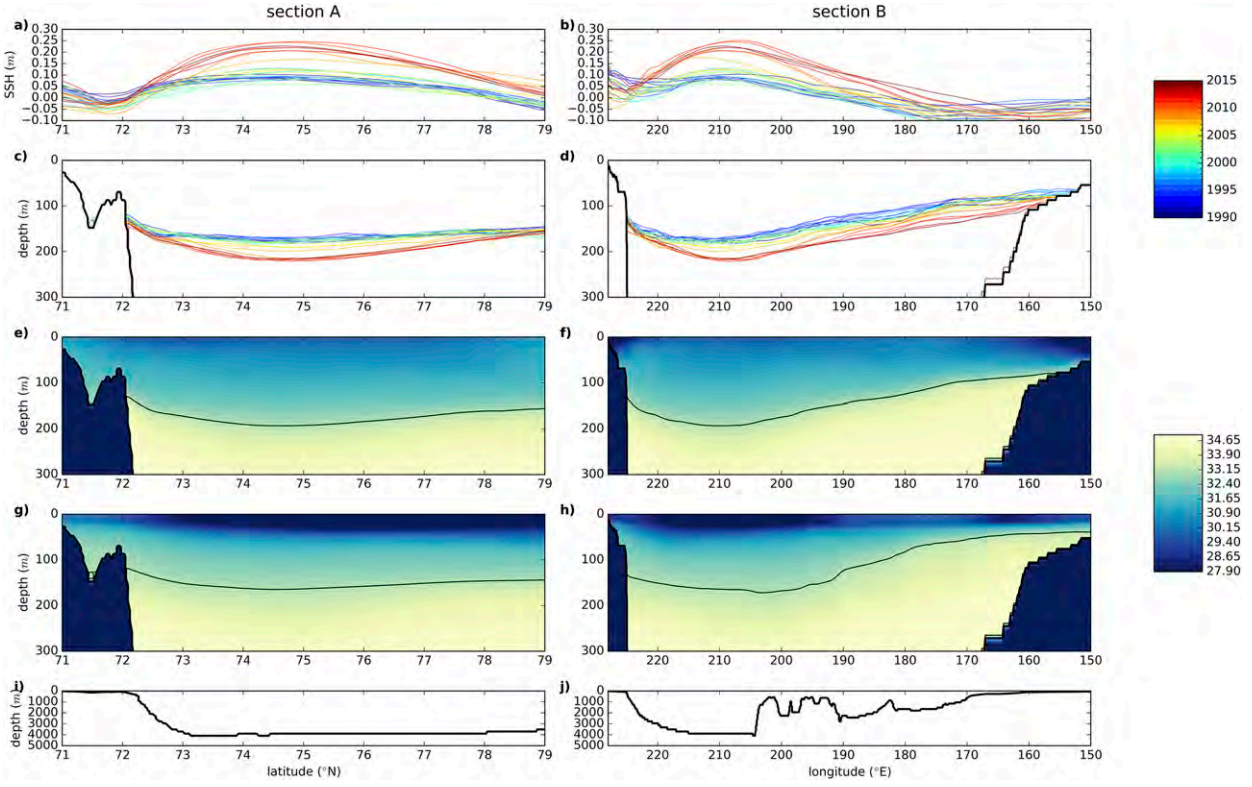

FIG. 3. Annual-mean SSH across (a) section A and (b) section B (see Fig. 1 for the locations). (c),(d) Annual-mean depth of the 33-psu isohaline across sections A and B, respectively. (e),(f) The 1990–2014 model climatology of salinity across sections A and B, with the 33-psu isohaline drawn in black. (g),(h) Salinity from the MIMOC climatology (Schmidtko et al. 2013), interpolated onto the model grid across the same sections, also with the 33-psu isohaline drawn in black. (i),(j) The bathymetry across sections A and B; the shallow bathymetry from 205° to 190°E in section B is the Chukchi Plateau.

model is not as fresh at the surface as in observations. Note that this feature is most often poorly reproduced by state-of-the-art ocean–sea ice models (e.g., Lique et al. 2016; Wang et al. 2016). The deepest portion of the gyre occurs close to the southern and eastern bathymetry; on those sides of the gyre, isohalines are steep, while the northern and western portions have flatter isohalines. Over 1990–2014, the isohalines gradually deepen both at the center and over the portion of the gyre that is free to expand, whereas the side constrained by bathymetry varies less, as seen in the depression of the 33-psu isohaline (Figs. 3c,d). In conjunction with this, the center of the gyre moves farther away from the continental slope due to the northwest shift of the gyre as seen in Figs. 2a and 2b.

During the early 1990s, when surface forcing was often cyclonic (e.g., Fig. 2g; Proshutinsky et al. 2015), the 33-psu isohaline is roughly flat all across the gyre (Figs. 3c,d). After 2000, as the center starts to shift toward the northwest, the depth of the 33-psu isohaline at the center of the gyre also increases. This deepening is accelerated between 2005 and 2010, and in particular during the year 2007 when there was an anomalously anticyclonic summertime Beaufort Sea high (Serreze and Barrett 2011) associated with anomalously strong downwelling during the year (Fig. 2g; Meneghello et al. 2018b). Thus, as a result of the gyre spinup and increased freshwater content within the gyre, the 33-psu isohaline through the gyre is depressed by 36 m when comparing the 1990–2007 and 2008–14 averages, deepening from 181 to 217 m. A deepening of 15 m is seen between 2007 and 2008, and after 2010 the isohaline deepens west of 200°E, which is concurrent with the expansion over the Chukchi Plateau. In the interior of the Beaufort Sea, Timmermans et al. (2014) observed a deepening of around 20 and 30 m of the 31- and 33-psu isohalines, respectively, between 2007 and 2008, which is similar to the rapid deepening in the center that we find here. The deepening of the isohalines is also consistent with the observed deepening of ~30 m of the nutricline and chlorophyll maximum in the interior of the Canada Basin over the period 2003–09 reported by McLaughlin and Carmack (2010). One should remember, however, that the changes in isohaline depth are not solely a response

to the dynamical wind forcing and might also reflect changes in water masses found in the halocline. For instance, using oxygen, temperature, and salinity measurements, Shimada et al. (2005) suggest that depressions in isohalines between 32.5 and 33.5 psu observed during summer 2002 and 2003 along 150°W could be attributed to a shift in the respective contributions of summer and winter Pacific Water inflow. This contribution is also likely to be affected by interannual changes to pathways and advection (Zhong et al. 2019a).

In summary, the model reproduces well the observed properties of the Beaufort Gyre and their spatial and temporal variability. The 3D description of the gyre obtained from the model suggests large changes of the depth and slope of the different isopycnals as the gyre spins up and stabilizes over time, suggesting potential implications for the development of baroclinic instability. In the following, we explore the response of the levels of total and eddy kinetic energy to the changes of the large-scale gyre circulation.

4. Energetics of the Canada Basin

a. Computation of the total and eddy kinetic energy

We start by defining the different metrics we use to examine the energetics in the Canada Basin, and explain how their calculations are performed. First, we compute the total kinetic energy KE as $\mathrm{KE} = 0.5(u^2 + v^2)$. We use the 5-day mean velocities (u, v) for the computation. The velocities can be further decomposed into a time-mean and an eddy part, $(u, v) = (\overline{u} + u', \overline{v} + v')$, from which we can decompose KE into a mean kinetic energy $[\mathrm{MKE} = 0.5(\overline{u}^2 + \overline{v}^2)]$ and an eddy kinetic energy $[\mathrm{EKE} = 0.5(u'^2 + v'^2)]$ component. Here we follow Rieck et al. (2018) and use annual means to compute $\overline{u}$ and $\overline{v}$ as opposed to the long-term mean that is often considered (e.g., Hogg et al. 2015). This allows us to account for interannual variations of the mean currents and in particular for the effects of the gyre spinup that occurs over the period considered (Fig. 2). One should remember, however, that, while mesoscale eddies are expected to account for most of the EKE (Wunsch 2002), our EKE fields also account for short term variations of the large scale circulation as well as meanders and shifts of the current core and waves. In particular, we know that there is also some variability in the Beaufort Gyre circulation on seasonal time scales, but these variations remains small compared to the variations occurring on interannual-to-decadal time scales (e.g., Regan et al. 2019), and the EKE estimated using $\overline{u}$ and $\overline{v}$ computed as 3- and 12-month running means gives qualitatively the same results as those presented in the following. An additional Reynolds stress term arises from the correlations between the mean and the fluctuation of each velocity component as our mean is constructed of annual means as opposed to the long-term mean; this term is an order of magnitude smaller than the MKE and EKE terms and is therefore neglected.

b. Horizontal maps

To quantify the spatial variability of the gyre energetics, we first examine maps of the long term means of KE, MKE, and EKE, both at the surface and in the halocline at 147 m (Figs. 4a–c and 5a–c). The three fields are highly variable but there are a lot of similarities between them, both at the surface and in the halocline. Interestingly, the partition of KE into a mean and an eddy part reveals that the two are of the same order of magnitude both along the continental slope and in portions of the interior. This is at odds with what is observed in most of the open ocean at the surface, where EKE is thought to be one to two orders of magnitude more energetic than the MKE (e.g., Wunsch 2002), and is likely due to the small beta effect associated with the nonzonal mean flow (Spall 2000). The contrast is even more striking within the halocline at 147 m, where MKE in the interior of the basin toward the northwest portion of the gyre exceeds the contribution to KE from EKE.

The most energetic part of the region appears as high KE along the continental slope in the southern Canada Basin (between 200° and 230°E) both at the surface and in the halocline (Figs. 4a and 5a). The values of KE there are an order of magnitude higher than in the basin interior in the 1990–2014 mean. This is also a region of elevated MKE and EKE compared to the interior, where the maximum EKE in the interior is just 7% of the maximum EKE on the slope at both the surface and 147 m. Large surface MKE at this location is consistent with the highest geostrophic velocities observed by Armitage et al. (2017). The strongest mean currents are where most mesoscale eddies form (e.g., Manucharyan and Isachsen 2019), which here is reflected in the high levels of EKE found along the continental slope that regularly exceed $1 \times 10^{-2}\,\mathrm{m^2\,s^{-2}}$, and reach up to $4 \times 10^{-2}\,\mathrm{m^2\,s^{-2}}$ in isolated locations. This maximum in EKE in the boundary current corresponds to the largest lateral shear. Although high, the levels of EKE found there remain lower than in the energetic regions commonly found in the open ocean, for example the midlatitude western boundary currents and equatorial regions where EKE exceeds $5 \times 10^{-2}\,\mathrm{m^2\,s^{-2}}$ over large areas (Rieck et al. 2015) and the Gulf Stream region where EKE can approach $2 \times 10^{-1}\,\mathrm{m^2\,s^{-2}}$ in its most energetic part (Zhai et al. 2008). Nonetheless, the EKE along the continental slope in the Canada Basin is generally of a

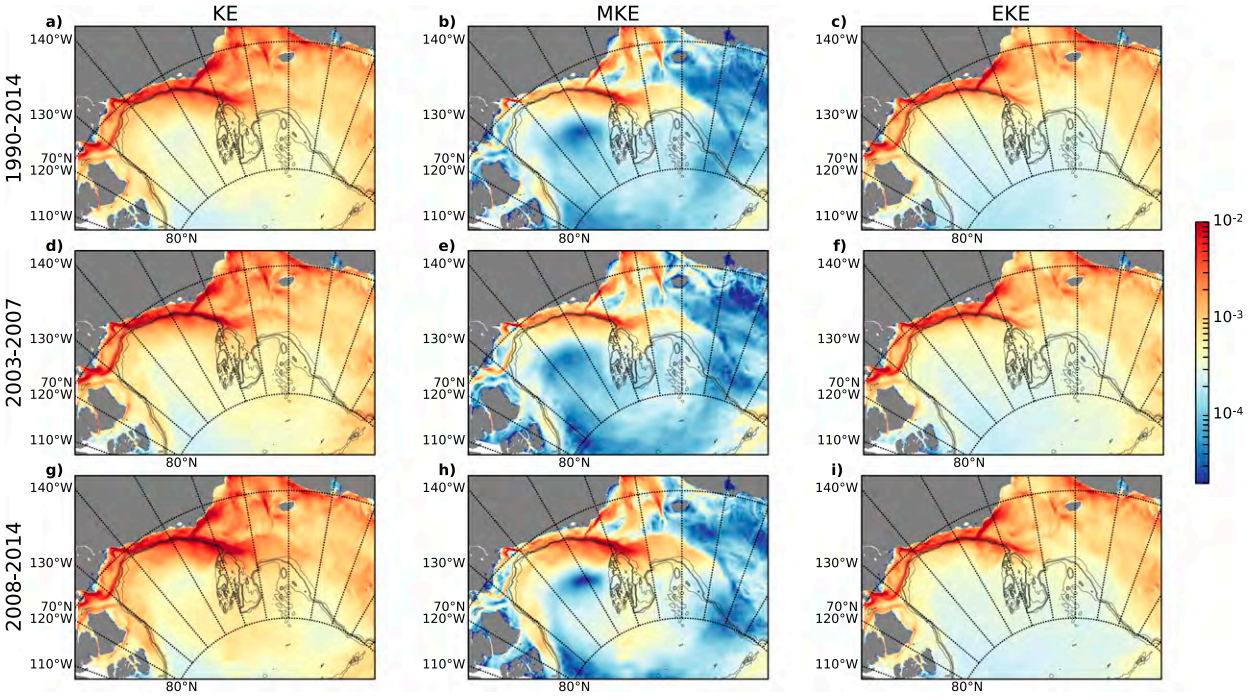

FIG. 4. Maps of (left) total KE, (center) MKE, and (right) EKE at the surface ($m^2 s^{-2}$). Shown are the (a)–(c) 1990–2014 average, (d)–(f) 2003–07 (spinup) average, and the (g)–(i) 2008–14 (post-spinup) average. Bathymetry contours are shown at 500, 1000, and 1500 m in gray.

similar magnitude to that of the modeled EKE found by Trodahl and Isachsen (2018) in the Labrador and Nordic seas, though here the EKE is concentrated to a very narrow band while Trodahl and Isachsen (2018) find more widespread bands around shallow bathymetry and in the deep basin. The narrow band arises from a combination of coherent eddies generated from the boundary current or from the Barrow Canyon inflow that then follow the continental slope (Spall et al. 2008; von Appen and Pickart 2012) and boundary currents that can vary in both magnitude and direction on subannual time scales (e.g., Pickart 2004; Spall et al. 2018). An illustration of this is the temporary reversal of the eastward Beaufort shelfbreak jet observed in November 2002 by Pickart et al. (2013). Similarly, the inflow through Barrow Canyon also reverses subannually in the model (not shown), and the expanded gyre toward the latter part of the time period also reaches this region in winter (Regan et al. 2019). These variations are not accounted for in the annual-mean currents and therefore have an imprint on EKE.

Away from the continental slope, the partitioning of KE into EKE and MKE reveals different spatial distributions (Figs. 4a–c and 5a–c). The mean EKE is qualitatively similar to the mean KE at both the surface and at 147 m across the Canada Basin, while the spatial distribution of MKE is more variable, with a clear imprint of the gyre within the basin interior. This is particularly visible on the northward extension of the gyre (north of 75°N), where the gyre is not constrained by bathymetry and can move more freely (Regan et al. 2019). At 147 m, the northward extension of the gyre also has a signature on the EKE pattern, though the EKE remains low over the Chukchi Plateau.

While the basin interior is less energetic than the slope, eddies have been observed there previously (e.g., Newton et al. 1974; Timmermans et al. 2008; Zhao et al. 2016). Manley and Hunkins (1985) investigated the interior gyre KE (at approximately 75°N, 150°W) using daily under-ice profiles over 1975–76, and found that the EKE made up over 98% of the total KE (with 37% of the EKE below 30 m attributable to individual eddies). This is at odds with our model results suggesting that MKE and EKE are of a similar order of magnitude in the interior, the average MKE and EKE as a percentage of KE in the central gyre (Fig. 1, red box) being 30% and 70% at the surface and 47% and 53% at 147 m, respectively. This different partitioning could likely be attributed to the difficulty of defining a mean flow in regions with very weak mean currents contrasting with the passage of several highly energetic eddies.

Comparison of the spinup (2003–07) and post-spinup (2008–14) periods demonstrates a clear shift in energetics (Figs. 4d–i and 5d–i). Indeed, the total KE significantly increases across the gyre during the latter period compared to the spinup phase, visible both at the

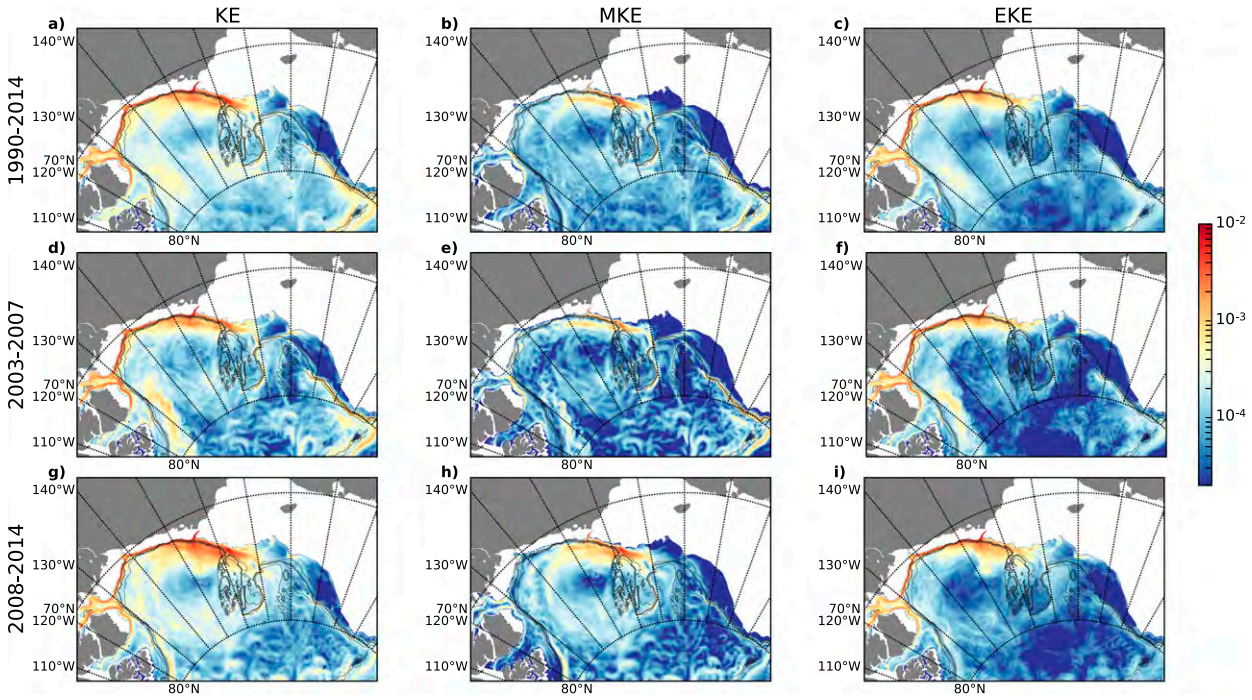

FIG. 5. Maps of (left) total KE, (center) MKE, and (right) EKE ($m^2\,s^{-2}$) at 147 m, in the halocline. Shown are the (a)–(c) 1990–2014 average, (d)–(f) 2003–07 (spinup) average, and the (g)–(i) 2008–14 (post-spinup) average. Bathymetry contours are shown at 500, 1000, and 1500 m in gray.

surface and in the halocline. Given that the main dynamical equilibrium of the gyre determined from simple process models is thought to be a balance between the Ekman pumping and eddy flux (Davis et al. 2014; Doddridge et al. 2019), one would expect that the spinup of the gyre would result in an increase of the EKE [although some delay of the response could be expected arising from the so-called eddy memory mode described by Manucharyan et al. (2017)]. Our simulation shows that this is not the case. Looking at the partitioning between MKE and EKE reveals that the raise in total KE is predominantly due to a raise in MKE, which increases by up to $2 \times 10^{-4}\,m^2\,s^{-2}$ both at the surface and at 147 m in the interior between the two periods. At 147 m, this results in MKE contributing over double that of EKE across the gyre interior. Along the continental slope, where Armitage et al. (2017) reported the strongest increase in geostrophic currents in 2007–10 compared to 2003–07, the MKE increases even more, with an increase exceeding $2 \times 10^{-3}\,m^2\,s^{-2}$ at the surface and $1 \times 10^{-3}\,m^2\,s^{-2}$ at 147 m around 200°E. The increase is particularly visible along the energetic southwestern portion of the basin, with a widening band at the surface appearing in the post-spinup period, extending from where the gyre reaches the continental slope by the Chukchi Sea (between 200° and 205°E) and into the gyre interior, particularly north of Barrow Canyon. In contrast, the EKE increases much less between the two periods, and the spatial pattern remains broadly similar.

c. *Vertical sections across the gyre*

To better understand the changes visible on the energy maps, we examine the vertical distribution of KE, MKE, and EKE across the gyre for the same three periods (Fig. 6), making use of section B (see Fig. 1 for the location of the section).

On the long-term mean, the total KE is intensified across the surface of the gyre, down to ~30 m, which corresponds broadly to the base of the mixed layer (Fig. 6a). Below this, extending down to around 200 m, there is an additional halocline signature. This is in line with the vertical structure of KE observed by Manley and Hunkins (1985): a surface peak in the top 0–30 m (due to energy in the mixed layer from ice motion and wind), followed by a subsurface KE peak with maxima at 120 m and extending from 30 m to the lower limit of the dataset (200 m). In the halocline, localized enhancements of KE reach up to $4 \times 10^{-4}\,m^2\,s^{-2}$, with values generally exceeding $1 \times 10^{-4}\,m^2\,s^{-2}$. Looking at the partitioning between MKE and EKE reveals that the structure of KE results from both contributions, depending on the region considered (Figs. 6b,c). In the interior of the gyre, away from the continental slope and below the mixed layer, MKE exhibits coherent values

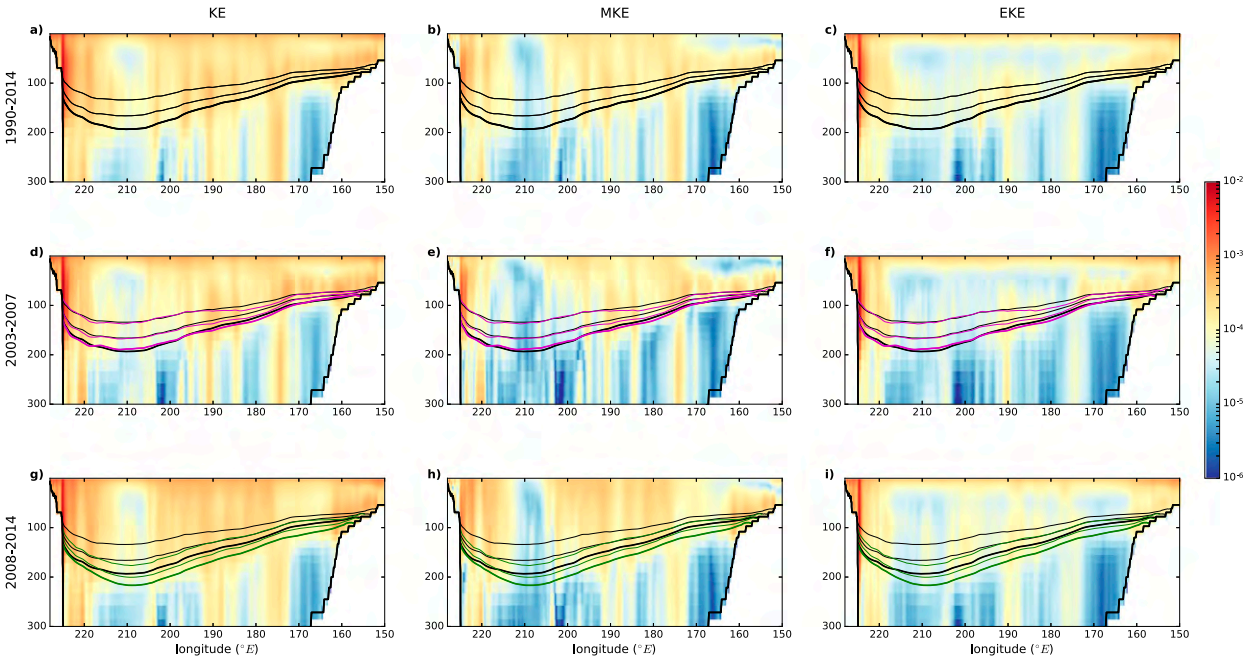

FIG. 6. Vertical sections of annual-mean (left) KE, (center) MKE, and (right) EKE ($m^2\,s^{-2}$) along section B (see Fig. 1). Shown are the (a)–(c) 1990–2014 average, (d)–(f) 2003–07 (spinup) average, and the (g)–(i) 2008–14 (post-spinup) average. Black lines indicate the 1990–2014 mean positions of the 32-, 32.5-, and 33-psu isohalines, with 33 psu in bold. Magenta and green lines indicate the same isohalines but for the 2003–07 and 2008–14 averages, respectively. Note that the Chukchi Plateau is located between 205° and 190°E here.

around $1 \times 10^{-4}\,m^2\,s^{-2}$ throughout the halocline excepting the gyre center and accounts for most of the KE, while the surface intensification of KE across the section reflects high levels of EKE. Along the continental slope and over the Chukchi Plateau (Figs. 6a–c, longitudes 230°–220°E and 205°–190°E, respectively), both MKE and EKE contribute significantly to KE, although the EKE is larger than the MKE.

A striking feature of the vertical section of EKE is the subsurface intensification, with, for example, values at 114 m, in the subsurface peak, being over 85% of the average EKE in the top 10 m at 190°E. This is again in sharp contrast with what is usually reported from observations or models in the open ocean, where EKE tends to decrease significantly with depth [e.g., in the Gulf Stream (Richardson 1983), the South China Sea (Z. Zhang et al. 2016), and the southeast Pacific (Balwada et al. 2016)]. A similar behavior was found in the Arctic modeling study of Maslowski et al. (2008) who reported that EKE can reach $1 \times 10^{-3}\,m^2\,s^{-2}$ at the surface and around 300 m offshore of the continental slope.

The general spatial and depth-dependent distributions of the energetics are enhanced when the gyre is spun up (Figs. 4g–i, 5g–i, and 6g–i). The spinup phase is comparable to the 1990–2014 mean (Figs. 6d–f), and the lower halocline EKE is actually reduced during the spinup over 2003–07 between 190° and 215°E (Figs. 6c,f). However, in the post-spinup phase (2008–14), all quantities increase as the isohalines in the gyre deepen from the 1990–2014 mean (Figs. 6g–i; also shown in Fig. 3). As already suggested by the maps, the MKE response is over double that of EKE in the interior gyre and more widespread consistently below 30 m, but the EKE response, while elevated at depth, is not increased greatly, despite the deepened isopycnals (Figs. 6c,i). Indeed, large reductions in EKE are visible on the continental slope (east of 218°E) at depth by over $1 \times 10^{-3}\,m^2\,s^{-2}$. In contrast to EKE, the MKE increases all across the gyre, again accounting for most of the increase in KE. The vertical sections also reveal that the widening of the boundary current along the eastern side of the gyre is coherent from the surface to the base of the halocline (Fig. 6h).

d. Temporal evolution

The clear shift in energetics between the two periods raises the question of how the transition occurs. Figure 7 shows Hovmöller plots of KE, MKE, and EKE averaged spatially across both the BG box (a region encompassing the full gyre; see blue box in Fig. 1) and the central gyre region (representative of the gyre interior; see red box in Fig. 1). There is a clear elevated signal in all quantities down to around 200 m, with this depth varying

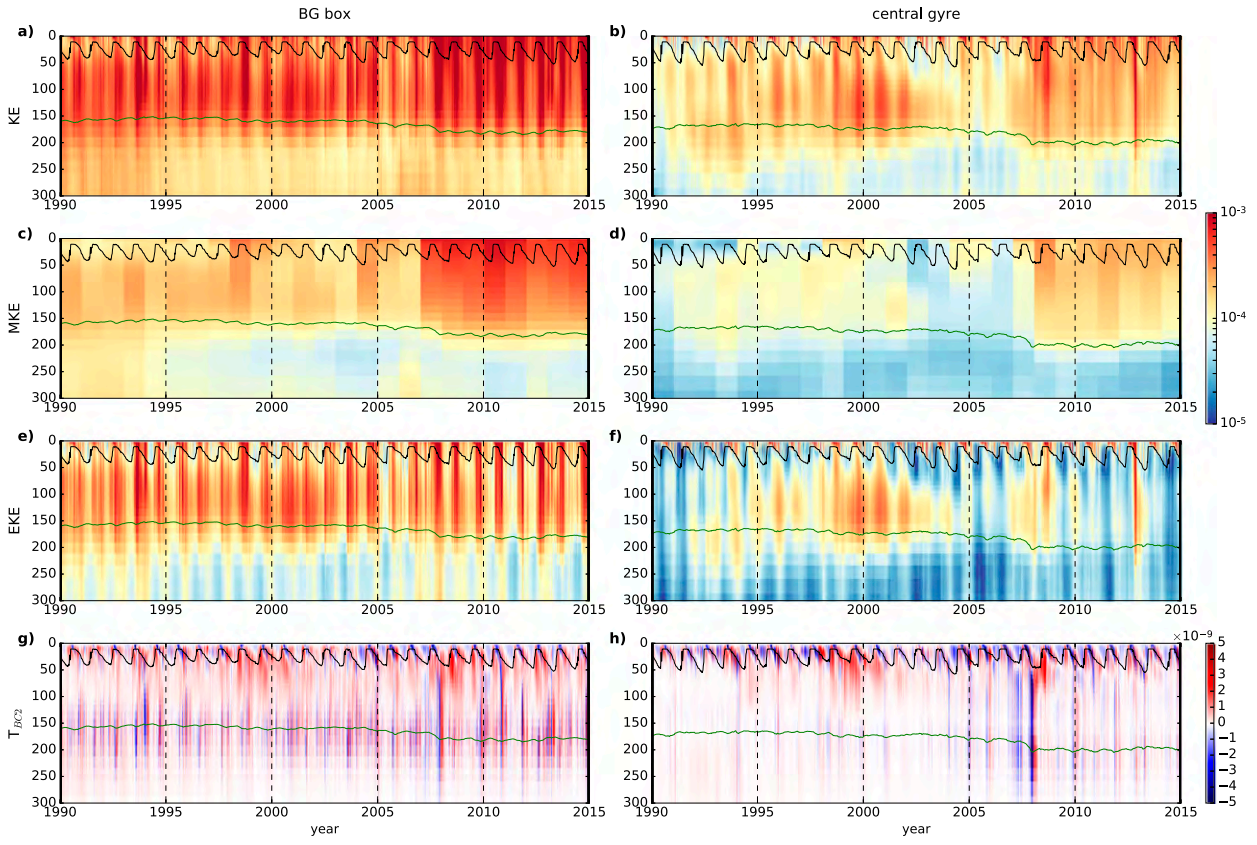

FIG. 7. Hovmöller diagrams of depth against time showing fields spatially averaged within the (left) BG box and (right) central gyre (see Fig. 1). Fields displayed are (a),(b) total KE, (c),(d) MKE, (e),(f) EKE (all in $m^2 s^{-2}$), and (g),(h) T_{BC2} ($m^2 s^{-3}$; positive = conversion to EKE). The average mixed layer depth and depth of the 33-psu isohaline in each region are shown in black and green, respectively.

slightly both interannually and seasonally. This depth corresponds broadly with the lower limit of the gyre defined by the 33-psu isohaline (Fig. 3). Comparing the energy levels within the full gyre to the interior, the Hovmöller plots reveal that the temporal evolution of KE and its partitioning are similar in both the BG box and central gyre, although the energy is roughly an order of magnitude lower when only the gyre interior is considered.

A strong increase in the top 200 m of the MKE (and thus of the total KE) is visible after 2008, with a doubling above 80 m and the top 20 m being over 3 times higher on the 2008–14 average compared to the 1990–2007 average, in line with the transition identified from the time series of the freshwater content and gyre intensity (Fig. 2), although here the transition seems sharper. This transition is likely the result of the strong anomalous downwelling occurring in 2007–08 (Fig. 2g; Regan et al. 2019; Meneghello et al. 2018b) that may have served to help shift the gyre into a new equilibrium, with higher mean currents, but also higher levels of EKE in 2007–08 visible on Fig. 7f in the central gyre. Yet, after 2008, the MKE remains high while the EKE appears to decrease again, resulting in the weak EKE signature in the spun-up vertical section compared to the elevated MKE (Figs. 6h,i).

In the central gyre, there is also an increase in KE in 1998 (Fig. 7b), due to the beginning of the anticyclonic phase of the atmospheric circulation (e.g., Proshutinsky et al. 2015). It results in temporary gyre spinup, with the raised total KE predominantly due to an increase in EKE as opposed to MKE, in contrast to the 2007–08 rise. It is also accompanied by a small rise in SSH and freshwater content (Fig. 2), but the interannual rise is dwarfed by seasonal variability. In this situation, the gyre appears to fully readjust to the pre-spinup values without reaching a new equilibrium.

It is also interesting to examine the seasonal variations of EKE, which strongly affect the temporal evolution of KE. Notably, the surface signal identified in the EKE section is a highly energetic, summer-intensified signal that quickly disappears in the autumn and does not return until the spring. This is most likely due to a combination of friction of sea ice at the surface dissipating

the energy (Ou and Gordon 1986) and also a lack of generation of surface baroclinic eddies in the winter due to the presence of sea ice, suggesting that an intensification of the surface EKE would likely not survive longer than the seasonal time scales. The surface intensification of the EKE appears more connected to subsurface EKE after 2007 in the BG box, likely due to the receding sea ice during that period reducing the dissipation of eddies at the surface in parts of the region. In contrast, the layer of enhanced EKE in the halocline intensifies and thickens over summer–autumn but remains year-round. The presence of some seasonality here is partly explained by the definition of EKE used, which encompasses the seasonal variations of the mean currents, and also the use of a fixed box for our average, both of which do not account for the seasonally expanding and contracting gyre. In the central gyre, the largest levels of EKE are found in 2012 and are related to a large individual eddy from Barrow Canyon entering the gyre during the August and remaining until the spring (not shown), that imprints strongly on the central gyre EKE and total KE (Figs. 7b,f). Timmermans et al. (2008) observed subsurface eddies such as this and suggested from current speed measurements that, assuming a straight path, they can have a lifetime of at least 6–18 months when advected into the interior of the basin.

In the next section we explore the mechanisms at play to generate the EKE in the context of the gyre spinup.

5. Generation of eddy kinetic energy in the gyre

a. *Computation of potential energy and energy transfer*

To better understand the variability in EKE in the gyre, we look at EKE generation via baroclinic instability, which idealized models suggest is the first-order response to Ekman pumping to stabilize the gyre (e.g., Manucharyan and Spall 2016; Davis et al. 2014; Doddridge et al. 2019). To do this, we compute the transfer of eddy potential energy (EPE) to eddy kinetic energy (EKE), which is associated with local baroclinic instability (e.g., Beckmann et al. 1994; Eden and Böning 2002; von Storch et al. 2012). This is the secondary stage of the Lorenz energy cycle, the first being mean potential energy (MPE) to EPE. The EPE → EKE transfer term can be written as a vertical buoyancy flux anomaly $T_{BC2} = \overline{w'b'}$ where w is vertical velocity, $b = -g(\rho/\rho_0)$ is buoyancy, and $\rho_0 = 1027.5\,\mathrm{kg\,m^{-3}}$. As in the EKE computation, the prime denotes the anomaly from the annual means, meaning that the seasonal cycles of both the Ekman pumping and the buoyancy might also contribute significantly to T_{BC2} without driving baroclinic instabilities. Overall, a positive value of T_{BC2} indicates a transfer from EPE to EKE, meaning that lighter water masses are associated with upward motions, and denser water masses are associated with downward motions (e.g., von Storch et al. 2012). In this situation, the model isohalines flatten, releasing potential energy, and EKE is generated in the process. A negative value of T_{BC2} indicates lighter water masses being associated with downward movements, such as a deepening of the isohalines in the gyre due to Ekman pumping. For comparison with this term, we also compute the MPE to EPE transfer term as $T_{BC1} = -(g/\rho_0)[(\partial z/\partial x)\overline{u'\rho'} + (\partial z/\partial y)\overline{v'\rho'}]$ (e.g., Beckmann et al. 1994). Negative values of both terms mean a transfer from EKE to the available potential energy (APE) reservoir, while positive values of both terms mean a transfer from the potential energy reservoir to EKE. Note that, in our model, we found that the generation of EKE through barotropic instability is an order of magnitude lower than that of baroclinic instability (not shown).

Given that the baroclinic instability results in an energy transfer between the potential and kinetic energy reservoirs, it is instructive to look briefly at the potential energy reservoir itself. This quantity is not well defined. It encompasses both available and background potential energy, of which only the former (APE) is readily available for exchange to kinetic energy (Winters et al. 1995). As such, attempting to rigorously estimate MPE, EPE, and APE is beyond the scope of the study. To step away from this complexity, we only look at the total APE, which has been suggested by Polyakov et al. (2018) to provide information on the stratification in the halocline and its stability. Following Polyakov et al. (2018), we estimate the vertically integrated total APE as $\mathrm{APE} = \int_{z=0}^{z_1} g(\rho - \rho_{\mathrm{ref}}) z\, dz$, where g is gravitational acceleration, z is depth, z_1 is the depth of the halocline base, and ρ_{ref} is the potential density at the base of the halocline. As in Polyakov et al. (2018) and Bourgain and Gascard (2011), the halocline depth here is the depth below the mixed layer at which $[\alpha(d\theta/dz)]/[\beta(dS/dz)] = 0.05$, where α and β are the thermal expansion and haline contraction coefficients, respectively. Bourgain and Gascard (2011) note that this ratio can be used to identify a shift from the halocline to the thermocline; they found that a ratio of 0.05 resulted in the best fit for identifying the transition in individual pressure, temperature, and salinity profiles. The total APE averaged in the BG box here (Fig. 2f) has a magnitude similar to that found in

observations from ships and ITP data within a similar box by Polyakov et al. (2018). They also found a monotonic increase in APE between 2005 and 2010 on their annual-mean computations, although our model results are around $1 \times 10^5\,\mathrm{J\,m^{-2}}$ larger in the spun-up phase after 2008 than the APE of Polyakov et al. (2018). We note here that, as expected, the total APE variability closely follows that of freshwater content (Figs. 2e,f). The elevated APE after 2008, being nearly 30% larger in the spun-up phase than in the pre-spinup phase, suggests that the gyre halocline is deeper and more stable in the post-spinup phase than before, potentially limiting the ability to mix heat between the surface and the Atlantic Water below despite increased surface forcing due to sea ice decline (Davis et al. 2016) and likely affecting the intensity of the circulation in the Atlantic Water layer (Lique and Johnson 2015).

b. *Time evolution of energy transfer*

To analyze the transfer of energy between EPE and EKE due to baroclinic instability in the region, we first look at Hovmöller plots of T_{BC2} averaged within the BG box and central gyre (Figs. 7g,h). Most of the energy transfer occurs within the top 200–300 m where the gyre resides. The magnitude of T_{BC2} is higher when considering the BG box rather than just the central gyre due to the inclusion of the boundary current, which is known to generate eddies via baroclinic instability (e.g., Spall et al. 2008). This can also be seen in horizontal maps of T_{BC2} at 147 m depth in 2007 and 2008 (Fig. 8). Just as for EKE (Figs. 7e,f), the vertical structure of T_{BC2} displays bands of different behavior with depth, although on the temporal average, T_{BC2} is positive below 15 m, suggesting an overall transfer to EKE. In the mixed layer itself, the predominant behavior is a weakly negative T_{BC2}, while at the mixed layer base, there is a seasonal shift between strongly positive and negative T_{BC2} as the mixed layer shoals and deepens. This seasonal cycle of T_{BC2} is consistent with the seasonal cycle exhibited by APE (Fig. 2f), and is likely driven by seasonal inputs of freshwater from sea ice melt and freezing and terrestrial runoff and interactions with the surface forcing. Reduced negative T_{BC2} in the mixed layer between 2001 and 2004 also corresponds to a period reduced seasonality of the APE (Fig. 2f).

Further down the water column, the transfer of energy is generally weaker, particularly in the central gyre, though there are still periods with elevated values (Figs. 7g,h). In the lower halocline there are short-lived episodes of both positive and negative T_{BC2} which may be due to the shifting position of the halocline base and associated isohalines as the gyre expands and contracts seasonally. The layer between the surface and lower halocline, where EKE is reduced (Fig. 7f), has a band of positive T_{BC2} in the BG box throughout the time period (which is also present in the central gyre but with a lower magnitude). Notably, in this layer in 1998–2002 and 2007–08 there is a strong positive T_{BC2} signal in both the BG box and the central gyre, corresponding to years when the EKE is also elevated in the halocline in the central gyre (Fig. 7f). The former is preceded by a strong negative T_{BC2} signal, suggesting conversion to potential energy that extends deep into the water column in the central gyre (Fig. 7h). The signatures of the elevated EKE extend deeper in the water column (down to the gyre base) than the positive T_{BC2} (down to 100 m), and appear with a time lag of the order of a few weeks, likely due to the growth time of the instabilities (G. Meneghello et al. 2019, unpublished manuscript).

The transition to higher total KE and MKE occurs abruptly over 2007–08 (Figs. 7a–d), unlike the gradual increase in freshwater content and APE during the 2000s (Figs. 2e,f). It coincides with the largest subsurface T_{BC2} in the central gyre (Fig. 7h) during a year of anomalously strong downwelling (Fig. 2g; Meneghello et al. 2018b). Zooming into the transition, Figs. 8a, 8b, 9b, and 9e show maps at 147 m and vertical sections across section B of T_{BC2} for the 2007 and 2008 annual means. The T_{BC1} term is also shown in Figs. 9c and 9f for comparison. The signature in 2007 is dominated by strong negative T_{BC1} down to around 50 m, and a gyre-wide negative T_{BC2}, which extends from around 50 to 300 m (Fig. 9b). There is an additional, weaker lower halocline signature in the eastern gyre in T_{BC1}. This strong negative signal of both T_{BC1} and T_{BC2} suggests an overall large transfer from EKE to the MPE reservoir. Figure 7h suggests that in 2008, there is a subsequent strong positive T_{BC2}, but this is more localized, mainly along the continental slopes (Fig. 8b) and close to the surface (Fig. 9e), and it does not dominate the interior gyre at depth like the negative signal in 2007 (Figs. 9b,e). In general, the localized distribution of T_{BC2} in 2008 is more typical of other years in the study period, though slightly enhanced (not shown). Thus, while the gyre usually experiences a net transfer to EKE via baroclinic instability, in 2007 there is instead a strong, gyre-wide transfer to MPE and EPE, the latter of which occurs down to the gyre base, and is reflected in the total APE (Fig. 2f).

A comparison of EKE, T_{BC1}, and T_{BC2} over the transition shows that areas of steeper isohalines compared to the 1990–2014 mean isohalines are accompanied by high levels of both positive T_{BC2}, T_{BC1}, and EKE

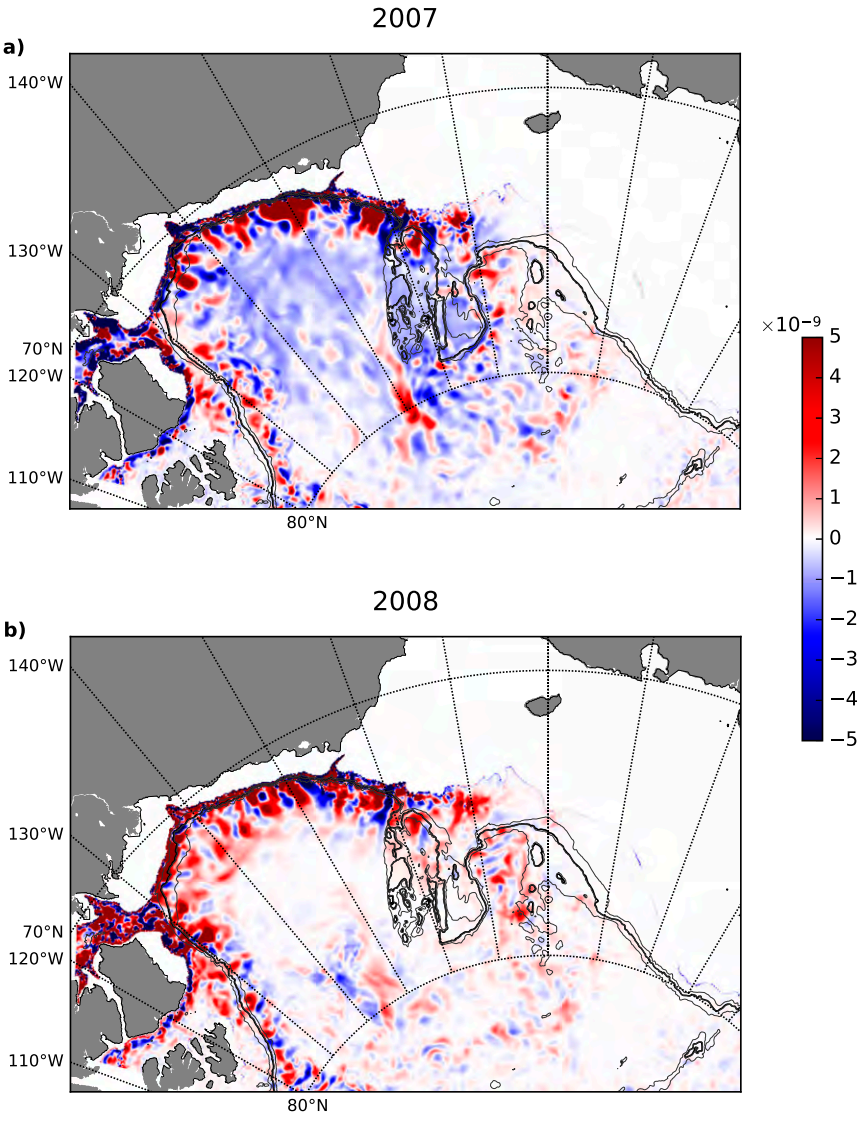

FIG. 8. Maps of annual-mean T_{BC2} ($m^2 s^{-3}$; positive = conversion to EKE), at 147-m depth for (a) the 2007 average and (b) the 2008 average. Bathymetry contours are outlined at 500, 1000, and 1500 m.

(e.g., between 50 and 150 m at 200°E in Figs. 9d–f). Therefore EKE is generated via baroclinic instability where isohalines steepen. However, this is not enhanced significantly (Figs. 9a,d) in response to the gyre-wide negative T_{BC2}. Thus, an anomalous year of Ekman pumping serves to change the mean state of the gyre, but EKE is only elevated temporarily (Fig. 7h). With the exception of Manucharyan and Spall (2016) and Manucharyan et al. (2017), idealized models have historically used a step change in surface forcing and analyzed the gyre response and its time scale. This differs from the scenario here, which is a short-lived change in surface forcing. It is clear from this analysis that such fluctuations of the magnitude of the forcing are an important consideration, affecting the gyre MKE and EKE on different time scales.

c. *Role of bathymetry and gyre asymmetry*

We have shown that, in contrast to what has been suggested from idealized process models, the spinup of the gyre is largely accompanied by an increase in MKE while the EKE does not increase significantly. We thus investigate how the interior of the gyre adjusts to its new state.

The continental slope, over which the gyre has expanded during the spinup phase (Fig. 2b), has recently been described as a feature that tends to impede the development of baroclinic instability (Manucharyan and Isachsen 2019). Starting from the Eady theory

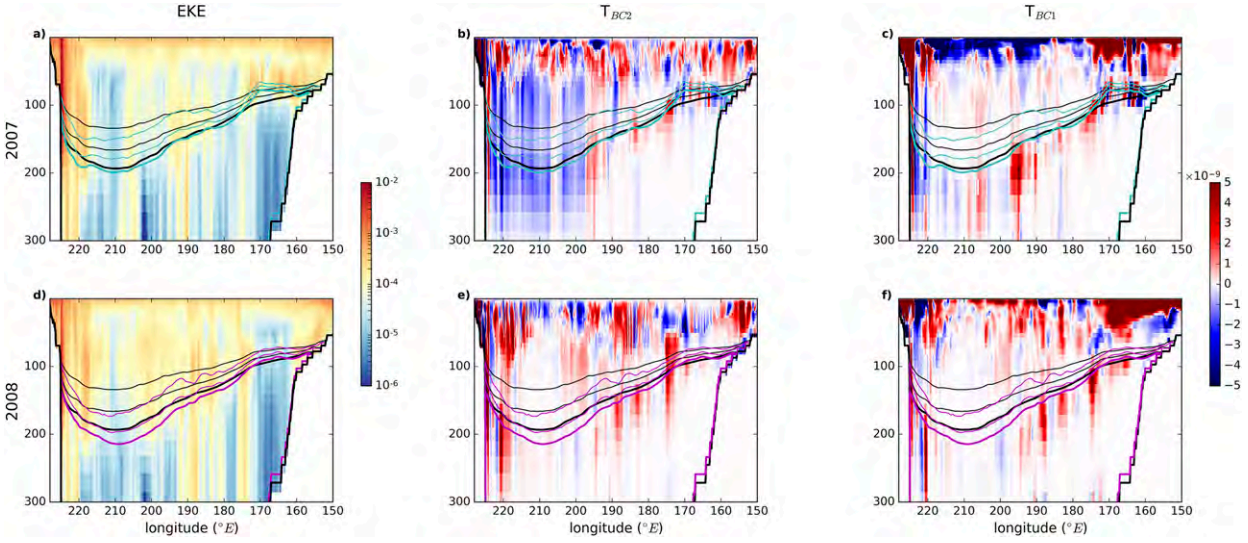

FIG. 9. Annual-mean vertical sections along section B (see Fig. 1) of (left) EKE ($m^2 s^{-2}$) and (center) T_{BC2} and (right) T_{BC1} (both in $m^2 s^{-3}$; positive = conversion to EKE). Plots are shown for the (a)–(c) 2007 average and (d)–(f) 2008 average. Black lines indicate the 1990–2014 mean positions of the 32-, 32.5-, and 33-psu isohalines, with 33 psu in bold. The annual-mean isohalines at 32, 32.5 and 33 psu are shown in cyan (2007) and magenta (2008). Note that the Chukchi Plateau is located between 205° and 190°E here.

(Eady 1949), a simple parameter $\delta = s_b/s$ (where s is the isopycnal (isohaline) slope and s_b is the slope of the bathymetry) can be defined and used to determine if the current over the slope is baroclinically stable or not. According to this simple formulation, the southern portion of the gyre lies within the $\delta > 1$ regime. This means that it is stable even when the gyre is spun up, since the isohaline slope is always much smaller than the continental slope (Figs. 3c,d; Manucharyan and Isachsen 2019). Yet, Figs. 4 and 5 do show elevated levels of EKE on the slope, and Figs. 8 and 9 also reveal the generation of EKE there. Despite the stabilizing effect of the slope, the Eady theory might be too simple to fully capture the complexity of the interactions between the gyre and the slope. First, the continental slope around part of the gyre is so steep that the dynamical regime found here may not differ largely from the regime that we would expect with a vertical wall instead of a slope (as in Meneghello et al. 2018a). Second, Manucharyan and Isachsen (2019) note that the Eady theory ignores eddy momentum fluxes, whereas, in reality, barotropic instability acts over the slope to transport the momentum into the interior where baroclinic instability is then able to develop. Indeed, similar to the results of Manucharyan and Isachsen (2019), our model also exhibits higher transfer of MKE to EKE associated with barotropic instability over the continental slope (not shown).

Away from the continental slope, the response to the strong forcing anomaly in 2007 is different. Comparing the isohaline on the northern and western portions of the gyre against the southern and eastern portions, we find that the latter slopes are generally flatter (Fig. 3). The gyre is also strongly asymmetrical (Fig. 2b), so that the center of the gyre is closer to the side of the gyre constrained by the continental slope. Notably, the spinup of the gyre results in a stronger steepening of the isohalines in the southern and eastern portions. This is because they are bounded by bathymetry and therefore are restricted by the continental slope. In contrast, in the north and west, expansion relaxes the isohalines, reducing the potential for baroclinic instability and EKE generation compared to what would be expected from just an intensification of the gyre bounded by bathymetry everywhere. This expansion is most likely a response of the time and space variations of the Beaufort Sea high (Regan et al. 2019). Figure 10 shows the average sea level pressure in the region for the full time period, and the spinup and spun-up phases (note that this is not directly equivalent to the Ekman pumping field due to the modulation by sea ice and surface geostrophic currents, but the spatial pattern is broadly the same). In the spinup phase (Fig. 10b), the intensity is greatly increased, depressing isohalines within the gyre. In the spun-up phase (Fig. 10c), the Beaufort Sea high is extended to the north and greatly to the west compared to the 1990–2014 mean (Fig. 10a), resulting in a local depression of the isohalines to the north and west due to increased downwelling there, and thus reducing their steepness. Other effects such as changes in the lateral advection may also have

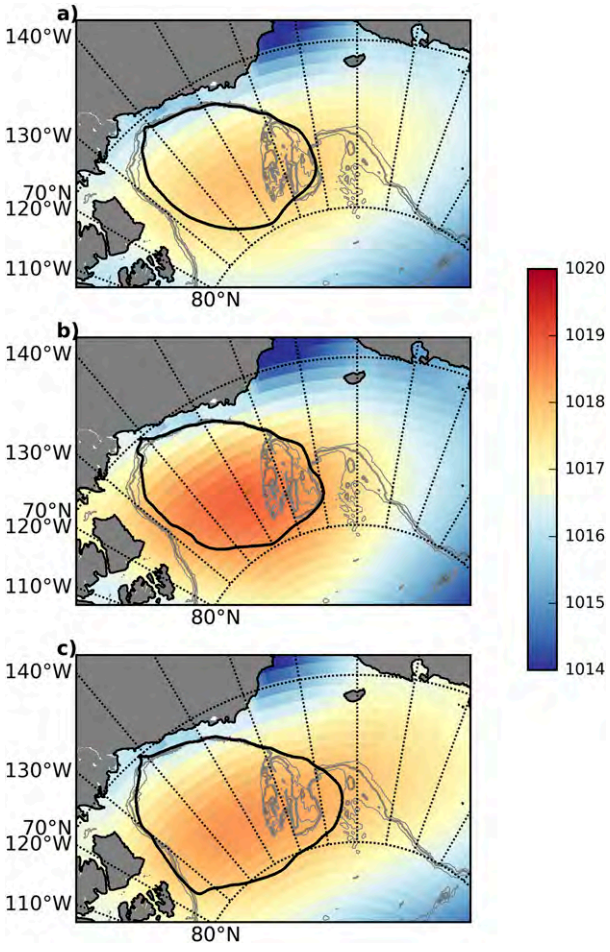

FIG. 10. Mean sea level pressure (hPa) from the DFS 5.2 atmospheric forcing dataset for (a) 1990–2014, (b) 2003–07 (spinup), and (c) 2008–14 (post-spinup). The average gyre contour over the respective years is shown in black. Bathymetry contours are shown at 500, 1000, and 1500 m in gray.

contributed to the expansion of the gyre, as discussed in Zhong et al. (2019a).

There are key differences between the realistic model used here and the previously used idealized models, in which the edge of the model domain—acting as a vertical wall—essentially marks the constant edge of the gyre, and the location of the surface forcing is held constant. This ability of the gyre to expand is an important mechanism by which the gyre is able to adjust to a change in Ekman pumping.

6. Conclusions

In this study, we have used a realistic high-resolution model to investigate the functioning of the Beaufort Gyre and its evolution over the period 1990–2014, which includes an observed period of strong spinup in response to changes in the atmospheric and sea ice conditions (Regan et al. 2019; Meneghello et al. 2018b). Previous studies, based on idealized models (Davis et al. 2014; Manucharyan and Spall 2016; Doddridge et al. 2019) or realistic low resolution models (Marshall et al. 2017) have suggested that such a spinup of the large scale gyre, driven by an increase in Ekman pumping, would be balanced by an increase in eddy flux that would arrest the steepening of the isohalines; some delay of the response might be expected due to the effect of the eddy memory (Manucharyan et al. 2017). This would also be consistent with the increase of the number of eddies found by Zhao et al. (2016) in 2013–14 compared to the previous decade in their ITP-based eddy survey, which could be an indication of intensified baroclinic instability in the southern portion of the gyre, although the limited number of eddies sampled questions the statistical significance of this finding.

Here the model allows us to describe the spatiotemporal evolutions of the total and eddy kinetic energy in the Canada Basin. In contrast to those previous results, we find that the gyre is able to spin up and sustain a higher level of mean kinetic energy that is generally not accompanied by higher levels of EKE. Two processes are invoked here to explain the discrepancies with the previous findings. On the southern side of the gyre, the presence of the continental slope tends to stabilize the gyre as suggested by Manucharyan and Isachsen (2019), so that the intensification of the mean current there only results in moderate enhanced levels of EKE. On the northern side of the gyre that is not directly constrained by bathymetry, the gyre is able to expand in response to an increase in Ekman pumping that extends to the northwest during and after the spinup, flattening the isohalines and thus limiting again the development of baroclinic instabilities. This, along with enhanced mean currents strengthening the ice–ocean governor, results in little increase in EKE after spinup. Indeed, on interannual time scales, the ice–ocean governor can dominate over EKE in equilibrating the gyre (Meneghello et al. 2020). These key ingredients, most likely important for the gyre equilibration, are currently not considered in most simple process models and should be included in future studies. The role of additional processes such as barotropic instabilities or dissipation through the effect of bottom drag may also be important here and should be investigated, as these have been shown to be important for the dynamical equilibrium of the Antarctic Circumpolar Current (e.g., Constantinou and Hogg 2019), which shares many similarities with the dynamics of the Beaufort Gyre.

Regardless of the link between its evolution and the gyre spinup, the EKE model fields exhibit some

interesting features. When looking at our results, one needs to remember that our definition of EKE is based on an anomaly from the annual-mean currents, so that our EKE fields actually also account for the seasonal variations of the large-scale circulation, which are particularly pronounced in the boundary currents. Hence, our EKE fields are not only reflecting the presence of coherent eddies. Keeping these caveats in mind, we find that EKE is generally low in the ice-covered Arctic and of the same order of magnitude as the MKE, consistent with previous observations (e.g., Timmermans et al. 2012; Marcinko et al. 2015). This is because some of the key ingredients generating turbulence in the open ocean are missing: low net surface stress, due to a dampening of wind stress by sea ice, and high stratification lead to low levels of energy (Rainville and Woodgate 2009). Another Arctic-specific feature is the subsurface intensification of EKE. Indeed, in contrast to the surface where sea ice represents an additional source of dissipation for mesoscale eddies, eddies generated within the halocline will tend to survive longer (G. Meneghello et al. 2019, unpublished manuscript).

Our analysis also reveals that different time scales are important for the dynamics of the Beaufort Gyre and its adjustment. Some of the key parameters used here to describe the gyre, such as the position of the center, the intensity of the gyre or the freshwater content within the gyre, appear to respond gradually to changes in atmospheric forcing and sea ice conditions, with a gradual spinup occurring over 2003–07. This contrasts with the response to the anomalously strong downwelling that occurs throughout 2007 (Fig. 2g; Meneghello et al. 2018b), which forces a sharp increase in both the mean and eddy kinetic energy in the gyre in 2007. Yet, while the doubling in mean kinetic energy lasts after the return to normal atmospheric conditions after 2008, the level of EKE decreases again in 2008. In line with the study of Johnson et al. (2018) that suggested that the Arctic freshwater content holds a memory of the previous decade of atmospheric forcing, our results suggest that different features of the gyre can respond differently to long term trends and strong anomalous events in the atmospheric forcing, but also show that the gyre can retain a strong memory of extreme atmospheric events. The projected increase in Arctic storminess (e.g., Day et al. 2018) may thus have an impact on the large scale circulation in the Arctic.

Acknowledgments. We thank Helen Johnson, Anne Marie Tréguier, and Andy Hogg for valuable discussions at an early stage of this study. We also thank Pauline Tedesco for useful discussions on ocean energetics. We are grateful to Mike Spall and an anonymous reviewer for their comments which helped to improve the manuscript. The pan-Arctic simulation was performed using HPC resources from GENCI-CINES (Grant 2018-A0050107420). We acknowledge funding from the French LEFE/INSU program through the project FREDY, from the French ANR through the project ImMEDIAT (Grant ANR-18-CE01-0010), and from the MISTI Global Seeds Funds for the project "The Arctic in a Warming World." This work is also part of the ARKTALAS Hoavva study funded by the European Space Agency under the Contract 4000127401/19/NL/LF. G. M. acknowledges support from the NSF program in Arctic Research, through the Grant 1603557. The freshwater content data were collected and made available by the Beaufort Gyre Exploration Program based at the Woods Hole Oceanographic Institution (http://www.whoi.edu/beaufortgyre) in collaboration with researchers from Fisheries and Oceans Canada at the Institute of Ocean Sciences. Arctic dynamic topography data were provided by the Centre for Polar Observation and Modelling, University College London (www.cpom.ucl.ac.uk/dynamic_topography) (Armitage et al. 2016, 2017).

REFERENCES

Armitage, T. W. K., S. Bacon, A. L. Ridout, S. Thomas, Y. Aksenov, and D. J. Wingham, 2016: Arctic sea surface height variability and change from satellite radar altimetry and GRACE, 2003–2014. *J. Geophys. Res. Oceans*, **121**, 4303–4322, https://doi.org/10.1002/2015JC011579.

——, ——, ——, A. A. Petty, S. Wolbach, and M. Tsamados, 2017: Arctic Ocean surface geostrophic circulation 2003–2014. *Cryosphere*, **11**, 1767–1780, https://doi.org/10.5194/tc-11-1767-2017.

Arzel, O., T. Fichefet, H. Goosse, and J.-L. Dufresne, 2008: Causes and impacts of changes in the Arctic freshwater budget during the twentieth and twenty-first centuries in an AOGCM. *Climate Dyn.*, **30**, 37–58, https://doi.org/10.1007/s00382-007-0258-5.

Balwada, D., K. G. Speer, J. H. LaCasce, W. B. Owens, J. Marshall, and R. Ferrari, 2016: Circulation and stirring in the southeast Pacific Ocean and the Scotia Sea sectors of the Antarctic Circumpolar Current. *J. Phys. Oceanogr.*, **46**, 2005–2027, https://doi.org/10.1175/JPO-D-15-0207.1.

Barnier, B., and Coauthors, 2006: Impact of partial steps and momentum advection schemes in a global ocean circulation model at eddy-permitting resolution. *Ocean Dyn.*, **56**, 543–567, https://doi.org/10.1007/s10236-006-0082-1.

Beckmann, A., C. W. Böning, B. Brügge, and D. Stammer, 1994: On the generation and role of eddy variability in the central North Atlantic Ocean. *J. Geophys. Res.*, **99**, 20 381–20 391, https://doi.org/10.1029/94JC01654.

Belkin, I. M., S. Levitus, J. Antonov, and S.-A. Malmberg, 1998: "Great salinity anomalies" in the North Atlantic. *Prog. Oceanogr.*, **41**, 1–68, https://doi.org/10.1016/S0079-6611(98)00015-9.

Bourgain, P., and J.-C. Gascard, 2011: The Arctic Ocean halocline and its interannual variability from 1997 to 2008. *Deep-Sea Res. I*, **58**, 745–756, https://doi.org/10.1016/j.dsr.2011.05.001.

Brannigan, L., H. Johnson, C. Lique, J. Nycander, and J. Nilsson, 2017: Generation of subsurface anticyclones at arctic surface fronts due to a surface stress. *J. Phys. Oceanogr.*, **47**, 2653–2671, https://doi.org/10.1175/JPO-D-17-0022.1.

Brodeau, L., B. Barnier, A.-M. Tréguier, T. Penduff, and S. K. Gulev, 2010: An ERA40-based atmospheric forcing for global ocean circulation models. *Ocean Modell.*, **31**, 88–104, https://doi.org/10.1016/j.ocemod.2009.10.005.

Carmack, E. C., and Coauthors, 2016: Freshwater and its role in the Arctic Marine System: Sources, disposition, storage, export, and physical and biogeochemical consequences in the Arctic and global oceans. *J. Geophys. Res. Biogeosci.*, **121**, 675–717, https://doi.org/10.1002/2015JG003140.

Constantinou, N. C., and A. M. Hogg, 2019: Eddy saturation of the Southern Ocean: A baroclinic versus barotropic perspective. *Geophys. Res. Lett.*, **46**, 12 202–12 212, https://doi.org/10.1029/2019GL084117.

Dai, A., and K. E. Trenberth, 2002: Estimates of freshwater discharge from continents: Latitudinal and longitudinal variations. *J. Hydrometeor.*, **3**, 660–687, https://doi.org/10.1175/1525-7541(2002)003<0660:EOFDFC>2.0.CO;2.

Davis, P. E. D., C. Lique, and H. L. Johnson, 2014: On the link between Arctic sea ice decline and the freshwater content of the Beaufort Gyre: Insights from a simple process model. *J. Climate*, **27**, 8170–8184, https://doi.org/10.1175/JCLI-D-14-00090.1.

——, ——, ——, and J. D. Guthrie, 2016: Competing effects of elevated vertical mixing and increased freshwater input on the stratification and sea ice cover in a changing arctic ocean. *J. Phys. Oceanogr.*, **46**, 1531–1553, https://doi.org/10.1175/JPO-D-15-0174.1.

Day, J. J., M. M. Holland, and K. I. Hodges, 2018: Seasonal differences in the response of Arctic cyclones to climate change in CESM1. *Climate Dyn.*, **50**, 3885–3903, https://doi.org/10.1007/s00382-017-3767-x.

de Lavergne, C., S. Falahat, G. Madec, F. Roquet, J. Nycander, and C. Vic, 2019: Toward global maps of internal tide energy sinks. *Ocean Modell.*, **137**, 52–75, https://doi.org/10.1016/j.ocemod.2019.03.010.

Dickson, R. R., J. Meincke, S.-A. Malmberg, and A. J. Lee, 1988: The "great salinity anomaly" in the northern North Atlantic 1968–1982. *Prog. Oceanogr.*, **20**, 103–151, https://doi.org/10.1016/0079-6611(88)90049-3.

Doddridge, E. W., G. Meneghello, J. Marshall, J. Scott, and C. Lique, 2019: A three-way balance in the Beaufort Gyre: The ice-ocean governor, wind stress, and eddy diffusivity. *J. Geophys. Res. Oceans*, **124**, 3107–3124, https://doi.org/10.1029/2018JC014897.

Dupont, F., and Coauthors, 2015: A high-resolution ocean and sea-ice modelling system for the Arctic and North Atlantic oceans. *Geosci. Model Dev.*, **8**, 1577–1594, https://doi.org/10.5194/gmd-8-1577-2015.

Eady, E. T., 1949: Long waves and cyclone waves. *Tellus*, **1**, 33–52, https://doi.org/10.3402/tellusa.v1i3.8507.

Eden, C., and C. Böning, 2002: Sources of eddy kinetic energy in the Labrador Sea. *J. Phys. Oceanogr.*, **32**, 3346–3363, https://doi.org/10.1175/1520-0485(2002)032<3346:SOEKEI>2.0.CO;2.

Giles, K. A., S. W. Laxon, A. L. Ridout, D. J. Wingham, and S. Bacon, 2012: Western Arctic Ocean freshwater storage increased by wind-driven spin-up of the Beaufort Gyre. *Nat. Geosci.*, **5**, 194–197, https://doi.org/10.1038/ngeo1379.

Haine, T. W. N., and Coauthors, 2015: Arctic freshwater export: Status, mechanisms, and prospects. *Global Planet. Change*, **125**, 13–35, https://doi.org/10.1016/j.gloplacha.2014.11.013.

Hogg, A. M., M. P. Meredith, D. P. Chambers, E. P. Abrahamsen, C. W. Hughes, and A. K. Morrison, 2015: Recent trends in the Southern Ocean eddy field. *J. Geophys. Res. Oceans*, **120**, 257–267, https://doi.org/10.1002/2014JC010470.

Hu, X., P. G. Myers, and Y. Lu, 2019: Pacific water pathway in the Arctic Ocean and Beaufort Gyre in two simulations with different horizontal resolutions. *J. Geophys. Res. Oceans*, **124**, 6414–6432, https://doi.org/10.1029/2019JC015111.

Hunkins, K., 1981: Arctic Ocean eddies and baroclinic instability. Tech. Rep. CU2-81, Lamont-Doherty Geol. Obs., 39 pp.

Jahn, A., and M. M. Holland, 2013: Implications of Arctic sea ice changes for North Atlantic deep convection and the meridional overturning circulation in CCSM4-CMIP5 simulations. *Geophys. Res. Lett.*, **40**, 1206–1211, https://doi.org/10.1002/grl.50183.

Johnson, H. L., S. Cornish, Y. Kostov, E. Beer, and C. Lique, 2018: Arctic Ocean freshwater content and its decadal memory of sea-level pressure. *Geophys. Res. Lett.*, **45**, 4991–5001, https://doi.org/10.1029/2017GL076870.

Krishfield, R. A., A. Proshutinsky, K. Tateyama, W. J. Williams, E. C. Carmack, F. A. McLaughlin, and M. L. Timmermans, 2014: Deterioration of perennial sea ice in the Beaufort Gyre from 2003 to 2012 and its impact on the oceanic freshwater cycle. *J. Geophys. Res. Oceans*, **119**, 1271–1305, https://doi.org/10.1002/2013JC008999.

Le Traon, P. Y., 1991: Time scales of mesoscale variability and their relationship with space scales in the North Atlantic. *J. Mar. Res.*, **49**, 467–492, https://doi.org/10.1357/002224091784995828.

Lique, C., and H. L. Johnson, 2015: Is there any imprint of the wind variability on the Atlantic water circulation within the Arctic Basin? *Geophys. Res. Lett.*, **42**, 9880–9888, https://doi.org/10.1002/2015GL066141.

——, ——, and P. E. D. Davis, 2015: On the interplay between the circulation in the surface and the intermediate layers of the Arctic Ocean. *J. Phys. Oceanogr.*, **45**, 1393–1409, https://doi.org/10.1175/JPO-D-14-0183.1.

——, M. M. Holland, Y. B. Dibike, D. M. Lawrence, and J. A. Screen, 2016: Modeling the Arctic freshwater system and its integration in the global system: Lessons learned and future challenges. *J. Geophys. Res. Biogeosci.*, **121**, 540–566, https://doi.org/10.1002/2015JG003120.

Madec, G., 2016: NEMO ocean engine. Note du Pôle de modélisation de l'Institut Pierre-Simon Laplace 27, 386 pp., https://www.nemo-ocean.eu/wp-content/uploads/NEMO_book.pdf.

Manley, T. O., and K. Hunkins, 1985: Mesoscale eddies of the Arctic Ocean. *J. Geophys. Res.*, **90**, 4911–4930, https://doi.org/10.1029/JC090iC03p04911.

Manucharyan, G. E., and M. A. Spall, 2016: Wind-driven freshwater buildup and release in the Beaufort Gyre constrained by mesoscale eddies. *Geophys. Res. Lett.*, **43**, 273–282, https://doi.org/10.1002/2015GL065957.

——, and P. Isachsen, 2019: Critical role of continental slopes in halocline and eddy dynamics of the Ekman-driven Beaufort Gyre. *J. Geophys. Res. Oceans*, **124**, 2679–2696, https://doi.org/10.1029/2018JC014624.

——, A. F. Thompson, and M. A. Spall, 2017: Eddy-Memory mode of multi-decadal variability in residual-mean ocean circulations with application to the Beaufort Gyre. *J. Phys. Oceanogr.*, **47**, 855–866, https://doi.org/10.1175/JPO-D-16-0194.1.

Marcinko, C., A. P. Martin, and J. T. Allen, 2015: Characterizing horizontal variability and energy spectra in the Arctic Ocean halocline. *J. Geophys. Res. Oceans*, **120**, 436–450, https://doi.org/10.1002/2014JC010381.

Marshall, J., J. Scott, and A. Proshutinsky, 2017: "Climate response functions" for the Arctic Ocean: A proposed coordinated modelling experiment. *Geosci. Model Dev.*, **10**, 2833–2848, https://doi.org/10.5194/gmd-10-2833-2017.

Maslowski, W., J. C. Kinney, D. C. Marble, and J. Jakacki, 2008: Towards eddy-resolving models of the Arctic Ocean. *Ocean Modeling in an Eddying Regime*, *Geophys. Monogr.*, Vol. 177, Amer. Geophys. Union, 241–264.

McLaughlin, F. A., and E. C. Carmack, 2010: Deepening of the nutricline and chlorophyll maximum in the Canada Basin interior, 2003–2009. *Geophys. Res. Lett.*, **37**, L24602, https://doi.org/10.1029/2010GL045459.

Meneghello, G., J. Marshall, S. T. Cole, and M.-L. Timmermans, 2017: Observational inferences of lateral eddy diffusivity in the halocline of the Beaufort Gyre. *Geophys. Res. Lett.*, **44**, 12 331–12 338, https://doi.org/10.1002/2017GL075126.

——, ——, J.-M. Campin, E. Doddridge, and M.-L. Timmermanns, 2018a: The ice-ocean governor: Ice-ocean stress feedback limits Beaufort Gyre spinup. *Geophys. Res. Lett.*, **45**, 11 293–11 299, https://doi.org/10.1029/2018GL080171.

——, ——, M.-L. Timmermans, and J. Scott, 2018b: Observations of seasonal upwelling and downwelling in the Beaufort Sea mediated by sea ice. *J. Phys. Oceanogr.*, **48**, 795–805, https://doi.org/10.1175/JPO-D-17-0188.1.

——, E. Doddridge, J. Marshall, J. Scott, and J.-M. Campin, 2020: Exploring the role of the "ice–ocean governor" and mesoscale eddies in the equilibration of the Beaufort Gyre: Lessons from observations. *J. Phys. Oceanogr.*, **50**, 269–277, https://doi.org/10.1175/JPO-D-18-0223.1.

Newton, J. L., K. Aagaard, and L. K. Coachman, 1974: Baroclinic eddies in the Arctic Ocean. *Deep-Sea Res. Oceanogr. Abstr.*, **21**, 707–719, https://doi.org/10.1016/0011-7471(74)90078-3.

Nurser, A. J., and S. Bacon, 2014: The Rossby radius in the Arctic Ocean. *Ocean Sci.*, **10**, 967–975, https://doi.org/10.5194/os-10-967-2014.

Ou, H. W., and A. L. Gordon, 1986: Spin-down of baroclinic eddies under sea ice. *J. Geophys. Res.*, **91**, 7623–7630, https://doi.org/10.1029/JC091iC06p07623.

Pickart, R. S., 2004: Shelfbreak circulation in the Alaskan Beaufort Sea: Mean structure and variability. *J. Geophys. Res.*, **109**, C04024, https://doi.org/10.1029/2003JC001912.

——, M. A. Spall, and J. T. Mathis, 2013: Dynamics of upwelling in the Alaskan Beaufort Sea and associated shelf-basin fluxes. *Deep-Sea Res. I*, **76**, 35–51, https://doi.org/10.1016/j.dsr.2013.01.007.

Plueddemann, A. J., R. Krishfield, T. Takizawa, K. Hatakeyama, and S. Honjo, 1998: Upper ocean velocities in the Beaufort Gyre. *Geophys. Res. Lett.*, **25**, 183–186, https://doi.org/10.1029/97GL53638.

Polyakov, I. V., A. V. Pnyushkov, and E. C. Carmack, 2018: Stability of the arctic halocline: A new indicator of arctic climate change. *Environ. Res. Lett.*, **13**, 125008, https://doi.org/10.1088/1748-9326/AAEC1E.

Proshutinsky, A., and Coauthors, 2009: Beaufort Gyre freshwater reservoir: State and variability from observations. *J. Geophys. Res.*, **114**, C00A10, https://doi.org/10.1029/2008JC005104.

——, D. Dukhovskoy, M.-L. Timmermanns, R. Krishfield, and J. Bamber, 2015: Arctic circulation regimes. *Philos. Trans. Roy. Soc. A*, **373**, 20140160, https://doi.org/10.1098/rsta.2014.0160.

——, and Coauthors, 2020: Analysis of the Beaufort Gyre freshwater content in 2003–2018. *J. Geophys. Res. Oceans*, **124**, 9658–9689, https://doi.org/10.1029/2019JC015281.

Rainville, L., and R. A. Woodgate, 2009: Observations of internal wave generation in the seasonally ice-free Arctic. *Geophys. Res. Lett.*, **36**, L23604, https://doi.org/10.1029/2009GL041291.

Regan, H. C., C. Lique, and T. W. K. Armitage, 2019: The Beaufort Gyre extent, shape, and location between 2003 and 2014 from satellite observations. *J. Geophys. Res. Oceans*, **124**, 844–862, https://doi.org/10.1029/2018JC014379.

Richardson, P. L., 1983: A vertical section of eddy kinetic energy through the Gulf Stream system. *J. Geophys. Res.*, **88**, 2705–2709, https://doi.org/10.1029/JC088iC04p02705.

Rieck, J. K., C. W. Böning, R. J. Greatbatch, and M. Scheinert, 2015: Seasonal variability of eddy kinetic energy in a global high-resolution ocean model. *Geophys. Res. Lett.*, **42**, 9379–9386, https://doi.org/10.1002/2015GL066152.

——, ——, and ——, 2018: Decadal variability of eddy kinetic energy in the South Pacific subtropical countercurrent in an ocean general circulation model. *J. Phys. Oceanogr.*, **48**, 757–771, https://doi.org/10.1175/JPO-D-17-0173.1.

Rousset, C., and Coauthors, 2015: The Louvain-La-Neuve sea ice model LIM3.6: Global and regional capabilities. *Geosci. Model Dev.*, **8**, 2991–3005, https://doi.org/10.5194/gmd-8-2991-2015.

Schmidtko, S., G. C. Johnson, and J. M. Lyman, 2013: MIMOC: A global monthly isopycnal upper-ocean climatology with mixed layers. *J. Geophys. Res. Oceans*, **118**, 1658–1672, https://doi.org/10.1002/jgrc.20122.

Serreze, M. C., and A. P. Barrett, 2011: Characteristics of the Beaufort Sea high. *J. Climate*, **24**, 159–182, https://doi.org/10.1175/2010JCLI3636.1.

Shimada, K., M. Itoh, S. Nishino, F. McLaughlin, E. Carmack, and A. Proshutinsky, 2005: Halocline structure in the Canada Basin of the Arctic Ocean. *Geophys. Res. Lett.*, **32**, L03605, https://doi.org/10.1029/2004GL021358.

Spall, M., 2000: Generation of strong mesoscale eddies by weak ocean gyres. *J. Mar. Res.*, **58**, 97–116, https://doi.org/10.1357/002224000321511214.

Spall, M. A., R. S. Pickart, P. S. Fratantoni, and A. J. Plueddemann, 2008: Western Arctic shelfbreak eddies: Formation and transport. *J. Phys. Oceanogr.*, **38**, 1644–1668, https://doi.org/10.1175/2007JPO3829.1.

——, ——, M. Li, M. Itoh, P. Lin, T. Kikuchi, and Y. Qi, 2018: Transport of Pacific water into the Canada Basin and the formation of the Chukchi slope current. *J. Geophys. Res. Oceans*, **123**, 7453–7471, https://doi.org/10.1029/2018JC013825.

Timmermans, M.-L., J. Toole, A. Proshutinsky, R. Krishfield, and A. Plueddemann, 2008: Eddies in the Canada Basin, Arctic Ocean, observed from ice-tethered profilers. *J. Phys. Oceanogr.*, **38**, 133–145, https://doi.org/10.1175/2007JPO3782.1.

——, S. Cole, and J. Toole, 2012: Horizontal density structure and restratification of the Arctic Ocean surface layer. *J. Phys. Oceanogr.*, **42**, 659–668, https://doi.org/10.1175/JPO-D-11-0125.1.

——, and Coauthors, 2014: Mechanisms of Pacific summer water variability in the Arctic's Central Canada Basin. *J. Geophys. Res.*, **119**, 7523–7548, https://doi.org/10.1002/2014JC010273.

Toole, J., R. Krishfield, M.-L. Timmermans, and A. Proshutinsky, 2011: The ice-tethered profiler: Argo of the Arctic. *Oceanography*, **24**, 126–135, https://doi.org/10.5670/oceanog.2011.64.

Tréguier, A.-M., and Coauthors, 2014: Meridional transport of salt in the global ocean from an eddy-resolving model. *Ocean Sci.*, **10**, 243–255, https://doi.org/10.5194/os-10-243-2014.

Trodahl, M., and P. E. Isachsen, 2018: Topographic influence on baroclinic instability and the mesoscale eddy field in the

Northern North Atlantic Ocean and the Nordic Seas. *J. Phys. Oceanogr.*, **48**, 2593–2607, https://doi.org/10.1175/JPO-D-17-0220.1.

von Appen, W.-J., and R. S. Pickart, 2012: Two configurations of the Western Arctic shelfbreak current in summer. *J. Phys. Oceanogr.*, **42**, 329–351, https://doi.org/10.1175/JPO-D-11-026.1.

von Storch, J. S., C. Eden, I. Fast, H. Haak, D. Hernández, E. Maier-Reimer, J. Marotzke, and D. Stammer, 2012: An estimate of the Lorenz energy cycle for the World Ocean based on the STORM/NCEP simulation. *J. Phys. Oceanogr.*, **42**, 2185–2205, https://doi.org/10.1175/JPO-D-12-079.1.

Wang, Q., and Coauthors, 2016: An assessment of the arctic ocean in a suite of interannual core-II simulations. Part II: Liquid freshwater. *Ocean Modell.*, **99**, 86–109, https://doi.org/10.1016/j.ocemod.2015.12.009.

Watanabe, E., and H. Hasumi, 2009: Pacific water transport in the Western Arctic Ocean simulated by an eddy-resolving coupled sea ice-ocean model. *J. Phys. Oceanogr.*, **39**, 2194–2211, https://doi.org/10.1175/2009JPO4010.1.

——, and Coauthors, 2014: Enhanced role of eddies in the Arctic marine biological pump. *Nat. Commun.*, **5**, 3950, https://doi.org/10.1038/ncomms4950.

Winters, K. B., P. N. Lombard, J. J. Riley, and E. A. D'Asaro, 1995: Available potential energy and mixing in density-stratified fluids. *J. Fluid Mech.*, **289**, 115–128, https://doi.org/10.1017/S002211209500125X.

Woodgate, R. A., K. M. Stafford, and F. G. Prahl, 2015: A synthesis of year-round interdisciplinary mooring measurements in the Bering Strait (1990-2014) and the RUSALCA years (2004-2011). *Oceanography*, **28**, 46–67, https://doi.org/10.5670/oceanog.2015.57.

Wunsch, C., 2002: Ocean observations and the climate forecast problem. *Meteorology at the Millennium*, R. Pearce, Ed., International Geophysics Series, Vol. 83, Academic Press, 233–245.

Zhai, X., R. J. Greatbatch, and J.-D. Kohlmann, 2008: On the seasonal variability of eddy kinetic energy in the Gulf Stream region. *Geophys. Res. Lett.*, **35**, L24609, https://doi.org/10.1029/2008GL036412.

Zhang, J., and Coauthors, 2016: The Beaufort Gyre intensification and stabilization: A model-observation synthesis. *J. Geophys. Res. Oceans*, **121**, 7933–7952, https://doi.org/10.1002/2016JC012196.

Zhang, Z., J. Tian, B. Qiu, W. Zhao, P. Chang, D. Wu, and X. Wan 2016: Observed 3D structure, generation, and dissipation of oceanic mesoscale eddies in the South China Sea. *Sci. Rep.*, **6**, 24349, https://doi.org/10.1038/srep24349.

Zhao, M., M. L. Timmermans, S. Cole, R. Krishfield, A. Proshutinsky, and J. Toole, 2014: Characterizing the eddy field in the Arctic Ocean halocline. *J. Geophys. Res. Oceans*, **119**, 8800–8817, https://doi.org/10.1002/2014JC010488.

——, ——, ——, ——, and J. Toole, 2016: Evolution of the eddy field in the Arctic Ocean's Canada Basin, 2005–2015. *Geophys. Res. Lett.*, **43**, 8106–8114, https://doi.org/10.1002/2016GL069671.

Zhong, W., M. Steele, J. Zhang, and S. T. Cole, 2019a: Circulation of Pacific winter water in the Western Arctic Ocean. *J. Geophys. Res. Oceans*, **124**, 863–881, https://doi.org/10.1029/2018JC014604.

——, J. Zhang, M. Steele, J. Zhao, and T. Wang, 2019b: Episodic extrema of surface stress energy input to the Western Arctic Ocean contributed to step changes of freshwater content in the Beaufort Gyre. *Geophys. Res. Lett.*, **46**, 12 173–12 182, https://doi.org/10.1029/2019GL084652.

Geophysical Research Letters

RESEARCH LETTER
10.1029/2020GL092066

Key Points:

- We develop a new method to identify under-ice ocean surface eddy in the Arctic from ice vorticity based on synthetic-aperture radar images
- We detect the signature of an eddy dipole with a horizontal scale of 80–100 km, persistent on a week, which was also sampled by a mooring

Correspondence to:

A. Cassianides,
angelina.cassianides@ifremer.fr

Citation:

Cassianides, A., Lique, C., & Korosov, A. (2021). Ocean eddy signature on SAR-derived sea ice drift and vorticity. *Geophysical Research Letters*, *48*, e2020GL092066. https://doi.org/10.1029/2020GL092066

Received 7 SEP 2020
Accepted 11 FEB 2021

Ocean Eddy Signature on SAR-Derived Sea Ice Drift and Vorticity

Angelina Cassianides[1], Camille Lique[1], and Anton Korosov[2]

[1]Univ. Brest, CNRS, IRD, Ifremer, Laboratoire d'Océanographie Physique et Spatiale (LOPS), IUEM, Brest, France, [2]Nansen Environmental and Remote Sensing Center, Bergen, Norway

Abstract In the Arctic Ocean, the observation of mesoscale eddies is impeded by the presence of sea ice. To address this problem, we develop a new method of ocean eddy detection based on their signature in sea ice vorticity retrieved from synthetic-aperture radar (SAR) images. We examine the case of one eddy in October 2017 in the marginal ice zone of the Canadian Basin, which was sampled by mooring observations. Although the eddy could not be identified by visual inspection of the SAR images, its signature is revealed as a dipole anomaly in sea ice vorticity, which suggests that the eddy is a dipole composed of a cyclone and an anticyclone, with a horizontal scale of 80–100 km and persisted over a week. The robustness of our method will allow us to detect more eddies as more SAR observations become available in the future.

Plain Language Summary Mesoscale eddies are routinely observed by satellites in the ocean. Yet, in the ice-covered Arctic Basin, the presence of sea ice makes it challenging to characterize the eddy field. Here, we present a detection method of surface ocean eddies based on their signature in the displacement of sea ice, using high spatial resolution satellite images. A dipole composed of a cyclonic and an anticyclonic eddy is identified over a week in mid-October 2017 with a horizontal scale of 80–100 km. Its presence is confirmed by high values of ocean speed in the surface layer during the same period. This work demonstrates that processing is required for identifying the signature of eddies in sea ice, which is not always obvious at first sight.

1. Introduction

For decades, many studies have reported on the presence of mesoscale eddies in the ice-covered Arctic, randomly captured by in situ measurements (e.g., Manley & Hunkins, 1985; Newton et al., 1974). Recently, observations of high temporal and spatial resolution temperature and salinity profiles from Ice-Tethered Profilers (ITP; Toole et al., 2011) and moorings have allowed for the first time a census of the eddy characteristics (Carpenter & Timmermans, 2012; Zhao et al., 2014, 2016), revealing the presence of numerous small scale eddies at all depths in the Arctic interior, with horizontal length scales ranging from 5 to 20 km. Yet, the sampling of the Arctic Ocean by ITPs remains uneven, preventing us from obtaining a full description of the mesoscale activity at a Pan-Arctic scale. Moreover, in the ice-covered regions, satellites primarily return observations of the sea ice conditions, which do not allow for the usual identification of eddies based on the detection of their signature on surface properties (anomaly of sea level, temperature or tracers). Satellite-based detection of eddies is thus restricted to the ice-free regions of the Arctic and the marginal ice zone (MIZ).

There is growing evidence in the literature that the Arctic mesoscale activity and the sea ice might mutually influence each other. Aerial surveys (Johannessen et al., 1987) or high resolution satellite observations (Kozlov et al., 2019) of the Arctic MIZ have revealed swirling movements of sea ice that are the signature of ocean eddies. An example is shown in Figure 1a for October 2018 in the MIZ of the Canadian Basin. Using an idealized process model representing the MIZ, Manucharyan and Thompson (2017) have rationalized the imprint of (sub-)mesoscale eddies on sea ice, suggesting that, in the MIZ, sea ice tends to be trapped and accumulated in surface cyclonic eddies. Sea ice transported by eddies can locally affect the sea ice drift, producing strong sea ice deformation (Zhang et al., 1999). So far, the eddy detection in the MIZ was mostly based on visual inspection of satellite images (e.g., Kozlov et al., 2019), and may have missed a significant number of eddies when their signature is not directly recognizable. This method of detection is also based

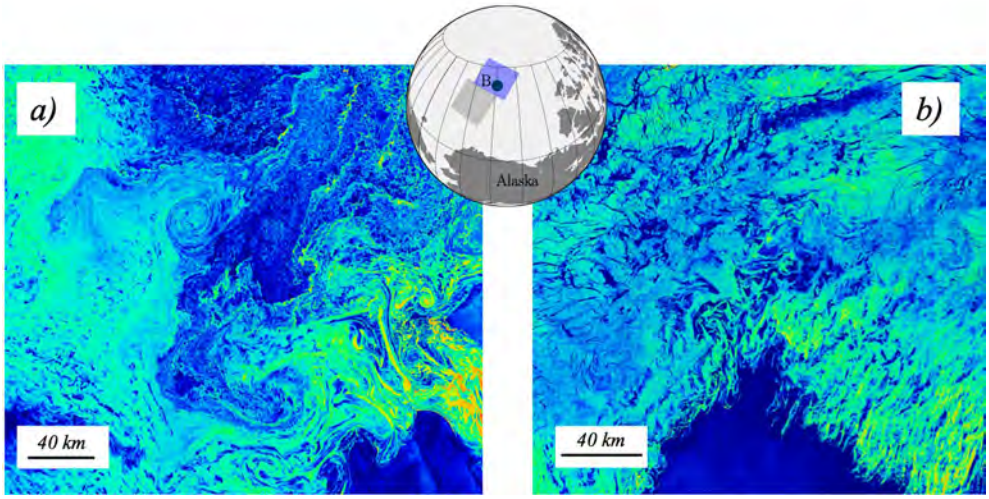

Figure 1. Examples of synthetic-aperture radar (SAR) images in the marginal ice zone (MIZ) of the Canadian Basin for (a) October 19, 2018 (centered around 76°N, 160°W) and (b) October 9, 2017 (centered around 78°N, 150°W). The inset map indicates the position of the two images (gray shading for (a) and purple for (b)), and the green dot is the position of mooring B. Colors visualize the SAR backscatter, with dark blue indicating ocean and green and yellow the presence of sea ice.

on the overly strong assumption that the signature of one eddy on sea ice would mimic exactly the shape and scale of the ocean feature itself, which is likely not the case in many instances (Gupta et al., 2020).

The goal of this paper is to present a new method to detect the signature of ocean surface eddies in sea ice vorticity, based on the analysis of high resolution images from synthetic-aperture radar (SAR). Here we mostly focus on one case study shown in Figure 1b, located in a MIZ of the Canadian Basin (around 78°N-150°W) in October 2017. This case is chosen as both sea ice and ocean observations are available at that time and location. Although no eddy imprint can be seen at first sight, we will show how further processing of the SAR images can reveal the presence of an ocean eddy. This paper is structured as follows. Section 2 briefly presents the data sets analyzed in this study. In Section 3, an ocean eddy is detected from mooring observations. The processing of SAR images and the eddy signature in sea ice vorticity are presented in Section 4. The robustness of the method is discussed in Section 5 and conclusions are given in Section 6.

2. Data

The primary in situ data used in this study are mooring observations from the Beaufort Gyre Exploration Project (BGEP; https://www.whoi.edu, Proshutinsky et al., 2009). Four moorings are deployed over the Beaufort Gyre since 2003. Upward-looking acoustic Doppler current profilers (ADCPs) are installed on the top of each mooring, returning profiles of ocean horizontal currents in the top ~30 m of the water column, with a resolution of 1 h and 2 m. Additionally, upward looking sonars (ULSs) are installed on the same moorings and provide a time series of ice draft with uncertainty of 5–10 cm (Krishfield & Proshutinsky, 2006). In the following, we use data from mooring B located at 78°N-150°W during 2017.

The sea ice response to the presence of mesoscale eddies is investigated using SAR imagery. The Sentinel-1 imaging radar mission, led by the European Space Agency (ESA), includes two satellites equipped with C-band SAR sensors: Sentinel-1A and Sentinel-1B launched in 2014 and 2016, respectively. The data product used here is the Level-1 Extra-Wide Swath mode ground range detected with medium resolution, available at the Copernicus Open Access Hub (scihub.copernicus.eu). The swath width is 400 km and the pixels are spaced by 40 × 40 m. HH (horizontal emission, horizontal receive) and HV (horizontal emission, vertical receive) polarization modes are used separately. The temporal resolution over the mooring location is uneven and depends on various factors such as the satellite's orbit or the acquisition mode. Hence, the time interval between two images varies from a few hours to a few days.

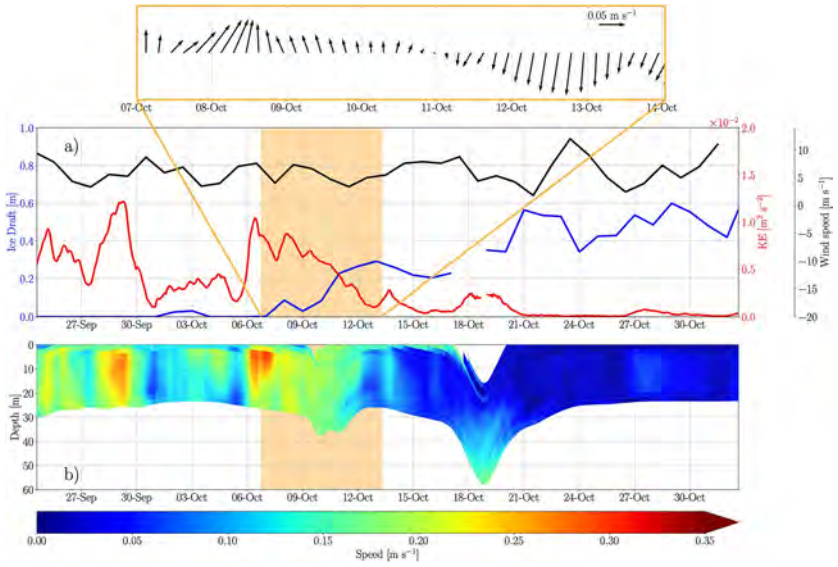

Figure 2. (a) Time series of ice draft (blue), KE (0–30 m, red) from the Acoustic Doppler Current Profiler (ADCP) and wind speed (black) in 2017. A stick diagram of the ocean current anomalies (relative to the mean over October 7–13) is shown in the orange box. (b) Ocean speed profiles from the ADCP.

We also make use of the Polar Pathfinder Sea Ice Motion Vectors version 4 from the National Snow and Ice Center (NSIDC, https://nsidc.org), which provides daily sea ice drift at the pan-Arctic scale with a resolution of 25 km over 1978 to 2019 (Tschudi et al., 2019). The error variance associated tends to be particularly large in the MIZ (Tschudi et al., 2020).

Finally, we estimate wind speed using the hourly averaged u_w and v_w wind speed at 10 m ($U_{10} = \sqrt{(u_w^2 + v_w^2)}$) from the ERA5 reanalysis data with a spatial resolution of ~0.25° (provided by ECMWF; Hersbach et al., 2020).

3. Ocean Eddy Detection from Mooring Observations

The first step of this study consists of the detection of an ocean eddy under sea ice. Zhao and Timmermans (2015) have shown that mesoscale eddies contribute to most of the kinetic energy sampled by the BGEP moorings below 60 m. Here, we follow the same method and apply it to the surface layer to identify an eddy passing by the mooring location by a large anomaly of kinetic energy. Using velocity measurements from mooring B's ADCP, we compute a time series of the depth-integrated kinetic energy (KE, normalized by the thickness of the surface layer h) as:

$$KE = \int \left(\frac{1}{2}(u_o^2 + v_o^2)dz \right) / h \tag{1}$$

with u_o and v_o the ocean horizontal velocity components. Note that we have first filtered the high frequency fluctuations (likely induced by the inertial motion) in ocean velocity by applying a moving average with a 12 h moving window, as we are only interested in events that last over a few days.

Figure 2 displays time series of sea ice draft, KE integrated from 0 to ~30 m depth and wind speed during September and October 2017, as well as the ocean speed profiles at mooring B. Before October 7, there is no sea ice at the mooring location (the sea ice draft is zero). High values of KE (close to $1.3 \times 10^{-2} m^2 \cdot s^{-2}$) are observed on two instances on September 28 and October 7. These two periods of high KE are related to increases in ocean speed from 0.15 to 0.3 $m \cdot s^{-1}$ (Figure 2b). After October 7, the sea ice draft increases drastically from 0 to more than 0.6 m while the KE decreases largely. The background flow under sea ice is weak, with mean velocities of 0.05 $m \cdot s^{-1}$ directed northward. After October 16, KE remains lower than $0.5 \times 10^{-2} m^2 \cdot s^{-2}$. The time in between (October 7–13, the orange box) corresponds to the transition from

a period with high kinetic energy and no sea ice to a period with sea ice and very low kinetic energy on average. The anomaly in KE during that period suggests that the mooring is sampling an eddy passing by in the surface layer. The stick diagram of the ocean current anomalies (with respect to the mean over October 7–13; top inset in Figure 2) reveals a sign change, typical of the structure found in the core of an eddy. The ADCP data (and lack of associated density measurements) are not sufficient to allow a direct determination of the eddy's direction of rotation nor of its length scale. Using hydrographic data from CTD cast gathered during the deployment or recovery of the mooring, we estimate that the first deformation radius R_d in the interior of the Canadian Basin is on the order of ∼13 km, similar to the values suggested by Nurser and Bacon (2014) and Zhao et al. (2018). Following for instance Tulloch et al. (2011), this would imply that eddies generated by geostrophic turbulence would have a length scale around $2\pi R_d \approx 82$ km.

Figure 2b also reveals two deep excursions of the ADCP on October 10 and 19, which are most likely the signature of eddies passing by the sub-surface layer, dragging the ADCP deeper (Krishfield & Proshutinsky, 2006). Note that the moorings are also equipped with a McLane Moored Profiler (MMP) that samples velocity, temperature and salinity profiles below 50 m. An examination of the MMP data confirms the presence of an anticyclonic eddy below the mixed-layer on October 18, with a core at 160 m depth (not shown). We are therefore in presence of two eddies propagating on top of each other under sea ice, with an anticyclone as the subsurface component. We hypothesize that these two eddies are the two parts of a dipole, as such features are frequently observed in the Arctic basin (Zhao et al., 2014). Indeed, results from idealized process models have suggested that dipoles are generated at surface front under sea ice (Brannigan et al., 2017), resulting in a cyclone in the surface layer on top of an anticyclone. In our case, it would mean that the surface part of the dipole sampled by the ADCP is a cyclone too.

It is worth noting that, during the full period considered here (September 25–October 30), wind speed remains relatively constant and weak at the mooring location, with an average of 6 $m{\cdot}s^{-1}$ directed southwestward and no storm (Figure 2a). The lack of correlation between wind speed and kinetic energy suggests that the winds are not directly driving the evolution of the kinetic energy.

4. Ocean Eddy Detection from Its Signature in Sea Ice Vorticity

Now that we have detected a pair of eddies from the mooring observations, the next step is to examine the sea ice conditions over that period. According to the OSISAF product (Tonboe et al., 2017, not shown), sea ice concentration at the mooring location is increasing rapidly as the sea ice starts freezing and the draft starts to increase after October 6, and reaches more than 50% from October 7 onward. Over October 7–13, eightSAR images covering the mooring position are available (one for the 7th, 8th, 9th, 10th, two for the 12th and 13th). Consecutive pairs of raw SAR images are first processed with the open-source software Nansat (Korosov et al., 2016). Sea ice drift is then estimated using an algorithm combining feature tracking and pattern matching techniques (Korosov & Rampal, 2017; Muckenhuber et al., 2016). The calculation is performed on a regular orthogonal grid of 4 km. The accuracy of this algorithm is below 300 m (Korosov & Rampal, 2017), resulting in an uncertainty of less than 0.3 $cm{\cdot}s^{-1}$ for the sea ice drift. An example of a sea ice drift field for October 12–13 is presented in Figure 3a. The drift is directed westward and does not present a visible signature of swirling movement characteristic of the presence of mesoscale eddies.

We further compute the relative vorticity of sea ice, which presents the advantage of being a scalar, as:

$$\zeta_{ice} = \frac{\partial v_{ice}}{\partial x} - \frac{\partial u_{ice}}{\partial y} \tag{2}$$

with u_{ice} and v_{ice} the horizontal components of sea ice velocity. The sea ice vorticity estimated for October 12–13 is presented in Figure 3b. West of the mooring (green dot), there is a cyclonic signal (positive vorticity) with a horizontal scale of ∼80 km and values reaching more than 2×10^{-6} s^{-1}. The background sea ice vorticity over most of the domain is negative (i.e., anticyclonic) with an intensity varying between -2×10^{-7} s^{-1} and -6×10^{-6} s^{-1}.

Ocean eddy are often identified through their strong anomaly in ocean vorticity. One would logically expect that an eddy advected under sea ice would exert a strong stress onto sea ice, possibly generating this way an

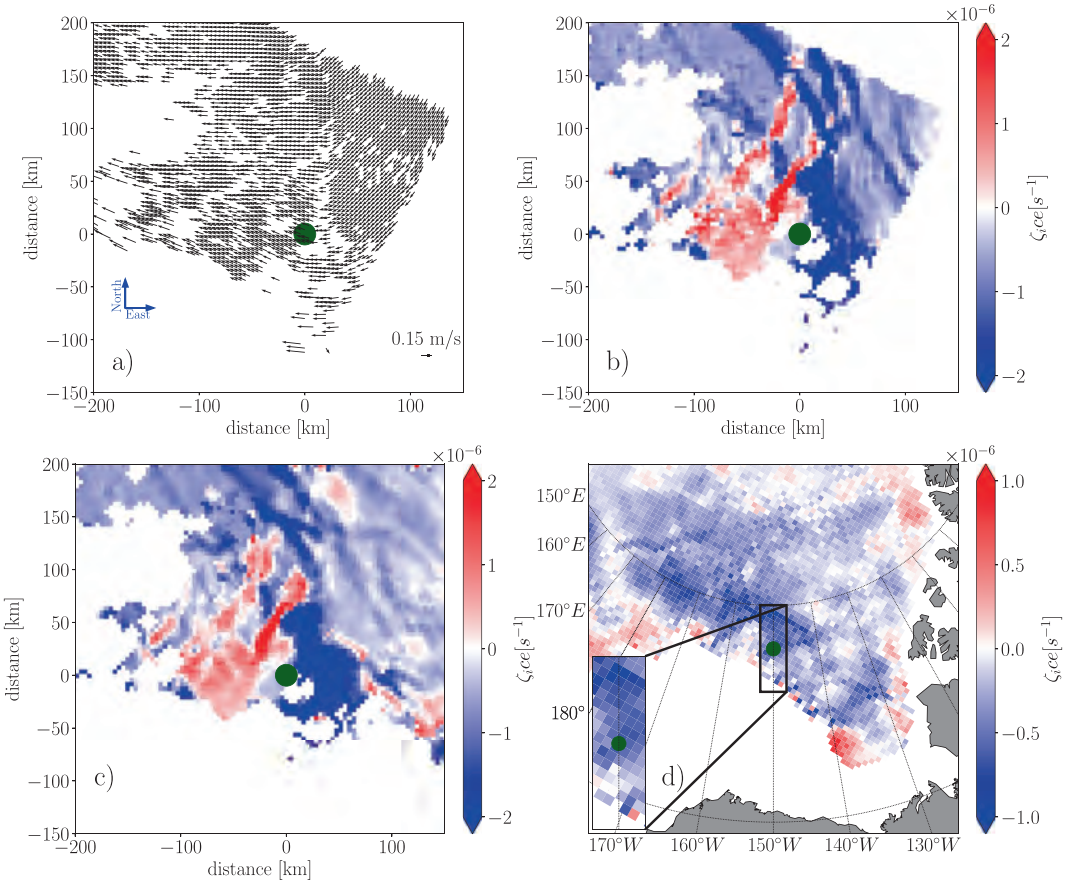

Figure 3. (a) Sea ice drift field and (b) sea ice vorticity from one pair of SAR images for October 12–13; (c) average of sea ice vorticity from five pairs of SAR images for October 7–13 and (d) from the National Snow and Ice Center (NSIDC) for October 7–13. The green dot indicates the position of mooring B, and the black box indicates the window of (a, b, and c).

anomaly in sea ice vorticity (Manucharyan & Thompson, 2017). Nonetheless, we do not expect fully similar ocean and sea ice vorticity fields, as both the wind forcing and the sea ice internal stress are also playing a role in the determination of the sea ice drift and vorticity (Hibler, 1979). In order to attribute the origin of anomaly in sea ice vorticity, we examine the different possible drivers. Our region of interest corresponds to the MIZ with low concentration and highly fractured sea ice, meaning that the rheology effects are relatively small. Over the period considered, there is no storm passing by the location of the mooring, while we have previously identified the presence of a surface eddy (Figure 2), suggesting that the eddy is most likely the primary driver of the sea ice vorticity signal.

Based on simple scaling arguments, we reinforce this attribution of the relative roles possibly played by the wind and the ocean eddy. First, the spatial scale of the cyclonic signal in sea ice vorticity (~80 km) is roughly similar to the expected length scale of the surface eddy. In contrast, atmospheric mesoscale features found in the Arctic have much larger characteristic scales. Polar lows (the most intense category of mesoscale atmospheric eddies), for instance, have scales ranging from 200 to 1,000 km (Terpstra et al., 2020; Wagner et al., 2011). Second, these storms have very short lifetime (typically a day or two). The availability of SAR images allows us to examine the persistence of the signal. Figure 3c shows the sea ice vorticity averaged over a week (October 7–13), estimated from all available SAR images (five pairs). The pattern is similar to the one obtained from any single pair of SAR images, although the intensity tends to be more pronounced when we average over a week (compare panels b and c of Figure 3). On average, two strong anomalies are visible close to the mooring: a cyclonic signal West of the mooring and an anticyclonic one East of it, both with

a horizontal scale of 80–100 km. Considering that our ocean dipole would be advected by the background flow with velocity of ∼0.05 m·s^{-1}, it would have roughly travel northward by only 30 km over the week considered, consistent with the persistence of the sea ice vorticity pattern.

Finally, the intensity of the sea ice vorticity itself indicates that the ocean eddy is the most plausible driver. Following D'Asaro (1988) and Manley and Hunkins (1985), the ocean relative vorticity associated with a cyclonic eddy scales to $\frac{2 \times U}{R}$, with U the maximum azimuthal velocity of the eddy and R its radius. In the case of the cyclone sampled by mooring B, U is 0.3 m·s^{-1}, R is 41 km (corresponding to half the eddy length scale $\frac{(2\pi R_d)}{2}$), resulting in a relative vorticity associated with the eddy of 1.5×10^{-5} s^{-1}, larger than the intensity of the sea ice vorticity anomalies, which are around 3×10^{-6} s^{-1} and -5×10^{-6} s^{-1} for the cyclone and the anticyclone, respectively. In order to estimate the order of magnitude of the sea ice vorticity driven by the wind, we compute the wind driven sea ice drift solely estimated from the wind, making used of the rule-of-thumb formulae of Thorndike and Colony (1982), that sea ice drifts at 2% of the wind speed with a direction of 45° to the right of the wind. Applying this computation to the ERA5 winds over the period considered (October 7-13), we obtain a widespread anticyclonic wind-driven ice vorticity over the region of the mooring, with a weak intensity of $\sim -2 \times 10^{-7}$ s^{-1} (not shown). This is an order of magnitude weaker than the strong sea ice vorticity detected by the SAR images, and a hundred time weaker than the vorticity found in the ocean eddy. It does, however, match well the intensity of the background sea ice vorticity (Figure 3c). More generally, the spatial pattern of the wind-driven sea ice vorticity matches closely the NSIDC vorticity, related to the large scale anticyclonic sea ice circulation within the wind-driven Beaufort gyre, suggesting that the NSIDC data set (with its resolution of 25 km and its large uncertainty of ±5 cm·s^{-1} for the period and region considered) is only able to capture the large scale wind driven drift, but not the smaller scale features driven by the ocean.

The combination of the sea ice vorticity anomaly and the presence of eddies captured by the mooring, the lack of a significant wind forcing over that period, and the scaling arguments presented before, allow us to attribute the signal to the signature of the ocean mesoscale eddies. The presence of two vorticity anomalies with opposite signs indicates that the signal is indeed a dipole, composed of a cyclone and an anticyclone.

5. Robustness of the Method

The analysis of our case study has revealed that the signature of the eddy (captured by the mooring observations) can be detected in the form of strong anomalies of sea ice vorticity over a few days. In order to ensure the robustness of our method, one must check that such anomalies in sea ice vorticity are not found in periods without ocean eddy detected by the mooring. As an example, we analyze a period of 4 days at the end of May 2018, during which 6 SAR images are available at the location of the mooring. Note that the low availability of Sentinel-1 SAR images largely limits the number of cases that can be examined. Between May 23–26, the sea ice draft fluctuates between 1.3 and 1.8 m and the KE remains very low, suggesting that no eddy is passing by during that period (Figure 4a). Applying the method described in the previous section, we estimate the sea ice drift for three pairs of SAR images and then the average ice vorticity (Figure 4b). The negative vorticity estimated from the SAR images matches well the amplitude of the vorticity estimated from the NSIDC sea ice drift, with values around -0.5×10^{-6} s^{-1} (Figure 4c). In contrast with the previous case, no local anomaly of ice vorticity is observed here, except for a localized positive anomaly whose shape suggests that is most likely the signature of a fracture in the ice pack. The results thus suggest that our method does not generate an eddy signature in sea ice vorticity when no eddy is captured in the surface layer, making us confident that our detection method is robust.

6. Conclusion

Mesoscale eddies are ubiquitous features in the Arctic Ocean but they are not easily observed from space because of the presence of sea ice. As a consequence, the detection of eddies has been limited to open water regions and MIZ. In this paper, a new methodology of ocean eddy detection has been presented, based on

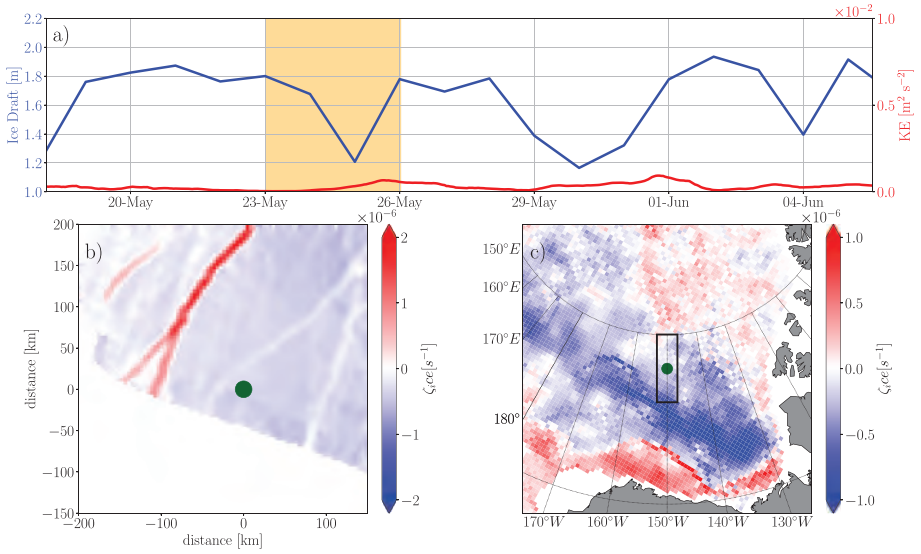

Figure 4. Time series of ice draft (blue) and KE (0–30 m, red) from the ADCP in 2018 (a). The orange box in (a) shows the period of interest between May 23–26. Average of sea ice vorticity from three pairs of SAR images (b) and from NSIDC (c) for May 23–26, 2018. The green dot is the position of the mooring and the black box in (c) indicates the window of (b).

the response of the sea ice drift to the passage of an ocean eddy. A case study is presented for October 2017 in the Canadian Basin: in situ data from one mooring have efficiently allowed us to detect eddies under sea ice in the MIZ. Pairs of SAR images are used to determine the sea ice drift and vorticity at a spatial resolution high enough to detect the signature of mesoscale features. The sea ice vorticity indeed reveals the presence of a dipole with two anomalies of different signs. These are the signatures of eddies detected by a mooring, which samples two anomalies that are likely a dipole composed of a cyclone and an anticyclone. We suggest that the method presented here could be efficiently used to perform semi-automatic detection of ocean eddy in the surface layer of the ice-covered Arctic, in the MIZ and beyond. The main limitation is the availability of data which severely constrains the number of cases that can be captured. However, as moorings and ITPs are routinely deployed in the Arctic and the spatiotemporal coverage of SAR satellites is improving, future data will be available for identifying other cases of eddy imprint. Sea ice conditions are also an important factor limiting the detection. In late spring and summer, the sea ice drift cannot be recovered from the algorithm used here as sea ice is largely fragmented or covered by numerous melt ponds. Conversely, in winter, thicker sea ice tends to dissipate surface eddies (Meneghello et al., 2020). As the sea ice pack transitions toward a thinner, more mobile pack, the dissipation exerted by sea ice on eddies will likely decrease, possibly modifying the nature of the Arctic mesoscale activity. Improving the observability of the Arctic eddy is a major challenge in order to better understand the functioning of the Arctic system and predict its evolution.

Further investigations should also focus on the mechanisms at play for the eddy signature on sea ice, in order to improve the method presented here. Anomalies of vorticity presented here suggest that the ocean dipole generates regions of strong sea ice deformation and divergence. Zhang et al. (1999) simulated such sea ice behaviors in the presence of ocean eddies, resulting in thinner and less compact ice and even in regions of open water when ice deformation becomes large, in which we expect intensified air-sea heat exchanges and sea ice melt. Besides, vertical heat fluxes located in cyclonic eddies could bring warm waters in the surface layer and contribute to sea ice melt (Manucharyan & Thompson, 2017). In addition to the dynamical effects, such thermodynamical mechanisms could modify the sea ice conditions and thus enhance the eddy signature (Gupta et al., 2020). All these possible interactions between mesoscale eddy and sea ice need to be better understood in order to explain the different signals found in satellite observations of sea ice.

Data Availability Statement

The hydrographic data were collected and made available by the Beaufort Gyre Exploration Program based at the Woods Hole Oceanographic Institution (http://www.whoi.edu/beaufortgyre). The satellite data was provided by the European Space Agency and the National Snow and Ice Data Center. The wind reanalysis data are provided by the European Centre for Medium-Range Weather Forecasts.

Acknowledgments
We acknowledge funding from the French ANR through the project IMMEDIAT (Grant ANR-18-CE01-0010) as well as funding from Ifremer. The study was supported by Arktalas Hoavva project (no AO/1-9595/18/NL/LF) funded by European Space Agency.

References

Brannigan, L., Johnson, H., Lique, C., Nycander, J., & Nilsson, J. (2017). Generation of subsurface anticyclones at Arctic surface fronts due to a surface stress. *Journal of Physical Oceanography*, *47*(11), 2653–2671. https://doi.org/10.1175/JPO-D-17-0022.1

Carpenter, J. R., & Timmermans, M. (2012). Deep mesoscale eddies in the Canada Basin, Arctic Ocean. *Geophysical Research Letters*, *39*(20). https://doi.org/10.1029/2012GL053025

D'Asaro, E. A. (1988). Observations of small eddies in the Beaufort Sea. *Journal of Geophysical Research*, *93*(C6), 6669. https://doi.org/10.1029/jc093ic06p06669

Gupta, M., Marshall, J., Song, H., Campin, J., & Meneghello, G. (2020). Sea-ice melt driven by ice-ocean stresses on the mesoscale. *Journal of Geophysical Research: Oceans*, *125*(11), e2020JC016404. https://doi.org/10.1029/2020jc016404

Hersbach, H., Bell, B., Berrisford, P., Hirahara, S., Horányi, A., Muñoz-Sabater, J., et al. (2020). The ERA5 global reanalysis. *Quarterly Journal of the Royal Meteorological Society*, *146*(730), 1999–2049. https://doi.org/10.1002/qj.3803

Hibler, W. D. (1979). A dynamic thermodynamic sea ice model. *Journal of Physical Oceanography*, *9*(4), 815–846. https://doi.org/10.1175/1520-0485(1979)009⟨0815:adtsim⟩2.0.co;2

Johannessen, O. M., Johannessen, J. A., Svendsen, E., Shuchman, R. A., Campbell, W. J., & Josberger, E. (1987). Ice-edge eddies in the Fram Strait marginal ice zone. *Science*, *236*(4800), 427–429. https://doi.org/10.1126/science.236.4800.427

Korosov, A., Hansen, M. W., Dagestad, K.-F., Yamakawa, A., Vines, A., & Riechert, M. (2016). Nansat: A scientist-orientated python package for geospatial data processing. *Journal of Open Research Software*, *4*(1), 39. https://doi.org/10.5334/jors.120

Korosov, A., & Rampal, P. (2017). A combination of feature tracking and pattern matching with optimal parametrization for sea ice drift retrieval from SAR data. *Remote Sensing*, *9*(3), 258. https://doi.org/10.3390/rs9030258

Kozlov, I. E., Artamonova, A. V., Manucharyan, G. E., & Kubryakov, A. A. (2019). Eddies in the Western Arctic Ocean from spaceborne SAR observations over open ocean and marginal ice zones. *Journal of Geophysical Research: Oceans*, *124*(9), 6601–6616. https://doi.org/10.1029/2019JC015113

Krishfield, R., & Proshutinsky, A. (2006). *BGOS ULS data processing procedure* (Technical Report). Woods Hole Oceanographic Institution.

Manley, T. O., & Hunkins, K. (1985). Mesoscale eddies of the Arctic Ocean. *Journal of Geophysical Research*, *90*(C3), 4911. https://doi.org/10.1029/jc090ic03p04911

Manucharyan, G. E., & Thompson, A. F. (2017). Submesoscale sea ice-ocean interactions in marginal ice zones. *Journal of Geophysical Research: Oceans*, *122*(12), 9455–9475. https://doi.org/10.1002/2017JC012895

Meneghello, G., Marshall, J., Lique, C., Isachsen, P. E., Doddridge, E., Campin, J.-M., & Talandier, C. (2020). Genesis and decay of mesoscale baroclinic eddies in the seasonally ice-covered interior Arctic Ocean. *Journal of Physical Oceanography*, *51*(1), 115–129. https://doi.org/10.1175/JPO-D-20-0054.1

Muckenhuber, S., Korosov, A., & Sandven, S. (2016). Open-source feature-tracking algorithm for sea ice drift retrieval from Sentinel-1 SAR imagery. *The Cryosphere*, *10*(2), 913–925. https://doi.org/10.5194/tc-10-913-2016

Newton, J. L., Aagaard, K., & Coachman, L. K. (1974). Baroclinic eddies in the Arctic Ocean. *Deep Sea Research and Oceanographic Abstracts*, *21*(9), 707–719. https://doi.org/10.1016/0011-7471(74)90078-3

Nurser, A. J. G., & Bacon, S. (2014). The Rossby radius in the Arctic Ocean. *Ocean Science*, *10*(6), 967–975. https://doi.org/10.5194/os-10-967-2014

Proshutinsky, A., Krishfield, R., Timmermans, M.-L., Toole, J., Carmack, E., McLaughlin, F., et al. (2009). Beaufort Gyre freshwater reservoir: State and variability from observations. *Journal of Geophysical Research*, *114*(C1). https://doi.org/10.1029/2008JC005104

Terpstra, A., Watanabe, S.-I., Terpstra, A., & Watanabe, S.-I. (2020). Polar lows. In *Oxford research encyclopedia of climate science*. Oxford University Press. https://doi.org/10.1093/acrefore/9780190228620.013.775

Thorndike, A. S., & Colony, R. (1982). Sea ice motion in response to geostrophic winds. *Journal of Geophysical Research*, *87*(C8), 5845. https://doi.org/10.1029/jc087ic08p05845

Tonboe, R., Lavelle, J., Pfeiffer, R.-H., & Howe, E. (2017). *Ocean & sea ice SAF product user manual for OSI SAF global sea ice concentration* (Technical Report). Danish Meteorological Institute.

Toole, J., Krishfield, R., Timmermans, M.-L., & Proshutinsky, A. (2011). The Ice-Tethered Profiler: Argo of the Arctic. *Oceanography*, *24*(3), 126–135. https://doi.org/10.5670/oceanog.2011.64

Tschudi, M., Meier, W. N., & Stewart, J. S. (2020). An enhancement to sea ice motion and age products at the National Snow and Ice Data Center (NSIDC). *The Cryosphere*, *14*(5), 1519–1536. https://doi.org/10.5194/tc-14-1519-2020

Tschudi, M., Meier, W. N., Stewart, J. S., Fowler, C., & Maslanik, J. (2019). *Polar Pathfinder Daily 25 km EASE-Grid Sea Ice Motion Vectors, version 4*. Boulder, CA, USA: National Snow and Ice Data Center. Retrieved from https://doi.org/10.5067/INAWUWO7QH7B

Tulloch, R., Marshall, J., Hill, C., & Smith, K. S. (2011). Scales, growth rates, and spectral fluxes of baroclinic instability in the ocean. *Journal of Physical Oceanography*, *41*(6), 1057–1076. https://doi.org/10.1175/2011JPO4404.1

Wagner, J. S., Gohm, A., Dörnbrack, A., & Schäfler, A. (2011). The mesoscale structure of a polar low: Airborne lidar measurements and simulations. *Quarterly Journal of the Royal Meteorological Society*, *137*(659), 1516–1531. https://doi.org/10.1002/qj.857

Zhang, Y., Maslowski, W., & Semtner, A. J. (1999). Impact of mesoscale ocean currents on sea ice in high-resolution Arctic ice and ocean simulations. *Journal of Geophysical Research: Oceans*, *104*(C8), 18409–18429. https://doi.org/10.1029/1999jc900158

Zhao, M., & Timmermans, M. (2015). Vertical scales and dynamics of eddies in the Arctic Ocean's Canada Basin. *Journal of Geophysical Research: Oceans*, *120*(12), 8195–8209. https://doi.org/10.1002/2015JC011251

Zhao, M., Timmermans, M., Krishfield, R., & Manucharyan, G. (2018). Partitioning of kinetic energy in the Arctic Ocean's Beaufort Gyre. *Journal of Geophysical Research: Oceans*, *123*(7), 4806–4819. https://doi.org/10.1029/2018JC014037

Zhao, M., Timmermans, M.-L., Cole, S., Krishfield, R., Proshutinsky, A., & Toole, J. (2014). Characterizing the eddy field in the Arctic Ocean halocline. *Journal of Geophysical Research: Oceans*, *119*(12), 8800–8817. https://doi.org/10.1002/2014JC010488

Zhao, M., Timmermans, M.-L., Cole, S., Krishfield, R., & Toole, J. (2016). Evolution of the eddy field in the Arctic Ocean's Canada Basin, 2005–2015. *Geophysical Research Letters*, *43*(15), 8106–8114. https://doi.org/10.1002/2016GL069671

Impact of sea ice friction on ocean tides in the Arctic Ocean, modelling insights at various time and space scales

Mathilde Cancet[1], Florent H. Lyard[2], Ergane Fouchet[1]

[1]NOVELTIS S.A.S., Labège, 31670, France
[2]LEGOS, Université de Toulouse, CNES, CNRS, IRD, Toulouse, 31400, France

Correspondence to: Ergane Fouchet (Ergane.fouchet@noveltis.fr)

Abstract. Although ocean tides are one of the major contributors to the energy dissipation in the Arctic Ocean, they remain relatively poorly known, and particularly their interactions with the ice cover (sea ice and grounded ice). These interactions are often simply ignored in tidal models, or considered through relatively simple combinations with the bottom friction. In this paper, we investigate this aspect with a sensitivity analysis of a regional pan-Arctic ocean tidal model to the friction under the sea ice cover, in order to generate more realistic simulations. Different periods of time, at the decadal scale, were considered to analyze the impact of the long-term reduction of the sea ice cover on the ocean tides in the region, as well as at global scale. Tide gauge and satellite altimetry observations were specifically processed to retrieve the tidal harmonic constituents over different periods and different sea ice conditions, to assess the model simulations. Improving the knowledge on the interaction between the tides and the sea ice cover, and thus the performance of the tidal models in the Polar regions, is of particular interest to generate more realistic simulations with ocean circulation models, to contribute to scientific investigations on the changes in the Arctic Ocean, and also to improve the satellite altimetry observation retrievals at high latitudes, as the tidal signals remain a major contributor to the error budget of the satellite altimetry observations in the Arctic Ocean..

1 Introduction

The ocean tides are one of the major contributors to the energy dissipation in the Arctic Ocean (Rippeth et al., 2015). In particular, barotropic tides are quite sensitive to friction processes, and thus to the possible presence of sea ice in Polar regions. However, the interaction between the tides and the ice cover (both sea ice and grounded ice) is poorly known and still not well modelled, although the friction between the ice and the water due to the tide motions is an important source of energy dissipation and has a direct impact on the ice melting (Padman and Siegfried, 2018).

The question of the impact of the sea ice on the tides in the Arctic has been investigated by different groups (Godin, 1980 & 1986; Kowalik, 1981; St-Laurent et al., 2008; Kagan and Sofina, 2010). They generally observe that the seasonal variations of the global patterns of the M2 semidiurnal tide (the main tidal component in the Arctic Ocean) are minor in open ocean regions and in basins that are connected to the open ocean through deep channels. By contrast, the impact of the seasonal sea ice cover friction can reach several centimeters in terms of tidal elevations in semi-enclosed basins and on the Siberian continental shelf.

In the context of climate change in the Arctic Ocean, not only the extent of the sea ice cover shrinks decade after decade, but the average ice thickness has also significantly reduced. In present time, contrary to early climate change era, most of the ice is “new ice”, i.e. formed in the year, and “old” ice is in permanent decline. Climate change not only affects the extent but also the nature of the sea ice, and this may have an impact on Arctic tides, as young thin ice is more subject to breakage than older thicker ice.

To investigate the impact of Arctic Ocean Sea ice change on ocean tides, it is necessary to account for the friction occurring at the bottom of ocean ice shelves and sea ice (ice/free ocean water interface) in addition to the ocean bottom friction. However, the precise parameterization of the sea ice cover friction at the top of the water column is very complex. Indeed, the friction coefficient depends upon the micro to macro morphology of the ice base, which itself can vary with the age of the ice and/or the conditions where it was formed and further transported and modified. Also, the friction drag is a function of the velocity

difference between the ocean upper layer and the ice displacement, which knowledge would require a full sea-ice modelling module in the hydrodynamic model. Implementing such a module would be at the price of a considerable increase of the modelling system complexity, with no guaranty of getting a proper answer today.

To overcome these difficulties, a very common strategy consists in implementing an empirical approach, such as defining polygons for different areas covered by sea ice, each of them being assigned an empirical value of sea ice friction coefficient. These values can be tuned in a trial/check process based on comparisons with validation observations (such as tidal elevation), retrieved by using optimal control technics, or relaxed in data assimilation approach. In the case of sea ice, the coverage of ice will strongly depend on the seasons, and the model friction will need to be modulated accordingly.

The most basic solution consists in considering that, in regions covered with sea ice, the friction parameter is a combination of the friction at the bottom and at the top of the water column. The simplest approach is to multiply the friction by a given factor (for example by a factor of two, such as in Lyard, 1997) in the regions covered with sea ice. A more complex approach consists in considering that, in this combination between the friction at the bottom and the friction at the top of the water column, the friction due to the sea ice depends on the sea ice concentration (Dunphy et al., 2005; Hannah et al., 2008; Collins et al., 2011; Kleptsova and Pietrzak, 2018).

In this paper, we investigate the sensitivity of a hydrodynamic tidal model to the friction under the sea ice cover, in order to generate more realistic simulations. Using a regional tidal model over the whole Arctic Ocean, various approaches for the definition of the sea ice friction are explored (simple multiplying factor applied to the friction parameter, and dependency between the friction under the sea ice and the sea ice concentration, seasonal configurations). Different periods of time have been considered, in order to analyze the impact of the long-term reduction of the sea ice cover on the ocean tides in the region. The effect on the ocean tides at the global scale are also explored.

This work is part of the ARKTALAS Hoavva study funded by the European Space Agency under the Contract 4000127401/19/NL/LF.

2 Data and methods

2.1 Hydrodynamic simulations

For the tidal simulations, we used the TUGO-m hydrodynamic model, which is developed at LEGOS. TUGO is a 2-D/3-D unstructured grid model based on the Navier–Stokes equation in the Boussinesq approximation. It can be used either in time stepping, i.e. running a long simulation (e.g. one year) and then performing tidal harmonic analyses on the resulting tidal elevations and velocities, or in the frequency domain, i.e. directly solving the tidal wave equations for each tidal component separately. The second approach is much less time-consuming in terms of computation, and provides equivalent results to the time-stepping mode for the main linear tidal components. We used the frequency domain approach for all the simulations performed in this study.

New developments have been implemented in the TUGO-m model to allow more flexibility in the way to handle the friction with the ice, in particular for the sea ice. The legacy, and quite limited, T-UGOm method to take into account the ice frictional effects, is to double the bottom friction coefficient (thus assuming similar roughness at the ocean bottom and below the floating ice) inside regions defined by polygons given as input parameters to the hydrodynamic model. This is an obstacle to investigate optimal ice bottom roughness value, to include the numerous smaller floating ice shelves (mostly found in the Antarctic regions) in the model input polygons, and to represent varying sea ice cover effects. New input settings for ice frictional effects have thus been implemented in T-UGOm, both to provide a more flexible ice roughness setting, and to allow for more precise and possible time varying ice cover. A run-time level, ice thickness raster-based method has been implemented to define the ocean ice shelves cover. Ice thickness raster inputs such as the RTopo-2.0.4 global dataset (Schaffer et al., 2019) can be directly used by the model. A similar sea ice concentration raster-based method (based on satellite imagery) has been implemented to

define the sea ice cover and tested from the NSIDC daily and monthly products (https://nsidc.org). A pre-processing step is necessary to handle the NSIDC products and to aggregate the daily or monthly files in a unique annual input file containing the corresponding time frames. Last but not least, the ice friction parameters setting has been dissociated from the ocean bottom one. It allows for choosing between the different parameterization used in friction computation (Nikuradse law, Manning or Cd coefficients), and for prescribing specific friction parameters values in regions defined with polygons. In particular, it allows for specifying different friction for ice shelves and sea ice, and potentially to locally modulate sea ice friction to account for roughness heterogeneity due to actual local ice age or state (compact, fractured …).

The sea ice roughness's setting in numerical models still remains mostly simple, arbitrary and at the best empirical. Not only the basic knowledge about the sea ice bottom roughness itself is barely known, but this is the case also for the sea ice motion, necessary to compute the differential velocity with the ocean surface level needed by the friction stress derivation. In the tidal simulation presented in this paper, we have used a uniform roughness length for the whole domain. The treatment of ice motion effect is also quite basic. Below an arbitrary sea ice concentration threshold (typically 0.7 for concentration ranging between zero and one), sea ice is considered to freely follow tidal flow, hence not triggering any or negligible friction effects. The friction coefficient then linearly increases from the concentration threshold up to the maximum concentration, for which sea ice can be considered as fasten, at least at tidal period time scales.

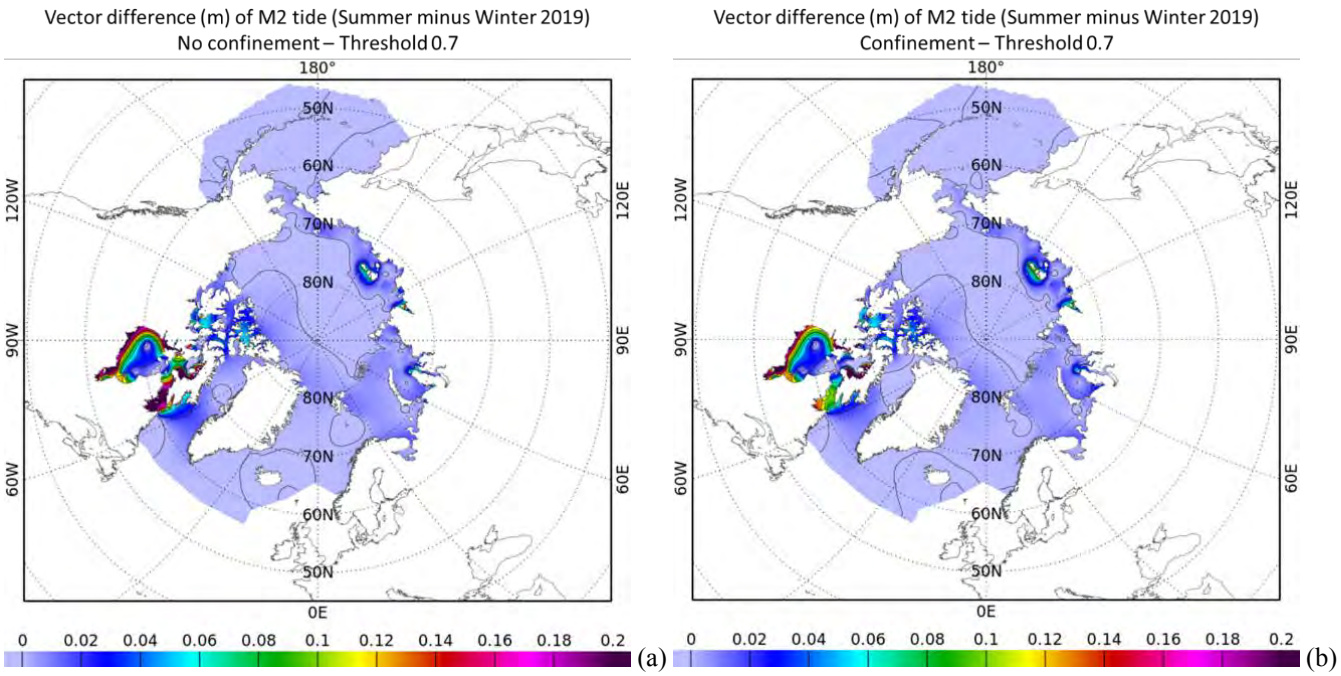

Figure 1: Impact of confinement modulation of sea ice friction, winter/summer differences in M2 tide (vector difference) for 2019, without confinement modulation (a), with confinement modulation (b)

However, using a uniform sea-ice concentration threshold value does not account for the ocean geometry constraints (called hereafter confinement) on sea ice displacement. Following its value, it tends to over-estimate the sea-ice friction effects in the open sea and/or minder them in narrow channels or close to the shoreline. To overcome this issue, a confinement length has been deduced by defining and computing a characteristic "free water extent" length, based on an ad hoc transform of minimum distance to coast metrics. The confinement allows for tuning the threshold value (typically 0.7 in confined areas up to 0.9 in open sea areas). Comparisons to tide gauges for the two approaches (with and without confinement) have demonstrated that the use of confinement length globally reduces the misfits between the simulations and the observations. The largest impact of the confinement approach can be observed in the Hudson Strait, between the Baffin Sea and the Hudson Bay, when comparing summer versus winter M2 tidal simulations (Figure **1**). This region is of particular importance as there is a tight connexion between the Hudson Bay and the whole Atlantic Ocean in terms of tidal energy fluxes.

For the regional simulations over the Arctic Ocean, we used the Arctide2017 regional model configuration described in Cancet et al., 2018, with a number of improvements. First, the Hudson Bay and the Foxe Basin were added to the model domain, which strongly improves the model tidal estimates in the Baffin Bay. Second, the model domain was extended South of Iceland and South of the Bering Strait, in order to reduce model instabilities due to the interactions between the tides and locally steep bathymetry gradients that had been identified in the Arctide2017 configuration. Finally, recent bathymetry datasets have been assessed and merged into the model bathymetry where relevant (BedMachine Arctic (Morlighem et al. 2017), GEBCO-2020 (https://www.gebco.net), and NOAA data in the Anchorage Bay).

The global configuration used for this study is the FES2014 one, described in Lyard et al., 2021. Except for the sea ice cover aspect, the only other addition to the FES2014 configuration is the use of the RTopo-2.0.4 ice-thickness map to define the ice-shelf regions in Antarctica, whereas only very basic polygons were used in the FES2014 original configuration, over the Amery ice shelf and the ice shelves in the Weddell Sea and in the Ross Sea.

In order to evaluate the impact of the evolution of the sea ice cover on the ocean tides in the Arctic Ocean and at global scale, a series of simulations was performed, considering seasonal sea ice concentration, for a time period ranging from 1980 to 2020. The seasonal sea ice concentration maps were computed using the NSIDC monthly sea ice concentration products provided in GEOTIFF format, available from 1979 to today. For the global simulations, global maps of the Arctic and Antarctic sea ice concentration were built from the NSIDC products to feed the hydrodynamic model with a single map for each simulation. For each year, the seasonal maps were computed as the mean of the monthly sea ice concentration maps over three months: Winter (January, February, March), Spring (April, May, June), Summer (July, August, September) and Fall (October, November, December). The range of sea ice concentration considered by the model was set to 0.7-1.0 (i.e. 70% to 100%) in order to limit the introduction of additional friction because of possible artefacts in the low sea ice concentration estimates.

For both configurations (regional and global), we performed one hydrodynamic simulation for each season of each year from 1980 to 2020 (i.e. 164 simulations for each configuration).

2.2 Satellite altimetry observations

Satellite altimetry sea surface height measurements sample the global ocean tide signals at each revisit of the satellite. Because the satellite revisit period is of several days, the high frequency tidal signals are projected onto much longer aliasing periods, as presented in Table 1. In general, the Topex/Jason repeat orbit of about 10 days is the most favourable to estimate the tidal harmonic constituents (amplitude and phase lag) from satellite altimetry time series. In the case of sun-synchronous orbits such as ENVISAT, SARAL and Sentinel-3, the S2 main solar tide component is aliased to an infinite period and cannot be estimated. For all the missions, time series of several years of observations are necessary to accurately separate the various tidal components thanks to harmonic analysis processing. In the Arctic Ocean, the spatial coverage of the Topex/Jason suite missions is limited to 66°N. In addition, the conventional altimeters are strongly impacted by the intermittent presence of sea ice, which leads to seasonal gaps in the time series and degrades the tidal estimates. Unfortunately, the satellite altimetry missions that reach higher latitudes and provide the longest time series in the Arctic Ocean (ERS-1/ERS-2/ENVISAT/SARAL) are sun-synchronous, which affects the tidal retrievals and the possibility to accurately separate some of the tidal components (like K1 and P1, for which the separation period is infinite is such cases). Sentinel-3A&B are also on sun-synchronous orbits, spatially shifted from the ENVISAT orbit. With more than 10 years of measurements up to 88°N on a non-sun-synchronous orbit, the CryoSat-2 mission provides invaluable sea surface height observations that can be analysed to accurately estimate the tidal harmonic constituents, despite its long-period repeat cycle. In addition, the SAR and SARin modes of the altimeter are less affected by the presence of sea ice, thanks to their higher along-track resolution.

Table 1: Aliasing periods of the main tidal components depending on the satellite repeat cycle

Tidal component	Topex/Jason 9.915600-day orbit Latitude max. 66°	Sentinel-3 27-day orbit Latitude max. 82°	ENVISAT/SARAL 35-day orbit Latitude max. 82°	CryoSat-2 368.2396-day orbit Latitude max. 88°
M2	62 days	157 days	94 days	800 days
S2	59 days	Inf.	Inf.	768 days
K1	173 days	365 days	365 days	1486 days
O1	46 days	277 days	75 days	1262 days

We have estimated the tidal harmonic constituents from the CryoSat-2 sea surface height measurements, considering more than 11 years (July 2010 to December 2020) of observations. We used the ESA Level-2 GOP Baseline C products, which provide sea surface height information for the three modes of the altimeter (LRM, SAR and SARin) and thus cover the whole Arctic Ocean, up to the orbit limit of 88°N. In order to improve the separation of the tidal components, the altimetry observations were binned into cells of 1° by 1° and time series were built in each cell. A prior tidal solution, based on the regional Arctic model configuration, was removed from the altimeter sea surface height before performing harmonic analysis, and then restored into the computed tidal constituents.

Because time series of more than 10 years are needed to accurately estimate the tidal harmonic constituents from the altimetry observations, the CryoSat-2 tidal estimates are representative of average tides over the most recent period (2010-2020). They were thus used for comparison purposes with the model simulation in the generic configuration, without considering any sea ice cover. The ENVISAT observations could be used to estimate the tidal constituents for the period 2002-2012, but the signal to noise ratio is less favourable as explained above, and the uncertainties in the tidal estimates can reach several centimetres. Finally, because the satellite altimeter radar signal is affected by the presence of sea ice, the computation of seasonal tidal estimates from satellite altimetry observations, separating Summer and Winter data for example, results in uncertainties of several centimetres in sea-ice covered regions, i.e. in the range of the seasonal differences that can be observed in the tidal estimates at tide gauges. For this reason, we did not use such approach for this study.

2.3 Tide gauge in situ observations

In order to compare the model results with independent observations at seasonal time scale, and on a longer period than the recent satellite altimetry era, we considered long time series of hourly tide gauge measurements. We used data from the GESLAv3 database (Haigh et al., 2021), completed with more recent data from the UHSLC database (Caldwell et al., 2015) where available and relevant. Although a large number of tide gauge stations can be identified in the Arctic Ocean, most of the time series are very short (a few weeks to a few months) and often prior to 1980. In particular, most of the Canadian tide gauge observations in the Canadian Archipelago and in the Hudson Bay were collected in the 1970s. Based on the statistical analyses performed on the seasonal tidal simulations (see section 3), we have identified eight tide gauge stations (see Figure 2) located in regions of interest in terms of tidal amplitude, and that more or less cover the 1980-2020 period, in general with gaps of several months (up to several years), especially in the 1980-1990s period: the Honningsvag and Vardø stations are located on the northernmost coast of Norway, the Fort Churchill station is located in the Hudson Bay, the Alert station is located in the northern part of the Canadian Archipelago, close to Greenland, the Anchorage, Nikiski and Seldovia stations are located in the Anchorage Bay, and the Village Cove station is located in the Bering Strait. In addition, two stations located in the Baffin Bay (Nain and Qikiqtarjuaq) were considered but provide much shorter time series, starting only in 2006 with many gaps.

Each hourly time series was carefully verified, and split into three-month subsets corresponding to the seasons previously defined. Harmonic analysis processing was then performed on each seasonal subset, in order to obtain time series of seasonal

tidal constituents (amplitude and phase lag) for the main tidal components (M2, K1, S2 and O1 mainly). The stations were separated into two subsets, corresponding to those that highlight a clear seasonal tidal signal (in red on Figure 2) and those with no seasonal tidal signal (in black).

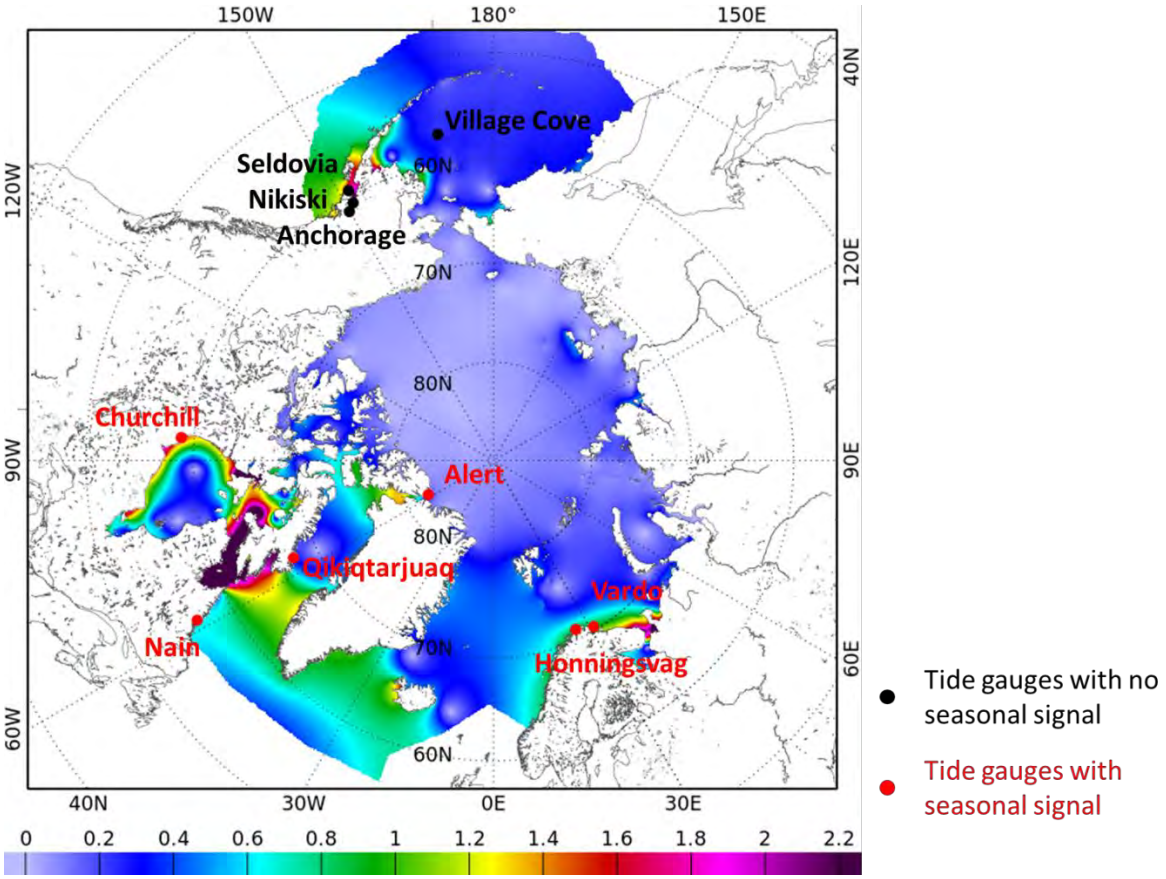

Figure 2: Amplitude (in m) of the M2 tidal component from the regional model, and locations of the tide gauge stations considered in the study.

3 Results

3.1 Sea-ice related variability in tidal elevations

The seasonal changes in sea ice cover modulate the associated ocean/sea ice friction over the year. The effect on tide can be significant if changes occur in regions where the tidal currents are large, with local and possibly remote effects. In addition, and because of the effect of climate change, the sea ice cover is diminishing decades after decades. This raises the question of the rate of change of Arctic tides due to this evolution, and possible subsequent changes in tides in other parts of the world ocean. For most science or engineering applications, the barotropic tides are usually considered as unchanging, and at some limited degree of accuracy, this is a perfectly workable assumption. However, in some more demanding tidal applications such as satellite altimetry corrections, which require the best available tidal prediction accuracy and consistency, the seasonal, inter-annual and long term changes in tidal amplitude or phase, in particular those linked with sea ice concentration variability (Figure 3 and Figure 4 e), can become an issue.

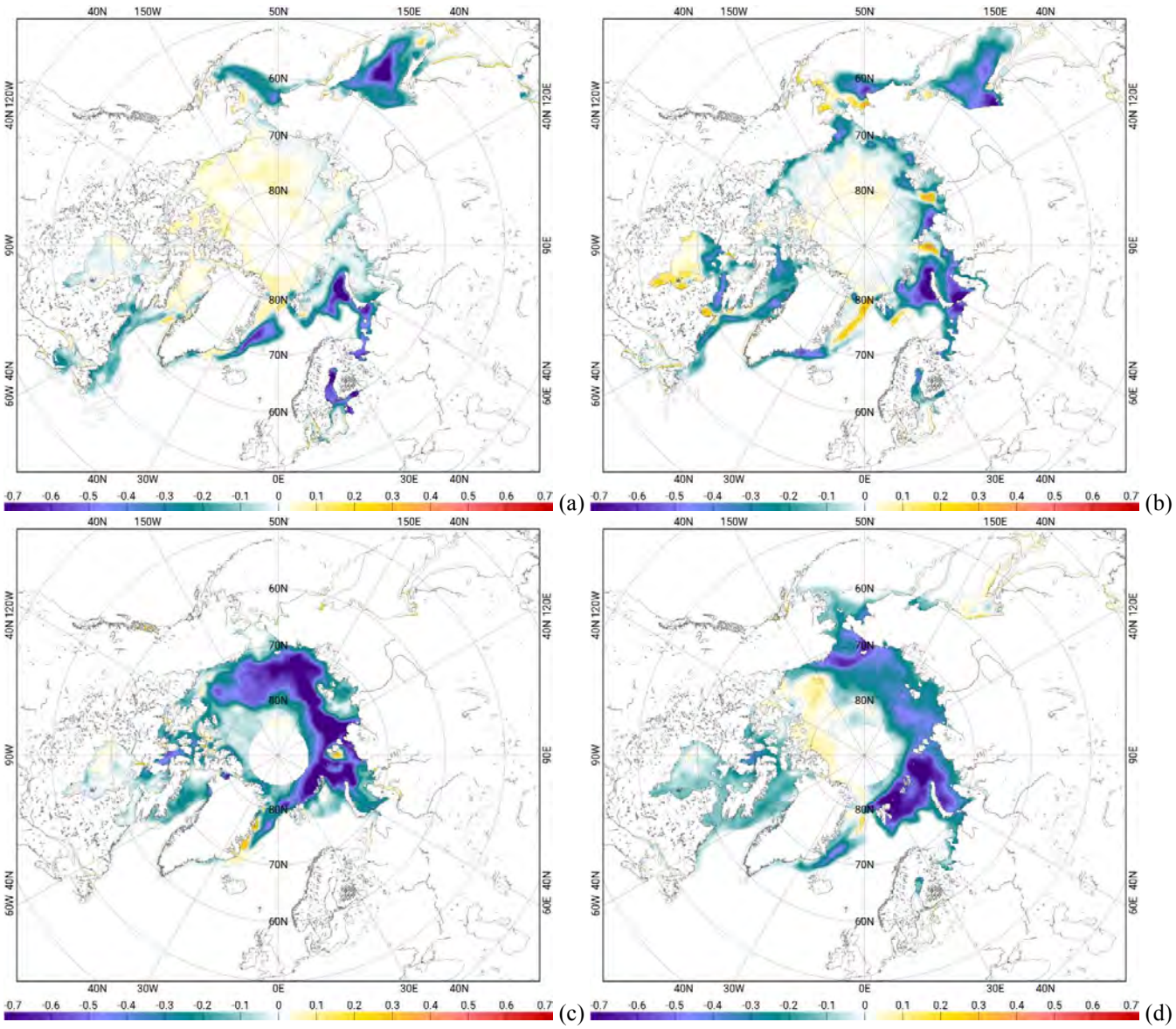

Figure 3: Difference of seasonal sea ice concentration (NSIDC products) between the years 1980 and 2020 (2020-1980): winter (a), spring (b), summer (c), fall (d).

Because of the global warming effects, the sea ice concentration is decaying in the Arctic Ocean, with a large, clearly visible diminution of the sea ice cover in the central Arctic Ocean during the "warm" season (see Figure 3). Because of the rather weak tidal currents in this region, this has probably a minor impact on tides. Even in the absence of long term changes, the seasonal changes in sea ice are not exactly the same from one year to another, in terms of intensity and timing. Figure 4 (a to d) shows the sea-ice cover variability for each season (RMS of seasonally averaged concentrations) over the 1980-2020 time period. The RMS reaches value as high as 30% of the maximum concentration, which is a rather large proportion. Again, effects on tides will be limited over regions where tidal currents are large, such as the Canadian Archipelago and the vicinity of the White Sea.

In the following, we will assume that most of the sea-ice-induced tidal changes are dominated by seasonal and inter-annual variability, focusing on standard deviation to illustrate this variability.

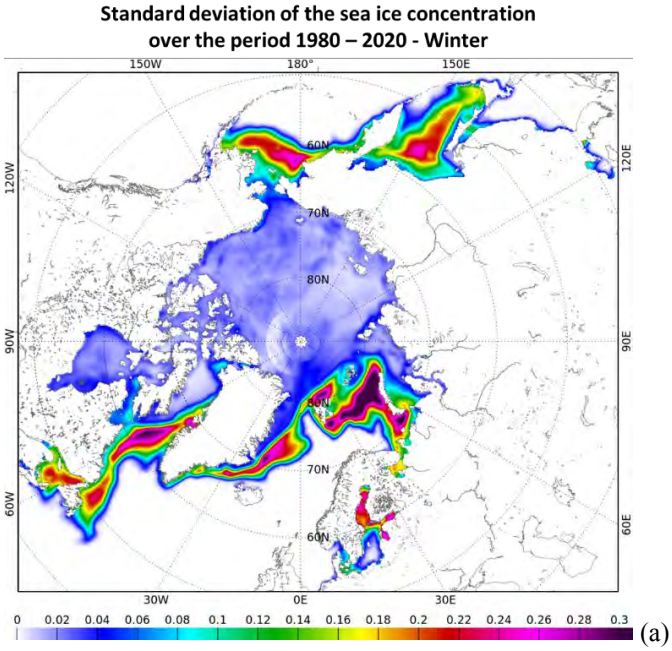
Standard deviation of the sea ice concentration
over the period 1980 – 2020 - Winter
150W
180°
150E
120W
120E
90W
90E
60W
60E
60N
70N
80N
30W
0E
30E
0 0.02 0.04 0.06 0.08 0.1 0.12 0.14 0.16 0.18 0.2 0.22 0.24 0.26 0.28 0.3

(a)

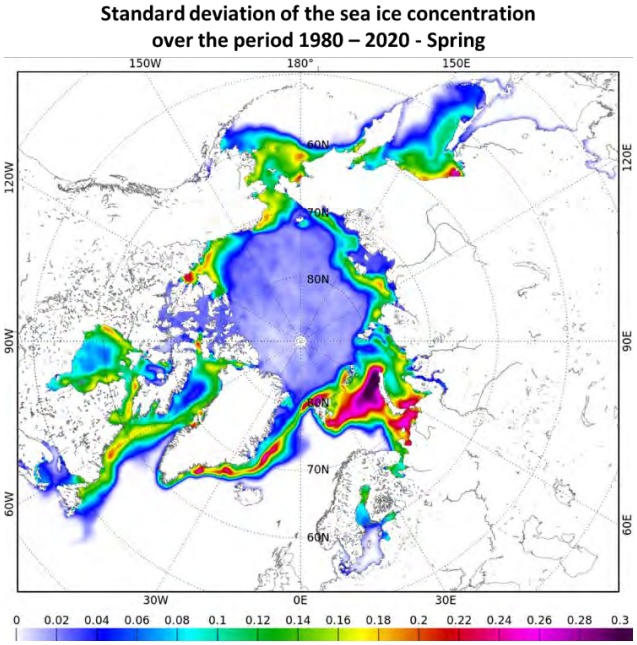
Standard deviation of the sea ice concentration
over the period 1980 – 2020 - Spring
150W
180°
150E
120W
120E
90W
90E
60W
60E
60N
70N
80N
30W
0E
30E
0 0.02 0.04 0.06 0.08 0.1 0.12 0.14 0.16 0.18 0.2 0.22 0.24 0.26 0.28 0.3

(b)

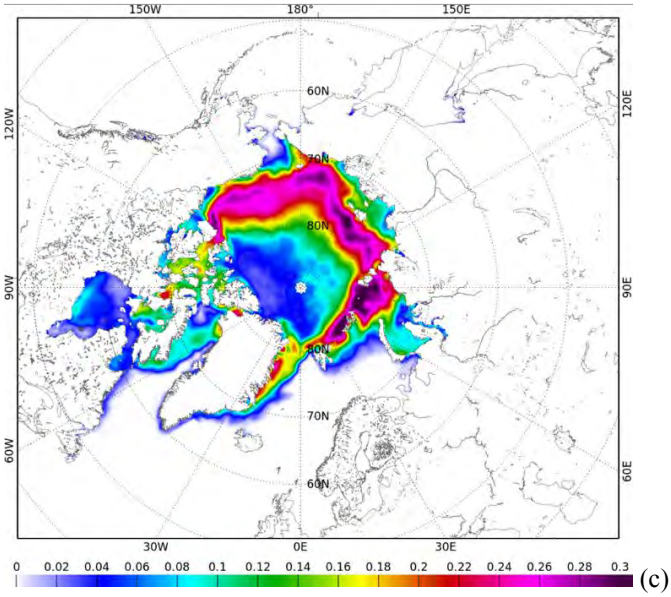
Standard deviation of the sea ice concentration
over the period 1980 – 2020 - Summer
150W
180°
150E
120W
120E
90W
90E
60W
60E
60N
70N
80N
30W
0E
30E
0 0.02 0.04 0.06 0.08 0.1 0.12 0.14 0.16 0.18 0.2 0.22 0.24 0.26 0.28 0.3

(c)

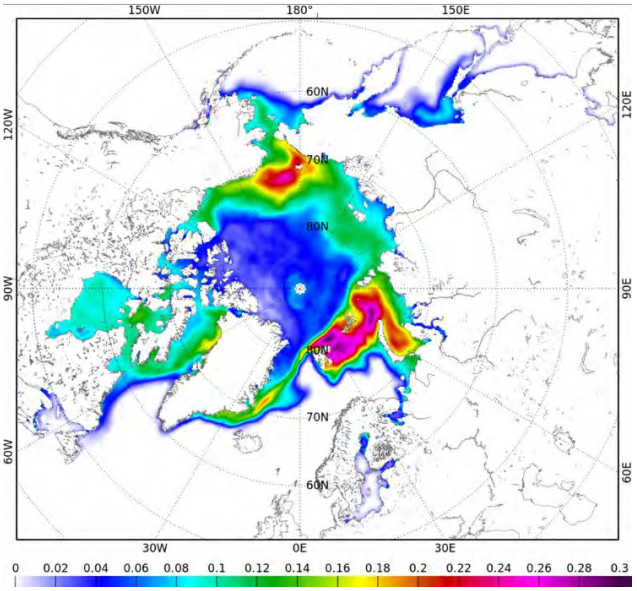
Standard deviation of the sea ice concentration
over the period 1980 – 2020 - Fall
150W
180°
150E
120W
120E
90W
90E
60W
60E
60N
70N
80N
30W
0E
30E
0 0.02 0.04 0.06 0.08 0.1 0.12 0.14 0.16 0.18 0.2 0.22 0.24 0.26 0.28 0.3

(d)

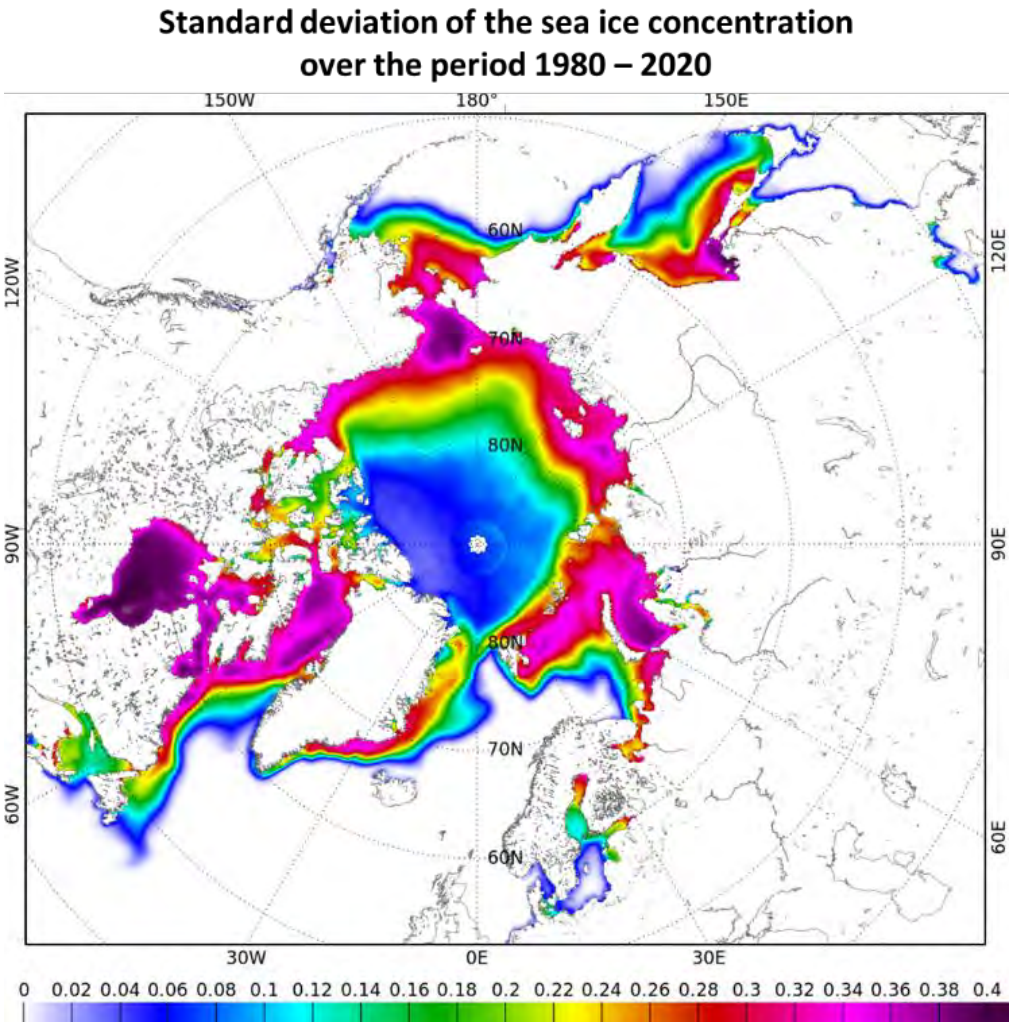

(e)

Figure 4: RMS of sea ice concentration (ranging from 0 to 1) over the 1980-2020 time period (NSIDC products): winter (a), spring (b), summer (c), fall (d), and all seasons combined (e)

3.2 Regional simulations over the 1980-2020 period

To address possible long term changes in Arctic tides, we have produced tidal simulations with seasonal sea ice conditions processed for each year from 1980 to 2020. In the following, only the cases of M2 and K1, the main tidal components in the region, are discussed.

For the M2 tide, the complex RMS computed from the seasonal atlas is maximum (reaching about 3cm locally) in winter and spring conditions (Figure 5 a and b). This is likely linked with the much reduced sea ice cover in summer/fall seasons (Figure 5 c and d) compared to winter/spring seasons, hence minimizing the sea ice climatic changes effects. During winter and spring, the Hudson Bay, the Foxe Basin and the White and Kara Seas are the regions showing the most significant modifications. The summer and fall conditions are much less affected (locally 1 to 2cm), and mostly in the Canadian Archipelago and along the Siberian coast.

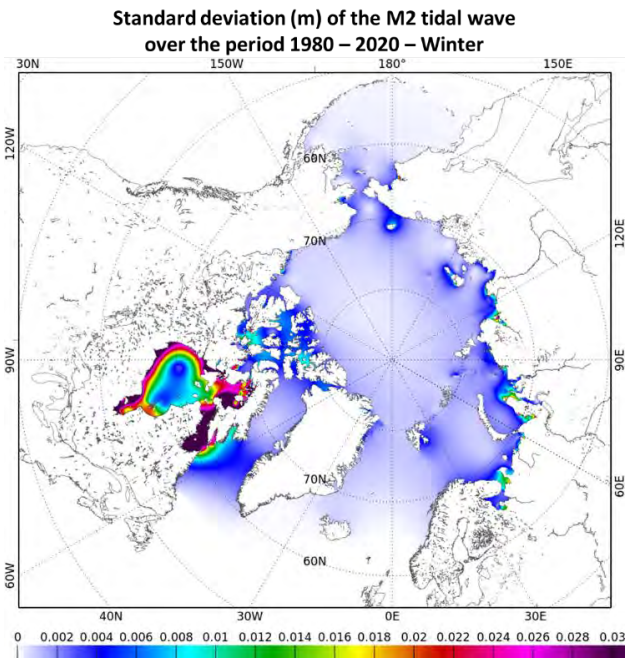
Standard deviation (m) of the M2 tidal wave
over the period 1980 – 2020 – Winter
30N
150W
180°
150E
120W
90W
60W
120E
90E
60E
60N
70N
40N
30W
0E
30E
0 0.002 0.004 0.006 0.008 0.01 0.012 0.014 0.016 0.018 0.02 0.022 0.024 0.026 0.028 0.03

(a)

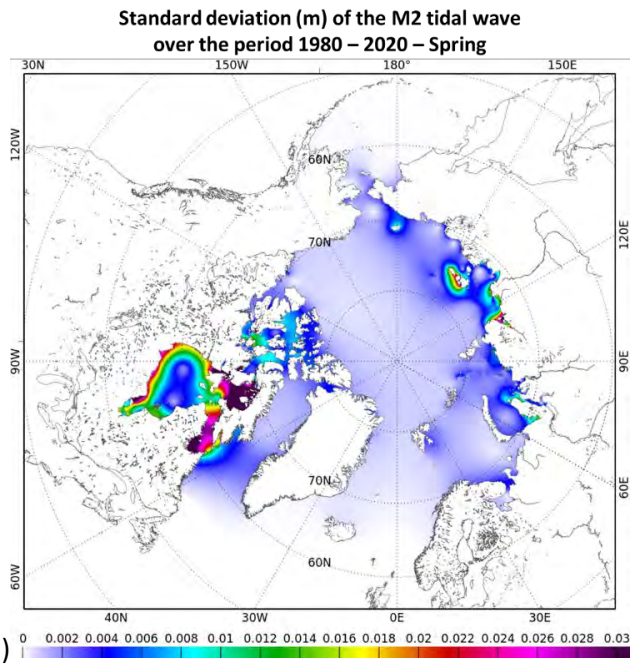
Standard deviation (m) of the M2 tidal wave
over the period 1980 – 2020 – Spring
30N
150W
180°
150E
120W
90W
60W
120E
90E
60E
60N
70N
40N
30W
0E
30E
0 0.002 0.004 0.006 0.008 0.01 0.012 0.014 0.016 0.018 0.02 0.022 0.024 0.026 0.028 0.03

(b)

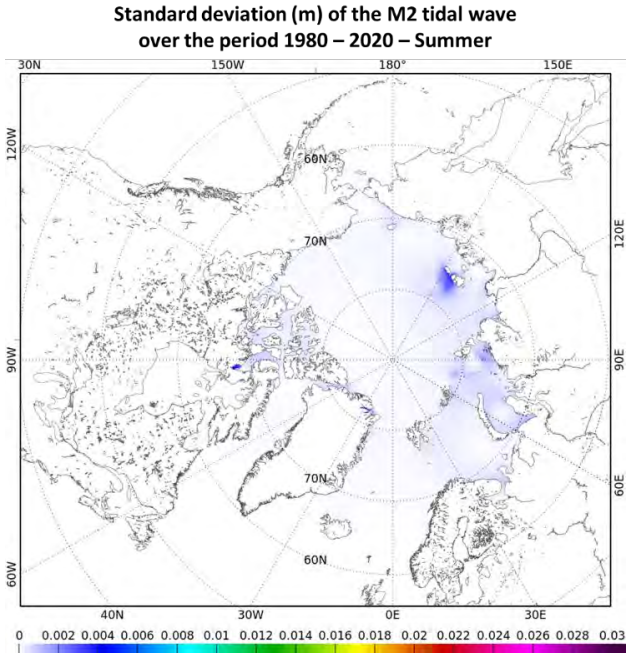
Standard deviation (m) of the M2 tidal wave
over the period 1980 – 2020 – Summer
30N
150W
180°
150E
120W
90W
60W
120E
90E
60E
60N
70N
40N
30W
0E
30E
0 0.002 0.004 0.006 0.008 0.01 0.012 0.014 0.016 0.018 0.02 0.022 0.024 0.026 0.028 0.03

(c)

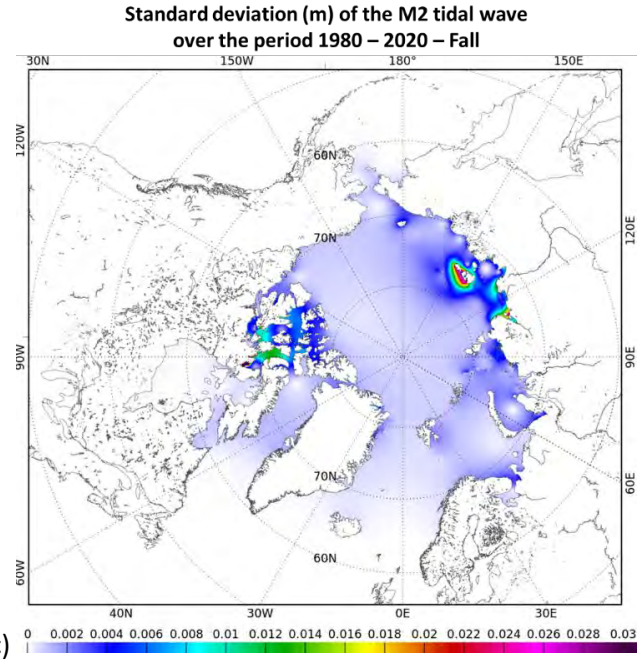
Standard deviation (m) of the M2 tidal wave
over the period 1980 – 2020 – Fall
30N
150W
180°
150E
120W
90W
60W
120E
90E
60E
60N
70N
40N
30W
0E
30E
0 0.002 0.004 0.006 0.008 0.01 0.012 0.014 0.016 0.018 0.02 0.022 0.024 0.026 0.028 0.03

(d)

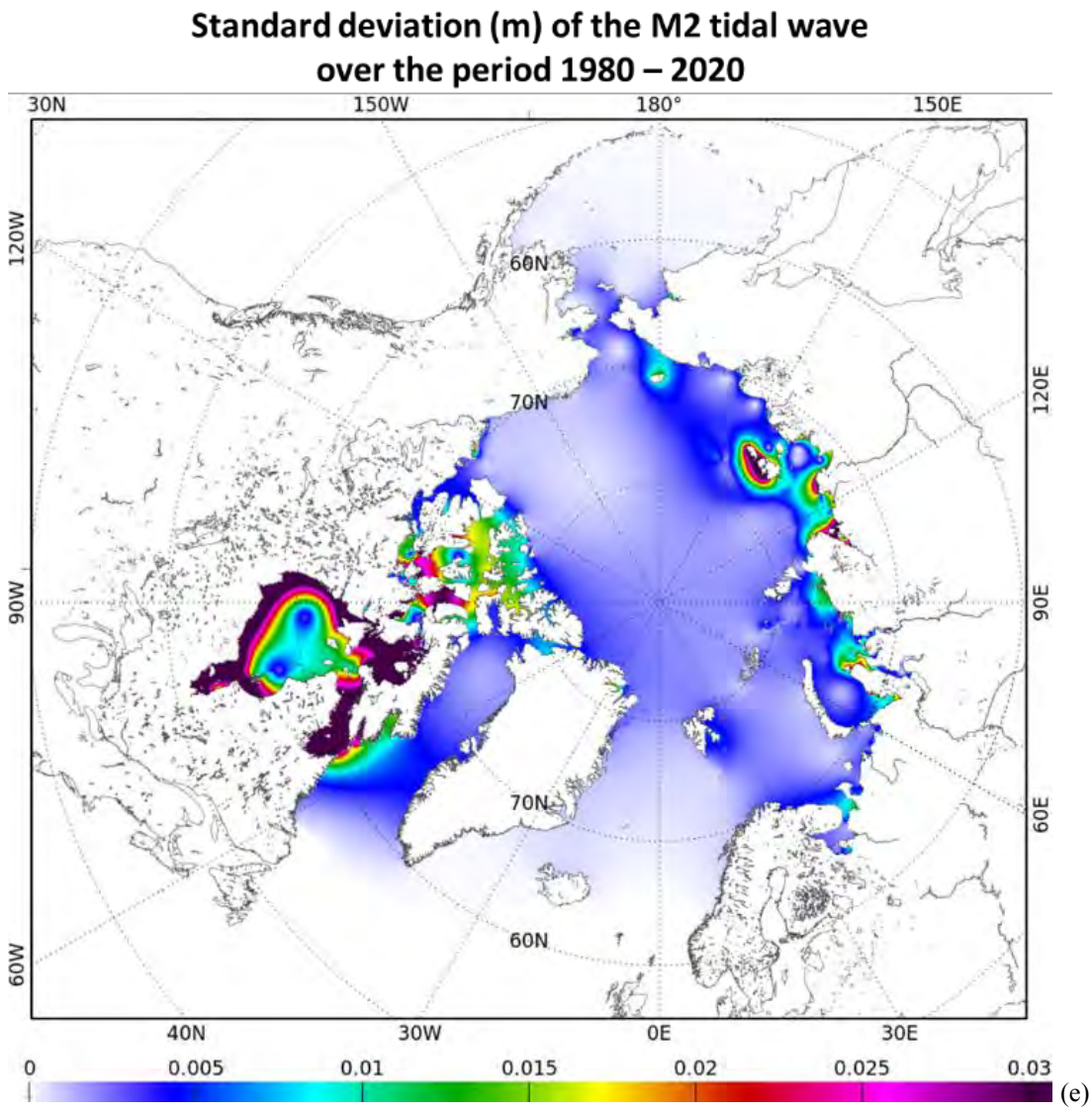

Figure 5: Complex standard deviation (m) of the M2 tide over the 1980-2020 time period, for seasonal sea ice conditions: winter (a), spring (b), summer (c), fall (d), and all seasons combined (e)

The K1 tide case is slightly more surprising (Figure 6). While winter and spring seasons show higher tidal changes compared to summer, the fall season is the one with the largest modifications, mostly in the northern Baffin Sea and Canadian Archipelago. The explanation can be found in the latter place, which dynamically controls the K1 resonance in the Baffin Sea and seems more affected by long terms sea ice changes in fall season (this can also be observed for the M2 tide, without of course the diurnal resonance effects in the Baffin sea). It might explain the differences in the K1 tide that have been historically observed in this region between the various global tidal atlases (GOT, TPXO, FES). These atlases were produced at different time, and used satellite altimetry data for data assimilation or optimal mapping processing collected over epoch-dependent time periods.

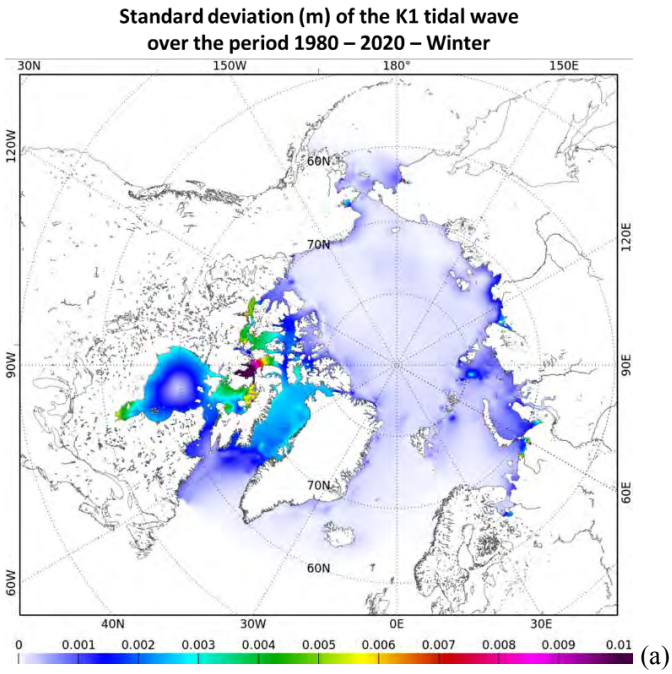
Standard deviation (m) of the K1 tidal wave
over the period 1980 – 2020 – Winter
30N
150W
180°
150E
120W
120E
90W
90E
60W
60E
60N
70N
40N
30W
0E
30E
0
0.001
0.002
0.003
0.004
0.005
0.006
0.007
0.008
0.009
0.01

(a)

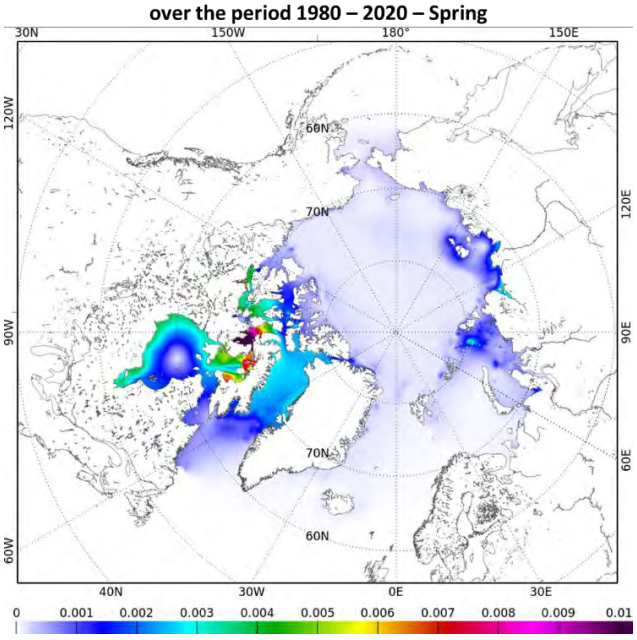
Standard deviation (m) of the K1 tidal wave
over the period 1980 – 2020 – Spring
30N
150W
180°
150E
120W
120E
90W
90E
60W
60E
60N
70N
40N
30W
0E
30E
0
0.001
0.002
0.003
0.004
0.005
0.006
0.007
0.008
0.009
0.01

(b)

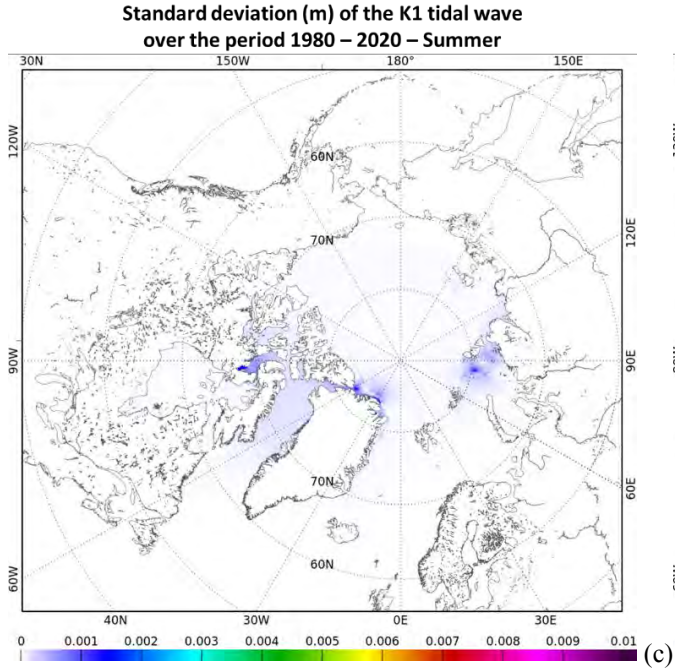
Standard deviation (m) of the K1 tidal wave
over the period 1980 – 2020 – Summer
30N
150W
180°
150E
120W
120E
90W
90E
60W
60E
60N
70N
40N
30W
0E
30E
0
0.001
0.002
0.003
0.004
0.005
0.006
0.007
0.008
0.009
0.01

(c)

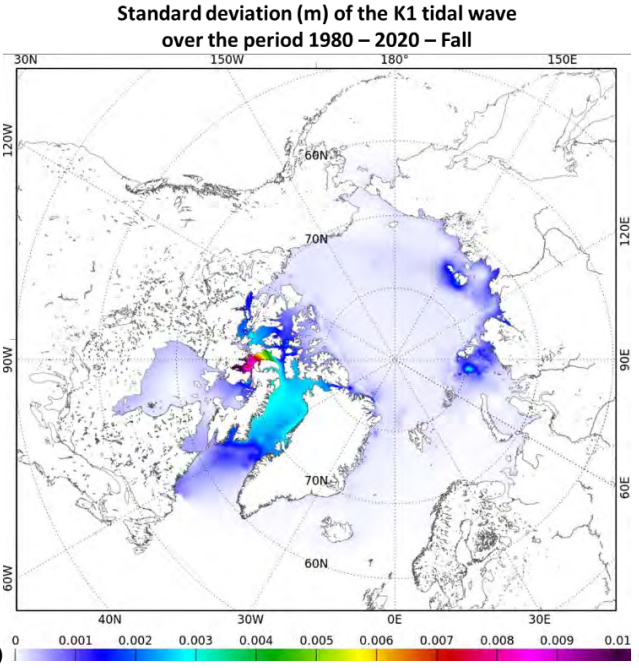
Standard deviation (m) of the K1 tidal wave
over the period 1980 – 2020 – Fall
30N
150W
180°
150E
120W
120E
90W
90E
60W
60E
60N
70N
40N
30W
0E
30E
0
0.001
0.002
0.003
0.004
0.005
0.006
0.007
0.008
0.009
0.01

(d)

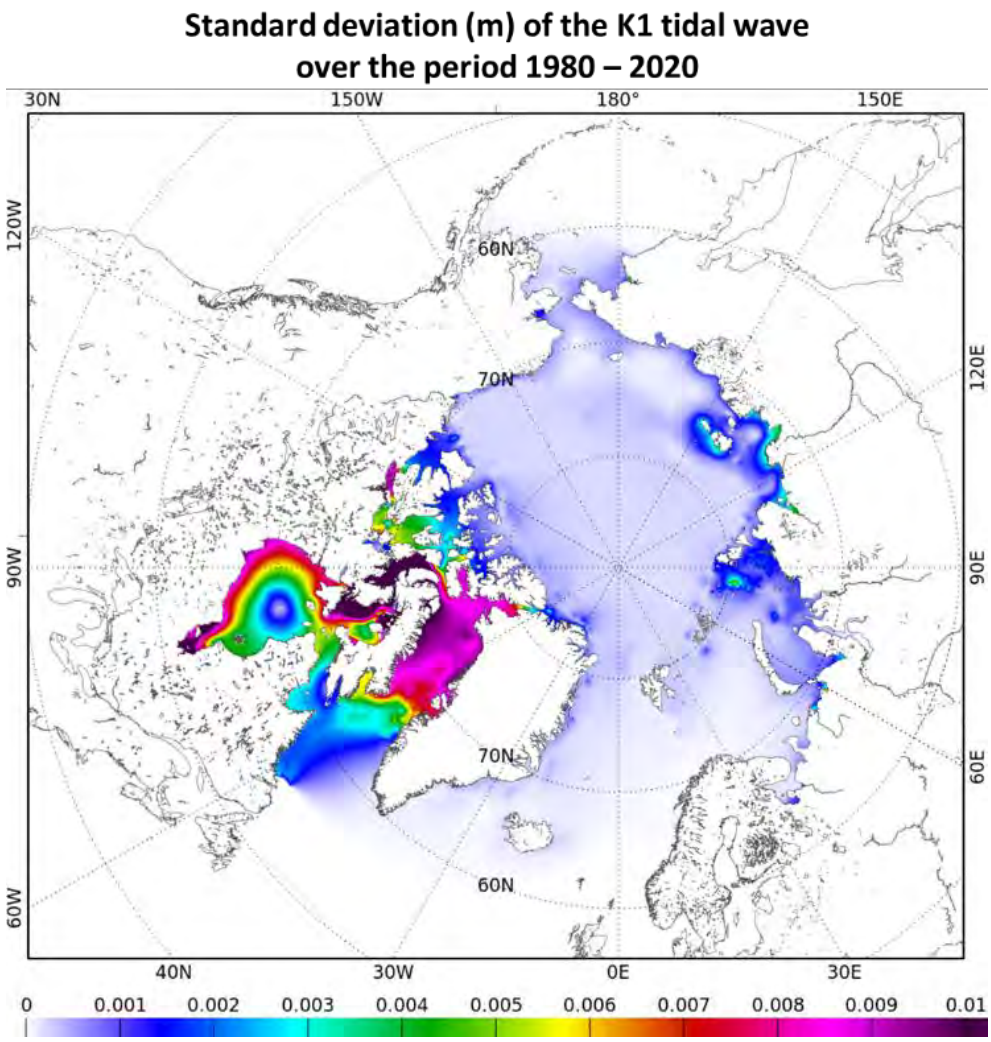

(e)

Figure 6: Complex standard deviation (m) of the K1 tide over the 1980-2020 time period, at seasonal sea ice conditions: winter (a), spring (b), summer (c), fall (d), and all seasons combined (e)

3.3 Tidal variability from tide gauge data

The seasonal regional tidal simulations have been compared to the seasonal in situ tidal observations at each of the ten tide gauge stations presented in section 2.3, for the main tidal components M2 and K1. Figure **7** to Figure **12** show the seasonal times series of the amplitude of the M2 and K1 tides extracted from the model and analysed from the tide gauge data, for stations that highlight a clear seasonal cycle for tides (red dots on Figure 2). Figure **13** to Figure **16** show the seasonal time series analysed from the tide gauge data at the stations with no clear seasonal cycle (black dots on Figure 2). We do not show the model time series for these latter stations, as they do not highlight any seasonal nor inter-annual variability (the model time series are very close from one another and completely flat).

In general, the results are very heterogeneous, depending on the in situ station, and on the tidal constituent. The set of convenient in situ data available to examine the tidal variability is extremely reduced, and the necessity to seasonally split the harmonic analysis is a source for harmonic constant analysis errors, which undermines the possibility to draw firm conclusions. In particular, 3 months of tide gauge data may not be enough to accurately separate the K1 and S1 tides in the harmonic analysis process. In some stations, we can observe some qualitative agreement between simulations and observations, and significant differences can be noticed at other stations. For the M2 tide, consistently with the idea that sea ice friction will drive the tidal amplitude, the summer season amplitude is usually larger, and the winter or spring amplitudes are the weaker, but it can also be quite the opposite such as can be observed at the Alert and Nain stations.

The best agreement occurs at the two stations located north of Norway (Honningsvåg and Vardø), in a year-round sea-ice free region, where the evolution in the tidal amplitudes is not due to local effects of the sea ice cover, but may be linked with remote effects. There is a clear seasonal difference at these two stations, with M2 amplitudes about 2-cm larger in summer than for the other seasons. One can also note positive trends in the tidal estimates from observations for all the seasons at these in situ stations, while the model provides negative trends.

In Churchill (Figure **10**), the time series show a large decay in the M2 tidal amplitudes for all the seasons. This was already identified and investigated by Ray (2016), and no clear explanation for such an unexpected behaviour is available yet. The tide gauge is located in an estuarine region, and may be affected by some specific river regime. The CryoSat-2 altimetry observations in the area (representative of an averaged 2010-2020 period) provide M2 amplitudes of 1.4 m, but are not located exactly in the estuary like the tide gauge instrument. A slight decay is also observed for the K1 component but not at the same level, as the amplitudes are much lower (Figure **10**, b). The largest changes in the seasonal sea-ice concentration at Churchill occur in spring, with a reduction over the years, and increased interannual variability in the sea-ice concentration since 1985. The case of the Churchill station is a typical issue and limitation to the study of long-term variations of the ocean tides in the Arctic region, as this is the only tide gauge that has provided measurements in the Hudson Bay since the 1980s. Although tens of other stations are available in the area, the data were generally acquired in the 1970s or in the 1990s, and all the time series are too short to estimate seasonal tides (time series of a few weeks, in general in summer). Modelling is thus the most complete approach to investigate high-frequency processes like tides in the Arctic Ocean, providing estimates over the whole ocean, and the whole period of interest. However, there is a dramatic lack of observations to validate the model simulations, particularly in such a quickly-changing environment.

Finally, the lack of seasonal and inter-annual variability in the model simulations at the stations located in Alaska (Nikiski, Seldovia, Anchorage, and Village Cove) may reflect some lack of connection between the Pacific Ocean and the Arctic Ocean through the Bering Strait. The open boundary conditions of the model in the Pacific Ocean, constrained with the same FES2014 global solution (no seasonal nor inter-annual variations) for all the seasonal simulations and for each year of the 1980-2020 period, may be located to close to the Bering Strait, and may prevent the regional model from developing its own tidal variability in the region.

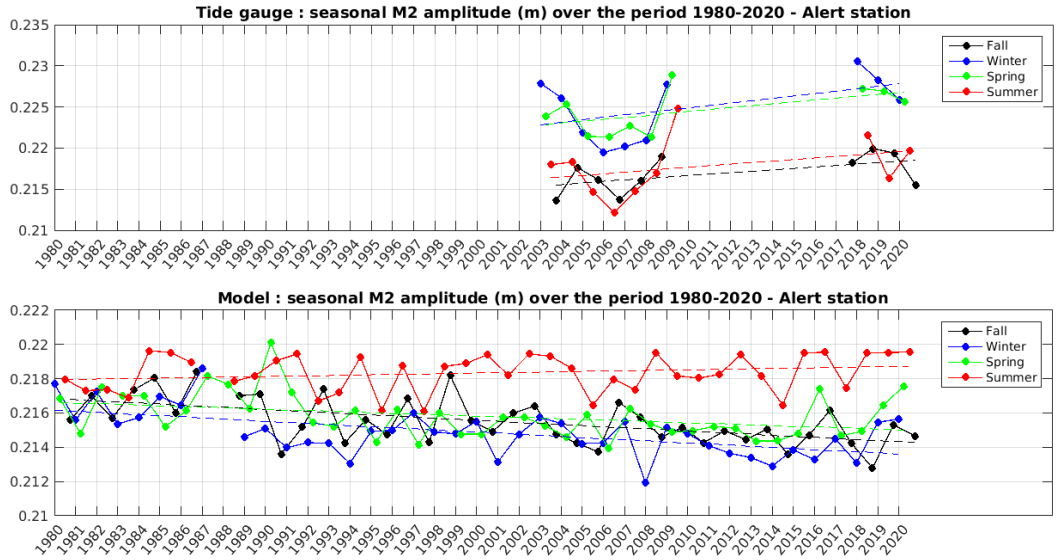

(a)

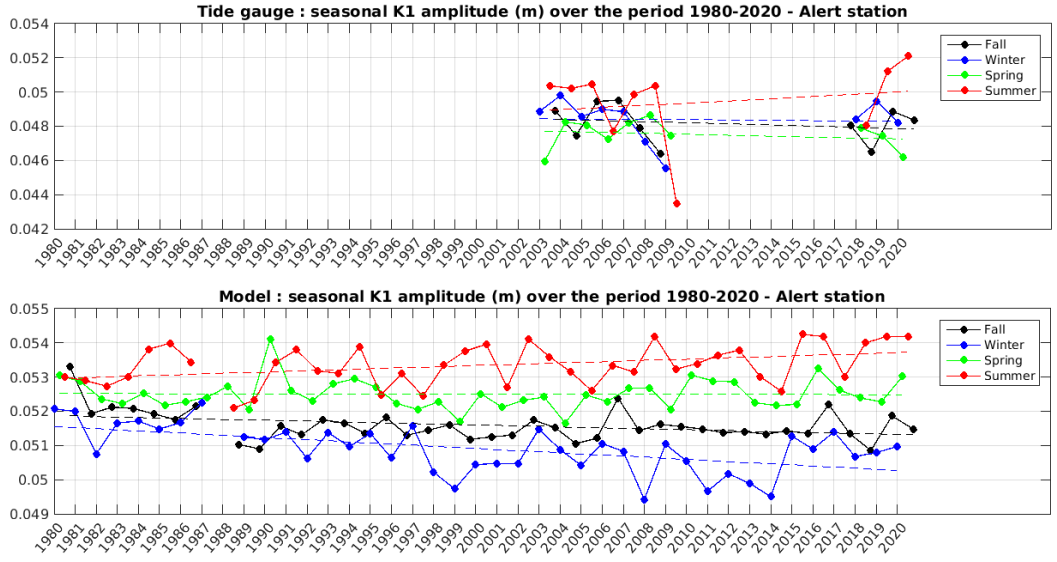

(b)

Figure 7: Alert tide gauge, seasonal tidal amplitude for the M2 (a) and K1 (b) tides from observations (upper panels) and simulation (lower panels) over the 1980-2020 time period. The coloured dashed lines show the linear trends of the time series.

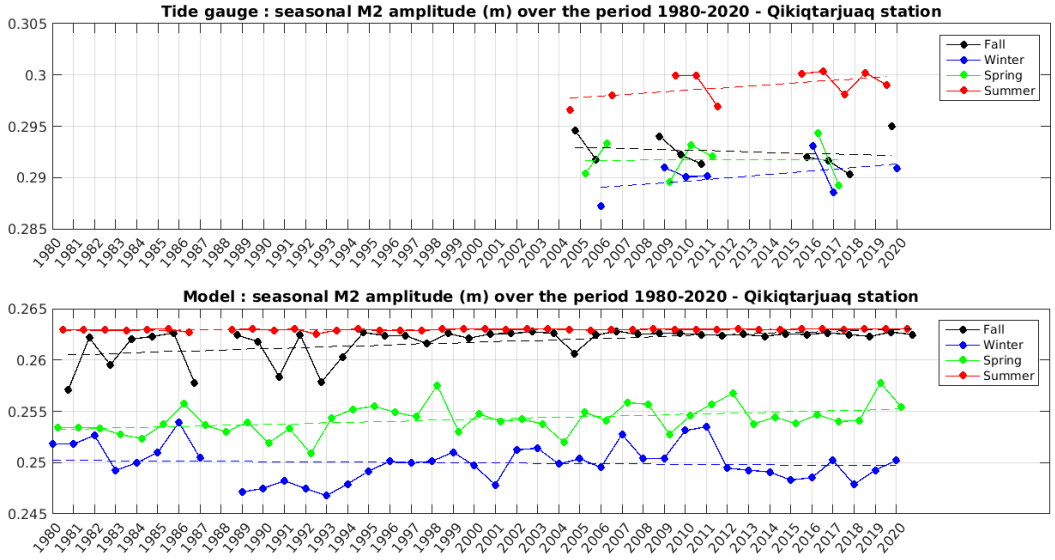

(a)

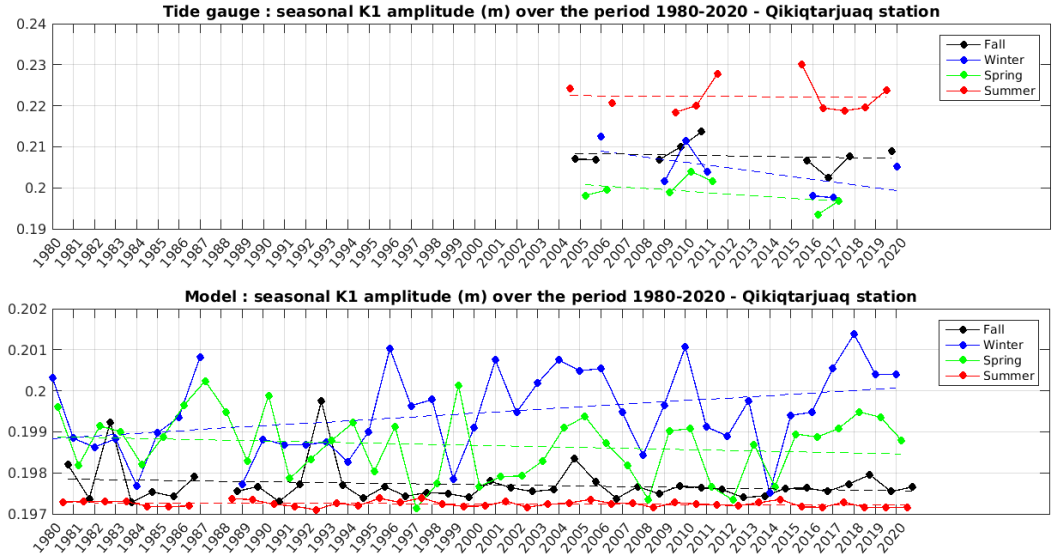

(b)

Figure 8: Qikiqtarjuaq tide gauge, seasonal tidal amplitude for the M2 (a) and K1 (b) tides from observations (upper panels) and simulation (lower panels) over the 1980-2020 time period. The coloured dashed lines show the linear trends of the time series.

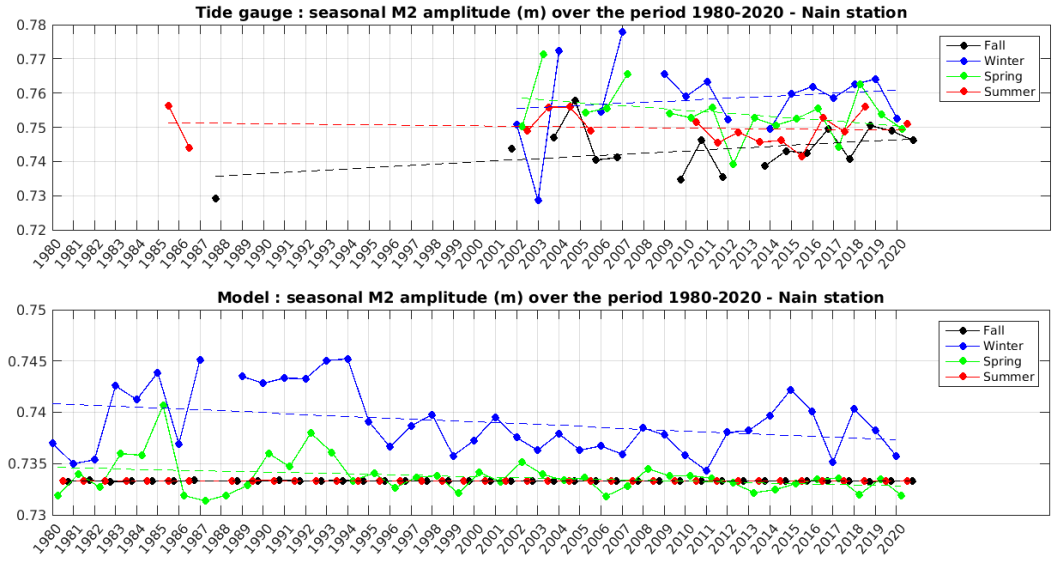

(a)

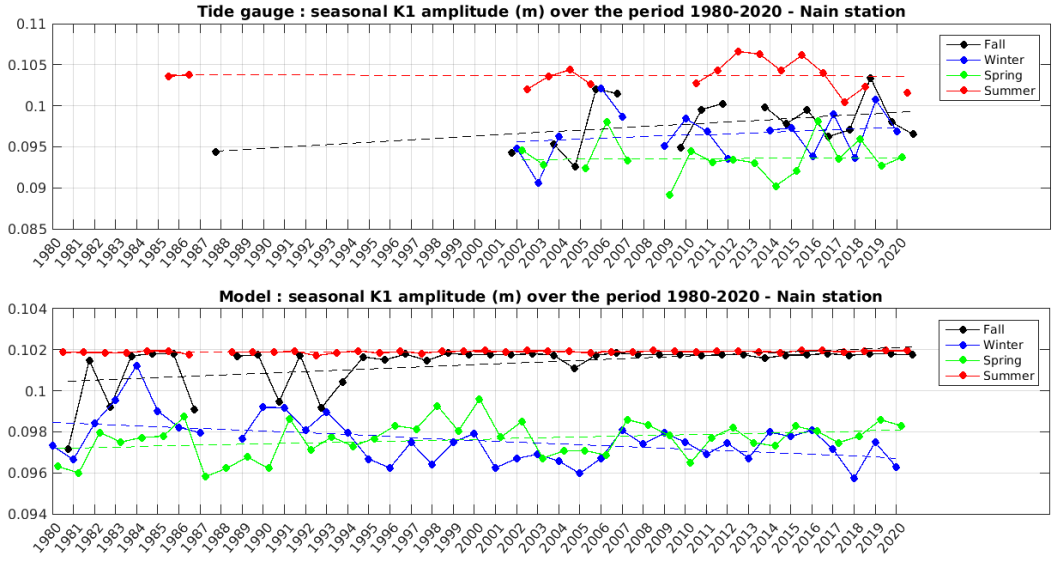

(b)

Figure 9: Nain tide gauge, seasonal tidal amplitude for the M2 (a) and K1 (b) tides from observations (upper panels) and simulation (lower panels) over the 1980-2020 time period. The coloured dashed lines show the linear trends of the time series.

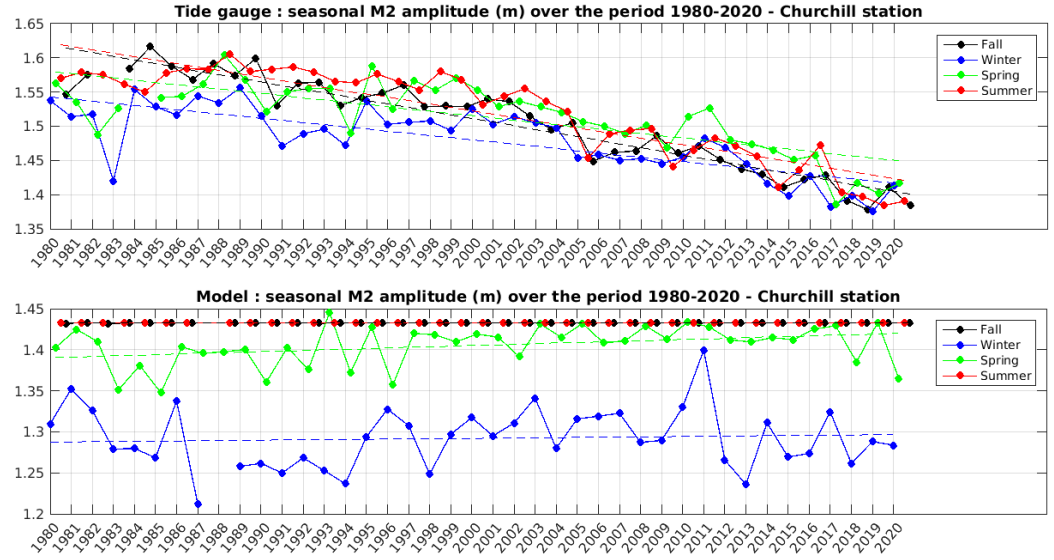

(a)

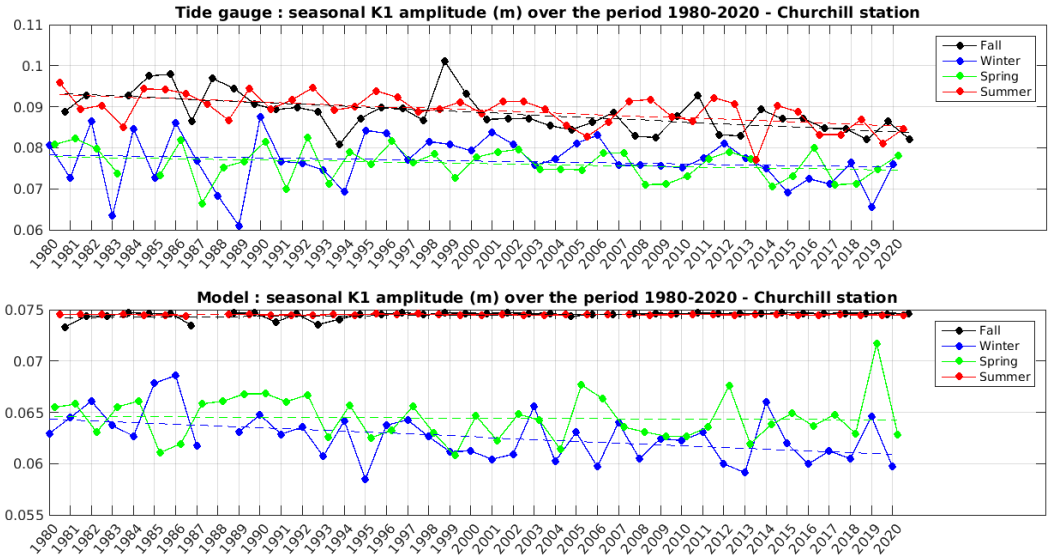

315 (b)

Figure 10: Churchill tide gauge, seasonal tidal amplitude for the M2 (a) and K1 (b) tides from observations (upper panels) and simulation (lower panels) over the 1980-2020 time period. The coloured dashed lines show the linear trends of the time series.

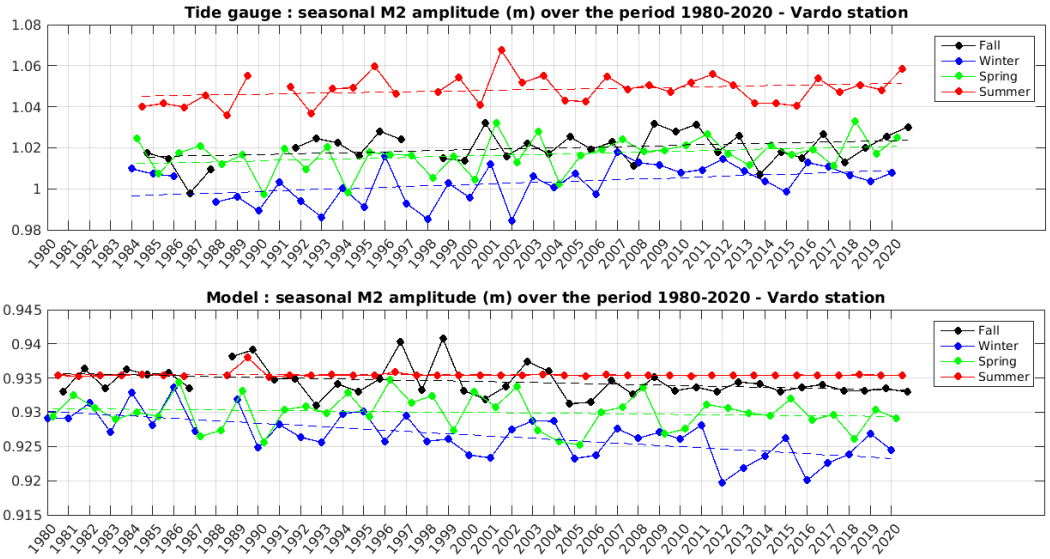

(a)

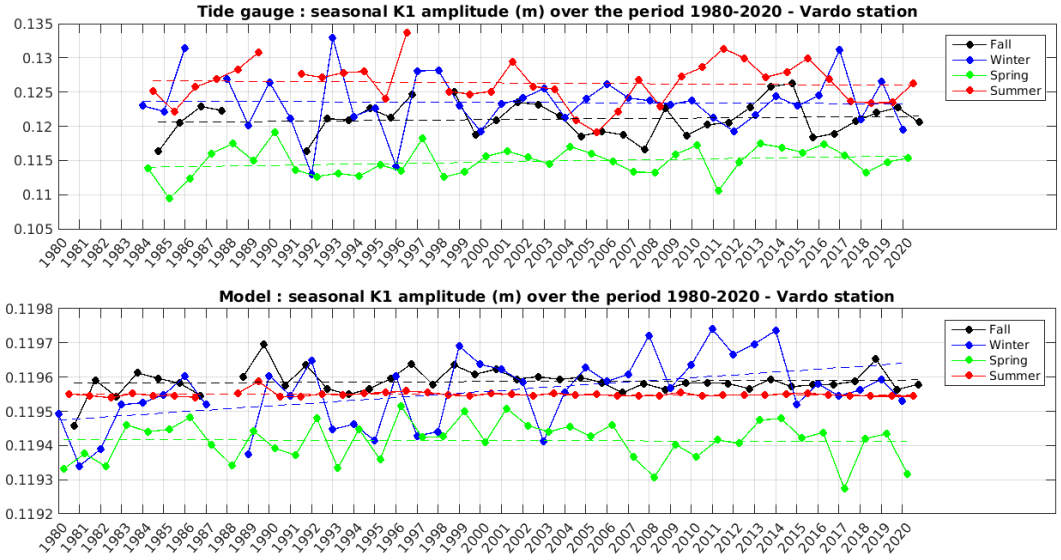

(b)

320 Figure 11: Vardo tide gauge, seasonal tidal amplitude for the M2 (a) and K1 (b) tides from observations (upper panels) and simulation (lower panels) over the 1980-2020 time period. The coloured dashed lines show the linear trends of the time series.

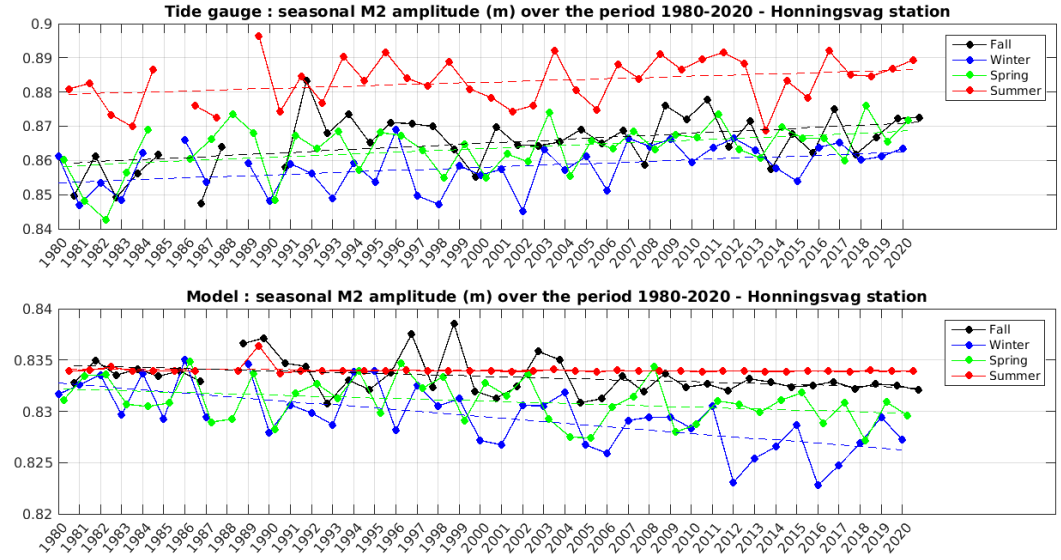

(a)

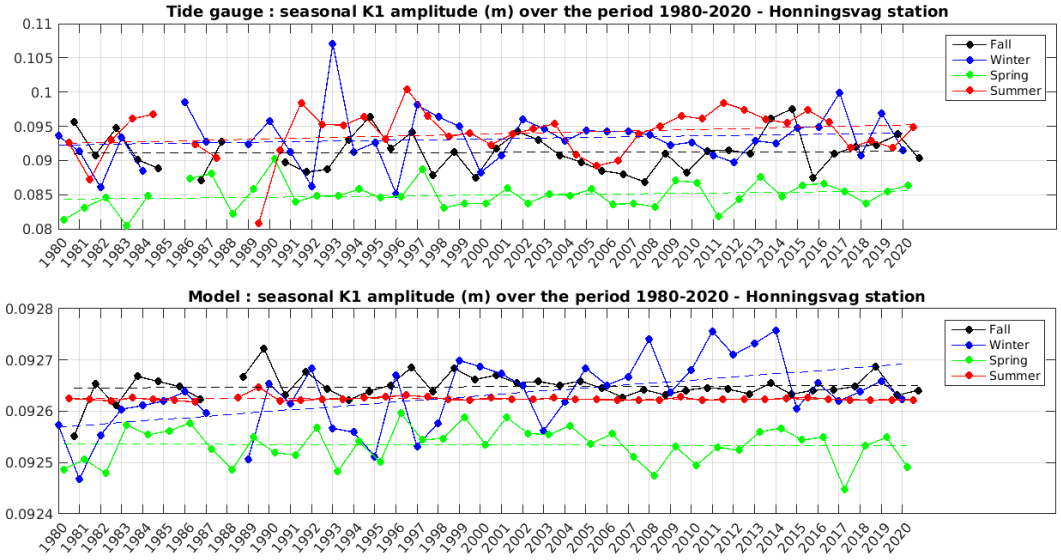

(b)

Figure 12: Honningsvag tide gauge, seasonal tidal amplitude for the M2 (a) and K1 (b) tides from observations (upper panels) and simulation (lower panels) over the 1980-2020 time period. The coloured dashed lines show the linear trends of the time series.

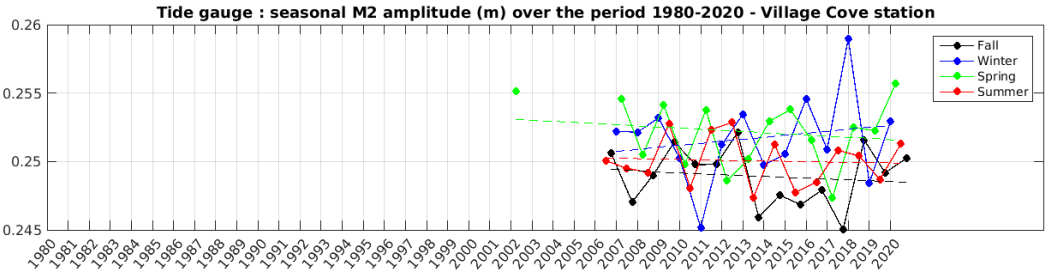

(a)

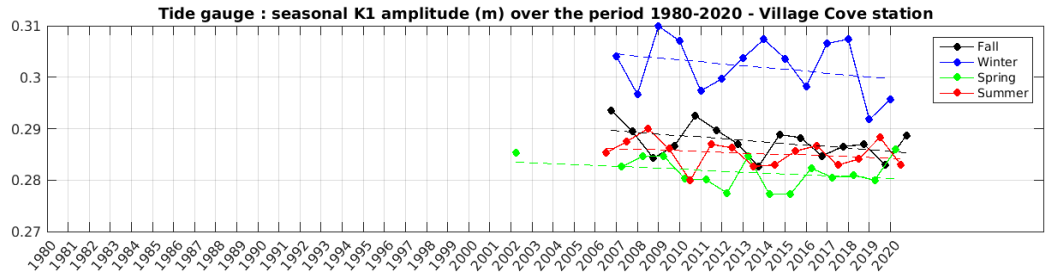

(b)

Figure 13: Village Cove tide gauge, seasonal tidal amplitude for the M2 (a) and K1 (b) tides from observations over the 1980-2020 time period. The coloured dashed lines show the linear trends of the time series.

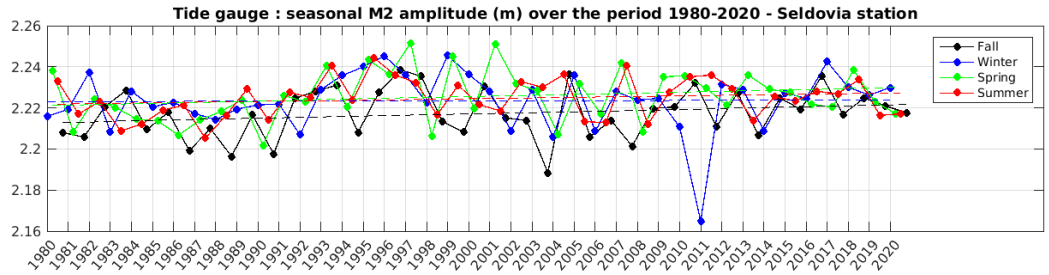

(a).

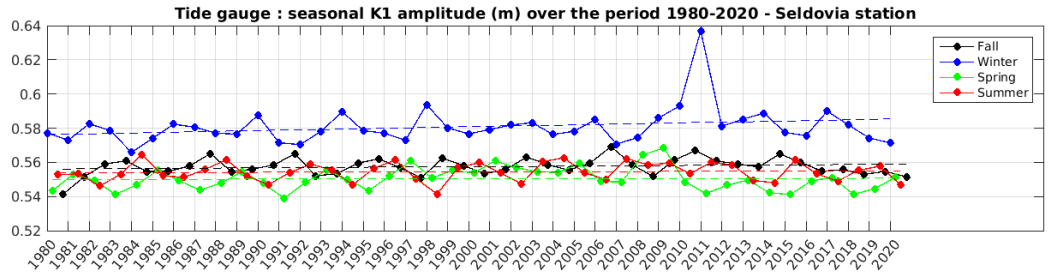

(b)

Figure 14: Seldovia tide gauge, seasonal tidal amplitude for the M2 (a) and K1 (b) tides from observations over the 1980-2020 time period. The coloured dashed lines show the linear trends of the time series.

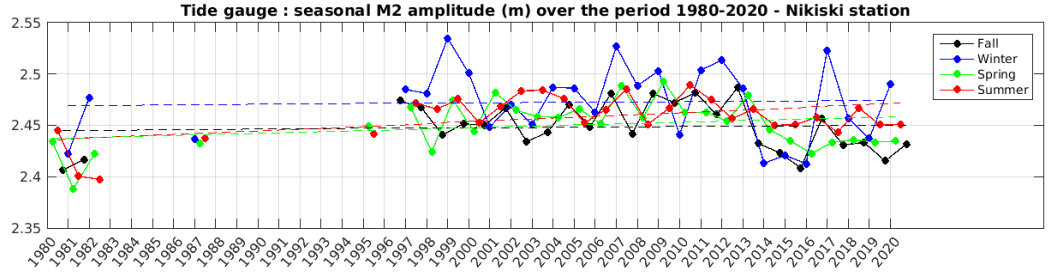

(a)

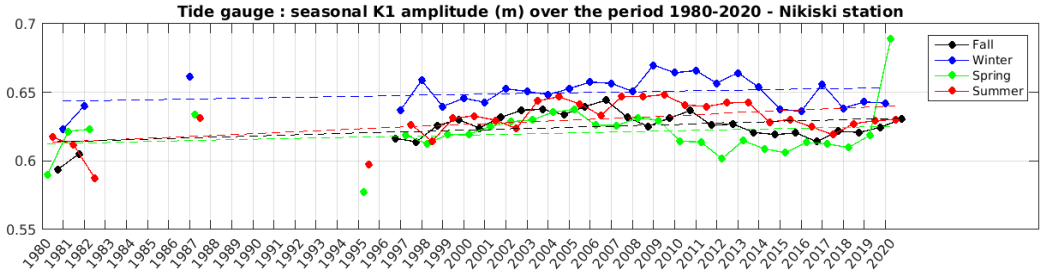

(b)

Figure 15: Nikiski tide gauge, seasonal tidal amplitude for M2 (a) and K1 (b) tides from observations over the 1980-2020 time period. The coloured dashed lines show the linear trends of the time series.

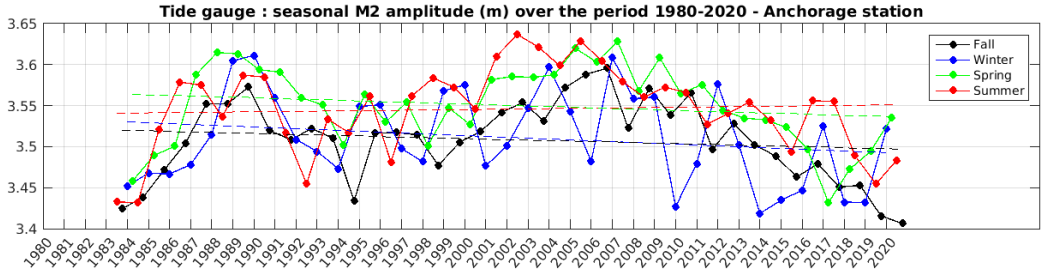

(a)

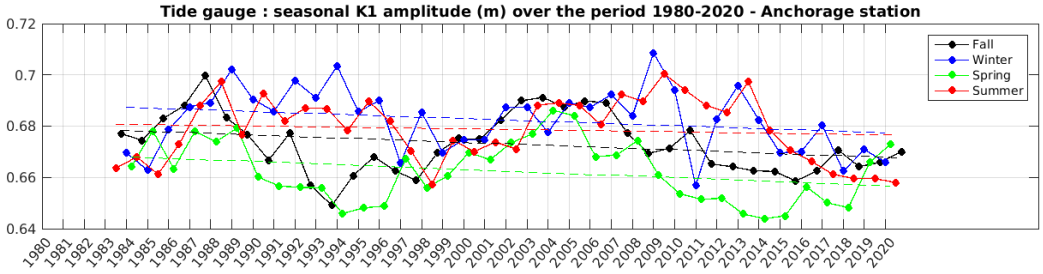

(b)

Figure 16: Anchorage tide gauge, seasonal tidal amplitude for the M2 (a) and K1 (b) tides from observations over the 1980-2020 time period. The coloured dashed lines show the linear trends of the time series.

3.3 Global simulations over the 1980-2020 period

In order to investigate the possible long-distance effect of the changing sea ice cover in the Arctic Ocean, global simulations based on the FES2014 global model configuration have been performed every year over the period 1980-2020, considering the sea-ice friction scheme depending on the seasonal sea ice concentration (default threshold of 70%, modulated by ice confinement). The only input parameter that changes from one simulation to the other is the sea ice concentration in the Arctic and Antarctic Oceans, there is no other temporal aspect in the model (spectral mode). For each season, the standard deviations of the M2 and K1 tidal components have been computed over the whole period, and are shown on the maps presented on Figure 17 and Figure 18. First, the overall tidal variability (Figure 17 e for M2 and Figure 18 e for K1), which is computed over the 1980-2020 time period from all seasonal solutions, shows larger values than the seasonal variability (Figure 17 a-d for M2 and Figure 18 a-d for K1) because of the dominant intra-annual variability. For M2, the overall tidal variability is dominant in the Arctic and North Atlantic Ocean, the Okhotsk Sea, the Arabian Sea and in the Mozambique Channel, reaching centimetre values and larger, with maximum mostly reached in the Hudson Bay and Foxe Basin.

The variability is globally twice smaller for K1, and mainly concentrated in the Arctic Ocean (Baffin Bay, Canadian Archipelago), in the Mid-Atlantic Bight and in the Okhotsk Sea. As one could expect, the smallest variability occurs in Summer, when the sea ice cover is minimal in the Arctic Ocean. This result also highlights the lower impact of the Antarctic sea ice cover on the global tidal simulations, even during the Southern Winter season, as there are less open-sea continental shelves in the Southern Ocean. For the other seasons, and in particular Winter and Spring, some regions outside the Arctic Ocean clearly show variations at the centimetre level on M2, especially in the Atlantic Ocean, all along the US coast down to Florida, and along the European coast up to the English Channel. Variability patterns are also observed in Spring along the

Nicaragua coast in the Caribbean Sea, as well as on the Amazon shelf. Bij de Vaate et al. (2021) also showed that the Arctic land-fast ice impacts the seasonal modulation of M2 in these regions. Such patterns are consistent with the strong energetic connection that exists between the Hudson Bay/Foxe Basin area and the North Atlantic Ocean, in terms of tidal energy fluxes. The sea-ice impact outside the Arctic Ocean appears to be amplified in regions of tidal resonance, such as the European continental shelf. For K1, the impact outside the Arctic Ocean is much smaller (note that the scale is not the same as for the M2 maps), but one can clearly see the difference in variability in the Baffin Bay and in the Okhotsk Sea, depending on the season. It should be noted that the sea ice concentration maps include the Okhotsk Sea, which explains the large variability in this region.

The seasonal time series of the M2 and K1 amplitudes from the model are shown in Figure 19 at two points, the first one along the US East coast, off Georgia, and the second one in the English Channel, off Normandy, in France. In both cases, the M2 amplitudes vary of several centimetres from one year to the next, and from one season to the other. However, although tide gauge observations (not shown here) show similar ranges of M2 variability, it is difficult to find a correlation between the time series of in situ data and from the model. Further analyses with in situ data are necessary, at larger scale like Bij de Vaate et al. (2021), to better understand the long-distance effect of the Arctic sea ice cover on the seasonal tides in the global ocean. Given the scale of the modelled tidal variability, and the associated uncertainties, it appears difficult to estimate the impact of the sea-ice cover decay in the Arctic over the years without considering more tide gauge stations (still, the difficulty is to find long time series of hourly observations covering the 1980-2020 period).

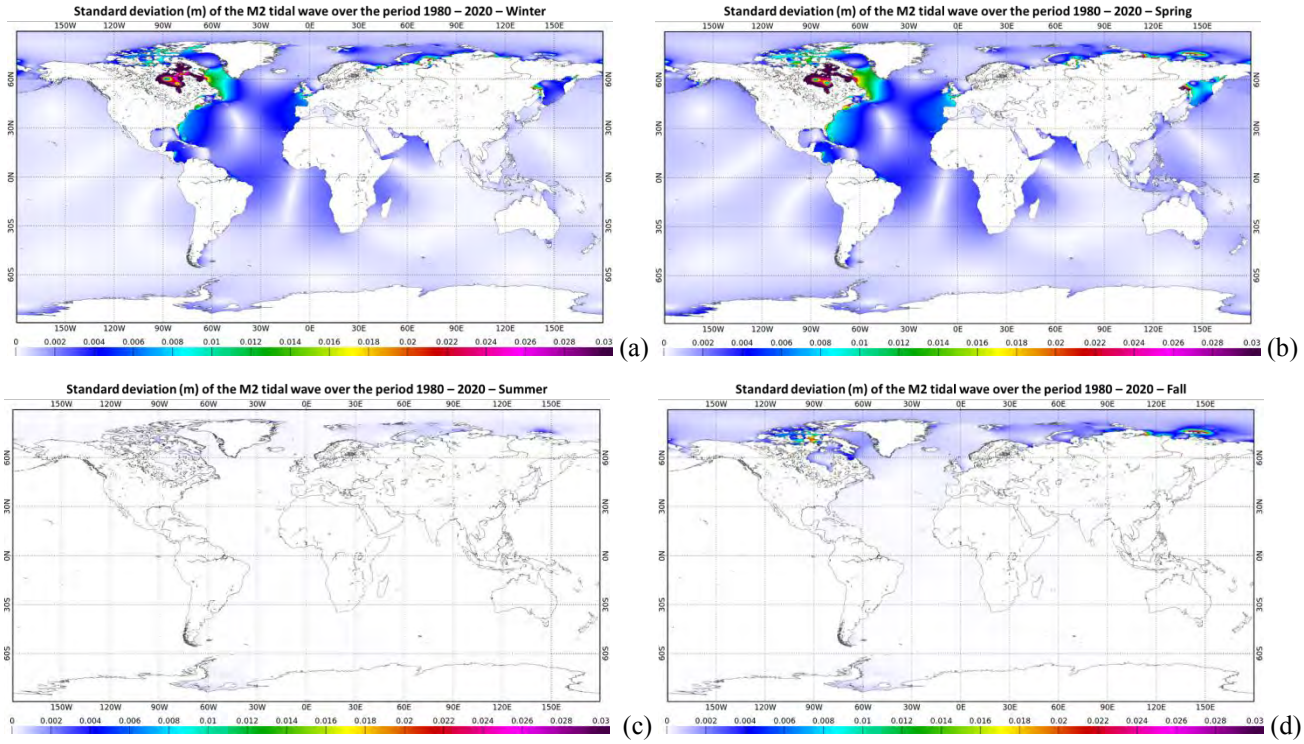

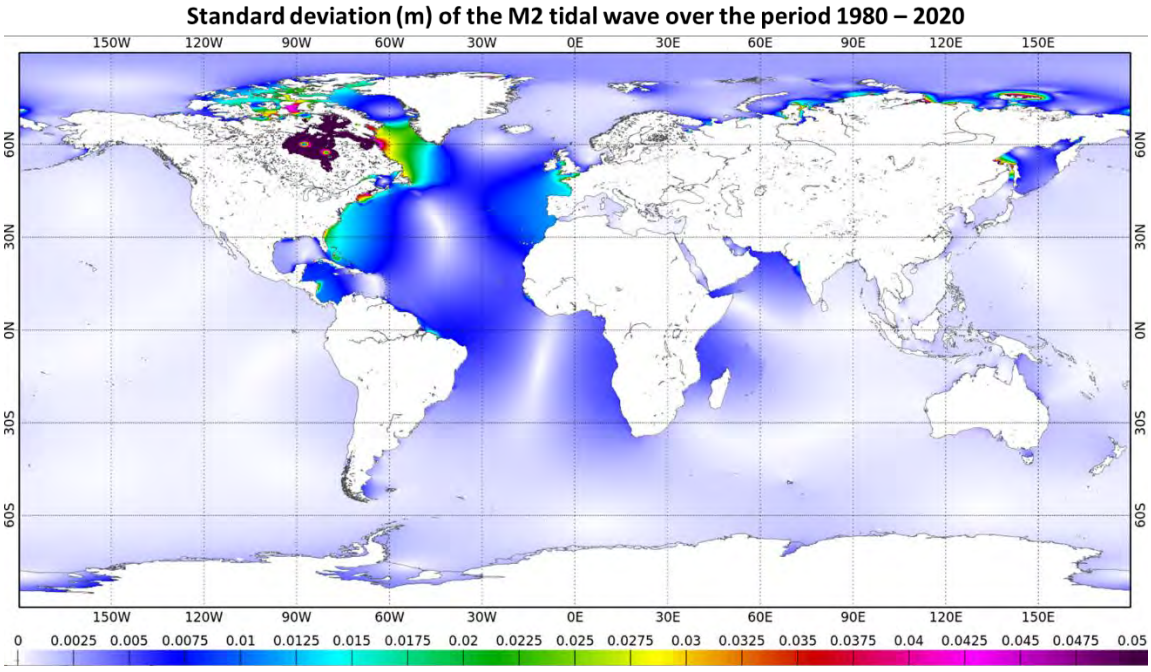

(e)

Figure 17: Complex standard deviation (m) of the M2 tide over the 1980-2020 time period at global scale, at seasonal sea ice conditions: winter (a), spring (b), summer (c), fall (d), and all seasons combined (e)

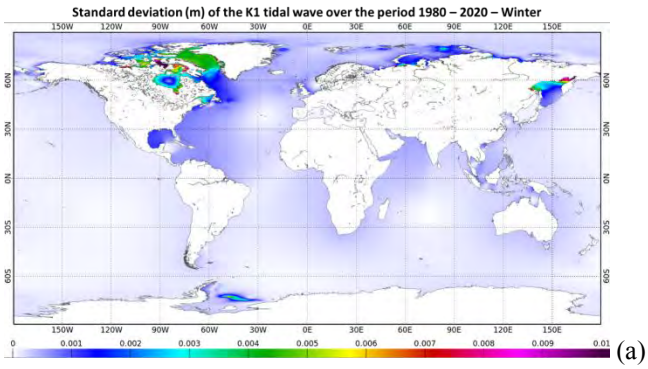

(a)

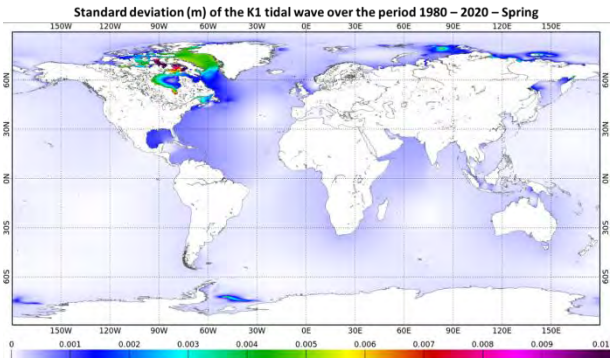

(b)

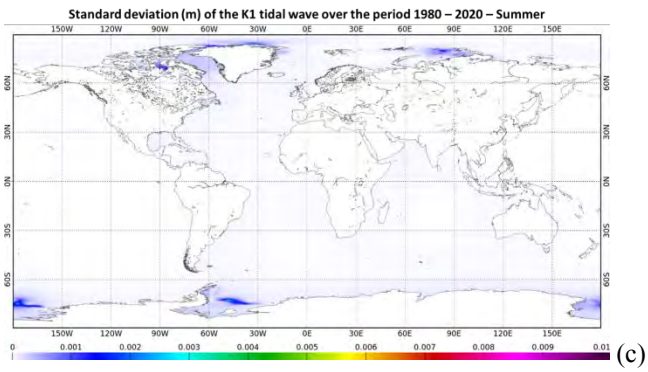

(c)

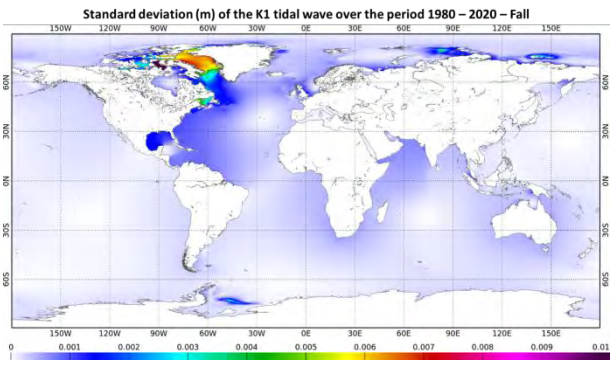

(d)

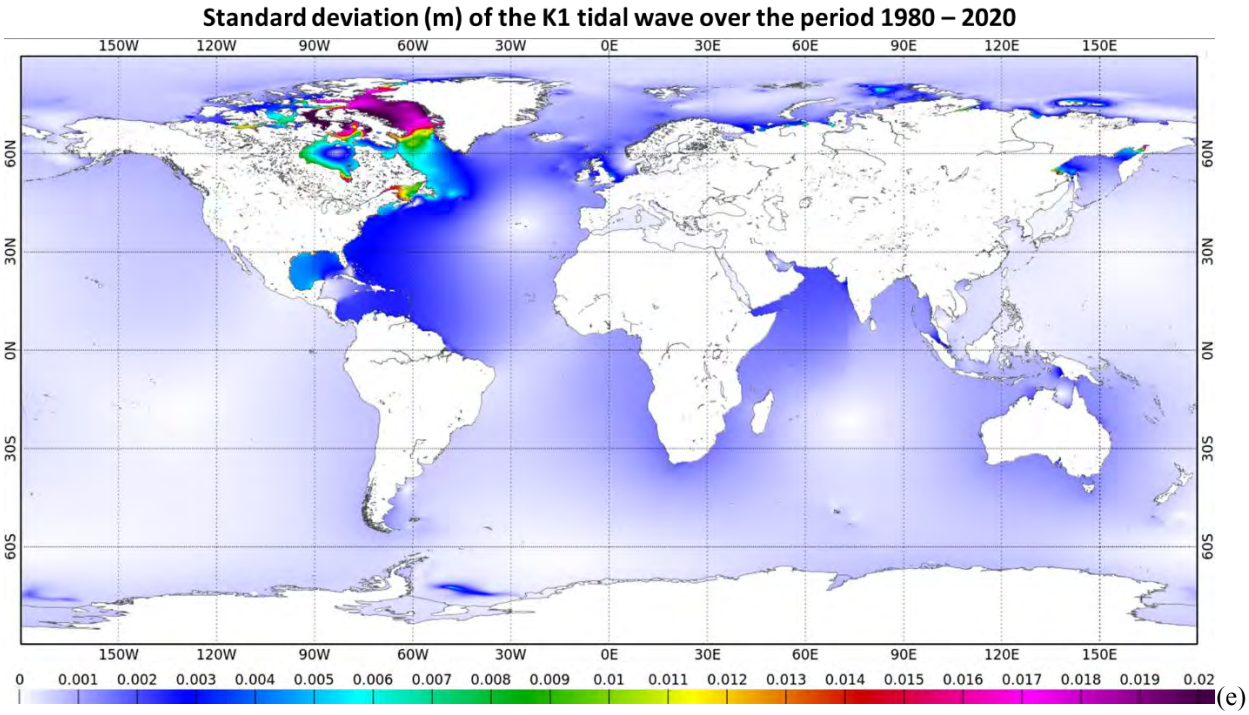

(e)

Figure 18: Complex standard deviation (m) of the K1 tide over the 1980-2020 time period at global scale, at seasonal sea ice conditions: winter (a), spring (b), summer (c), fall (d), and all seasons combined (e)

390

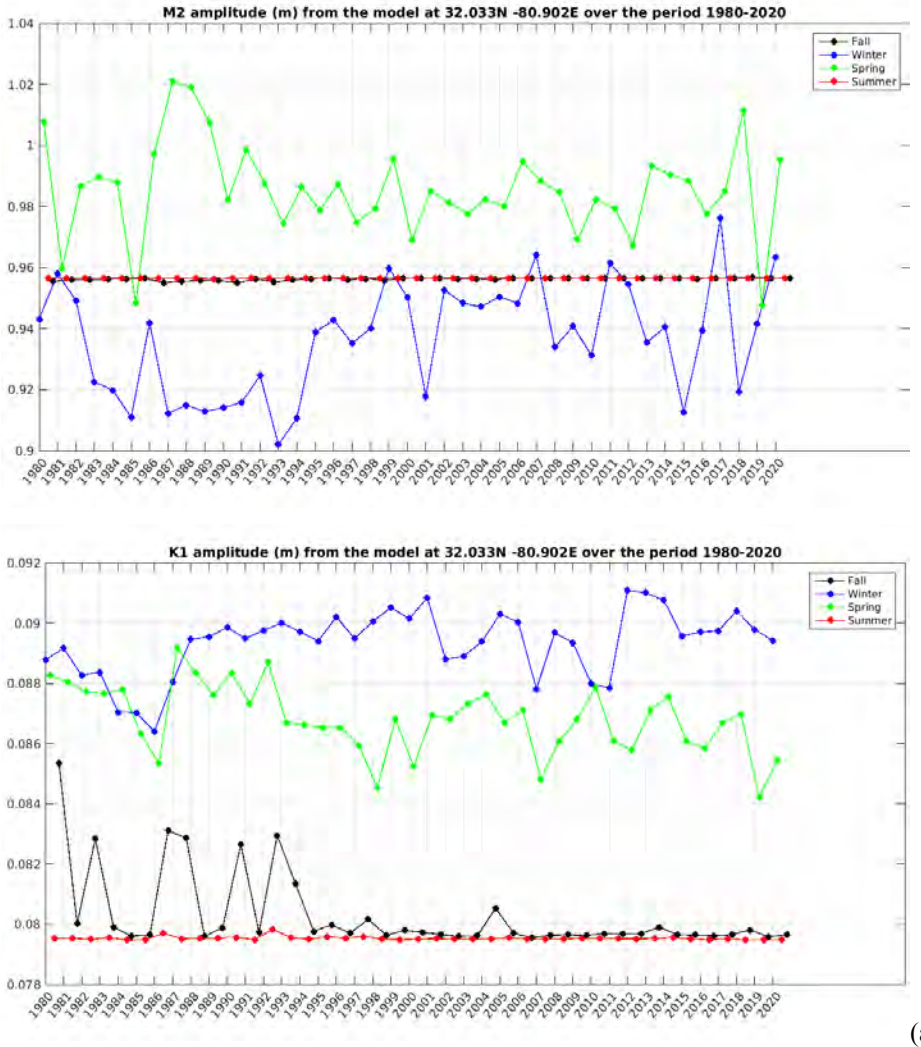

(a)

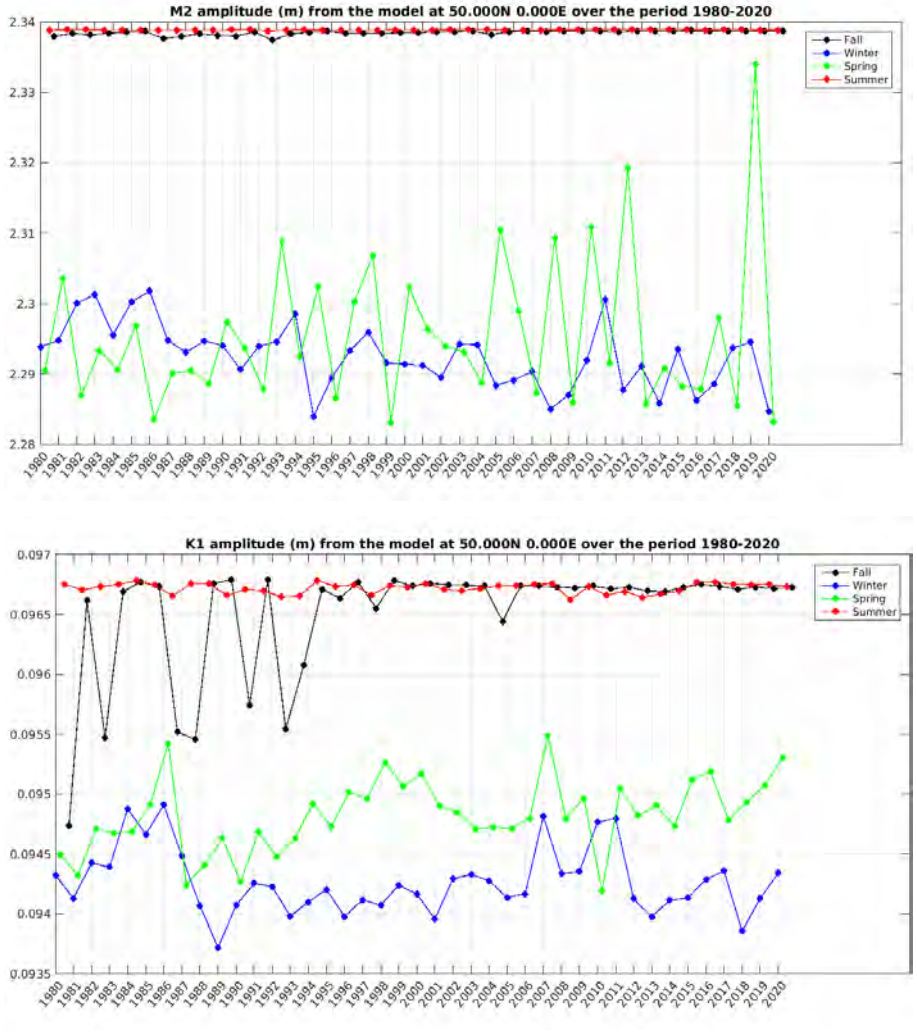

(b)

Figure 19: Seasonal time series of the M2 (upper plots) and K1 (lower plots) tidal amplitude (in m) from the global model, at points located along the coast of Georgia (a) and in the English Channel, off France (b)

4 Discussion and conclusion

The investigations about the tidal variability associated with the sea ice cover variability, both from situ records or through numerical simulations, remain a complex and uncertain challenge. The different variability time scales (seasonal, inter-annual, long term) driving the sea-ice cover and its impact on tidal variability mix up with more or less comparable amplitude. It is difficult to deliver a general conclusion about this study, as the tidal response to sea ice changes is far from uniform in space, and may differ when considering the M2 or K1 tides. Let just state that the seasonal tidal variability is the dominant one, the inter-annual variability comes second and that long-term tidal variability, when detectable, remains the weakest one. By nature, the tidal spatial scales, which range between a few kilometres to thousands of kilometres, also make it difficult to assess the impact of the long-term/inter-annual/seasonal sea-ice cover variability in the Arctic Ocean, as some effects can be very local, and other may occur at long distances, as can be observed at the ice-free Norwegian in situ stations, or outside the Arctic Ocean, with the global simulations.

In general, the simulations reproduce large scale effects, related to the energy budget and connections between basins. However, they generally do not represent well the local effects that may be more related to sea-ice thickness (and age) in shallow waters, which is not taken into account in the model today (only the sea-ice concentration has been considered for now).

Another important aspect that can have an impact on the regional simulations is the location of the open-boundary conditions (OBC). Indeed, such conditions are generally imposed from a static global tidal model (no temporal variability) and if the limits of the regional model domain are too close to regions with tidal temporal variability, the OBC may be too constraining or even inject errors from the global model into the regional model.

Finally, the lack of long time series of in situ data at high frequency (hourly) is a strong limitation to such studies in the Arctic Ocean. Satellite altimetry observations can provide complementary information, but they are representative of an average over a 10-year period, mainly thanks to the CryoSat-2 mission. The CRISTAL mission is expected to continue the time series and provide data for the next ten years. In such a context, models are extremely useful tools to fill gaps, but they need accurate observations to be validated, at least during the most recent period. Unfortunately, it seems the trend is not favourable in terms of in situ instrumentation in the Arctic Ocean, as many regions remain uncovered with recent observations, while research programs provided a lot of data in the 1970-1980s. With the continuous decay of the sea ice cover in the Arctic Ocean, and the intensification of navigation and maritime activities in the region, we may expect that more measurements will be available in the future, to ensure safety of operations in an environment that may become more accessible but remains a remote region with harsh environmental conditions.

References

Armitage, T. W. K., Bacon, S., Ridout, A. L., Thomas, S. F., Aksenov, Y., and Wingham, D. J.: Arctic sea surface height variability and change from satellite radar altimetry and GRACE, 2003–2014, J. Geophys. Res. Oceans, 121, 4303–4322, doi:10.1002/2015JC011579, 2016.

Bij de Vaat, I., Vasulkar, A. N., Slobbe, D. C., & Verlaan, M. (2021). The influence of Arctic landfast ice on seasonal modulation of the M2 tide. Journal of Geophysical Research: Oceans, 126, e2020JC016630. https://doi.org/10.1029/2020JC016630

Caldwell, P. C., M. A. Merrifield, P. R. Thompson (2015), Sea level measured by tide gauges from global oceans — the Joint Archive for Sea Level holdings (NCEI Accession 0019568), Version 5.5, NOAA National Centers for Environmental Information, Dataset, doi:10.7289/V5V40S7W.

Cancet, M., Andersen, O., Lyard, F., Cotton, D., and Benveniste, J.: Arctide2017, a high-resolution regional tidal model in the Arctic Ocean, Advances in Space Research, Vol. 62, No. 6, p. 1324-1343, https://doi.org/10.1016/j.asr.2018.01.007, 2018

Collins, A.K., Hannah, C.G., and Greenberg, D.: Validation of a High-Resolution Modelling System for Tides in the Canadian Arctic Archipelago. Can. Tech. Rep. Hydrogr. Ocean Sci. 273. vii+72pp, 2011

Dunphy, M., F. Dupont, C. G. Hannah, D. Greenberg. 2005. Validation of a Modelling System for Tides in the Canadian Arctic Archipelago. Can. Tech. Rep. Hydrogr. Ocean Sci. 243: vi + 70 pp.

Godin, G. (1980), Modification of the tide in the Canadian Arctic by an ice cover, Manuscript Rep. Ser., 56, Dep. of Fish. and Oceans, Ottawa, Ont., Canada

Godin, G. (1986), Modification by an Ice Cover of the Tide in James Bay and Hudson Bay, Arctic, Vol. 39, No. 1, March 1986, pp. 65-67

Haigh, I., Marcos, M., Talke, S.A., Woodworth, P., Hunter, J., Haugh, B., Arns, A., Bradshaw, E., Thompson, P. (2021). GESLA Version 3: A major update to the global higher-frequency sea-level dataset. 10.31223/X5MP65.

Hannah, C., Dupont, F., Collins, A., Dunphy, M., Greenberg, D., 2008. Revisions to a modelling system for tides in the Canadian Arctic Archipelago. Can. Tech. Rep. Hydrogr. Ocean Sci. 259. vi+62pp

Kagan, B. A. and E.V. Sofina (2010), Ice-induced seasonal variability of tidal constants in the Arctic Ocean, Continental Shelf Research, Vol. 30, pp. 643–647, http://dx.doi.org/10.1016/j.csr.2009.05.010

Kleptsova, O., and Pietrzak J.D. (2018), High resolution tidal model of Canadian Arctic Archipelago, Baffin and Hudson Bay, Ocean Modelling, Vol. 128, pages 15-47, https://doi.org/10.1016/j.ocemod.2018.06.001

Kowalik, Z., and Proshutinsky, A. Y. (1994), The Arctic Ocean Tides, in The Polar Oceans and Their Role in Shaping the Global Environment (eds O. M. Johannessen, R. D. Muench and J. E. Overland), American Geophysical Union, Washington, D. C. doi: 10.1029/GM085p0137

Kulikov, M., Medvedev, I. and Kondrin, A. (2018). Seasonal variability of tides in the Arctic Seas. Russian Journal of Earth Sciences. 18. 5003. 10.2205/2018ES000633.

Lyard, F (1997), The tides in the Arctic Ocean from a finite element model, Journal of Geophysical Research, Vol. 102, No. C7, pp. 15611-15638, http://dx.doi.org/10.1029/96JC02596

Lyard, F. H., Allain, D. J., Cancet, M., Carrère, L., and Picot, N.: FES2014 global ocean tide atlas: design and performance, Ocean Sci., 17, 615–649, https://doi.org/10.5194/os-17-615-2021, 2021.

Müller, M., Cherniawsky, J., Foreman, M. and Storch, J.-S. (2014). Seasonal variation of the M2 tide. Ocean Modelling. 10.1007/s10236-013-0679-0.

Morlighem, M. et al. (2017), BedMachine v3: Complete Bed Topography and Ocean Bathymetry Mapping of Greenland From Multibeam Echo Sounding Combined With Mass Conservation, GRL, Vol. 44, 21, pp 11051-11061, https://doi.org/10.1002/2017GL074954

Padman, L., and M. R. Siegfried (2018), Ocean tides affect ice loss from large polar ice sheets, Eos, 99, https://doi.org/10.1029/2018EO092835. Published on 20 February 2018.

Prandi, P., M. Ablain, A. Cazenave, and N. Picot (2012), A new estimation of mean sea level in the Arctic Ocean from satellite altimetry, Mar. Geod., 35, 61–81, doi:10.1080/01490419.2012.718222

Ray, R. (2016) On Measurements of the Tide at Churchill, Hudson Bay, Atmosphere-Ocean, 54:2, 108-116, DOI: 10.1080/07055900.2016.1139540

Rippeth, T. P., B. J. Likncoln, Y-D. Lenn, J. A. Mattias Green, A. Sundfjord and S. Bacon, 2015, Tide-mediated warming of arctic halocline by atlantic heat fluxes over rough topography, Nature Geoscience volume8, pages 191–194 (2015)

Schaffer, J., Timmermann, R., Arndt, J. E., Rosier, S. H. R., Anker, P. G. D., Callard, S. L., Davis, P. E. D., Dorschel, B., Grob, H., Hattermann, T., Hofstede, C. M., Kanzow, T., Kappelsberger, M., Lloyd, J. M., Ó Cofaigh, C., Roberts, D. H. (2019): An update to Greenland and Antarctic ice sheet topography, cavity geometry, and global bathymetry (RTopo-2.0.4). PANGAEA, https://doi.org/10.1594/PANGAEA.905295, Supplement to: Schaffer, J. et al. (2020): Bathymetry constrains ocean heat supply to Greenland's largest glacier tongue. Nature Geoscience, 13(3), 227-231, https://doi.org/10.1038/s41561-019-0529-x

St-Laurent, P., F. J. Saucier, and J.-F. Dumais (2008), On the modification of tides in a seasonally ice-covered sea, J. Geophys. Res., 113, C11014, http://dx.doi.org/10.1029/2007JC004614

remote sensing

MDPI

Review

Knowledge Gaps and Impact of Future Satellite Missions to Facilitate Monitoring of Changes in the Arctic Ocean

Sylvain Lucas [1,†], Johnny A. Johannessen [2,3], Mathilde Cancet [1], Lasse H. Pettersson [2], Igor Esau [2,4], Jonathan W. Rheinlænder [2], Fabrice Ardhuin [5], Bertrand Chapron [5], Anton Korosov [2], Fabrice Collard [6], Sylvain Herlédan [6], Einar Olason [2], Ramiro Ferrari [1], Ergane Fouchet [1,*] and Craig Donlon [7]

1 NOVELTIS, 31670 Labege, France; ramiro.ferrari@noveltis.fr (R.F.)
2 Nansen Environmental and Remote Sensing Center (NERSC), 5007 Bergen, Norway
3 Geophysical Institute, University of Bergen, 5020 Bergen, Norway
4 Department of Physics and Technology, UiT—The Arctic University of Norway, 9019 Tromsø, Norway
5 Ifremer, 17390 La Tremblade, France; fabrice.ardhuin@ifremer.fr (F.A.)
6 OceanDataLab, 29280 Locmaria-Plouzane, France; fabrice.collard@oceandatalab.com (F.C.); sylvain.herledan@oceandatalab.com (S.H.)
7 ESA/ESTEC, 2201 Noordwijk, The Netherlands
* Correspondence: ergane.fouchet@noveltis.fr
† Current address: French Space Agency (CNES), 31400 Toulouse, France.

Abstract: Polar-orbiting satellite observations are of fundamental importance to explore the main scientific challenges in the Arctic Ocean, as they provide information on bio-geo-physical variables with a denser spatial and temporal coverage than in-situ instruments in such a harsh and inaccessible environment. However, they are limited by the lack of coverage near the North Pole (Polar gap), the polar night, and frequent cloud cover or haze over the ocean and sea ice, which prevent the use of optical satellite instruments, as well as by the limited availability of external validation data. The satellite sensors' coverage and repeat cycles may also have limitations in properly identifying and resolving the dominant spatial and temporal scales of atmospheric, ocean, cryosphere and land variability and their interactive processes and feedback mechanisms. In this paper, we provide a state of the art of contribution of satellite observations to the understanding of the polar environment and climate scientific challenges tackled within the Arktalas Hoavva project funded by the European Space Agency. We identify the current limitations to the wider use of polar orbiting remote sensing data, as well as the observational gaps of the existing satellite missions. A comprehensive overview of all satellite missions and applications is given provided with a primary focus on the European satellites. Finally, we assess the expected capability of the approved future satellite missions to answer today's scientific challenges in the Arctic Ocean.

Keywords: satellite observation; arctic ocean; bio-geo-physical variables; future missions

Citation: Lucas, S.; Johannessen, J.A.; Cancet, M.; Pettersson, L.H.; Esau, I.; Rheinlænder, J.W.; Ardhuin, F.; Chapron, B.; Korosov, A.; Collard, F.; et al. Knowledge Gaps and Impact of Future Satellite Missions to Facilitate Monitoring of Changes in the Arctic Ocean. *Remote Sens.* **2023**, *15*, 2852. https://doi.org/10.3390/rs15112852

Academic Editor: Gareth Rees

Received: 12 April 2023
Revised: 22 May 2023
Accepted: 24 May 2023
Published: 30 May 2023

1. Introduction

Since the 1990s, the Arctic summer sea ice extent has declined by about 50% and the sea ice thickness by about 40% (e.g., [1–3]). A new vulnerable sea ice state has emerged in the Arctic Ocean with significant reductions of the thicker multi-year sea ice, predominant presence of the thinner first-year ice, longer periods of open water, enhanced surface melt rates and presence of melt ponds and increased frequency of lead fractions within the sea ice cover. Minimum sea ice extent is typically observed in mid-September and absolute minimum extent records, during the more than 40-year era of satellite observations, were reported in 2007, 2012 and 2020, with all the lowest minimum extents observed in the last 15 years (e.g., [4–6]). The extents in 2021 and 2022 were the 12th and 13th lowest extents observed during the satellite observational era, reflecting also the natural interannual variability of the sea ice. The fact that the Arctic warming has been reported to be 2–3 times

(most recent studies even indicating 4–5 times) as large as the temperature increase in any other area of the globe is known as the Arctic Amplification (e.g., [7–9]). In addition to Arctic Amplification, complex interactive processes and mutual feedback are contributing to this dramatic change in the sea ice extent, thickness and hence the ice volume [10], altering the human accessibility and activities in the Arctic with societal and economic implications (e.g., [11]). However, we lack a quantitative understanding of the interactive processes and feedback across a wide range of spatial and temporal scales. Hence, we are confronted with challenges in using computer models to quantify, characterize, and simulate the leading drivers of the regional Arctic climate change, and to predict their local and global impacts.

Satellite observations are and will be key elements to understanding such a remote and harsh environment where in-situ observations are limited in space and frequency. In fact, most of our knowledge today about the surface properties, both for the Arctic and Antarctic, is derived from satellite data over the last 40 years, supplemented by sparse in-situ measurements derived largely from scientific expeditions. The continuity of satellite observations over several decades, with no or limited gaps between the satellite missions, is consequently key for the study of long-term changes. However, although the Earth Observation polar-orbiting satellite constellation is particularly dense today, gaps remain in the satellite observations, in terms of observed physical variables, spatial and temporal coverage, and resolution. In turn, the ability to understand the processes and characterize the changes in the Arctic Ocean is deficient. This is recognized in the approved future satellite missions that will carry new instruments dedicated to Polar regions, bringing a new observation capacity and new scientific insight into the processes in the Arctic Ocean.

In this paper, we present an overview of the past and present satellite observation capabilities to address major scientific challenges in the Arctic Ocean, highlighting the observational gaps that must be filled by future approved satellite missions. However, the paper is primarily addressing the ESA and Eumetsat (European) satellite missions complemented with selected satellite missions from other space agencies including NASA (USA), CSA (Canada), NSOAS (China), JAXA (Japan) and ISRO (India). This choice is made to reduce the complexity and improve the readability of the figure presentations of the results, without excluding the major application areas. The availability of relevant and similar type sensor data from missions planned by the other countries will complement and expand the availability of satellite missions to be available for future studies of the Arctic Ocean. The study is undertaken within the framework of the Arktalas Hoavva (Arctic Ocean in the Sami language) project funded by the European Space Agency (ESA) with the aim to advance the use of satellite measurements in synergy with in-situ data and computer models to characterize and quantify the processes driving changes in the Arctic sea ice cover and in the Arctic Ocean. In so doing, knowledge gaps must be removed to advance our quantitative understanding of sea ice, ocean and atmosphere interactive processes and mutual feedback at various temporal and spatial scales. In the Arktalas Hoavva project, four major interlinked Arctic Scientific Challenges (ASC) have been investigated, addressing the need to:

- Characterize the Arctic Amplification and its impact (ASC-1)
- Characterize the impact of more persistent and larger areas of open water on sea ice dynamics (ASC-2)
- Characterize and predict the impact of extreme event storms on sea ice formation patterns and structures (ASC-3)
- Characterize and predict the Arctic Ocean spin-up (ASC-4)

These ASCs are particularly presented and discussed in seven scientific publications emerging from the Arktalas Hoavva project [12–18], to be further outlined in Section 2. In this paper, we address the state-of-art satellite observations of the Arctic Ocean in the context of the Arktalas major scientific challenges in Section 2. In Section 3, we focus on the assessment of the limitations and gaps of the current and past satellite measurements

in view of the four challenges. The capabilities of future missions are then addressed in Section 4, followed by a summary and conclusion in Section 5.

2. Use of Satellite Observations to Address the Arktalas Hoavva Scientific Challenges in the Arctic Ocean

Satellite measurements in the Arctic are of fundamental importance, although they are influenced by a number of technical, observational, and environmental challenges. Limited coverage from polar-orbiting satellites across the true North Pole of the central Arctic Ocean invokes the Polar gaps without specific satellite payload design considerations (e.g., very wide swath and specific choice of orbit inclination). On the other hand, the Earth's curvature in the polar regions and the convergence of the ground tracks of polar-orbiting satellites contribute to improved coverage and repeat cycles. Moreover, as the polar night and harsh meteorological conditions, including clouds and haze, limit the use of optical satellite instruments, the main demand relies on all-weather day and night microwave radiometry, laser altimetry and active microwave (Synthetic Aperture Radar (SAR), altimeter, scatterometer) observations. However, radiative transfer models are incomplete, radar backscatter from mixed pixels is often difficult to quantify and partition into individual geophysical signal sources, spatial resolution of measurements is largely insufficient, frequency selections have been limited, and empirical-based relationships are predominantly driving the retrieval algorithms. In addition, proper satellite-based identification and resolution of dominant spatial and temporal scales in the polar regions are sometimes deficient.

Several decades of satellite observations from space agencies worldwide have revealed dramatic changes in the Arctic, although they are inadequate for systematic multi-disciplinary monitoring and process-based studies that integrate components of the regional environment and climate [19,20]. Further efforts to improve synergies within a comprehensive Arctic Observing Network are, therefore, recommended [21].

Based on this the Arktalas Hoavva study project has adopted a stepwise multi-modal analyses framework approach to address the four major Arctic Scientific Challenges listed above, benefitting from multiscale resolution satellite observations together with complementary in-situ data, computer model simulations, data assimilation, analyses, and integrated visualization tools.

In the high-latitude seas and the Arctic Ocean, global warming and Arctic Amplification are considered to occur across a range of environmental state variables with complex interactions and feedback mechanisms at regional to global scales. Central among these are changes in the radiation balance, changes in ocean-sea ice-atmosphere momentum, heat and gas exchanges, reduction in the sea ice extent and thickness, and changes in the bio-optical properties in the upper ocean. In turn, the Arctic Polar Regions experience increased air temperature, delayed onset of sea ice freezing, early onset of sea ice melting, increasing area of melt ponds, polynyas and surface meltwater, increased lead fraction and sea ice drift, reduction in near-shore fast ice area, changes in snow cover, snow water equivalent (SWE), changes in albedo, a much larger wind fetch and enhanced wave-sea ice interaction leading to sea ice break-up and delays in freeze-up, as well as shifts in and expansions of the Marginal Ice Zone (MIZ). Moreover, the atmospheric boundary layer adjustment to these changes is anticipated to alter the weather patterns and influence the Arctic vortex, with atmospheric teleconnection to lower latitudes.

Esau et al. [17] have reviewed and assessed how the remote sensing data, and particularly climate products, have captured signals of the Arctic Amplification such as the rapid and massive transition from multiyear to seasonal sea ice, and from tundra to tall shrubs and forest.

Cancet et al. [18] have investigated the impact of sea ice change on ocean tides in the Arctic Ocean, considering model simulations and observations from satellite altimetry and tide gauges. Although ocean tides are one of the major contributors to the energy dissipation in the Arctic Ocean, their characteristics are poorly known [22]. In particular,

the interactions between tides, the sea ice, grounded-ice and fast-ice cover are often simply ignored in tidal modeling simulations or considered through relatively simple combinations with the bottom friction.

Characterizing the impact of more persistent and larger areas of open water on the sea ice dynamics is also coupled with Arctic Amplification issues. However, the direct observation of mesoscale eddies has been impeded by the presence of compact sea ice concentration in the past. Cassianides et al. [13] have developed a new method to detect ocean eddies based on the response in the sea ice drift and vorticity fields retrieved from SAR images, which is particularly promising.

Thanks to the innovative use of data from ICESat-2, Sentinel-2, Sentinel-1, and Sentinel-3 Fully-Focused SAR altimetry and the Chinese-French Oceanographic Satellite Surface Waves Investigation and Monitoring instrument (CFOSAT-SWIM), wave patterns have been clearly detected in the sea ice and ocean of the MIZ by Collard et al. [14]. This clearly advocates for a synergetic approach, building co-located datasets to achieve a better quantitative understanding of the propagation and interactions of waves and sea ice.

As thinning sea ice and growing areas of open water within the Arctic Ocean will also be more effectively exposed to extreme events, it is important to better understand, characterize and predict the impact of extreme storms on sea ice formation and break-up. A central question is also whether the changes in the sea ice extent and thickness will favor increasing frequency and strengthening of extreme events. Rheinlaender et al. [15] investigated the driving mechanisms behind a large sea ice breakup event in the Beaufort Sea in response to a series of storms in February–March 2013. Lead detection products based on Moderate Resolution Imaging Spectroradiometer (MODIS) thermal infrared imagery [23] were used to evaluate the simulations results and demonstrated that the model could successfully reproduce the timing, location, and propagation of sea ice leads associated with the storm-induced breakup. The choice of horizontal resolution for the atmospheric forcing and the sea ice rheology scheme in the model was also of prime importance to be able to reproduce the sea ice dynamics in the model in the case of such extreme events.

Finally, the impact of increased temperatures in the Arctic—manifested through the Arctic Amplification—on the basin scale atmospheric and ocean circulation was explored by Regan et al. [12] with a focus on the Beaufort gyre and its evolution over the period 1990–2014. Using altimetry-based Dynamic Ocean Topography datasets [24,25] together with a high-resolution eddy-resolving model, they concluded that the accumulation of freshwater due to changes in the wind forcing and sea ice conditions led to the spin-up of the Beaufort Gyre. Clearly, the changes taking place in the Arctic today may have profound impacts on the general circulation of the Arctic and its interaction with other ocean basins and the global thermohaline circulation [26].

3. Today's Challenges, Limitations and Key Issues with Satellite Observations

The studies of the different Arctic Scientific Challenges reported in the previous section strongly advocate the importance of the multi-sensor and -disciplinary satellite-based observing capabilities. Tables 1 and 2 synthesize the types of satellite sensors that can be used to retrieve the ocean and sea ice geophysical variables, respectively. Figure 1 displays the past, present and approved future satellite missions equipped with suitable payload sensors allowing the retrieval of these ocean and sea ice variables, considering the satellite mission timeline, spatial coverage and instrument measuring modes. We focus on European satellite missions, although some major international missions are also included. All in all, a large number of relevant satellite missions from all major international space agencies will be and will become available to monitor environmental and climate change in the Arctic Ocean. Efficient and timely exploitation of the growing and vast amounts of data is, therefore, urgently needed.

Table 1. Overview of ocean geophysical variables observed by or derived from satellite sensor types. The (X) indicate strong limitations or exploratory retrieval methods. Also, note that the spectrometer and infrared radiometer instruments are sensitive to cloud cover.

Geophysical Variable \ Sensor Type	Spectrometer	Infrared Radiometer	Microwave Radiometer	Scatterometer	Imaging SAR	Radar Altimeter	Lidar Altimeter	Gravimeter
Ocean color	X							
Near Surface Scalar Wind			X	X	X	X		
Near Surface Vector Wind			(X)	X				
Radial Surface Velocity					X			
Sea Surface Height						X	X	
Sea Level						X		
Mass changes								X
Sea Surface Salinity			X					
Sea Surface Temperature		X	X					
Significant Wave Height						X		
Ocean Wave Spectra	(X) Partly in sunglitter areas				X (wave mode)	CFOSAT-SWIM		

Table 2. Overview of sea ice geophysical variables observed by or derived from satellite sensor types. The (X) indicate strong limitations or exploratory retrieval methods. Also, note that the spectrometer and infrared radiometer instruments are sensitive to cloud cover.

Geophysical Variable \ Sensor Type	Spectrometer	Infrared Radiometer	Microwave Radiometer	Scatterometer	Imaging SAR	Radar Altimeter	Lidar Altimeter
Sea Ice Cover and Extent	(X)	(X)	X	(X)	(X)		
Sea Ice Type	X		X	(X)	(X)		
Sea Ice Albedo		X					
Sea Ice Surface Temperature		X	X				
Sea Ice Freeboard						X	X
Sea Ice Thickness			Thinner than 50 cm			Thicker than 50 cm	Thicker than 50 cm
Sea Ice Drift	(X)		X	X	X		
Snow Depth on Sea Ice			First year ice			X	X
Sea Ice Leads	X	X			X	X	X
Melt Ponds on Sea Ice	X	(X)			X		(X)
Waves in Sea Ice	(X)				X	(X)	

The environmental variables are predominantly retrieved from imaging sensors with varying swath widths, except for the altimetry nadir profiling sensing method. The largest observation gaps in the Polar regions are related to radar and laser altimetry. However, thanks to the launch of CryoSat-2 in its near Polar orbit in 2010, the altimeter-based observation gap has been significantly reduced from south of 82°N to 89°N. Moreover, observations of waves and sea ice drift from SAR imagers are often subject to acquisition priorities whereby a larger swath is favored for sea ice mapping and drift while imagette/vignette modes are usually favored for retrievals of ocean waves. Nevertheless, a large "Hole over the geographical Poles" remains for the majority of satellite sensors, due to the orbit inclination.

The Sankey diagrams displayed in Figures 2 and 3, for a selected number of missions, link the past, present and future approved satellite missions with the observed ocean and sea-ice-related parameters and quantities, respectively. The figures provide another synthetic view of the remote sensing observational continuity and complementarity, although not all relevant missions are included in order to maintain the readability of the diagrams.

Remote Sens. 2023, 15, x FOR PEER REVIEW 6 of 19

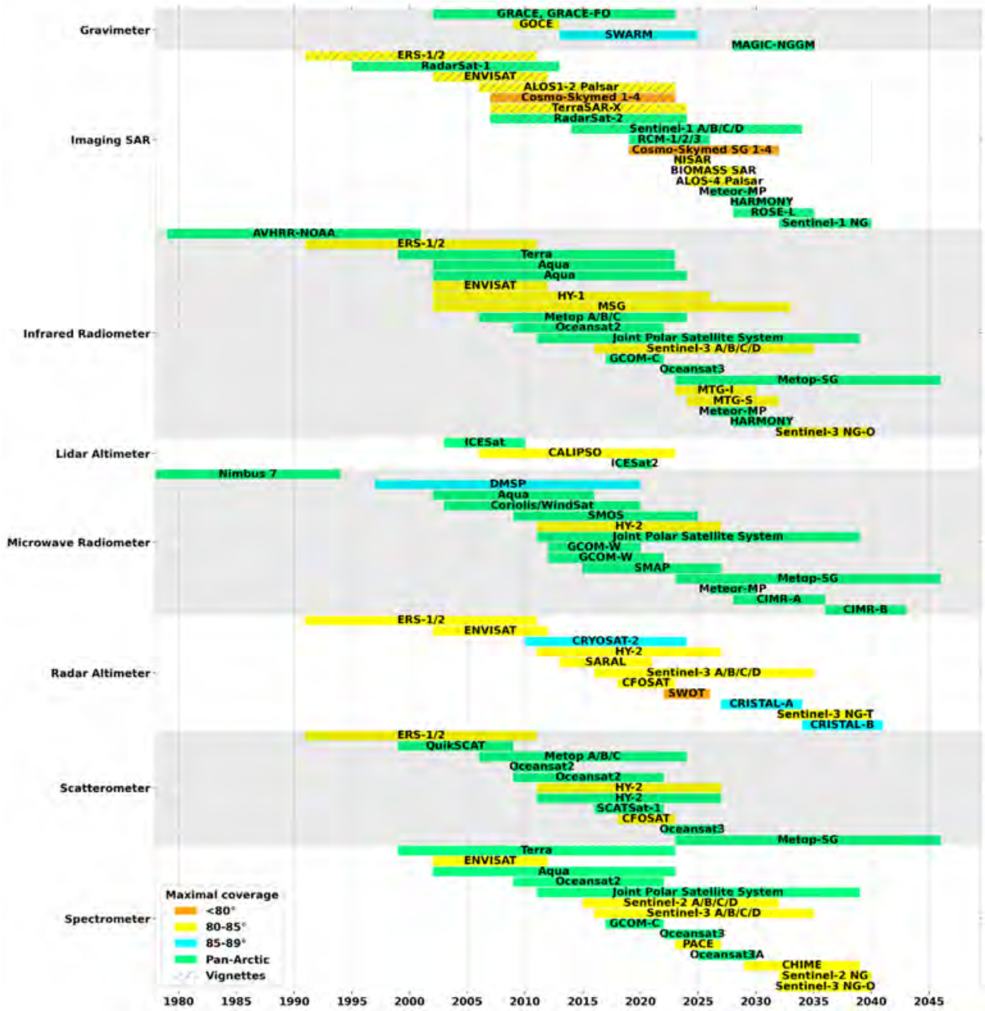

Figure 1. Timelines of a selection of the polar orbiting satellite-based observational capabilities of ocean and sea ice variables, per sensor type. Both the spatial and temporal extent of past, present and approved future missions are presented, considering the mission duration and its coverage (marked with color-bars) in the Arctic as limited by the satellite orbits and sensor configuration. The selection is tailored towards the European satellite missions but are applicable to many similar sensors and missions launched by other space agencies.

Despite their fundamental importance to examine the main Arctic Ocean scientific challenges, satellite observations still have limitations, justifying the need for complementary information sources. These limitations are further addressed below.

First, the compilation of satellite observations to build homogenous, cross-calibrated and cross-validated, long and continuous data records of climate quality across multiple satellite missions, is difficult. Sensors and platforms degrade with time, sometimes stop functioning, and need to be substituted with new ones, some with different technical specifications. The inter-calibration of datasets is very challenging, as Esau et al. [17] show in an extensive literature discussion. As environmental changes in the Arctic are known to be relatively fast (e.g., [8]), and the observational records are rather short (in the climatic sense), even a single year with lower-quality data can cause significant deviations and uncertainty for long-term climate records. Literature is, therefore, very inconclusive as to what degree satellite sensor calibration and inter-calibration properly apply to climate-quality long-term data records in the Polar regions.

The environmental variables are predominantly retrieved from imaging sensors with varying swath widths, except for the altimetry nadir profiling sensing method. The largest observation gaps in the Polar regions are related to radar and laser altimetry. However, thanks to the launch of CryoSat-2 in its near Polar orbit in 2010, the altimeter-based observation gap has been significantly reduced from south of 82° N to 89° N. Moreover, observations of waves and sea ice drift from SAR imagers are often subject to acquisition priorities whereby a larger swath is favored for sea ice mapping and drift while, imagette/vignette mode, are usually favored for retrievals of ocean waves. Nevertheless, a large "Hole over the geographical Pole" of data sets remains, due to the orbit inclination.

The Sankey diagrams displayed in Figures 2 and 3, for a selected number of missions, link the past, present and future approved satellite missions with the observed ocean and sea-ice related parameters and quantities, respectively. The figures provide another synthetic view of the remote sensing observational continuity and complementarity, although not all relevant missions are included in order to maintain the readability of the diagrams.

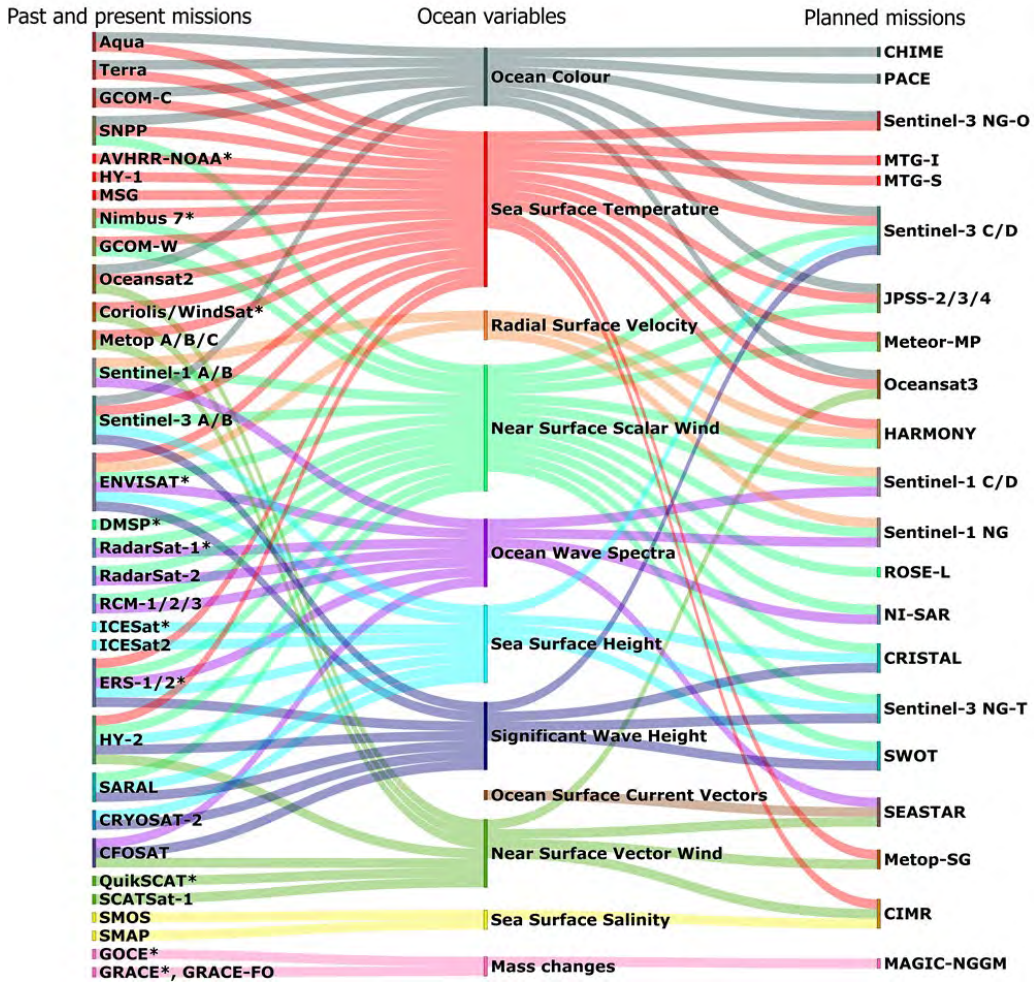

Figure 2. Sankey diagram linking past, present and future approved satellite missions and their ocean measurement capabilities. (**left**) Past (identified with *) and present satellite missions; (**center**) retrieved ocean variables; (**right**) future approved missions.

The lack of Fiducial Reference Measurement (FRM) [27] in-situ data to accurately calibrate and validate the satellite observations in the Arctic Ocean is also a major limitation in the generation and validation of homogeneous datasets and for the evaluation of new processing strategies. Several initiatives have been launched by ESA to define FRM strategies for satellite observations, but these are currently limited to a few types of observations (FRM4SOC for Ocean Colour, FRM4STS for Surface Temperature, FRM4Alt and St3TART for radar altimetry topography of the ocean, inland waters, sea ice and land ice). Each study is designed to develop and apply rigorous metrology approaches to ensure that satellite data are traceable to S.I units with a full uncertainty budget. More generally, comparing satellite observations with in-situ data in the Arctic Ocean, for instance, to better understand local dynamical processes and interactions, is highly challenging as the limited amount of in-situ data is usually available in given locations for practical logistic reasons. As such, the dynamical marginal ice zones are not properly sampled with in-situ data. In other cases, in-situ observations may exist but are not publicly available, or only distributed at low temporal resolutions (typically monthly) that are not suited to study high-frequency processes and interactions. The heterogeneity, in time and space, of ocean and ice processes also imposes challenges in terms of sampling strategies for satellite data validation and the use of multiple data sets in synergy, since the acquisition times and locations introduce uncertainties due to natural geophysical variability.

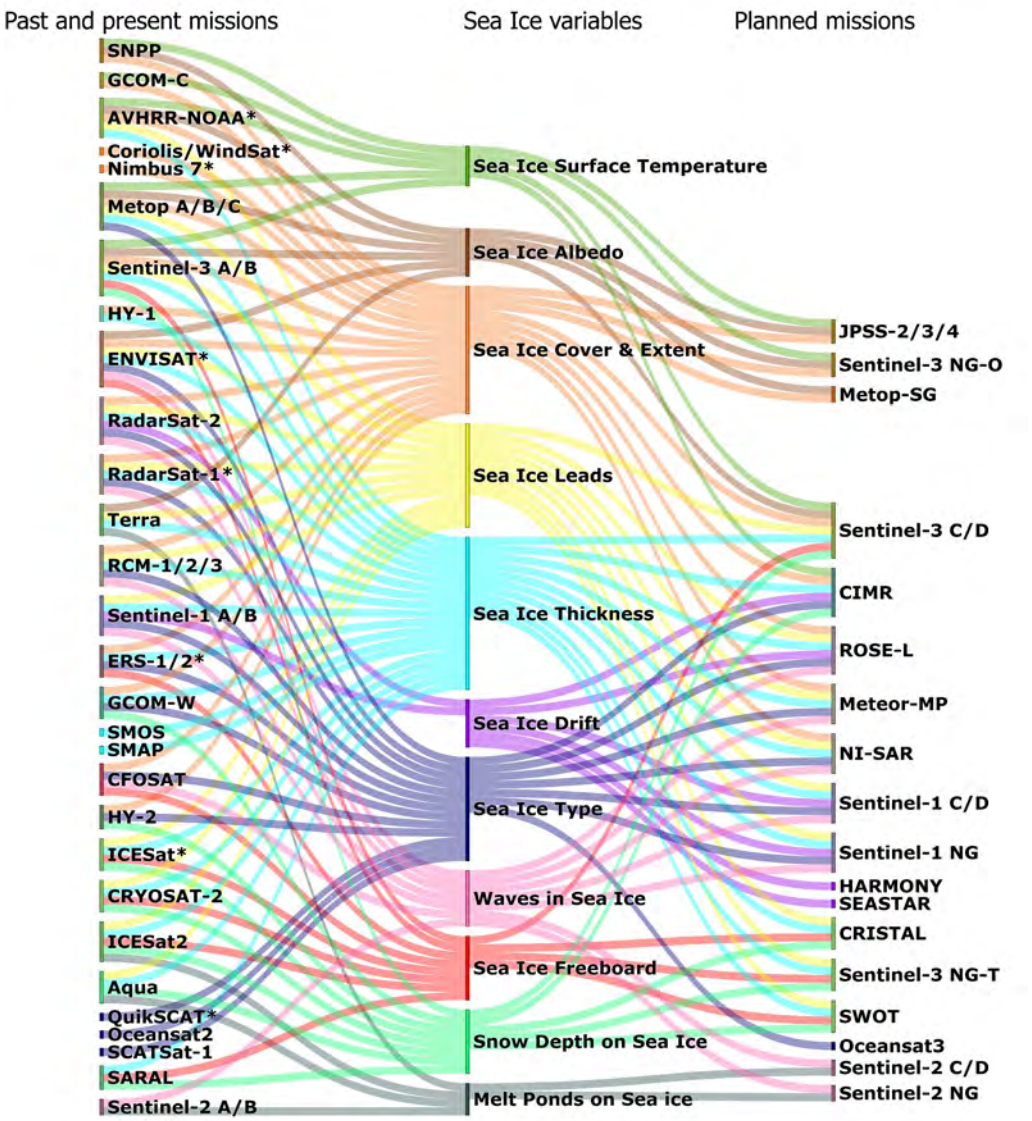

Figure 3. Sankey diagram linking past, present and future approved satellite missions and their sea ice measurement capabilities. (**left**) Past (identified with *) and present satellite missions; (**center**) retrieved sea ice variables; (**right**) future approved missions.

Despite their fundamental importance to examine the main Arctic Ocean scientific challenges, satellite observations still have limitations, justifying the need for complementary information sources. These limitations are further addressed below.

First, the compilation of satellite observations to build homogenous, cross-calibrated and cross-validated, long and continuous data records of climate quality, across multiple satellite missions, is difficult. Sensors and platforms degrade with time, sometimes stop functioning, and need to be substituted with new ones, some with different technical specifications. The reconciliation of data sets is very challenging, as Esau et al. [17] show in an extensive literature discussion. As environmental changes in the Arctic are known to be relatively fast (e.g., [8]), and the observational records are rather short (in the climatic sense), even a single year with lower-quality data can cause significant deviations and uncertainty for long-term climate records. Literature is, therefore, very inconclusive as to what degree satellite sensor calibration and inter-calibration properly apply to climate-quality long-term data records in the Polar regions.

The lack of Fiducial Reference Measurement (FRM) [27] in-situ data to accurately calibrate and validate the satellite observations in the Arctic Ocean is also a major

Second, many long-term optical (visible to thermal infrared) satellite data products are fragmented due to cloud cover, haze, and daylight variability. Therefore, a strong bias towards observations in clear sky conditions is observed, with both seasonal and geographical variations, as winter darkness is an additional challenge in the Polar regions. Interpolation and gap closure methods are thus questionable as they rely on an unjustified assumption that the statistics under a clear sky and overcast are the same. This is not the case in the Arctic boundary layer, but detailed studies of this problem from a climate perspective are lacking. In turn, climate datasets such as the ESA Climate Change Initiative (CCI) [28] may still encounter limitations such as scarcity and low resolutions, in addition to a lack of sufficiently long time series of consistent and high-quality measurements.

In addition, other types of limitations are more specific to individual missions, instrument type, cross-calibration between similar sensors at different missions, and retrieved variables. The following paragraphs summarize some of these issues.

The potential of using satellite sun glitter imagery such as the Sentinel-2 Multi-Spectral Instrument (MSI) for ocean wave detection has been successfully demonstrated [29], and even in the presence of sea ice [14]. Such an approach could be used to complement the Sentinel-1 measurements, with the advantage of giving access to 2-D wave spectra.

However, strong temperature and humidity gradients in the atmospheric boundary layer make the Arctic a very cloudy and hazy place, which severely limits the availability of exploitable Sentinel-2 optical images. Moreover, wave pattern detection from imaging spectrometers such as Sentinel-2 requires favorable Sun illumination angle, and alignment between the instrument and the surface wave field. The seasonal sun cycle at polar latitudes, with winter darkness and 24-h summer sunlight, limits the data availability during most of the year.

Regarding satellite radar altimetry, the current processing of conventional Low-Resolution Mode (LRM) altimeters such as ERS-1/2, ENVISAT Ku-band and SARAL Ka-band radars was developed for open water surfaces. In the presence of sea ice, these algorithms break down, meaning that the accuracy of the sea surface height (SSH) observations and the sea ice freeboard estimation can be strongly impacted in large areas of the Arctic Ocean and adjacent seas [24,25]. The Ku-band SAR altimeters onboard the CryoSat-2 and Sentinel-3 missions have proven to be extremely valuable in sea ice-covered regions, thanks to higher along-track resolution (typical processing delivering an along-track resolution of about 300 m), which enables to better detect sea ice leads from specular reflection signals in the radar echo return. However, for open ocean applications, the across-track resolution of the SAR altimeter is variable from ~2 to 16 km depending on the sea state. Additional complications emerge when using SAR altimetry at high along-track resolution due to the Doppler signals induced by moving ocean swell waves, which impact altimeter geophysical retrievals if not handled properly. Moreover, most combined products are still experimental and incomplete, which makes them difficult to use for climate change studies [30]. Still, one can expect some progress thanks to the Sentinel-6-MF altimetry mission, launched in 2020 [31] and simultaneously operated in SAR and LRM modes. Despite its orbit inclination being limited to 66°N, it reaches seasonally sea ice-covered regions such as the Hudson Bay. Further analyses and comparisons between the simultaneous measurements in both modes may help improve the LRM processing method in the presence of sea ice, opening the possibility to reprocess 30 years of LRM altimetry data measured by ERS-1/2, ENVISAT, SARAL/AltiKa, and CryoSat-2 in the Arctic region.

In addition to the sea ice contamination in conventional radar altimetry SSH measurements, Cancet et al. [18] highlight the fact that most of the past and present altimetry missions that reach high latitudes are sun-synchronous. This strongly limits their capability to observe part of the ocean tidal cycles. However, thanks to the higher density of ground tracks in high latitude regions, it is possible to bin the altimetry measurements to reconstruct time series with higher time sampling and consequently reduce the tidal aliasing effects. A mission such as CryoSat-2 brings remarkable measurements to improve the tidal estimates in the Arctic Ocean, thanks both to its SAR and SAR-interferometric modes that enable to obtain more accurate SSH observations in sea ice covered coastal regions, and to the fact that it is non-sun-synchronous, which gives access to major tidal components that are aliased to infinite periods in sun-synchronous observations. As such, a long observational gap between the CryoSat-2 and CRISTAL missions would have a serious impact on the quality of the tidal retrievals. This would limit the uncertainty estimates of the tidal models in the Arctic Ocean, which are, among other applications, used to remove the ocean tide signals from the altimeter SSH measurements to build the climate products.

The penetration depth of the altimeter pulse transmitted from a radar (e.g., ENVISAT, CryoSat-2, Sentinel-3 and Sentinel-6 in Ku-band, SARAL/AltiKa in Ka-band) or a laser (ICESat-2) signal in the snow layer that covers the sea ice is also a source of uncertainty when estimating the sea ice freeboard and hence the sea ice thickness. Meanwhile, this effect can be exploited as an indirect means to estimate the snow-cover depth on sea ice, as the Ku band penetrates into the snow and thus measures the range to the bottom of the snow layer, while laser observations measure the range to the top of the snow layer ([32,33]). Ka-band radar pulses are considered to reflect at a different scattering horizon in the snow ice layers although this appears to be somewhat dependent on specific snow properties and ice layering. Such combination requires that missions with the necessary

instrumental characteristics fly simultaneously and that collocated measurements can be used (lidar altimetry being impacted by cloud cover, unlike radar altimetry), for instance taking advantage of experiments such as Cryo2Ice, which started in 2020 and aimed at maximizing the number of coinciding orbits for the CryoSat-2 and ICESat-2 missions thanks to satellite maneuvers. In practice, such an approach is currently limited to the concurrent measurements of SARAL/AltiKa (only radar altimeter in Ka band, launched in 2013), or ICESat-2 (launched in 2018), with Ku-band altimeters, i.e., mainly CryoSat-2 and Sentinel-3 in the area.

The uncertainty of the sea ice thickness estimated from radar altimeter sea ice freeboard observations strongly increases in the case of thin ice (less than 0.5 m). This is mainly due to the remaining errors and associated uncertainty in the retracking algorithms in sea ice-covered regions and to the uncertainties linked with the penetration into the snow layer on top of the sea ice. Radar altimeter estimates of sea ice thickness are also strongly impacted by the presence of meltwater ponds on the ice in summer, which makes it challenging to differentiate from leads, and high-quality products are generally only available in winter. Laser altimetry can also be used but is, as already emphasized, affected by the presence of clouds. Thin sea ice thickness can be retrieved more accurately thanks to microwave radiometers such as MIRAS onboard SMOS, or the conically scanning SMAP mission, both operating at L-band. However, brightness temperatures must provide data at high radiometric fidelity. Additional observations from spectroradiometers such as Sentinel-3 OLCI (visible spectrum) and SLSTR (shortwave and thermal infrared) or MODIS onboard the NASA Aqua mission and AVHRR onboard past NOAA satellite missions, are also very useful. Merged sea ice thickness products can then be generated, such as the weekly CS2SMOS products [34] that are delivered at 25 km resolution. SAR imagery from ENVISAT, RadarSat-2 or Sentinel-1 can also be used to infer sea ice thickness, considering the ratio of backscattering at different polarizations (e.g., [35,36]); however, this approach still has strong limitations as it is based on strong empirical assumptions on the relationship between sea ice thickness and the polarimetric response, and only works for some sea ice types. New approaches based on machine learning trained with in-situ sea ice thickness data and applied to Sentinel-1 SAR data show promising results [37]. Optical and SAR images have also been recently used to train a neural network algorithm and produce an unprecedented and promising record of 10 years of Summer sea ice thickness based on CryoSat-2 altimetry, but still with some underestimates in regions of thick multi-year ice [38].

Vertical in-water profiles of temperature, salinity, oxygen, etc., obtained from gliders, ARGO floats, fixed moorings and research shipborne expeditions provide a vital set of measurements that are necessary to complement satellite measurements in the open ocean. In ice-covered waters, icebreakers of polar-class vessels are required. With the notable exception of ocean color radiometry, satellite observations measure signals expressed at the very surface of the water column. Such signals are surface expressions of all the processes occurring at the same time in the water column and are typically related intimately to the processes occurring beneath the surface within the upper ocean. While satellite data sets are the backbone of our observing system in many areas (and particularly in the polar regions), only with a sufficient density of surface and subsurface oceanographic and sea ice measurements can we target to gain a full picture of their dynamics.

4. Future Missions, and Their Expected Capability to Answer Today's Challenges

As emphasized in Section 3, the following list of environmental variables is still not retrieved with sufficient temporal and spatial coverage, spatial and temporal resolution, and accuracy to further understand the changes in the Arctic Ocean:

- Sea ice thickness
- Sea ice freeboard height
- Lead fraction
- Snow depth on sea ice

- Melt pond extent and coverage
- Waves in sea ice
- Sea ice drift
- Total surface current
- Sea surface height
- Sea surface salinity
- Mass changes
- Near-surface wind over the sea ice field

In addition, there is a number of interactive processes and mutual feedbacks that challenge studies of the high latitude seas and the Arctic Ocean, including:

a. Boundary layer atmosphere/sea ice/upper ocean interactions
b. Momentum, gas and heat exchange between the atmosphere, sea ice and ocean
c. Mesoscale ocean dynamics
d. Marginal ice zone processes
e. Freshwater and biogeochemical inputs from rivers and land (e.g., permafrost melt)

The approved future satellite missions, both European and other third-party missions, will provide extended observational capacity to address these challenges and advance the understanding of the complexity of the Arctic Ocean changes and multi-disciplinary interactions. This is further detailed hereinafter with references to the selected missions presented in Figures 2 and 3.

The continuity of currently operational radar and infrared radiometer missions is already ensured, allowing the creation of long-term overlapping of high qualitative datasets. Sentinel-1 C and D will sustain C-band SAR measurements up to 2034, while Sentinel-3 C and D SRAL, SLSTR and OLCI instruments are planned to fly up to 2035, providing valuable ice and ocean measurements up to 82°N and thus covering the regions with most of the human activities in the Arctic Ocean. Concept studies are also ongoing to prepare the future Sentinel Next Generation missions (beyond 2032), in particular, the Sentinel-3 NG Topography mission. Several approaches (i/a constellation of a dozen of nadir radar altimeters, ii/a constellation of two swath radar altimeters, or iii/a constellation of one swath altimeter and several nadir altimeters) have been evaluated, that should, whatever the selected configuration, provide unprecedented coverage of the global ocean for a topography mission. The selected configuration is currently (in December 2022) the constellation of two swath radar altimeters, but this will strongly depend on the outcomes of the SWOT mission and further studies are ongoing.

The Surface Water and Ocean Topography (SWOT) mission developed by NASA and CNES [39] was launched in December 2022, with a lifetime until at least 2026. It has two main instruments. The conventional low-resolution mode (LRM) POSEIDON-3 nadir pointing radar altimeter operating in the Ku band will measure the ocean topography, significant wave height, and wind speed at 25 km resolution, with a repeat orbit of 22 days. While offering no SAR capability, the heritage of this class of instruments is very long and stable. The completely new Ka-band radar interferometer instrument (KARIN) will be the first swath instrument to provide measurements of inland water river and lake elevations and sea surface height over the ocean supporting applications such as ocean circulation and internal tides. KARIN operates as two off-nadir swaths of 50 km width on either side of the nadir altimeter. Additional information may also be accessible from SWOT such as sea ice elevation, sea ice thickness and ice sheet topography following further research and development using in-orbit SWOT data. However, the mission will have limited Arctic coverage due to its 78° orbit inclination, excluding most of the central Arctic Ocean.

EUMETSAT Metop—Second Generation (Metop-SG) polar-orbiting satellites [40] will ensure continued meteorological observations from 2023 to 2043. The multi-spectral imager METImage will measure sea surface temperature and sea ice cover and temperature with a ground sampling of 500 m. The SCAT scatterometer will derive sea ice coverage and drift at a resolution of 12–24 km while the Microwave Sounder MWS will deliver horizontal wind speed over sea ice products with a footprint up to 40 km. The Microwave Imager

(MWI) provides 18 channels from 18–183 GHz and Ice Cloud Imager (ICI) offers 11 channels at frequencies from 183 to 664 GHz. Both instruments use a conical scanning approach (offering a wide swath) and will provide information on some relevant surface parameters (snow, sea ice) at a relatively coarse resolution of ~50 km together with a host of products related to precipitation and atmospheric state. The observation will be pan-Arctic with an exact repeat cycle of 29 days, but with partly swath overlap at high latitudes, ensuring higher repeatability.

The Copernicus Imaging Microwave Radiometer (CIMR) expansion mission [41] is one of the six Copernicus Expansion Missions currently being implemented by the European Space Agency and the European Commission. CIMR is designed to provide measurement evidence in support of developing, implementing, and monitoring the impact of the European Integrated Policy for the Arctic. Since the impact of changes in the Polar regions has profound impacts globally, CIMR will provide measurements over the global domain serving users in the Copernicus Ocean, Land, Climate and other Service application domains. Two satellites are being implemented (to be launched sequentially), each with a design lifetime of 7.5 years and sufficient fuel to last for up to 12 years (thus providing up to ~20 years of continuous data). CIMR will provide high-spatial resolution microwave imaging radiometry measurements and derived products with global coverage and sub-daily revisit in the polar regions and adjacent seas. The primary instrument is a conically scanning low-frequency, high spatial resolution multi-channel microwave radiometer. A dawn-dusk orbit has been selected to fly in coordination with MetOp-SG-B1 allowing collocated data from both missions to be obtained in the Polar regions within $+/-10$ min. A conical scanning approach utilizing a large 8m diameter deployable mesh reflector with an incidence angle of 55 degrees results in a large swath width of ~2000 km. This approach ensures 95% global coverage each day with a single satellite and no hole at the pole in terms of coverage. Channels centered at L-, C-, X-, Ku- and Ka-band are dual polarised with an effective spatial resolution of <60 km, $\leq$15 km, $\leq$15 km and <5 km (both Ka- and Ku-band with a goal of 4 km), respectively. Measurements are obtained using both a forward scan and a backward scan arc. In-flight calibration is implemented using active cold loads and a hot load complemented by periodic pitch maneuvers for both deep space and the Earth's surface. On-board processing is implemented to provide robustness against radio frequency interference and enables the computation of modified third and fourth Stokes parameters for all channels. This solution allows many Level-2 geophysical products to be derived over all earth surfaces including sea ice (concentration, thickness, drift, ice type, ice surface temperature) sea surface temperature, sea surface salinity, wind vector over the ocean surface, snow parameters, soil moisture, land surface temperature, vegetation indices, and atmospheric water parameters serving all of the Copernicus Services. The CIMR mission will be a game-changer for satellite measurements in the polar regions with a first launch expected in 2029.

The Copernicus polaR Ice and Snow Topography ALtimeter (CRISTAL) expansion mission [42] is dedicated to the measurement and monitoring of sea ice thickness and overlying snow depth. Building on the ESA CryoSat Earth Explorer and Sentinel-3 and Sentinel-6 SAR nadir pointing altimeters, it is designed to fly in an optimized orbit covering polar regions with each satellite (two are in preparation) having a design lifetime of 7.5 years. The polar omission will be lower than 2 degrees (88° inclination) and the mission will have a repeat sub-cycle shorter than 10 days. IRIS, the dual frequency Ku and Ka nadir pointing Interferometric Radar altimeter for Ice and Snow, will measure and monitor the variability of ice elevation and thickness in polar regions, as well as sea surface height, significant wave height, and ocean surface wind, with an optimized ~80m resolution along the track. The first launch of CRISTAL is currently expected in 2027.

Copernicus Hyperspectral Imaging Mission for the Environment (CHIME) [43,44] is also part of the Copernicus Expansion Missions. From 2029 to 2039, it will support agricultural services and sustainable agricultural management, meanwhile providing valuable measurements of ocean color in the coastal and ocean regions. With its 84° orbit

inclination, the hyperspectral imager is expected to provide information on phytoplankton abundance, colored dissolved organic matter and total suspended matter in the open waters and the MIZ, complementing other multispectral sensors such as Sentinel-3 OLCI, during the polar daylight season.

The Radar Observing System for Europe L-band (ROSE-L) mission is also one of the six Copernicus Expansion Missions [45] and will provide day-and-night all-weather monitoring of Earth's land, oceans and ice from 2028 to 2035. It will significantly contribute to the monitoring of polar ice sheets and ice caps, sea ice extent and seasonal snow thanks to its pan-Arctic coverage. The L-band SAR will provide complementary measurements to the C-band SAR of Sentinel-1. Sea ice-related (type, concentration, drift) measurements will have a daily revisit and a resolution better than 200 m for Level-2 processed data.

The ESA Earth Explorer 9 Far-infrared-Outgoing-Radiation Understanding and Monitoring (FORUM) mission [46], planned to fly from 2027 to 2031, will provide new insight into the Earth's radiation budget. Its sounding instrument will deliver, among many other geophysical variables, pan-Arctic cloud-sensitive sea-surface temperature measurements.

The ESA Earth Explorer 10 bi-static HARMONY mission [47] will fly in formation with the Sentinel-1D satellite, from 2028 to 2033. It will be dedicated to the observation and quantification of small-scale motion and deformation fields at (i) the air-sea interface induced by winds, waves and surface currents; (ii) solid Earth and (iii) in the cryosphere (sea ice and glacier flows). Two HARMONY satellites will be equipped with receive-only SAR antennas and will fly close to Sentinel-1D, acquiring the reflected signals from Sentinel-1D and thus providing valuable angular diversity to retrieve the respective deformation fields. An Infrared Radiometer instrument will provide complementary cloud-sensitive sea surface temperature measurements. The Arctic will be sampled every 1 to 4 days, in a 98° inclination similar to Sentinel-1.

If selected, the ESA Earth Explorer 11 candidate mission SEASTAR, a mission to study ocean sub-mesoscale dynamics and small-scale atmosphere-ocean processes [48], is expected to provide Arctic-wide ocean surface current, sea ice drift and surface wind vectors at 1 km resolution across a 100 km swath. Its Along-Track Interferometric (ATI) SAR would be the first instrument to provide observing capability for total surface current and sea ice drift vectors in a single-pass with the creation of synoptic 2D maps of the current field. Those current vectors shall be collocated with wind vectors and wave spectra. Great benefits are expected from HARMONY and SEASTAR as combining ATI Doppler estimates of current and ice drift with waves at high resolution across the ice edge would advance the understanding of wave–ice–ocean interaction in the marginal ice zone.

Finally, the Sea surface KInematics Multiscale monitoring (SKIM) mission [49] was a candidate satellite for the ESA Earth Explorer 9. It is aimed at mapping ocean surface currents, waves and ice drift up to 82° of latitude. It would have implemented a Doppler radar inherited from Chinese-French CFOSAT SWIM, allowing surface current observations with a resolution better than 40 km and a repeat cycle shorter than 10 days. It would have allowed the characterization and quantification of ocean surface kinematics and their impact on multi-scale ocean-atmosphere exchanges. Further development of the SKIM concept in preparation for future Earth Explorer opportunities is anticipated.

These future European satellite missions, either already approved or still under preparatory studies, will ensure continuity of observation with the current missions, with an improvement of the time and space sampling, as well as expanding the ocean and ice variables monitored from satellite sensors. In general, they will considerably improve the Arctic Ocean coverage. Future satellite missions are also planned by other space agencies, notably Canada, China, India, Japan, Russia and the USA with, e.g., the Joint Polar Satellite System (JPSS), MAGIC-NGGM, OceanSat-3, the NASA/ISRO NI-SAR mission and the Meteor-MP constellation, that will further improve the observational capacity in the Arctic, in combination with the European missions.

The expected benefits of these future satellite missions, and possible remaining gaps, in the observation of the sea ice and ocean geophysical parameters, are discussed in more detail in the following sub-sections.

4.1. Sea Ice-Related Parameters

From 2028, sea ice drift and deformation observations will be well covered by the approved CIMR, ROSE-L and HARMONY missions, complementing Sentinel-1 capacities. Until then, studies will, however, be limited by the spatiotemporal restricted coverage of SAR acquisitions in HH and HV modes.

Regarding sea ice freeboard height and sea ice thickness, an observational gap is expected in the near future. The CryoSat-2 and SMOS (for thin ice) missions (end-of-life (EOL) currently planned in 2024 and 2025, respectively) are far beyond their design lifetimes of 3 years, and while functioning well today, are coming toward the end of their operational lives due to depletion of consumables (fuel used to maintain the orbit and battery life). This means that there is a significant risk that these variables will not be measured beyond the Sentinel-3 orbit limit (81.5°N) until the launch of the CIMR and CRISTAL missions in 2028–2029. The NASA SMAP mission may provide continuity to L-band measurements of this sea ice. NASA/CNES SWOT (planned to be operated between 2022 and 2026) will complement the Sentinel-3 measurements only up to 78°N. Hence, there may be a major step-back for Arctic sea ice thickness monitoring and studies due to orbit limitations of the available satellites during the period 2026–2027.

Sea ice concentration/extent observations are presently obtained by AMSR-2 on Aqua, MetOp and Sentinel-3. CIMR will provide a step change in functionality offering C-band at a gridded spatial resolution of 5–10 km in addition to K- and Ka-band measurements at <5 km spatial resolution. MetOp-SG, ROSE-L and S3-NG-T will secure extensive observational capability, sufficient for continuous regular assimilation and updates of Arctic Ocean forecasting systems such as, e.g., the Copernicus Arctic Monitoring and Forecasting Service. The Sentinel-3 Next Generation Topography mission (S3-NG-T) will include an imaging interferometer and a nadir altimeter that will guarantee the future of Sentinel-3 SRAL measurements while enhancing performance in the 2032+ timeframe.

4.2. Ocean-Related Parameters

Ocean color analysis is currently performed with Sentinel-3 and Aqua MODIS data. CHIME will ensure an observational continuity in the coastal zones starting in 2029, but the coverage will remain limited to 84°N, covering most of the ice-free waters during the daylight season, including the productive MIZ. The Sentinel-3 Next Generation Optical mission (S3NG-O) will include an advanced OLCI instrument (AOLCI) that will guarantee the future of OLCI measurements while enhancing performance in the 2032+ timeframe.

Sea Surface Temperature is currently provided by the Sentinel-3 Sea and Land Surface Temperature Radiometer (SLSTR). This multi-frequency thermal infrared radiometer is the reference SST mission providing accurate SST based on the use of cooled detectors, the use of two onboard calibration blackbodies with performance traceable to ST and an innovative dual view conical scanning technique. These design elements have a long unbroken heritage from ATSR-1 first flown on ERS-1 in the 1990s out to 2032 in the form of Sentinel-3C and Sentinel-3D. After this, the Sentinel-3 Next Generation Optical mission (S3NG-O) will include an advanced SLSTR instrument (ASLSTR) that will guarantee the future of SLSTR measurements while enhancing performance in the 2032+ timeframe.

As for the sea ice freeboard parameter, sea surface height observation in the Arctic Ocean highly relies on CryoSat-2 and Sentinel-3. A CryoSat-2 EOL in 2024 as it is planned today, before the CRISTAL launch expected end of 2027, will strongly limit the Arctic coverage with high-quality radar altimeter data (SAR and SARin modes), as the orbits of the Sentinel-3 and SWOT missions, which should be still operated during the CryoSat-2/CRISTAL gap, are limited to 81.5°N and 78°N, respectively. The Sentinel-3 Next Generation Topography mission (S3-NG-T) will include an imaging interferometer and

a nadir altimeter that will guarantee the future of Sentinel-3 SRAL measurements while enhancing performance in the 2032+ timeframe.

The same applies to significant wave height measurements, which rely on Cryosat-2 for higher latitudes and to a more limited extent, Sentinel-3 SRAL. Despite the currently flying CFOSAT and planned SWOT missions, observations will be limited to the Sentinel-3 orbit coverage until 2027 and CRISTAL launch. ROSE-L will provide additional capacity with pan-Arctic coverage from 2028.

Ocean surface currents are currently only partially observed, either in terms of radial velocity derived from the Doppler shift from SAR observations (Sentinel-1) or as cross-track geostrophic currents derived from the radar altimeter sea surface height measurements. Reprocessing existing SAR data for retrieval of the Doppler shift is, therefore, highly recommended. Moreover, HARMONY will bring new bistatic observations in this field in 2028. A few years later, the proposed Earth Explorer mission SEASTAR could allow pan-Arctic surface current and sea ice drift measurement at 1 km resolution. Additionally, a future decision for the SKIM-like mission could complement those observations up to 82°N at a mean repeat cycle of 4 days.

Despite the various missions measuring ocean surface wind, the observations will be limited to 82°N after CFOSAT EOL and before HARMONY, CRISTAL, CIMR and ROSE-L provide a complementary and multi-sensor complete coverage of the Arctic Ocean. In addition, it should be noted that none of these missions will retrieve near-surface wind speed and direction in the presence of sea ice, which will remain as an observational gap when addressing the challenge of better understanding the air/sea ice/ocean interactions, Arctic weather and ocean predictability in the high latitude and Arctic Ocean.

Finally, sea surface salinity was not measured before the SMOS mission in 2009. Today both the SMOS and SMAP missions provide measurements of salinity derived from L-band microwave radiometers. It is, therefore, highly desirable to sustain salinity measurement from SMOS and SMAP until CIMR-A is launched in 2029, to ensure continuity and overlap of measurements and stability of the climate data record of sea surface salinity.

5. Conclusions

Comprehensive and quantitative understanding of the Arctic Amplification, sea ice break-up event, gyre spin-up, eddy generation and decay and dynamics in the MIZ are all limited due to observational gaps and limited process understanding. Exploitation and full use of the multi-sensor satellite measurements are, therefore, urgently needed although still challenging due to the lack of high-quality validation. In the future, new products and estimates of variables are expected to gradually emerge from the existing observations due to novel strategies and approaches including data-driven co-variability analyses, machine learning and Artificial Intelligence. Blended with data from new satellite missions this is, therefore, anticipated to accelerate our quantitative understanding and knowledge, allowing for significant advances in re-analyses and provision of long time series resolving sea ice and ocean parameters as well as major interactive processes and mutual feedbacks in the Arctic Ocean.

Satellite observations are fundamental in the monitoring of the Arctic due to the harsh climate, accessibility, and the difficulty to gather relevant and quantitative in-situ measurements above, at, and below the ocean surface. Therefore, the quality, continuity and novelty of satellite acquisitions are of prime importance. As such it is also highly urgent to secure proper validation and uncertainty assessments, requiring also continued dedicated ground truth measurements of essential ocean and ice variables, process studies and under-ice observations within the Arctic Ocean, and particularly in the marginal ice zone. This will require regular access to icebreaker facilities and the utilization of new technological instrumentation built for long-term in-water and surface observations, with efficient energy demands and capabilities for data retrieval also in year-round and seasonally ice-covered waters. The sustainability of field investigations will also require

sharing of opportunities and data through international cooperation and coordination building on the FAIR principles.

In this review, we have evaluated the ability of future approved European missions, notably CRISTAL, CIMR, CHIME, ROSE-L, and HARMONY, blended with the continuity of existing operational missions such as Sentinel-1 C/D, Sentinel-3 C/D and MetOp-SG to fill observation gaps and advance the understanding and prediction of environmental and climate changes in the Arctic Ocean. In this context, complementarity and overlap of missions committed and planned by other space agencies will be important to overcome observational gaps. related to spatial-temporal coverage, sensor and product resolution, measurement capacity, and orbit inclinations. Some proposed but not yet selected missions such as SEASTAR will significantly contribute to filling some of these gaps for the ocean and sea ice aspects, as will mission concepts such as SKIM, building on the success of CFOSAT.

Because of the difficulty to observe the Arctic Ocean with the spatial-temporal resolution that would be needed, either from satellites or in-situ instruments, most studies rely today on the synergy between different types of satellite observations, in-situ measurements and numerical modeling, including re-analyses. Advances expected to emerge from the development of a Digital Arctic Twin, collocated and combined multi-modal data (in-situ and satellite) and model-driven physical constrained analyses, as well as the use of artificial intelligence, will strengthen the ability to deliver more reliable estimates, and hence predictions, of sea ice deformation, break-up, leads formation, new ice formation, sea ice freeboard height, sea ice volume and mean sea level. Such information about the Arctic environment and its changes will be increasingly important when human presence is expected to grow through increased shipping, fisheries and other activities in the Arctic Ocean. By bringing new observations, often at a higher spatial resolution, the approved future satellite missions will also contribute to improving the ability for validation of and assimilation in higher-resolution numerical models. They will thus contribute to a better understanding of the complex processes in the Arctic Ocean and allow the revision and upgrading of the sea ice thermodynamics and rheology modeling approaches to better reproduce the complexity of the ocean-air-sea ice interactions, including feedback processes. In turn, more accurate simulations, re-analyses and reliable reconstruction of long time series can be expected, which are of prime importance to characterize an Arctic Ocean in constant transformation.

Author Contributions: Conceptualization, J.A.J. and C.D.; methodology, S.L., M.C., J.A.J., L.H.P. and B.C.; data analysis, S.L., M.C., I.E., J.W.R., F.A., A.K., F.C., S.H., E.O. and L.H.P.; draft manuscript S.L. and M.C.; writing and review, M.C., S.L., J.A.J., L.H.P., I.E., B.C., R.F. and E.F.; project administration, J.A.J.; funding acquisition, J.A.J. and C.D. All authors have read and agreed to the published version of the manuscript.

Funding: This work is part of the ARKTALAS Hoavva study funded by the European Space Agency under the Contract 4000127401/19/NL/LF.

Data Availability Statement: Background data for all figures in this publication is based on The CEOS Database available at: http://database.eohandbook.com and on the WMO OSCAR database available at https://space.oscar.wmo.int/satellites.

Conflicts of Interest: C.D. is employed by the European Space Agency (ESA).

References

1. Ding, Q.; Schweiger, A.; L'heureux, M.; Steig, E.J.; Battisti, D.S.; Johnson, N.C.; Blanchard-Wrigglesworth, E.; Po-Chedley, S.; Zhang, Q.; Harnos, K.; et al. Fingerprints of internal drivers of Arctic sea ice loss in observations and model simulations. *Nat. Geosci.* **2019**, *12*, 28–33. [CrossRef]
2. Johannessen, O.M.; Alexandrov, V.; Frolov, I.Y.; Sandven, S.; Pettersson, L.H.; Bobylev, L.P.; Kloster, K.; Smirnov, V.G.; Mironov, Y.U.; Babich, N.G. *Remote Sensing of Sea Ice in the Northern Sea Route: Studies and Applications*; Nansen Centers Polar Series No. 4; Springer: Berlin/Heidelberg, Germany, 2007; p. 472. ISBN 3-540-24448-4. [CrossRef]
3. Johannessen, O.M.; Bobylev, L.; Shalina, E.V.; Sandven, S. (Eds.) *Sea Ice in the Arctic–Past, Present and Future*; Springer Polar Series; Springer: Cham, Switzerland, 2020; Volume 557. [CrossRef]

4. Stroeve, J.; Serreze, M.; Drobot, S.; Gearheard, S.; Holland, M.; Maslanik, J.; Meier, W.; Scambos, T. Arctic sea ice extent plummets in 2007. *Eos Trans. AGU* **2008**, *89*, 13–14. [CrossRef]
5. Parkinson, C.L.; Comiso, J.C. On the 2012 record low Arctic sea ice cover: Combined impact of preconditioning and an August storm. *Geophys. Res. Lett.* **2013**, *40*, 1356–1361. [CrossRef]
6. Landrum, L.; Holland, M.M. Extremes become routine in an emerging new Arctic. *Nat. Clim. Chang.* **2020**, *10*, 1108–1115. [CrossRef]
7. Serreze, M.C.; Francis, J.A. The Arctic amplification debate. *Clim. Change* **2006**, *76*, 241–264. [CrossRef]
8. Rantanen, M.; Karpechko, A.Y.; Lipponen, A.; Nordling, K.; Hyvärinen, O.; Ruosteenoja, K.; Vihma, T.; Laaksonen, A. The Arctic has warmed nearly four times faster than the globe since 1979. *Commun. Earth Environ.* **2022**, *3*, 168. [CrossRef]
9. Isaksen, K.; Nordli, Ø.; Ivanov, B.; Køltzow, M.A.Ø.; Aaboe, S.; Gjelten, H.M.; Mezghani, A.; Eastwood, S.; Førland, E.; Benestad, R.E.; et al. Exceptional warming over the Barents area. *Sci. Rep.* **2022**, *12*, 9371. [CrossRef]
10. Box, J.E.; Colgan, W.T.; Christensen, T.R.; Schmidt, N.M.; Lund, M.; Parmentier, F.-J.W.; Brown, R.; Bhatt, U.S.; Euskirchen, E.S.; Romanovsky, V.E.; et al. Key indicators of Arctic climate change: 1971–2017. *Environ. Res. Lett.* **2019**, *14*, 045010. [CrossRef]
11. Pettersson, L.H.; Kjelaas, A.G.; Kovalevsky, D.V.; Hasselmann, K. Climate Change Impact on the Arctic Economy. In *Sea Ice in the Arctic*; Springer Polar Sciences; Johannessen, O., Bobylev, L., Shalina, E., Sandven, S., Eds.; Springer: Cham, Switzerland, 2020. [CrossRef]
12. Regan, H.; Lique, C.; Talandier, C.; Meneghello, G. Response of total and eddy kinetic energy to the recent spinup of the Beaufort Gyre. *J. Phys. Oceanogr.* **2020**, *50*, 575–594. [CrossRef]
13. Cassianides, A.; Lique, C.; Korosov, A. Ocean Eddy Signature on SAR-Derived Sea Ice Drift and Vorticity. *Geophys. Res. Lett.* **2021**, *48*, e2020GL092066. [CrossRef]
14. Collard, F.; Marié, L.; Nouguier, F.; Kleinherenbrink, M.; Ehlers, F.; Ardhuin, F. Wind-Wave Attenuation in Arctic Sea Ice: A Discussion of Remote Sensing Capabilities. *J. Geophys. Res. Ocean* **2022**, *127*, e2022JC018654. [CrossRef]
15. Rheinlænder, J.W.; Davy, R.; Ólason, E.; Rampal, P.; Spensberger, C.; Williams, T.D.; Korosov, A.; Spengler, T. Driving mechanisms of an extreme winter sea-ice breakup event in the Beaufort Sea. *Geophys. Res. Lett.* **2021**, *49*, e2022GL099024. [CrossRef]
16. Boutin, G.; Williams, T.; Horvat, C.; Brodeau, L. Modelling the Arctic wave-affected marginal ice zone: A comparison with ICESat-2 observations. *Phil. Trans. R. Soc. A* **2022**, *380*, 20210262. [CrossRef]
17. Esau, I.; Pettersson, L.H.; Cancet, M.; Chapron, B.; Chernokulsky, A.; Donlon, C.; Sizov, O.; Soromotin, A.; Johannesen, J.A. The Arctic Amplification and Its Impact: A Synthesis through Satellite Observations. *Remote Sens.* **2023**, *15*, 1354. [CrossRef]
18. Cancet, M.; Lyard, F.; Fouchet, E. Impact of the sea ice friction on ocean tides in the Arctic Ocean, modelling insights at various time and space scales. *manuscript in preparation*.
19. Duncan, B.N.; Ott, L.E.; Abshire, J.B.; Brucker, L.; Carroll, M.L.; Carton, J.; Comiso, J.C.; Dinnat, E.P.; Forbes, B.C.; Gonsamo, A.; et al. Space-Based Observations for Understanding Changes in the Arctic-Boreal Zone. *Rev. Geophys.* **2020**, *58*, e2019RG000652. [CrossRef]
20. Myers-Smith, I.H.; Kerby, J.T.; Phoenix, G.K.; Bjerke, J.W.; Epstein, H.E.; Assmann, J.J.; John, C.; Andreu-Hayles, L.; Angers-Blondin, S.; Beck, P.S.A.; et al. Complexity revealed in the greening of the Arctic. *Nat. Clim. Change* **2020**, *10*, 106–117. [CrossRef]
21. Lawrence, H.; Bormann, N.; Sandu, I.; Day, J.; Farnan, J.; Bauer, P. Use and impact of Arctic observations in the ECMWF Numerical Weather Prediction system. *Q. J. R. Meteorol. Soc.* **2019**, *145*, 3432–3454. [CrossRef]
22. Stammer, D.; Ray, R.D.; Andersen, O.B.; Arbic, B.K.; Bosch, W.; Carrère, L.; Cheng, Y.; Chinn, D.S.; Dushaw, B.D.; Egbert, G.D.; et al. Accuracy assessment of global barotropic ocean tide models. *Rev. Geophys.* **2014**, *52*, 243–282. [CrossRef]
23. Willmes, S.; Heinemann, G. Pan-Arctic lead detection from MODIS thermal infrared imagery. *Ann. Glaciol.* **2015**, *56*, 29–37. [CrossRef]
24. Armitage, T.W.K.; Bacon, S.; Ridout, A.L.; Thomas, S.F.; Aksenov, Y.; Wingham, D.J. Arctic sea surface height variability and change from satellite radar altimetry and GRACE, 2003-2014. *J. Geophys. Res. Ocean.* **2016**, *121*, 4303–4322. [CrossRef]
25. Armitage, T.W.K.; Bacon, S.; Ridout, A.L.; Petty, A.A.; Wolbach, S.; Tsamados, M. Arctic Ocean surface geostrophic circulation 2003–2014. *Cryosphere* **2017**, *11*, 1767–1780. [CrossRef]
26. Gao, Y.; Drange, H.; Johannessen, O.M.; Pettersson, L.H. Sources and pathways of 90Sr in the North Atlantic–Arctic region: Present day and global warming. *J. Environ. Radioact.* **2009**, *100*, 375–395. [CrossRef]
27. Donlon, C.J.; Minnett, P.J.; Fox, N.; Wimmer, W. Strategies for the Laboratory and Field Deployment of Ship-Borne Fiducial Reference Thermal Infrared Radiometers in Support of Satellite-Derived Sea Surface Temperature Climate Data Records. In *Optical Radiometry for Oceans Climate Measurements*; Experimental Methods in Sciences; Zibordi, G., Donlon, C., Parr, A., Eds.; Elsevier: Amsterdam, The Netherlands, 2015; Volume 47, p. 697. ISBN 9780124170117.
28. Plummer, S.; Lecomte, P.; Doherty, M. The ESA Climate Change Initiative (CCI): A European contribution to the generation of the Global Climate Observing System. *Remote Sens. Environ.* **2017**, *203*, 2–8. [CrossRef]
29. Kudryavtsev, V.; Yurovskaya, M.; Chapron, B.; Collard, F.; Donlon, C. Sun glitter imagery of ocean surface waves. Part 1: Directional spectrum retrieval and validation. *J. Geophys. Res. Ocean.* **2017**, *122*, 1369–1383. [CrossRef]
30. Raj, R.P.; Andersen, O.B.; Johannessen, J.A.; Gutknecht, B.D.; Chatterjee, S.; Rose, S.K.; Bonaduce, A.; Horwath, M.; Ranndal, H.; Richter, K.; et al. Arctic Sea Level Budget Assessment during the GRACE/Argo Time Period. *Remote Sens.* **2020**, *12*, 2837. [CrossRef]

31. Donlon, C.; Berruti, B.; Buongiorno, A.; Ferreira, M.-H.; Féménias, P.; Frerick, J.; Goryl, P.; Klein, U.; Laur, H.; Mavrocordatos, C.; et al. The Global Monitoring for Environment and Security (GMES) Sentinel-3 mission. *Remote Sens. Environ.* **2012**, *120*, 37–57. [CrossRef]
32. Kwok, R.; Kacimi, S.; Webster, M.A.; Kurtz, N.T.; Petty, A.A. Arctic snow depth and sea ice thickness from ICESat-2 and CryoSat-2 freeboards: A first examination. *J. Geophys. Res. Ocean.* **2020**, *125*, e2019JC016008. [CrossRef]
33. Garnier, F.; Fleury, S.; Garric, G.; Bouffard, J.; Tsamados, M.; Laforge, A.; Bocquet, M.; Fredensborg Hansen, R.M.; Remy, F. Advances in altimetric snow depth estimates using bi-frequency SARAL and CryoSat-2 Ka–Ku measurements. *Cryosphere* **2021**, *15*, 5483–5512. [CrossRef]
34. Ricker, R.; Hendricks, S.; Kaleschke, L.; Tian-Kunze, X.; King, J.; Haas, C. A weekly Arctic sea-ice thickness data record from merged CryoSat-2 and SMOS satellite data. *Cryosphere* **2017**, *11*, 1607–1623. [CrossRef]
35. Nakamura, K.; Wakabayashi, H.; Uto, S.; Ushio, S.; Nishio, F. Observation of sea-ice thickness using envisat data from lützow-holm bay, East Antarctica. *IEEE Geosci. Remote Sens. Lett.* **2009**, *6*, 277–281. [CrossRef]
36. Wakabayashi, H.; Matsuoka, T.; Nakamura, K.; Nishio, F. Polarimetric characteristics of sea ice in the sea of okhotsk observed by airborne l-band SAR. *IEEE Trans. Geosci. Remote Sens.* **2004**, *42*, 2412–2425. [CrossRef]
37. Shamshiri, R.; Eide, E.; Høyland, K.V. Spatio-temporal distribution of sea-ice thickness using a machine learning approach with Google Earth Engine and Sentinel-1 GRD data. *Remote Sens. Environ.* **2022**, *270*, 112851. [CrossRef]
38. Dawson, G.J.; Landy, J.C.; Tsamados, M.; Komarov, A.S.; Howell, S.; Heorton, H.; Krumpen, T. A 10-year record of Arctic summer sea ice freeboard from CryoSat-2. *Remote Sens. Environ.* **2022**, *268*, 112744. [CrossRef]
39. Fu, L.L.; Alsdorf, D.; Morrow, R.; Rodriguez, E.; Mognard, N. *SWOT: The Surface Water and Ocean Topography Mission: Wide-Swath Altimetric Elevation on Earth*; Jet Propulsion Laboratory, National Aeronautics and Space Administration: Pasadena, CA, USA, 2012.
40. Accadia, C.; Schlüssel, P.; Phillips, P.L.; Wilson, J.W. The EUMETSAT polar system second generation (EPS-SG) Micro-Wave and Sub-millimetre wave imaging missions. *Proc. SPIE* **2013**, *8889*, 66–74. [CrossRef]
41. Donlon, C. (Ed.) *Copernicus Imaging Microwave Radiometer (CIMR) Mission Requirements Document*, version 5; ref. ESA-EOPSM-CIMR-MRD-3236; European Space Agency: Noordwijk, The Netherlands, 2022.
42. Kern, M.; Ressler, G.; Cullen, R.; Parrinello, T.; Casal, T.; Bouffard, J. *Copernicus polaR Ice and Snow Topography ALtimeter (CRISTAL) Mission Requirements Document*, version 2.0; European Space Agency, ESTEC: Noordwijk, The Netherlands, 2019.
43. Rast, M.; Ananasso, C.; Bach, H.; Ben-Dor, E.; Chabrillat, S.; Colombo, R.; Strobl, P. Copernicus Hyperspectral Imaging Mission for the Environment: Mission Requirements Document. 2019. Available online: https://ris.utwente.nl/ws/portalfiles/portal/228969030/Copernicus_CHIME_MRD_v2.1_Issued20190723.pdf (accessed on 11 April 2023).
44. Rast, M.; Nieke, J.; Adams, J.; Isola, C.; Gascon, F. Copernicus Hyperspectral Imaging Mission for the Environment (Chime). In Proceedings of the 2021 IEEE International Geoscience and Remote Sensing Symposium IGARSS, Brussels, Belgium, 11–16 July 2021; pp. 108–111.
45. Davidson, M.; Chini, M.; Dierking, W.; Djavidnia, S.; Haarpaintner, J.; Hajduch, G.; Laurin, G.; Lavalle, M.; López-Martínez, C.; Nagler, T.; et al. Copernicus L-band SAR Mission Requirements Document. 2018. Available online: https://esamultimedia.esa.int/docs/EarthObservation/Copernicus_L-band_SAR_mission_ROSE-L_MRD_v2.0_issued.pdf (accessed on 11 April 2023).
46. Pachot, C.; Dominguez, B.C.; Oetjen, H.; Sierk, B.; Mariani, F.; Riel, S.; Rodrigues, G.; Copano, M.; Carou, A.M.; Palchetti, L.; et al. The infrared Fourier transform spectrometer and the infrared imager instrument concepts for the FORUM mission, ESA's 9th Earth Explorer. In *Sensors, Systems, and Next-Generation Satellites XXIV*; International Society for Optics and Photonics: Bellingham, WA, USA, 2020; Volume 11530, p. 115300D.
47. Lopez-Dekker, J.F.; Biggs, J.; Chapron, B.; Hooper, A.; Kääb, A.; Massina, S.; Mouginot, J.; Buongiorno Nardelli, B.; Pasquero, C.; Prats-Iraola, P.; et al. The Harmony mission: Applications and preliminary performance. In Proceedings of the 6th Workshop on Advanced RF Sensors and Remote Sensing Instruments, ARSI'19, Noordwijk, The Netherlands, 11–13 November 2019.
48. Gommenginger, C.; Chapron, B.; Hogg, A.; Buckingham, C.; Fox-Kemper, B.; Eriksson, L.; Soulat, F.; Ubelmann, C.; Ocampo-Torres, F.; Nardelli, B.B.; et al. SEASTAR: A Mission to Study Ocean Submesoscale Dynamics and Small-Scale Atmosphere-Ocean Processes in Coastal, Shelf and Polar Seas. *Front. Mar. Sci.* **2019**, *6*, 457. [CrossRef]
49. Ardhuin, F.; Brandt, P.; Gaultier, L.; Donlon, C.; Battaglia, A.; Boy, F.; Casal, T.; Chapron, B.; Collard, F.; Cravatte, S.; et al. SKIM, a candidate satellite mission exploring global ocean currents and waves. *Front. Mar. Sci.* **2019**, *6*, 209. [CrossRef]